

UC Irvine

UC Irvine Electronic Theses and Dissertations

Title

Development of Synthetic Materials for RNA Delivery

Permalink

<https://escholarship.org/uc/item/4jb3f35w>

Author

Yang, Dongchu

Publication Date

2019

Peer reviewed|Thesis/dissertation

UNIVERSITY OF CALIFORNIA,
IRVINE

Development of Synthetic Materials for RNA Delivery

DISSERTATION

submitted in partial satisfaction of the requirements
for the degree of

DOCTOR OF PHILOSOPHY

in Chemistry

by

Dong-Chu Yang

Dissertation Committee:
Professor Zhibin Guan, Chair
Professor Kenneth Shea
Assistant Professor Shane Ardo

2019

DEDICATION

To

My parents and family

It is your love that keeps me moving forward.

To

My friends, teachers, and partners

I cannot accomplish this without your guidance, help, and support.

TABLE OF CONTENTS

	Page
LIST OF FIGURES	vi
LIST OF TABLES	xi
LIST OF SCHEMES	xii
ACKNOWLEDGMENTS	xiii
CURRICULUM VITAE	xiv
ABSTRACT OF THE DISSERTATION	xvii
CHAPTER 1: Introduction to Synthetic Materials for RNA Delivery	
1.1 Introduction to Gene Therapy and RNA Therapy	1
1.2 Therapeutics Based on RNA interference	3
1.3 mRNA Therapeutics	5
1.4 Gene Editing	9
1.5 Challenges of RNA Therapeutics	13
1.6 Overview: Gene Delivery Vehicles	14
1.7 Non-viral Synthetic Vectors	20
1.8 Previous Work in Guan Lab	26
1.9 Summary and outlook	29
1.10 References	30
CHAPTER 2: Multivalent Peptide-functionalized Bioreducible Polymers for Universal Delivery of Various RNAs	
2.1 Introduction and Project Design	38
2.2 Design and Synthesis of MPBP	41

2.3 Biophysical Study of MPBP-RNA Complexes	44
2.4 siRNA Delivery	51
2.5 Fluc mRNA and eGFP mRNA Delivery	55
2.6 Confocal Study of Cellular Uptake and Endosomal Escape	61
2.7 Replicon mRNA Delivery	66
2.8 CRISPR-Cas9 Delivery	67
2.9 Conclusions	70
2.10 Acknowledgement	71
2.11 References	71
2.12 Experimental	78
2.13 Flow cytometry Output	100
2.14 ^1H NMR Spectra	115
CHAPTER 3: Peptide-functionalized Bioreducible Amphiphilic Vectors for siRNA Delivery	
3.1 Introduction and Project Design	122
3.2 Design and Synthesis of PBAV	123
3.3 Biophysical Study of PBAV-siRNA Complexes	126
3.4 siRNA Delivery	128
3.5 Conclusions	136
3.6 References	137
3.7 Experimental	139
3.8 HPLC Traces and MALDI-MS Spectra	155
CHAPTER 4: Poly(thymine)-functionalized Bioreducible Polymers for mRNA Delivery	
4.1 Introduction and Project Design	161

4.2 Design and Synthesis of PTBP	166
4.3 Biophysical Study of PTBP-mRNA Complexes	169
4.4 mRNA Delivery	172
4.5 Conclusions	175
4.6 References	176
4.7 Experimental	178
4.8 ^1H NMR Spectra	189
 CHAPTER 5: Hybrid Organic-Inorganic Quantum Dot Superlattices for Enhanced Charge Transport	
5.1 Introduction and Project Design	192
5.2 Design, Synthesis and Characterization of Functional Molecular Wires	194
5.3 Solid-state Ligand Exchange with TPE and Characterization	198
5.4 Solution-phase Ligand Exchange with mTPE and Characterization	199
5.5 Film Construction and Morphology Study	202
5.6 FET Measurements	206
5.7 Conclusions	207
5.8 Acknoeledgeement	207
5.9 Notes and References	208
5.10 Experimental	211
5.11 References for Experimental	218
5.12 NMR Spectra	220

LIST OF FIGURES

	Page
Figure 1.1A The central dogma of molecular biology	2
Figure 1.1B Chemical structures of DNA subunits	2
Figure 1.1C Chemical structures of RNA subunits	2
Figure 1.2 The RNA interference pathway	5
Figure 1.3 Mechanisms of mRNA therapeutics	7
Figure 1.4 The mechanism of CRISPR-Cas9 gene editing	11
Figure 1.5A DNA method to deliver CRISPR/Cas9 machinery	12
Figure 1.5B RNA method to deliver CRISPR/Cas9 machinery	12
Figure 1.5C RNA and protein method to deliver CRISPR/Cas9 machinery	12
Figure 1.5D The mechanism of RNA-based CRISPR-Cas9 gene editing	12
Figure 1.6 Viral vectors and non-viral vectors for gene delivery	16
Figure 1.7 Different cellular uptake mechanisms of nanoparticles	17
Figure 1.8 Different mechanisms of endosomal escape.	19
Figure 1.9A Chemical structures of non-viral synthetic vectors for siRNA delivery	21
Figure 1.9B Chemical structures of non-viral synthetic vectors for mRNA delivery	21
Figure 1.10 Chemical structures of biodegradable polymers for gene delivery	24
Figure 1.11 Multifunctional dendronized peptide polymer system for siRNA delivery and mRNA delivery.	27
Figure 1.12A Dendritic peptide bolaamphiphiles for siRNA delivery.	29
Figure 1.12B Discrete dipeptide bolaamphiphiles for siRNA delivery.	29
Figure 2.1 Concept of multivalent peptide-functionalized bio reducible polymer (MPBP) vectors for universal RNA delivery	40

Figure 2.2	A small library of MPBPs with different polymer architectures and side chain functionalization	42
Figure 2.3	Initial Fluc mRNA delivery screening of different MPBPs functionalized with various linear peptides	43
Figure 2.4	Gel electrophoresis study of MPBP-siRNA complexation	45
Figure 2.5	Gel electrophoresis study of MPBP-eGFP mRNA complexation	45
Figure 2.6	Gel electrophoresis study to determine mRNA degradation and protection	47
Figure 2.7	DLS measurement of different MPBP-siRNA complexes	49
Figure 2.8	DLS measurement of different MPBP-Fluc mRNA complexes	49
Figure 2.9	Stability of different MPBP-Fluc mRNA complexes in PBS buffer	50
Figure 2.10	A representative stained TEM image of G1-100LP-siRNA complexes formed at N/P = 15	50
Figure 2.11	TEM images and size distribution of representative MPBP-RNA nanoparticle complexes stained with 2% wt uranyl acetate	51
Figure 2.12	Transfection screening of G0-100LP-siRNA complexes	53
Figure 2.13	Gene silencing and cell viability results of different MPBP-siRNA complexes in serum-free media	53
Figure 2.14	Transfection screening of different MPBP-siRNA complexes in firefly luciferase-expressing HEK-293 cells	54
Figure 2.15	Gene silencing and cell viability results of different MPBP-siRNA complexes in 10% FBS-containing media	55
Figure 2.16	Transfection screening of G0-100LP-Fluc mRNA complexes at various N/P ratios	57
Figure 2.17	Transfection screening of G1-100LP-Fluc mRNA complexes at various N/P ratios	57
Figure 2.18	Fluc mRNA transfection using different MPBPs at their optimal N/P ratios in serum-free media	58
Figure 2.19	eGFP mRNA transfection using different MPBPs at their optimal N/P ratios in serum-free media	59

Figure 2.20	Fluc mRNA transfection using different MPBPs at their optimal N/P ratios in 10% FBS-containing media	60
Figure 2.21	eGFP mRNA transfection using different MPBPs at their optimal N/P ratios in 10% FBS-containing media	60
Figure 2.22	Cytotoxicity of the MPBP vectors against NIH 3T3 cells assayed using a LDH assay	62
Figure 2.23	Cellular uptake of MPBP-Cy5 Fluc mRNA complexes as observed by confocal fluorescence microscopy	63
Figure 2.24	Cellular uptake of MPBP-Cy5 Fluc mRNA complexes in NIH 3T3 cells quantified by flow cytometry	64
Figure 2.25	Endosomal escape by intracellular trafficking for MPBP-Cy5 eGFP mRNA complexes	65
Figure 2.26	Replicon mRNA transfection of different MPBPs	66
Figure 2.27	Comparison of luciferase expression between replicon mRNA delivery and regular Fluc mRNA delivery	67
Figure 2.28	Transfection results of CRISPR-Cas9 delivery	69
Figure 2.29	Endosomal escape by intracellular trafficking for MPBP-Cy5 siRNA complexes	70
Figure 3.1	The designed library of PBAVs with different hydrophobic cores and peptide-functionalization	124
Figure 3.2	Gel electrophoresis study of PBAV-siRNA complexation	127
Figure 3.3	Gene silencing and cell viability results of representative bolaamphiphile-siRNA complexes transfection in serum-free media	129
Figure 3.4	Gene silencing and cell viability results of representative monoamphiphile-siRNA complexes transfection in serum-free media	130
Figure 3.5	Gene silencing and cell viability results of fluorocarbon PBAVs-siRNA complexes transfection in serum-free media	131
Figure 3.6	Gene silencing and cell viability results of fluorocarbon PBAVs-siRNA complexes transfection under different siRNA concentrations	132

Figure 3.7	Gene silencing and cell viability results of fluorocarbon PBAVs-siRNA complexes transfection at different N/P ratios	133
Figure 3.8	Concentration-dependent siRNA transfection studies of effective fluorocarbon bolaamphiphiles	134
Figure 3.9	Concentration-dependent cell viability studies of fluorocarbon monoamphiphile-siRNA complexes	135
Figure 3.10	Circular dichroism spectra of deprotected linear peptides	136
Figure 4.1	The general eukaryotic mRNA structure and hydrogen binding between adenine and thymine	163
Figure 4.2A	Chemical structures of DNA and PNA analogues	164
Figure 4.2B	Triple base pairing between different PNA and DNA	164
Figure 4.3	The design of poly(thymine)-functionalized bioreducible polymers (PTBP) for mRNA delivery	165
Figure 4.4	Graphic illustration of PTBP-mRNA complexation processes	170
Figure 4.5	Gel binding assays of PTBP-eGFP mRNA complexes	171
Figure 4.6	Fluc mRNA transfection using different PTBPs at different N/P ratios in NIH 3T3 cells	172
Figure 4.7	eGFP mRNA transfection using different PTBPs at different N/P ratios in NIH 3T3 cells	173
Figure 4.8	Models of initiation processes in protein synthesis	174
Figure 5.1	Hybrid superlattice nanocomposites (HSNs) of PbSe QDs and molecular wires	194
Figure 5.2	Structure and HOMO/LUMO positions of functional molecular wires	195
Figure 5.3	Normalized absorption spectra of nonfunctional molecular wire, mTPE and TPE in THF	197
Figure 5.4	Solid-state ligand exchange and characterization	199
Figure 5.5	Absorption spectrum of synthesized oleate-capped PbSe QDs	200
Figure 5.6	TEM image of synthesized oleate-capped PbSe QDs	201

Figure 5.7	Characterization of solution-phase ligand exchange	201
Figure 5.8	SEM plan view images and 2D GISAXS patterns of PbSe QD films	203
Figure 5.9	SEM plan view images and related fast fourier transformation analyses of PbSe QD films	203
Figure 5.10	SEM plan view images of PbSe-mTPE QD films after solvent annealing	205
Figure 5.11	Graphic illustration of methods for constructing QD superlattice films	205
Figure 5.12	<i>I-V</i> plot of TPE-capped PbSe QD FETs	206

LIST OF TABLES

	Page
Table 2.1 DLS measurements of size and Zeta potential of complexes between MPBPs and siRNA	48
Table 2.2 DLS measurements of size and Zeta potential of complexes between MPBPs and Fluc mRNA	48
Table 3.1 Chemical structures of PBAV library with different hydrophobic cores and peptide-functionalization	125
Table 3.2 Nanoparticle sizes of PBAV-siRNA complexes determined by DLS	128
Table 4.1 Detailed summary of synthesized PTBPs	168
Table 4.2 Nanoparticle sizes of PTBP-eGFP mRNA complexes	170
Table 5.1 Summary of the photophysical properties of compounds 7-9	198
Table 5.2 Results of solubility tests of PbSe-mTPE QDs	204
Table 5.3 Screening results of spin-coating conditions	204

LIST OF SCHEMES

	Page
Scheme 2.1 Synthetic scheme for MPBP vectors	80
Scheme 3.1 Synthetic route to PBAVs	126
Scheme 4.1 Synthetic route to PNA monomer and PTBP backbone	166
Scheme 4.2 Synthetic route to oligo T8 PNA	168
Scheme 4.3 Synthetic route to PTBP	168
Scheme 5.1 Synthetic route to mTPE and TPE	196

ACKNOWLEDGMENTS

I would like to thank Professor Zhibin Guan for supporting and mentoring my graduate study over the past 5 years. His scientific curiosity, discipline, and passion always inspire me to identify and solve challenging problems in material chemistry. His earnest mentorship and generous support helped me to accomplish a successful Ph.D. career and become an independent scientist.

I would like to thank my thesis committee members: Professor Shane Ardo and Professor Kenneth Shea. Prof. Ardo was the committee chair of my advanced candidacy exam. His kindness and rigorous scientific attitude were always my model to follow. Prof. Shea gave me a lot of helpful suggestions and guidance on my research projects for which I am extremely grateful.

I would like to thank several former members of the Guan Lab. Mark Johnson, thank you very much for introducing me into the biomaterial subgroup and teaching me a lot about biology. Dr. Nate Oldenhius, thanks a lot for your help and guidance on my research projects. Dr. James Neal, you are definitely a great person I admire. You are one of my best friends and thank you so much for your help and support in the Guan Lab. Dr. Jaeyoon Chung, thank you for plenty of helpful discussions on graduate courses and research projects. Dr. Justin Crumrine and Yoshio Nshimura, I enjoyed every meal we had in US and it was a great pleasure to explore various delicious foods with you.

I would like to thank the current members of the Guan Lab. Dr. Alex Eldredge, I really enjoyed every moment we spent together. Your enthusiastic help and reliable collaboration are the most important factors for our projects to succeed. I also sincerely appreciate your help on my life and career development. Dr. Tyler Albin, thank you for teaching me a lot about immunology and HPLC purification. Billy, your creativity always impresses me and is definitely something I admire a lot. Hurik, thank you very much for a lot of contribution to the lab. You always keep everything in order and spare no effort in helping everyone in the lab. You are a great senior mentor for all students in the lab. Chase, you are a very responsible person to work with. Thank you for taking care of numerous instruments in the lab. Collin, I really appreciate your help and efforts on our research projects. I have learned so much from you and I cannot achieve my current accomplishments without you. Dan, I sincerely wish you good luck on our CDN delivery project. It impresses me a lot that you can always propose novel strategies for our project. Your scientific creativity will definitely lead you to a successful Ph.D. Taylor and Joe, I also wish you the best luck on your research projects and graduate study.

I would like to thank my family, especially my parents. During my entire 5-year Ph.D. study in US, I have only come back home once. Your endless love and incessant support are the inexhaustible energy sources which keep me moving forward. Thank you so much for your understanding on everything and I am so lucky to be your son in my life.

I would like to thank my best friend, Zheng Fang. You are definitely one of a kind in my mind and you have been super supportive in my study, life, and career development. I enjoyed every second we spent together and every place we went to. It is so fortunate to get acquainted with you and have you as my best friend. Thank you very much for visiting me and bringing me numerous laughter and fun. I sincerely appreciate them and they will be an invaluable treasure in my life.

CURRICULUM VITAE

Dong-Chu Yang

EDUCATION

University of California, Irvine, Irvine, CA Aug. 2019
Department of Chemistry
Ph.D. Candidate and Researcher in Organic Chemistry
Advisor: Prof. Zhibin Guan, GPA: 3.97

Peking University, Beijing, P. R. China Jul. 2014
College of Chemistry and Molecular Engineering
Bachelor of Science in Chemistry
Advisor: Prof. Jian Pei, GPA: 3.41

HONORS AND AWARDS

- 2015 Student Award, *The American Institute of Chemists*
- 2015 American Institute of Chemists Foundation, *University of California, Irvine*
- 2013 National Fund for Fostering Talents of Basic Sciences (J1030413), *Peking University*

RESEARCH EXPERIENCE

Research Assistant – Guan Lab Sep. 2014 – Present
University of California, Irvine, Irvine, CA
Area of Focus: Organic Chemistry and Polymer Science

- Developed biodegradable materials for delivery of nucleic acids (siRNA, mRNA, and CRISPR-Cas9 machinery).
- Performed complete physical, chemical, and biological characterization of nanoparticle complexes formed by synthetic vectors and RNA molecules.
- Performed biological transfection and assays of nanoparticle complexes.
- Performed Theoretical DFT calculation to design conductive molecular wires.
- Synthesized and characterized conductive molecular wires and utilized them to mediate the assembly of PbSe Quantum Dots into superlattice thin films for enhanced electrical transport.

Undergraduate Researcher – Pei Group

Jan. 2011 – Jun. 2014

Peking University, Beijing, P. R. China

Thesis: Design, Synthesis and Characterization of Novel BN-Fused Polycyclic Aromatics

- Designed and synthesized polycyclic azaborine compounds for developing organic semiconductors.
- Developed regiospecific postfunctionalization methods to tune the optical and electrical properties of synthetic polycyclic aromatics.

TEACHING EXPERIENCE

Head Teaching Assistant, Teaching Assistant,

Sep. 2014 – Present

Department of Chemistry

University of California, Irvine, Irvine, CA

Taught courses:

General Chemistry (Lab), Organic Chemistry (Lab), Advanced Organic Synthesis (Lecture & Lab), Advanced Laboratory on the Synthesis and Characterization of Materials (Lecture & Lab)

TECHNICAL SKILLS

- Theoretical chemistry skills: DFT calculation, optimization of molecular structure
- Synthetic skills: Small molecule, polymer, and peptide synthesis, glovebox, flash chromatography, vacuum sublimation system, GPC, HPLC
- Biological skills: Cell culture, cell transfection, gel-shift assays
- Structural characterizations: ^1H and ^{13}C NMR, ESI-MS, MALDI-TOF MS, FT-IR, SEM
- Characterizations of material properties: UV/vis spectroscopy, fluorescence spectroscopy, cyclic voltammetry (CV), Dynamic light scattering (DLS), TGA, DSC, Instron

PUBLICATIONS AND PRESENTATIONS

• **Yang, D.-C.**; Abelson, A.; Mercado, B. Q.; Kushner, A. M.; Tolentino, J.; Joshi, B.; Guan, Z.; Law, M. Hybrid Organic-Inorganic Quantum Dot Superlattices for Enhanced Charge Transport [talk] *253rd American Chemical Society National Meeting & Exposition*, San Francisco, April 2017.

• **Yang, D.-C.**; Eldredge, A.; Hickey, C.; Muradyan, H.; Guan, Z. Multivalent Peptide-functionalized Bio reducible Polymers for Universal Delivery of Various RNAs. *Biomacromolecules* **2019**, under review.

• **Yang, D.-C.**; Eldredge, A.; Guan, Z. Peptide-functionalized Biodegradable Polymers for Universal, Safe, and Efficient Delivery of Various RNAs. **2019**, *US Patent* under review.

- Abelson, A.; **Yang, D.-C.**; Mercado, B. Q.; Kushner, A. M.; Joshi, B.; Guan, Z.; Law, M. "Enhanced Charge Transport in Ordered Quantum Dot-Molecular Wire Nanocomposite Thin Films [manuscript in preparation]
- Wang, X.-Y.; **Yang, D.-C.**; Zhuang, F.-D.; Liu, J.-J.; Wang, J.-Y.; Pei, J. Postfunctionalization of BN-Embedded Polycyclic Aromatic Compounds for Fine-Tuning of Their Molecular Properties *Chem. Eur. J.* **2015**, *21*, 8867.
- Wang, X.-Y.; Zhuang, F.-D.; Zhou, X.; **Yang, D.-C.**; Wang, J.-Y.; Pei, J. Influence of Alkyl Chain Length on the Solid-State Properties and Transistor Performance of BN-substituted Tetrathienonaphthalenes *J. Mater. Chem. C.* **2014**, *2*, 8152.
- Wang, X.-Y.; Lin, H.-R.; Lei, T.; **Yang, D.-C.**; Zhuang, F.-D.; Wang, J.-Y.; Yuan, S.-C.; Pei, J. Azaborine Compounds for Organic Field-Effect Transistors: Efficient Synthesis, Remarkable Stability and BN Dipole Interactions *Angew. Chem. Int. Ed.* **2013**, *52*, 3117.

ABSTRACT OF THE DISSERTATION

Development of Synthetic Materials for RNA Delivery

By

Dong-Chu Yang

Doctor of Philosophy in Chemistry

University of California, Irvine, 2019

Professor Zhibin Guan, Chair

RNA-based therapeutics has garnered tremendous attention due to their potential to revolutionize vaccination, protein replacement therapies, and the treatment of genetic diseases. However, safe and efficient RNA delivery is still a critical challenge for widespread therapeutic applications. In this dissertation, we developed a variety of biodegradable molecular carriers for the delivery of various RNA, including siRNA, mRNA, and CRISPR-Cas9 machinery.

Chapter 1 provides a concise introduction to gene therapy and RNA therapy, along with critical challenges and strategies for developing RNA delivery vehicles. It also summarizes different categories of current RNA delivery materials and previous work completed in our lab.

Chapter 2 describes the design and development of a multivalent peptide-functionalized bio-reducible polymer system for universal, safe, and efficient delivery of various RNAs of different lengths and structures. This work provides a novel promising vector system for universal RNA delivery, which may speed up the clinical application of RNA therapy and allow for the co-delivery of multiple RNAs.

Chapter 3 describes a series of peptide-functionalized bio reducible amphiphilic vectors for safe and efficient siRNA delivery. It also discusses the details of vector design and the correlations between chemical structures and biological functions.

Chapter 4 explores a family of poly(thymine) peptide nucleic acid-functionalized bio reducible polymers for mRNA delivery. This work provides a novel strategy for mRNA delivery by introducing hydrogen-binding into RNA-vector complexation.

In Chapter 5, I discussed another research project in my Ph.D. study, which is developing hybrid organic-inorganic quantum dot superlattices for next-generation photovoltaics. This work provides a hybrid quantum dot-molecular wire approach to construct highly-ordered nanocrystal films, which brings in significantly enhanced charge transport.

Chapter 1: Introduction to Synthetic Materials for RNA Delivery

1.1 Introduction to Gene Therapy and RNA Therapy

Deoxyribonucleic acid (DNA) and ribonucleic acid (RNA) are two kinds of crucial biomacromolecules which are essential for all known forms of life. As presented in the central dogma of molecular biology¹ (**Figure 1.1A**), DNA is used as a template to direct the synthesis of RNA (transcription) and RNA can serve as a template for protein production (translation). Gene, the DNA sequence which encodes an RNA sequence, carries important instruction for the biosynthesis in an organism. Genetic disorders happen when one gene or multiple genes are changed away from the normal DNA sequence. Over the past decades, researchers have been developing a variety of gene therapy technologies to treat inherited monogenic/multifactorial disorders.²⁻⁵ Gene therapy inherently corrects or deletes the faulty genes, which offers a permanent method to treat genetic disorders. Moreover, gene technology has allowed for the development of other therapeutic method, such as cancer immunotherapy, protein replacement therapy, and vaccination. For instance, genetic engineering of T cells with synthetic genes encoding a chimeric antigen receptor can generate durable responses in patients.⁶

DNA and plasmid-based therapy were the first few examples for gene therapy developed in 1980s.⁴⁻⁵ DNA-based gene therapy has been demonstrated powerful as it can provide sustained production of endogenous proteins and alleviate the need for lifelong drug administration.⁷ But its wide application is highly limited by the intrinsic features. First, all DNA-based gene therapy requires the subcellular delivery of exogenous DNAs into nucleus, which is challenging due to the large, negatively-charged, and double-stranded structure. In addition, most DNA-based gene therapy technology holds the risk of

integrating exogenous DNAs into genome, a number of systems were found to produce insertional genotoxicity, serious immunogenicity, and severe off-targeting effects.⁸⁻⁹

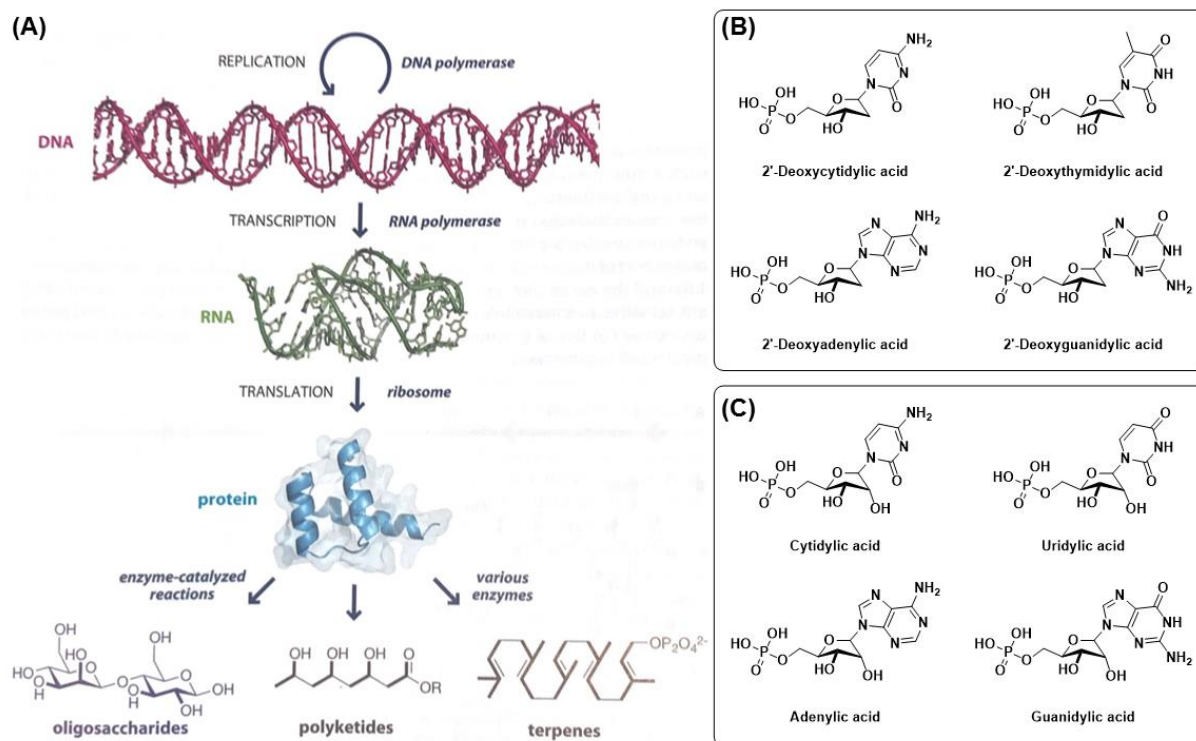


Figure 1.1 (A) The central dogma of molecular biology. Adapted and reprinted from ref.¹ (B, C) Chemical structures of DNA subunits and RNA subunits.

In contrast, RNA-based therapeutics has exhibited its unique advantages to manipulate gene expression. To start with, most therapeutic RNAs do not require the entrance to nucleus. They only need to be delivered to the cytoplasm to initiate protein production or gene-silencing. This bypasses the challenge of crossing the barrier of nuclear membrane and prevents the risk of genotoxicity. Moreover, compared to therapeutic DNAs, RNAs only induced transient effect, such as protein production and gene silencing. This eliminates the risk of generating permant genomic problems.

Over the past decades, RNA-based therapeutics has garnered tremendous attention because of its potential to revolutionize protein replacement therapies, immunotherapy,

and the treatment of genetic disorders.¹⁰⁻¹³ Particularly, a desired protein can be produced through the introduction of specific messenger RNA (mRNA) whereas a gene of interest can be temporarily silenced via RNA interference (RNAi).^{12,14} Additionally, the target gene can also be permanently edited through the delivery of Clustered Regularly Interspaced Short Palindromic Repeat (CRISPR)-Cas9 machinery involving RNA components.¹⁵

1.2 Therapeutics Based on RNA interference

RNAi was initially discovered by Fire and Mello in the form of a single microRNA (miRNA) in the *C. elegans* in 1998.¹⁶ Since then, tremendous efforts and investment have been put in developing RNAi technology.¹⁷ Generally, small (20-30 nucleotides) noncoding RNAs and their associated proteins are involved in RNAi pathways. Specifically, each small RNA associates with an Argonaute family protein to form a sequence-specific, gene-silencing ribonucleoprotein, which further recognizes and degrades the target mRNA.¹⁸ Here I describe two major RNAi pathways: small interfering RNA (siRNA) pathway and miRNA pathway.

siRNA is a group of 20-25 base pairs long, rigid, and double-stranded RNA (**Figure 1.2A**).¹⁹ They are typically generated from the trimming of endogenous or exogenous RNA by Dicer protein (**Figure 1.2B**). Dicer proteins are large endoribonucleases which can cut the RNAi precursors to dsRNA fragments of the appropriate size for loading onto an Argonaute protein.²⁰ One strand of the duplex, called guide strand, is used to bind to Argonaute protein and direct gene-silencing, while the other strand of the duplex, called passenger strand, is normally discarded in the following steps. The RNA-induced silencing complex (RISC) recognizes siRNA, loads the guide strand and releases the passenger

strand.²¹ After being activated, the RISC binds and cleaves the single-stranded mRNA which possesses sequences complementary to the Argonaute-bound guide strand.²²

miRNA pathway is similar to siRNA pathway, but with a few discrepancies. Unlike siRNA, miRNAs are derived from the genome in various organisms.²³ Additionally, these endogenous precursors often contain mismatches and extended terminal loops, called imperfect hairpin RNA structures (**Figure 1.2C**).²⁴ Dicer proteins can cut the ~70 nt hairpin mRNA precursors to afford ~22 nt miRNA. After miRNA is loaded onto the Argonaute protein, the activated miRNA-protein complex (miRNP) binds to the target mRNA which has partial sequences complementary to the loaded miRNA and inhibits the mRNA translation and protein synthesis.²⁵ Both siRNA and miRNA can knockdown gene expression from cleaving target mRNA. The major difference between them is that siRNA reduces the expression of one specific target mRNA whereas miRNA inhibit the expression of multiple mRNAs as miRNA is partially complementary to its target mRNA.²⁶

Due to the high specificity and efficacy of RNAi pathway, RNAi-based gene-silencing technology holds tremendous potential to transiently suppress the expression of target gene, without permanently changing the genome. Actually, siRNA technology has been developed into a powerful tool for gene knockdown *in vitro* and *in vivo*.²⁷ More importantly, in 2018, one siRNA-based therapeutic agent developed by Alnylam Pharmaceuticals, called Patisiran, was approved by U.S. Food and Drug Administration (FDA) to treat hereditary ATTR amyloidosis with polyneuropathy.²⁸ This is the first-ever FDA-approved therapeutic based on RNAi and it is recognized as a great milestone of RNA therapy. It is anticipated that more RNAi therapeutics will be approved and successfully utilized in clinic in the near future.

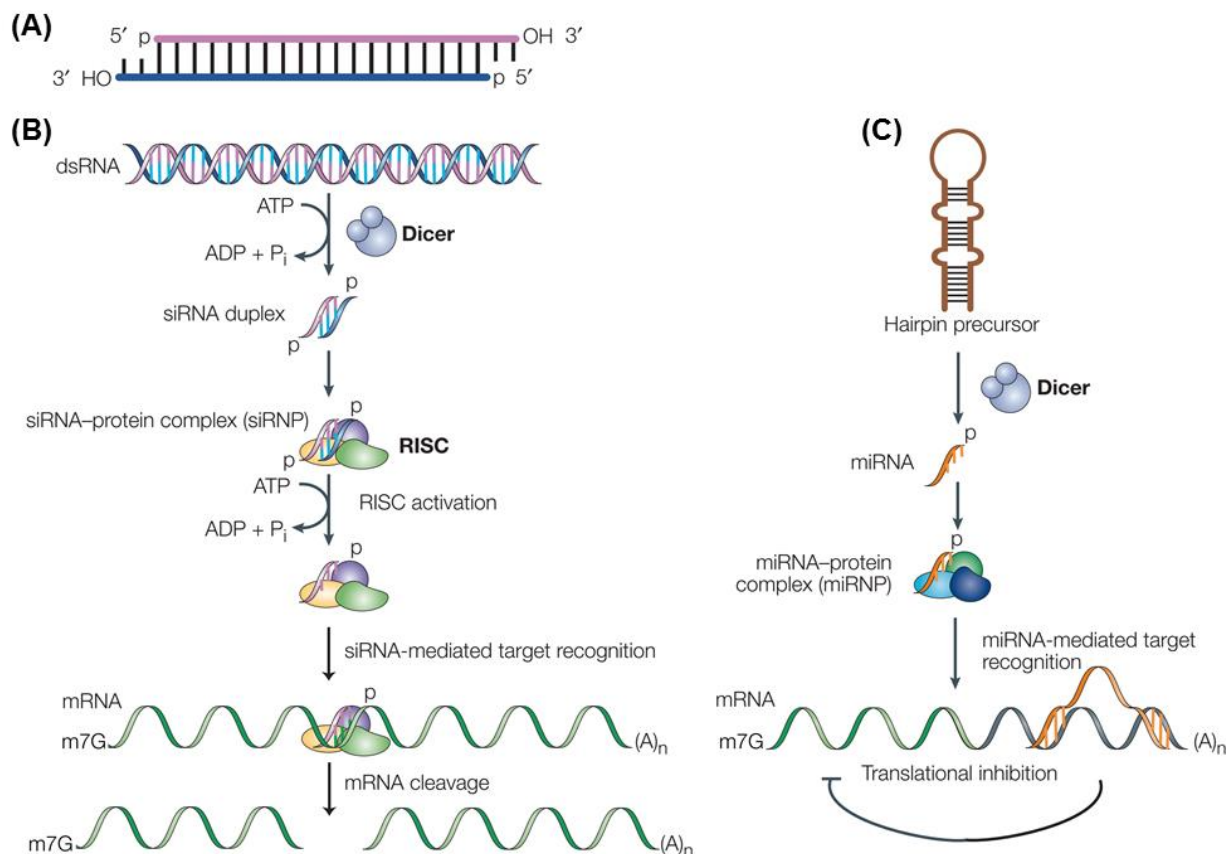


Figure 1.2 The RNA interference pathway. Adapted and reprinted from Ref.¹⁷ (A) Short interfering RNAs (siRNAs). (B) The siRNA pathway. (C) The micro RNA (miRNA) pathway.

1.3 mRNA Therapeutics

In the central dogma of molecular biology (**Figure 1.1A**), mRNA is located as the middleman between DNA and protein. This important ‘interchange’ position determines the crucial molecular function of mRNA: passage the genetic information from DNA and direct the protein synthesis. In recent years, mRNA therapeutics has been developed as a promising technology for protein replacement therapies, immunotherapy, and the treatment of genetic diseases.²⁹⁻³⁰

Protein is one of essential bio-macromolecules in all forms of life, performing the function of catalyzing biochemical reactions, transporting molecules within cells or among

organs, and forming receptors and channels in membranes. A number of diseases appear because of insufficient or aberrant protein expression, such as haemophilia B and muscular dystrophy.³¹⁻³² Protein therapeutics play a significant role in every field of medicine nowadays and protein drugs have already become one important class of medicines serving patients in clinic.³³ However, effective protein delivery has limited the wide application and development of protein therapies. Due to the large size, intricate molecular structure, and varying surface charge, therapeutic proteins cannot be easily transferred and delivered to the target location. The design and development of delivery vehicles for proteins has proven difficult. Additionally, large scale synthesis and purification of therapeutic proteins have been demonstrated to be challenging and expensive.

In contrast, mRNA therapy becomes an excellent alternative to protein therapy as mRNA directly guides the biological synthesis of functional proteins. Compared to protein therapy, mRNA therapy is much more efficient. A single mRNA molecule can be translated into multiple copies of protein in a short period of time.³⁴ Therefore only a small amount of mRNA molecules needs to be delivered in mRNA therapy, whereas protein therapy requires the effective delivery of large quantity of proteins. The mechanism of mRNA therapeutics in protein replacement is shown in **Figure 1.3A**. After the entry of cell cytosol, *in vitro*-transcribed (IVT) mRNA binds to the ribosomal complex in the host cell. The ribosomal complex screens the mRNA sequence until the start codon is recognized. Then the peptide synthesis starts and different amino acids are continuously added to the peptide chain. Once the stop codon is detected, elongation of the peptide chain stops and the original mRNA and synthesized peptide are released. Finally, the peptide chain is further modified and transformed to the new protein.³⁵

Since desired protein can be produced in cells via the introduction of target mRNA, a variety of protein-related therapeutics has been renovated based on mRNA technology. Antigen-encoding mRNA vaccine is one of the most promising therapeutic applications.³⁶ The related mechanism is presented in **Figure 1.3B**. In order to develop antigen-specific immunity, the mRNA vaccine needs to be transfected in antigen-presenting cells, such as dendritic cells. Upon entering the cytosol of antigen-presenting cells, antigen-encoding mRNA is translated into antigen polypeptides, which are further processed into small peptide epitopes. The peptide epitopes then bind to the major histocompatibility complex (MHC) and the MHCs are transferred and presented on the cell surface. The presented antigenic peptide epitopes promote the recognition from CD8⁺ and CD4⁺ T cells, which generates cellular immunity and antigen-specific antibody response.³⁷

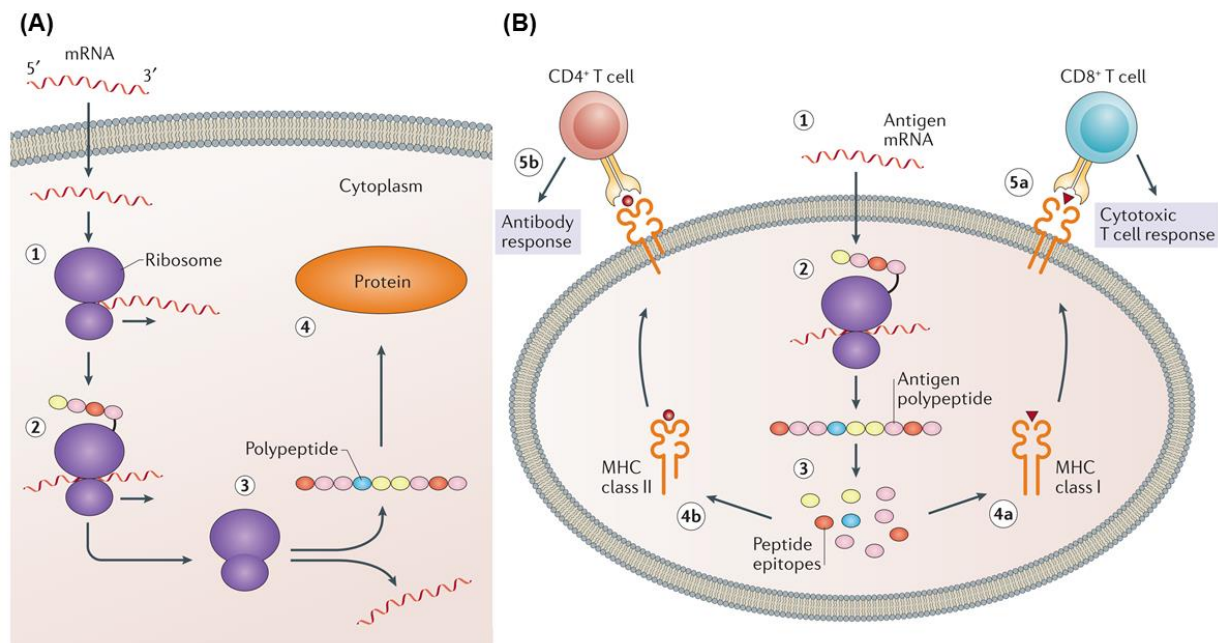


Figure 1.3 Mechanisms of mRNA therapeutics. Adapted and reprinted from Ref.³⁵ (A) The mechanism of *in vitro*-transcribed mRNA translation and protein replacement. (B) The mechanism of mRNA-mediated vaccination.

Unlike traditional vaccines, such as live-attenuated viruses, mRNA vaccines have less safety concerns as they do not introduce possible pathogens. In addition, both cellular and humoral immunity can be induced by mRNA vaccines.³⁸ Furthermore, a special class of mRNA, called self-replicating or replicon mRNA, holds great promise for vaccination via inducing a prolonged immune response.³⁹ Like DNA replication in living organisms such as prokaryotes and eukaryotes and DNA/RNA replication in viruses, replicon mRNAs can replicate themselves inside host cells. The origin of replication, the particular sequence which initiates RNA replication, is incorporated in replicon mRNA.⁴⁰ Thus the corresponding mRNA vaccines can express protein antigens of interest persistently. This increases the efficacy of the vaccines and reduces the need for booster shots.⁴¹ In short, mRNA-based vaccine is a new avenue to immunology and can provide novel routes to treat various diseases, such as influenza,⁴² Zika,⁴³ and rabies.⁴⁴

Besides developing next generation vaccines, mRNA therapeutics has also been utilized in cancer immunotherapy.⁴⁵ After dendritic cells are transfected *ex vivo* with mRNA which encodes tumor-associated peptide antigens, cytotoxic T cells can find cancer cells and destroy the tumors. Besides modifying dendritic cells, mRNA technology is utilized to engineer T cells in Chimeric Antigen Receptor (CAR) T cell therapy.⁴⁶ After transfected by mRNA encoding CARs, patient's T cells are able to locate tumor cells accurately through the specific binding between antigen receptors and tumor epitopes.⁴⁷

Even though mRNA therapeutics has been shown promising and powerful in many applications, several intrinsic aspects still remain challenging and require substantial development. Similar to other nucleic acids, mRNA can generate undesired immune response when being directly exposed to the cell environment. Unlike DNA and siRNA

which pose the double-stranded structure, mRNA is usually single-stranded, resulting a much lower stability. It is very susceptible to degradation by ribonucleases (RNases). In order to enhance the stability and maximize protein expression, numerous mRNA structural modifications have been developed, such as structural engineering of the 5' cap, elongation of the 3' poly(A) tail, and chemical base modification.⁴⁸ It is expected that with solving the issue of stability and immunogenicity, mRNA therapeutics will become a powerful tool to treat plenty of incurable diseases.

1.4 Gene Editing

As mentioned earlier, many genetic diseases occur because of the appearance of gene redundant, faulty genes or gene deletion. To inherently fix these errors, it is required to have a gene editing system which can specifically and efficiently alter the target genes. Many protein-DNA recognition genome-editing technologies, such as Meganucleases, Zinc finger nucleases, and TALEN, have been developed.⁴⁹ However, the protein engineering and cloning for different DNA targets limit the broad application of these technologies. The discovery of CRISPR sequences in *Streptococcus pyrogenes* uncovered a family of endonucleases with sequence specificity and unique gene editing behavior.⁵⁰ The target specificity of CRISPR technology is simply based on RNA-DNA base pairing. The emergence of CRISPR technology has revolutionized the field of gene therapy by enabling the permanent editing of faulty genes.¹⁵

In CRISPR system, target DNA sequences are transcribed to small RNA sequences which are complementary to the original DNA sequence (crRNAs). For simplicity, researchers hybridize these crRNAs with trans-activating RNAs (tracrRNAs) to form ~100

base pairs small guide RNAs (sgRNAs). Then sgRNAs bind to CRISPR-associated proteins (Cas proteins) and form Cas-ribonucleoproteins (RNPs).⁵¹ Many Cas proteins, such as Cas9 protein, exhibit strong endonuclease activity and can induce double-strand DNA break. As shown in **Figure 1.4**, with the guidance of sgRNA, the assembled CRISPR-Cas9 RNPs can specifically target the DNA sequence of interest and produce site-specific double-strand break (DSB). Then the created DSB is further repaired either by nonhomologous end joining (NHEJ) or by homology directed repair (HDR). NHEJ generates small random insertions, deletions, or substitutions while HDR results in precise gene modification with the help of homologous repair template.⁴⁹

There are three main methods to deliver CRISPR machinery into cells: delivery of DNA encoding CRISPR components (**Figure 1.5A**), co-delivery of targeting sgRNA and mRNA encoding Cas9 protein (**Figure 1.5B**), and direct delivery of preformed Cas9-RNP particles from complexation between sgRNA and Cas9 protein (**Figure 1.5C**).⁵² Cas9 RNP delivery is demonstrated to be challenging due to the large size of the protein. Large scale synthesis and purification of Cas9 proteins could be expensive. Plasmid DNA delivery has serious safety concern as the prolonged Cas9 protein expression could generate off-target effects, cutting the genome at undesired locations. Compared to DNA delivery, Cas9 mRNA/sgRNA co-delivery only produces transient Cas9 protein expression, reducing off-target effects and lowering cytotoxicity. But it requires the co-delivery of two RNA species: Cas9 mRNA and single guide RNA (sgRNA).⁵³⁻⁵⁴

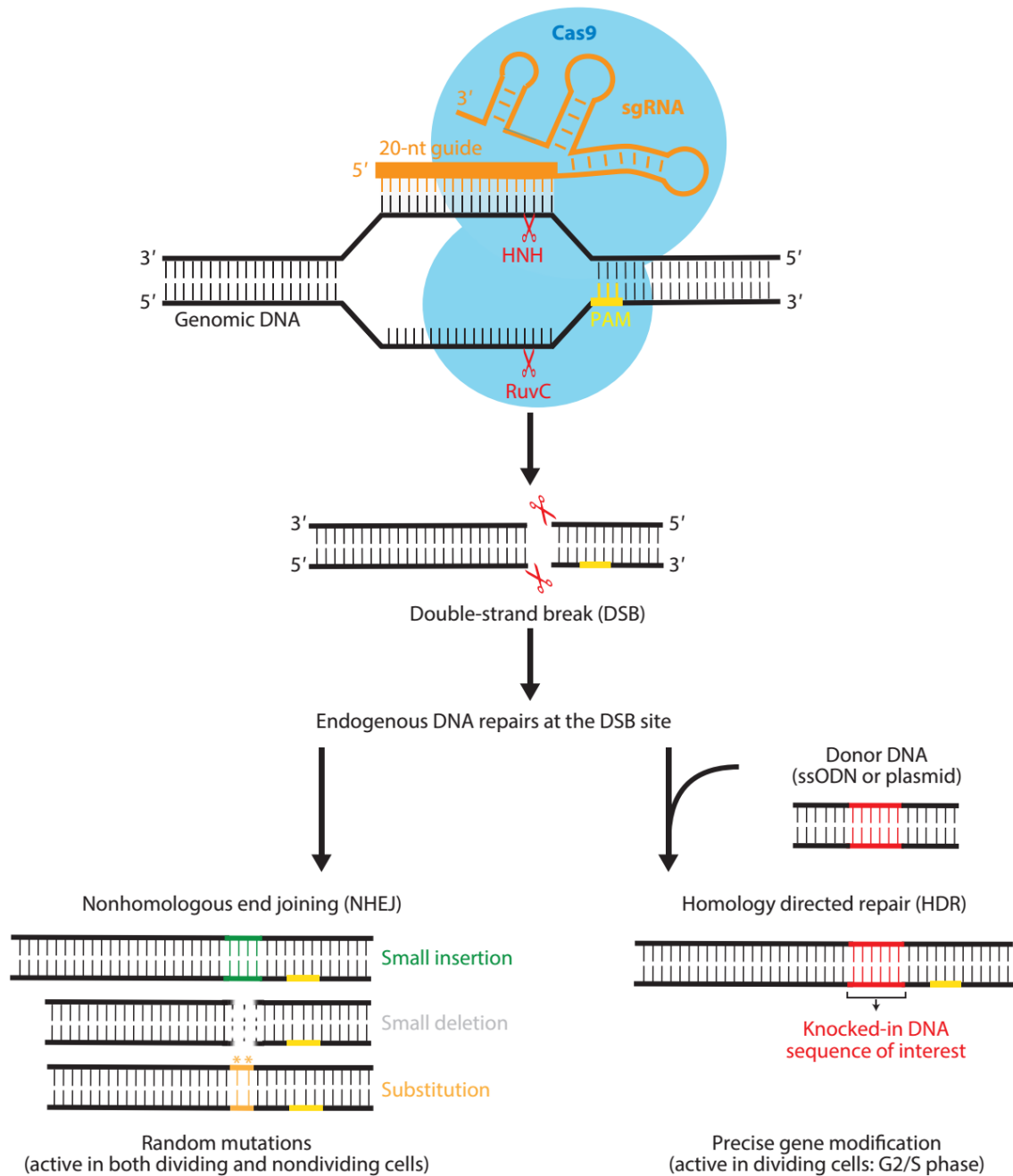


Figure 1.4 The mechanism of CRISPR-Cas9 gene editing. Adapted and reprinted from Ref.⁵¹

RNA-based CRISPR-Cas9 editing requires the delivery of two components: an mRNA encoding Cas9 protein and a sgRNA for targeting the specific site of genome for editing (**Figure 1.5C**). After entering the target cell, Cas9 mRNA is translated to Cas9 protein by the

ribosomal complex. Then Cas9 protein further associates with co-delivered sgRNA to form the RNP with affinity for the target DNA sequence. Finally, the RNP complex gets into the nucleus, binds to the target gene which has the DNA sequence complementary to the sgRNA, and breaks the double-stranded DNA (**Figure 1.5D**).

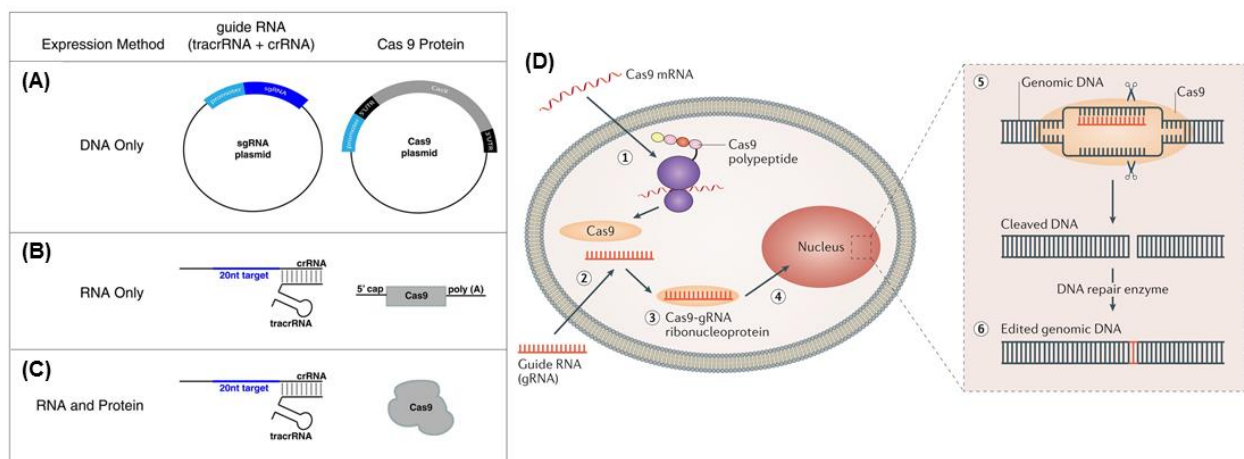


Figure 1.5 (A, B, C) Different methods to deliver CRISPR/Cas9 machinery. Adapted and reprinted from Ref.⁵² (D) The mechanism of RNA-based CRISPR-Cas9 gene editing. Adapted and reprinted from Ref.³⁵

In summary, CRISPR technology has been proven extremely powerful and holds great promise to treat a variety of genetic diseases and defects. Effective delivery of CRISPR machinery still hinders its wide application. Each delivery method has its own obstacles on the road of clinical trials, such as low delivery deficiency, difficult large scale production, high off-target effects and potential immunogenicity and cytotoxicity. But we believe that with fast advancements and development, CRISPR-based technology will be more and more mature and become the most prominent tool for gene therapy in the near future.

1.5 Challenges of RNA Therapeutics

Although RNA therapeutics holds great promise in various aforementioned applications, several critical challenges still limit the wide application of RNA technology.⁵⁵ The most challenging obstacle is safe and efficient delivery of RNA drugs *in vitro* and *in vivo*. As described in early sections, RNAs are large biomacromolecules with high density of anionic charges that do not readily penetrate cell membrane. The electrostatic repulsion between negatively charged RNA phosphate and negatively charged cell membranes inhibits the entrance of RNA molecules. Additionally, compared to DNAs, RNAs are much less stable because the 2'-OH groups in RNA structures (**Figure 1.1C**) can induce their self-cleavage. In addition, RNAs, especially long mRNAs, are very sensitive to nuclease degradation.⁵⁶ This high sensitivity issue has to be addressed because the RNA drugs need to survive in serum which contains a variety of RNases. Moreover, similar to DNAs, naked RNAs can induce undesired immune response which can cause severe side effects in clinical applications.⁵⁷

Therefore, it is necessary to develop safe and effective intracellular delivery vehicles for RNA-based therapeutics. Generally, an ideal delivery vehicle needs to fulfill the following requirements:^{55,58} (1) The delivery vectors need to be nontoxic and biodegradable. They should be naturally degraded and cleaved after delivering RNA cargos. (2) The delivery vectors need to be able to bind to RNAs either through intermolecular interactions or covalent bonds. The complex they formed should be stable under physiological conditions and be able to protect RNAs from degradation by RNases. (3) The RNA delivery needs to be realized in target cells/organs. (4) The delivery vehicle should facilitate cellular uptake of the vehicle-cargo complexes as the naked RNA cargos can

hardly get into cells by themselves. Additionally, the delivery vehicle should also facilitate endosomal escape of the vehicle-cargo complexes in order to release the complexes into cytoplasm. (5) The delivery vehicles need to release the cargos efficiently after arriving the desired destination. This requires a dynamic interaction between delivery vehicles and cargos or a stimuli-responsive motif in the structure of delivery vectors.

Many initial RNA delivery experiments are performed *in vitro*. However, realizing efficient delivery *in vivo* is the ultimate goal. The difficulty in translating *in vitro* success to *in vivo* delivery is one major challenge in the development of RNA therapeutics.⁵⁹ A large portion of vehicle-cargo complexes carry positive charges on the surface, which could aggregate with negatively charged proteins in serum.⁶⁰ The half-life of different delivery particles can vary dramatically and structural modification is often needed to increase the circulation time *in vivo*. Moreover, the nonuniform biodistribution of different delivery particles can also hinder the real application in clinic. For instance, it has been shown that positively charged particles are prone to accumulate in the lung and spleen.⁶¹ For each delivery system, delicate mechanistic biological study is required to elucidate the correlation between *in vivo* and *in vitro*.

1.6 Overview of Gene Delivery Vehicles

To address the critical RNA delivery challenges, researchers have developed a variety of delivery vehicles, including viral vectors, non-viral vectors, and extracellular vesicles.⁶² In this section, several important prospects of each kind of delivery vehicles were included. More details about non-viral vectors will be provided in **Section 1.7**.

Viral vectors are the most popular delivery vehicles for gene delivery and they have been utilized in a large number of clinical trials.⁶³ Viral vectors are highly infectious and they can infect a broad spectrum of cell types. Recombinant adenoviruses, adeno-associated viruses and viruses with enveloped virions (including retroviruses, lentiviruses, alphaviruses and herpes viruses) are the major viruses used for gene delivery *in vitro* and *in vivo*.⁶⁴

In gene delivery mediated via viral vectors, nucleic acid cargo is usually encased in a proteinaceous shell and then transferred into target cells. As shown in **Figure 1.6A**, after loading DNA cargos, adenovirus binds to the coxsackievirus adenovirus receptor and enter the cell through receptor-mediated endocytosis. As the pH of endosome environment decreases, the capsid is degraded and DNA cargo is released.⁶⁵ For DNA therapeutics, the released DNA then needs to enter the nucleus and initiate transcription. For another example of viral vectors (**Figure 1.6B**), herpes simplex virus (HSV) has also been used to deliver DNA. After binding to cell surface through interactions between glycoproteins and heparin sulphate proteoglycans (HSPG), the HSV virion envelope fuses with the plasma membrane and the capsid enters the cytoplasm. Then it is transferred to the nucleus via dynein-mediated transport and the DNA is released.

Even though viral vectors are broadly used in current gene delivery, they pose several significant limitations and safety concerns.⁶⁶ First, they can be detected by immune system and trigger immune responses. Second, the genetic cargo capacity is highly limited by the packaging size of viral vector. For instance, adeno-associated viral vectors can only deliver DNA-based cargos with relatively small size (~4.7 kb).⁶⁴ In addition, working with

viral vectors requires extra safety precautions as most viral vectors can generate inflammatory cytotoxicity and cause diseases.

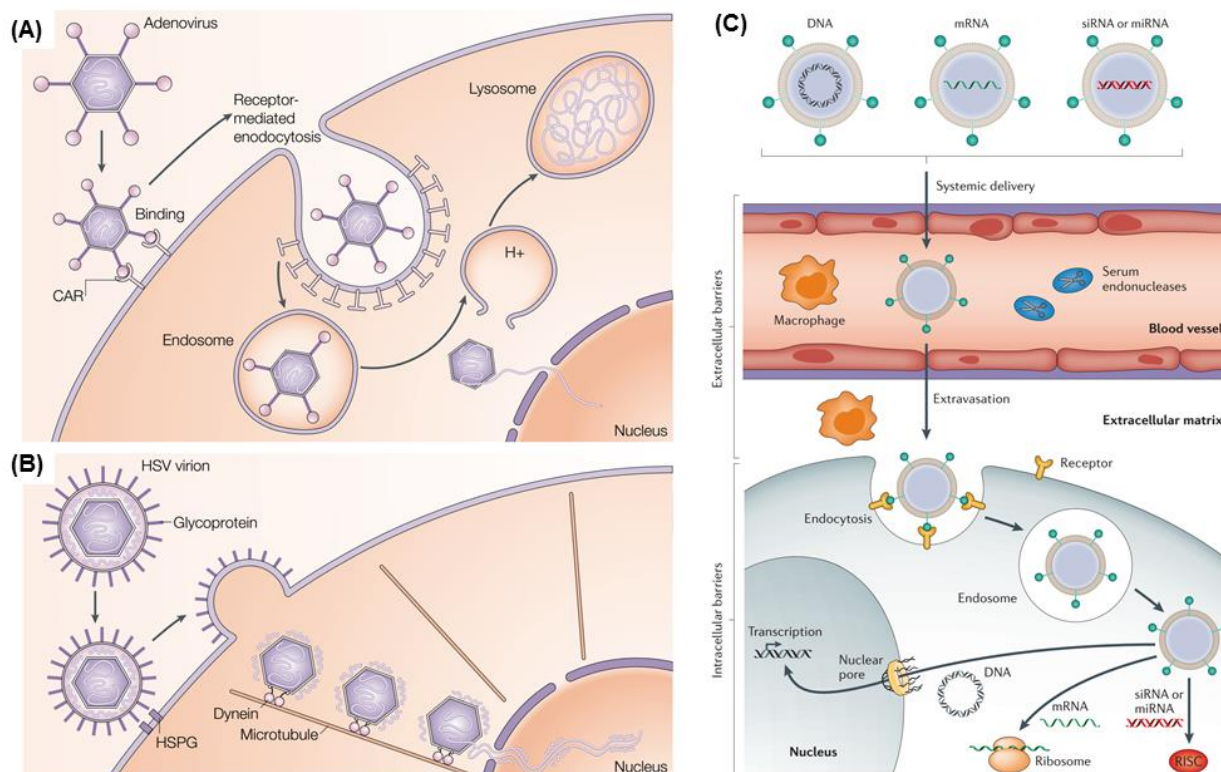


Figure 1.6 Viral vectors and non-viral vectors for gene delivery. (A) Gene delivery mediated by adenovirus. Adapted and reprinted from Ref.⁶⁴ (B) Gene delivery mediated by herpes simplex virus (HSV). Adapted and reprinted from Ref.⁶⁴ (C) Nucleic acid delivery mediated by non-viral vectors. Adapted and reprinted from Ref.⁶⁷

Due to the serious safety risks of viral vectors, numerous non-viral delivery vectors have been designed and developed over the past several decades, including cationic lipids and lipid-like nanoparticles, polymers, dendrimers, cell-penetrating peptides, and metal/inorganic nanoparticles.⁶⁷ In general, the non-viral vectors are designed to assemble with DNA/RNA cargos and form 100-200 nm nanoparticles via intermolecular interactions, such as electrostatic interaction, hydrophobic interaction, and hydrogen bonding. The nanoparticle formation can prevent nuclease degradation in serum and avoid immune

detection. After complexation, the formed nanoparticles need to enter the target cells, mostly through endocytosis pathways or membrane fusion.⁶⁸ Several components can determine the pathway of endocytosis, such as nanoparticle size, surface charge, morphology, and chemical structures (**Figure 1.7**).⁶⁹ Generally, nanoparticles with the size of 20 – 200 nm in diameter can readily get into the cells through endocytosis.⁷⁰ Moderate positive charges on the particle surface can promote the interactions with cell membrane as cell membrane is comprised of negatively charged phosphate lipids. It is also shown that some specific chemical structures can promote the cellular uptake. For instance, tryptophan (Trp) enhances the cellular uptake due to the intercalation of the indole ring and aliphatic chains facilitate the cellular uptake through hydrophobic interactions.⁷¹⁻⁷²

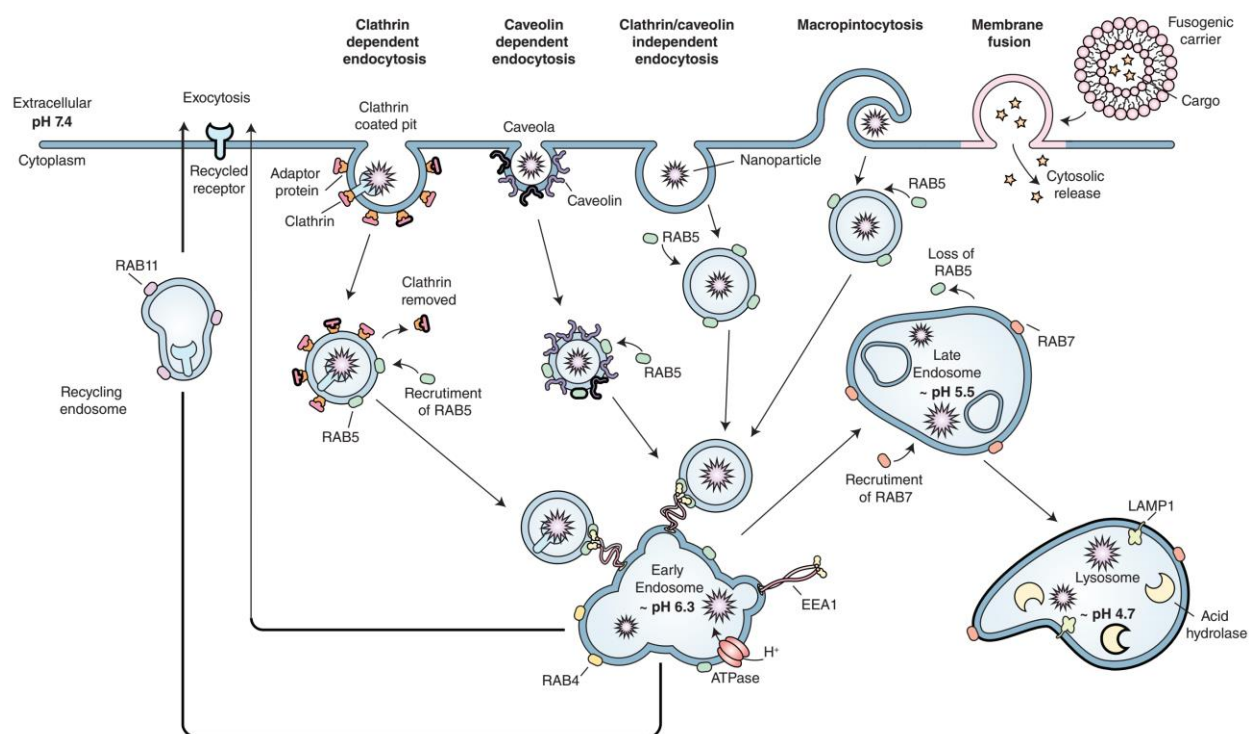


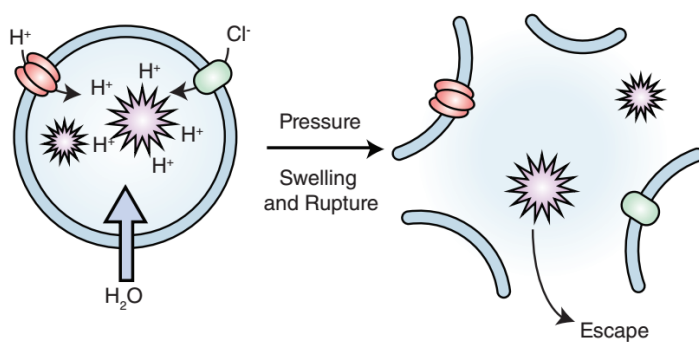
Figure 1.7 Different cellular uptake mechanisms of nanoparticles. Adapted and reprinted from Ref.⁶⁹ Nanoparticles can get into cytoplasm through different endocytosis pathways or membrane fusion.

After entering the cells through endocytosis, another important step is to release the vehicle-cargo complex from endosome. **Figure 1.8** illustrates the major mechanisms of endosomal escape.⁶⁹ efficient endosomal escape is another crucial consideration when designing the structure of delivery vehicles. Proton sponge effect and osmotic lysis is a common strategy to induce endosomal escape.⁷³

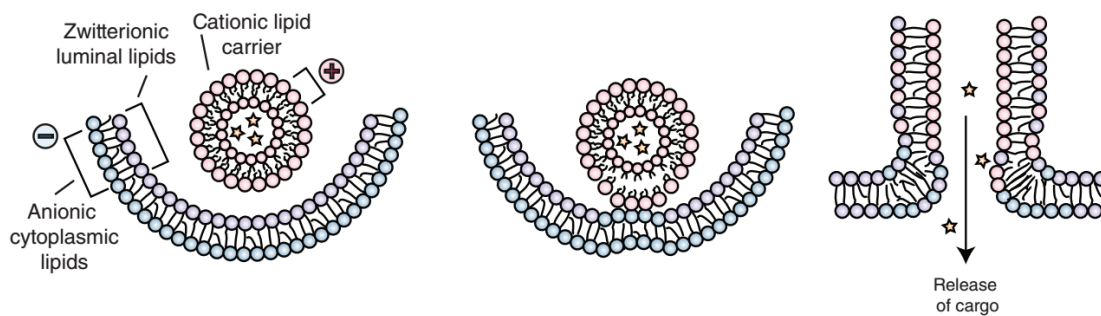
The proton sponge effect is based on the buffering effect of delivery vector which has a pKa in physiologically relevant range.⁷⁴ This pH-responsive behavior normally comes from the tertiary amine or imidazole on the vector structure. For instance, when early endosome matures and becomes lysosome, the pH of cellular environment decreases from 7.4 to 5. As the pH inside endosome drops, more protons are pumped into endosomes because of the buffering capacity of tertiary amines or imidazole rings. In the meantime, more chloride counter ions are also pumped into endosomes, generating a significant increase of osmotic pressure which leads the eventual endosome rupture. The strategy is commonly used in histidine-rich materials and polycationic materials, such as histidine-containing peptides, polyethylenimine (PEI) and poly(amidoamine) (PAMAM) dendrimers.⁷⁴⁻⁷⁵

It is also shown that assembled nanoparticles with lipids or amphiphilic materials can fuse with the endosomal membrane, which releases the cargo into cytoplasm.⁷⁶ In addition, some peptides can interact with the endosomal membrane and generate defined pores, which allows the cargo to move into cytoplasm.⁷⁷ Similarly, some polymers can also disrupt the endosomal membrane through intermolecular interactions and realize the cargo release.

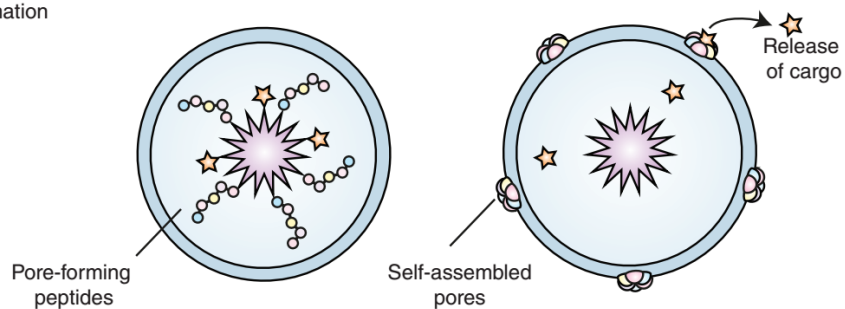
(a) Proton Sponge Effect



(b) Membrane Fusion



(c) Peptide Pore Formation



(d) Polymer-induced Disruption Membrane Disruption

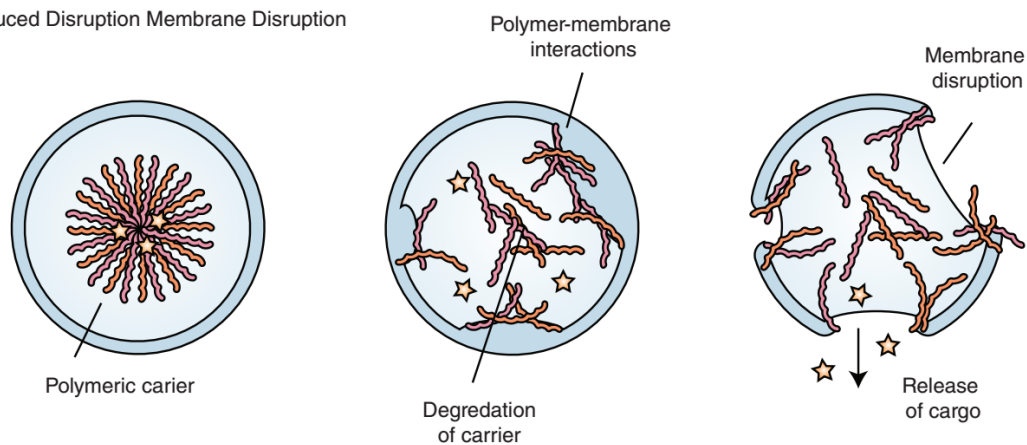


Figure 1.8 Different mechanisms of endosomal escape. Adapted and reprinted from Ref.⁶⁹

Besides viral vectors and non-viral synthetic vectors, a number of biological gene delivery vehicles have also been developed recently, such as bacteria, bacteriophage, virus-like particles, erythrocyte ghosts and exosomes.⁷⁸ They are often directly derived from biology and less toxic compared to viral vectors. Although less well-established than viral vectors and synthetic vectors, the potential of these non-viral biological agents as gene delivery vehicles has also been demonstrated in clinical trials.

1.7 Non-viral Synthetic Vectors

Among all kinds of non-viral synthetic vectors for gene delivery, lipids and lipid-like materials are the most widely used and well-developed.⁷⁹ They often contain amphiphilic structures which are comprised of hydrophilic phosphate head-groups and hydrophobic aliphatic tails. Due to this unique amphiphilic structure, lipid-based materials can form liposomes (**Figure 1.9**), which are spherical vesicles consisting of one or multiple phospholipid bilayers as the shell and aqueous environment as the core. When complexing the lipid-based materials with DNA/RNA cargos, liposomes form with the loading of nucleic acid cargos into the core, generating lipoplexes. The high structural similarity of lipid layers between liposome and cell membrane often produces membrane fusion, which facilitates the cellular uptake and endosomal escape of lipoplexes.

The commonly used lipid-based delivery system often consists of a variety of components, such as cationic lipids 1,2-di-*O*-octadecenyl-3-trimethylammonium-propane (DOTMA), zwitterionic lipids 1,2-dioleoyl-*sn*-glycero-3-phosphoethanolamine (DOPE), helper lipids 1,2-distearoyl-*sn*-glycero-3-phosphocholine (DSPC), cholesterol, and polyethylene glycol (PEG).

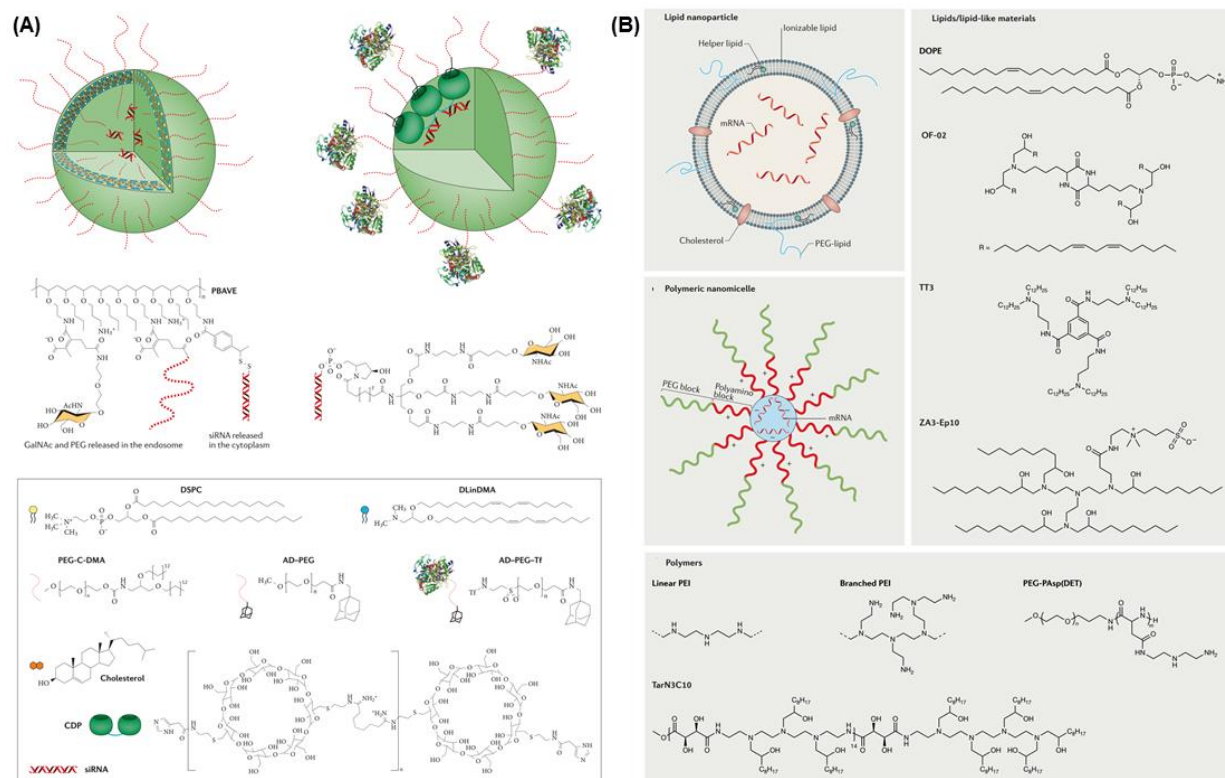


Figure 1.9 (A) Chemical structures of non-viral synthetic vectors for siRNA delivery. Reprinted from Ref.⁶⁷ (B) Chemical structures of non-viral synthetic vectors for mRNA delivery. Adapted and reprinted from Ref.³⁵

Cationic lipids can interact with anionic nucleic acids and form lipoplexes. But it has been shown that cationic lipid-based delivery systems can generate significant toxicity and immunogenicity.⁸⁰ In contrast, a few ionizable lipid systems have been developed to reduce the positive charges on particle surface.⁸¹ Their structures often contain tertiary amines which remain neutral under physiological pH whereas become positively charged at low pH (~5). This buffering capacity is also beneficial for endosomal escape as mentioned in Section 1.6. Helper lipids are incorporated to enhance cellular uptake and endosomal escape through facilitating membrane fusion. Cholesterol is often included to enhance vesicle stability as its hydrophobic structure can fill in the gaps between lipids. Additionally, the incorporation of PEG-lipids or PEG molecules relieves the electrostatic

interaction with anionic serum proteins, prevents aggregation and enhances nanoparticle stability.

The lipid-based delivery systems are highly versatile, with numerous recipes of formulation. The development of an optimal lipid delivery system for each specific drug cargo often requires substantial screening of various lipid combination. After intensive research and development, quite a few lipids and lipid-based materials, such as Lipofectamine system, have become the 'golden standards' for various gene delivery *in vitro*.

However, only few lipid-based delivery systems have been successfully demonstrated *in vivo*,^{54,82} mainly due to the low biodegradability, high toxicity, and high immunogenicity. It has been shown that most lipoplexes have the potency of targeting liver, limiting the wide delivery application of lipid technology in other organs.⁸³

Polymeric vector is another important class of material for gene delivery, including the delivery of DNA, siRNA, and mRNA. The most popular strategy is complexing cationic polymers and anionic DNA/RNA to form nano-size polyplexes, which can be taken up by the cells through endocytosis. The polymeric vectors often consist of cationic charges and secondary or tertiary amines, which afford buffering capacity for endosomal escape as mentioned earlier. Polyethylenimine (PEI) (**Figure 1.9B**) is the classic and well-established polymer for gene delivery. However, it has been shown that the high density of cationic charges in PEI leads to strong interaction with negatively charged serum proteins, resulting in aggregation and cytotoxicity.⁸³ In order to address these issues, PEI was further modified by different functional groups, such as hydrocarbon side chains, fluorocarbon side chains, cyclodextrin, and aromatic substitutions.⁸⁴⁻⁸⁵

Besides pure cationic polymers, different block copolymers have been designed and utilized in RNA delivery. For instance, the block copolymer poly(ethylene glycol)-poly(N'-(N-(2-aminoethyl)-2-aminoethyl)aspartamide) (PEG-PAsp(DET)) has been used to deliver mRNA into nasal neurons.⁸⁶ In this design, this block copolymer can assemble into nanomicelles in water. PEG chains construct the shell while PAsp(DET)-mRNA complexes form the core (**Figure 1.9B**). This complexation still relies on the electrostatic interactions between cationic polymer chains and anionic RNA cargos. Similar micelle strategy has also been reported to deliver hydrophobic small molecule drugs, despite the drug loading is based on hydrophobic interactions instead.

When designing polymeric gene delivery vehicles, another important aspect to consider is biodegradability. Introducing biodegradability into polymer vectors is essential for reducing cytotoxicity as well as promoting drug release after endosomal escape. Ideally, the drug-loaded delivery vehicle should be degraded upon a certain intracellular trigger, such as pH, redox potential, and presence of enzymes.⁸⁷ This will not only guarantee sufficient lifetime for the carrier to survive in blood circulation and reach the target cells but also control the intracellular release of the cargos. Different chemical motifs, including polyesters, disulfides, and acetal cross-linkers, are incorporated to construct the biodegradable polymers (**Figure 1.10**).⁸⁸

A few aspects need to be considered when designing polymeric gene delivery vehicles. First, the polymeric vector should consist of biodegradable structures, such as polydisulfides, polyesters, and polypeptides.⁸⁸ Second, the polymer vector should bind to DNA/RNA cargos efficiently. Cationic charges are often introduced in polymer system to afford electrostatic interaction with anionic charged cargos. However, high density of

cationic charges can often cause cytotoxicity and aggregation *in vivo*.⁸³ Hydrophilic side chains, such as PEG, are often incorporated to reduce cationic charge density and enhance serum stability while hydrophobic side chains are often included to promote nanoparticle assembly.^{72, 89} Third, in order to efficiently release DNA/RNA cargos, stimuli-response motifs need to be incorporated in the vector design. Redox-responsive,⁹⁰ pH-responsive,⁹¹ and self-emmolative⁹² polymers have been developed for gene delivery. Finally, the ideal nucleic acid delivery should be performed in target cells and organs. The target organ for *in vivo* transfection is highly depended on the biophysical properties of vector-cargo complexes. It has been shown that cationic polymers often exhibit efficient delivery to the lungs and spleen.⁹³ Different polymer functionalization strategies such as attaching targeting peptides have been developed to realize targeted gene delivery.⁹⁴

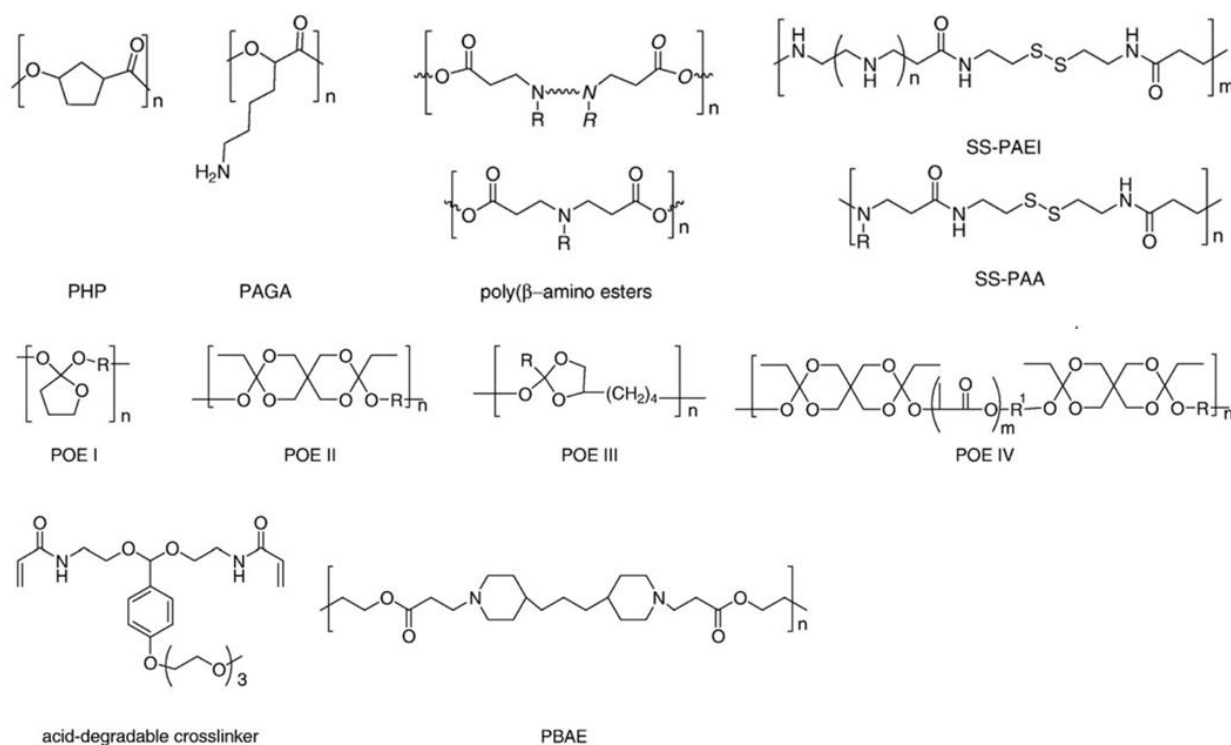


Figure 1.10 Chemical structures of biodegradable polymers for gene delivery. Adapted and reprinted from Ref.⁸⁸

In summary, biodegradable polymers are another important category of nucleic acid delivery vehicles. It provides a variety of benefits such as high scalability, high structural tunability, and low production cost compared to other classes of gene delivery vehicles. Currently cationic charges are often incorporated in the polymeric delivery vectors and they mediate the nucleic acid delivery through different mechanisms of endocytosis and endosomal escape, which offers different biological behaviors for further *in vivo* applications. With fine tuning and sufficient development, biodegradable polymers can be universal platforms for various gene delivery.

Besides lipid-based materials and polymeric vectors, cell-penetrating peptides (CPP) are another powerful delivery vehicle of nucleic acids.⁹⁵⁻⁹⁶ CPPs are a variety of peptides which can pass through tissue and cell membranes with no interactions with specific receptors. They are typically 5-30 amino acids long and they can be categorized into three major classes: cationic, amphiphilic, and hydrophobic peptides.

Cationic peptides contain positive charges at physiological pH which contain protonated guanidine groups in arginines (Arg) and protonated primary amines in lysines (Lys). The most famous cationic peptides include *trans*-activator of transcription (TAT)-derived peptides and polyarginines. TAT peptide is a short peptide found in TAT protein of HIV-1 which is responsible for cellular uptake.⁹⁷ It and its derivatives have been successfully utilized to mediate the cellular delivery of various drugs. Polyarginines usually consist of 8 or 9 arginine residues, which provide not only cationic charges for nucleic acid complexation and endocytosis, but also multiple guanidine head groups to interact with phosphate groups on the cell membrane through bidentate hydrogen bonding.⁹⁸

Similar to amphiphilic lipids, amphiphilic CPPs have both hydrophilic and hydrophobic regions of amino acids.⁹⁵ Amphiphilic CPPs can be either derived directly from natural proteins or synthesized via attaching a hydrophobic domain to a nuclear localization signal (NLS). They can form secondary structures such as α -helix and β -sheet to interact with cell membrane and facilitate cell internalization.⁹⁹⁻¹⁰⁰

Hydrophobic CPPs are less developed compared to cationic CPPs and amphiphilic CPPs. They are often constructed by nonpolar amino acid residues which can enhance cellular uptake through the interaction with hydrophobic domains of cell membrane.¹⁰¹

Although the cellular uptake mechanism is not fully elucidated, a number of CPPs have been used to link the drugs (such as nucleic acid, protein, and small drug molecule) through covalent bonds or non-covalent interactions and mediate their delivery in clinical trials.⁹⁶ The major drawbacks in CPP-mediated drug delivery are the lack of cell specificity, inefficient endosomal escape, and low serum stability.⁹⁵ Various approaches are being developed to address these issues, such as creating activatable CPPs to enhance cell/tissue specificity,¹⁰² incorporating histidines to facilitate endosomal escape,¹⁰³ and using unnatural amino acids to increase peptide stability.¹⁰⁴

1.8 Previous Work in Guan Lab

Our group has developed several biodegradable synthetic vectors for RNA delivery. A multifunctional dendronized peptide polymer (denpol) system for siRNA delivery was first reported by our group in 2013 (**Figure 1.11A**).¹⁰⁵ In the denpol system, a dicysteine unit is incorporated into each repeating unit of the polymer backbone to provide glutathione-triggered bioreducibility and lysine is included to provide dendritic

architectures of the polymer. Each dendron is further functionalized with different amino acids, aiming to provide buffering capacity for endosomal escape, hydrophobicity for cellular uptake, and cationic charges for RNA complexation. It is demonstrated that the denpol system is highly biodegradable, non-toxic, and be able to deliver siRNA efficiently in high serum percentage conditions.

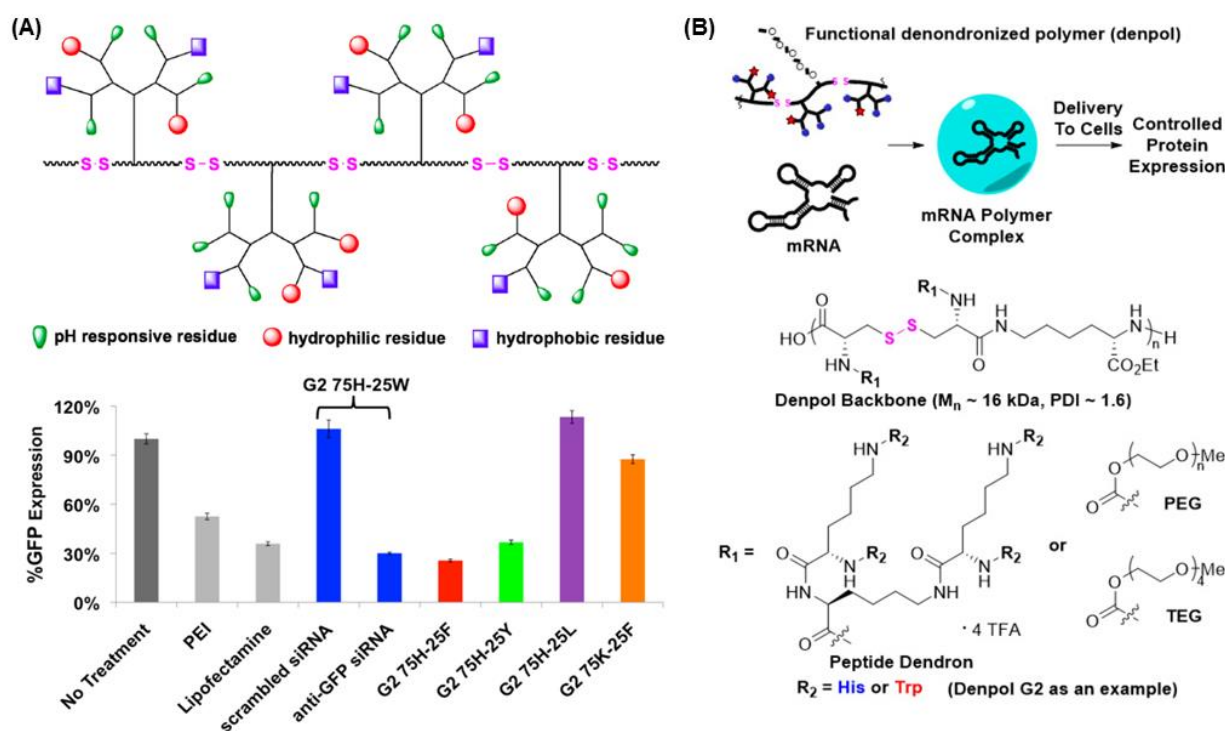


Figure 1.11 Multifunctional dendronized peptide polymer system for (A) siRNA delivery and (B) mRNA delivery. Adapted and reprinted from Ref.¹⁰⁵⁻¹⁰⁶

After being demonstrated for successful siRNA delivery, the denpol system was further engineered to deliver large mRNAs (**Figure 1.11B**).¹⁰⁶ Different hydrophilic side chains including tetraethylene glycol (TEG) and polyethylene glycol (PEG) were incorporated into the denpol system, in order to prevent aggregation and increase complex stability. This work showed that the functionalized denpol system was also able to deliver large mRNA molecules into multiple cell lines under serum-containing conditions.

Specifically, the functionalization of two amino acids, histidine (His) and tryptophan (Trp), are essential for successful RNA delivery. His affords 'proton sponge' effect through imidazole rings for enhancing endosomal escape while Trp promotes RNA binding and cellular uptake through the intercalation of the indole ring.

In addition, Guan lab developed another synthetic vector system, called dendritic peptide bolaamphiphile, for siRNA delivery (**Figure 1.12A**).¹⁰⁷ This biodegradable vector consists of a dumbbell shaped structure with two hydrophilic head groups and a hydrophobic core. It is also shown that these peptide bolaamphiphiles can deliver siRNAs in multiple cell lines with high transfection efficiency, excellent serum tolerance, and low cytotoxicity. Moreover, this work systematically investigated the structure-property correlation in this amphiphilic system. Monoamphiphiles were found to be highly toxic due to membrane insertion while bolaamphiphiles with fluorocarbon cores exhibited enhanced delivery efficiency and improved serum resistance.

Besides bolaamphiphiles with statically amino-acid functionalized dendrons on the head groups, our lab has developed a small focused library of dendritic bola vectors with different discrete dipeptide functionalization (**Figure 1.12B**).¹⁰⁸ More than 50% of the bolaamphiphiles created in this work exhibited prominent siRNA delivery efficiency. The vectors with His and Arg functionalization were found to be the most effective, inducing over 75% gene silencing in media containing 10% serum. This study provides a simple methodology to generate biodegradable siRNA delivery vectors with defined chemical structures, which can be applicable in the design of other synthetic materials of gene delivery.

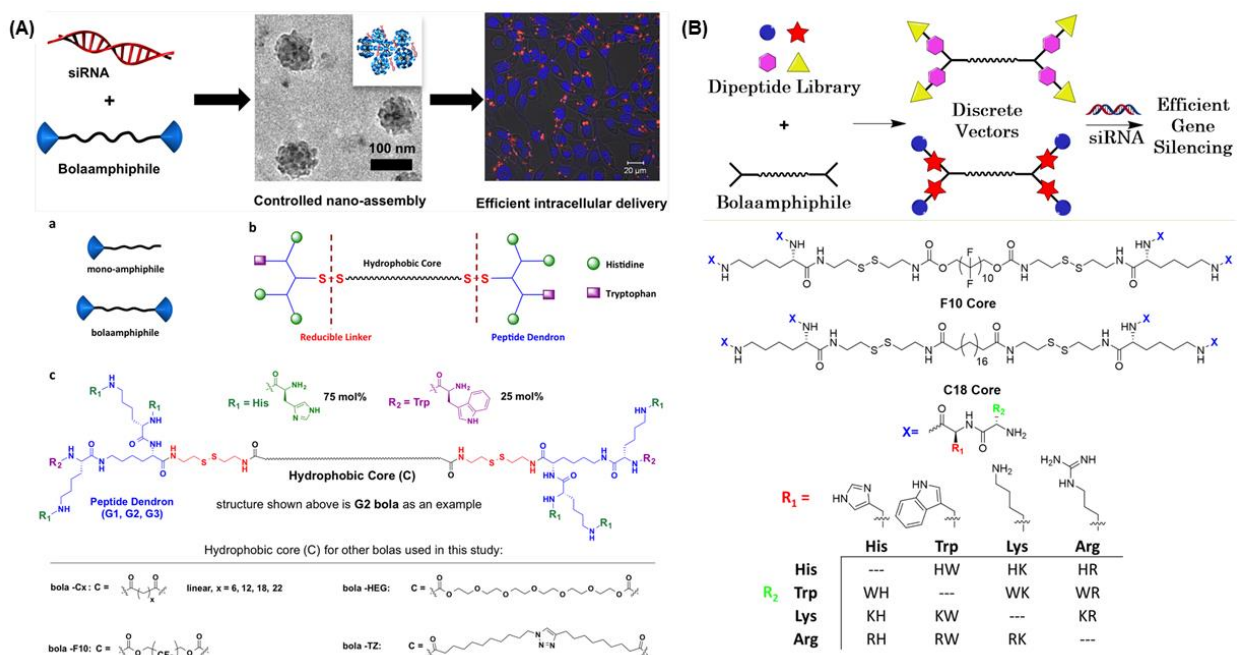


Figure 1.12 (A) Dendritic peptide bolaamphiphiles for siRNA delivery. Adapted and reprinted from Ref.¹⁰⁷ (B) Discrete dipeptide bolaamphiphiles for siRNA delivery. Adapted and reprinted from Ref.¹⁰⁸

1.9 Summary and outlook

Despite the tremendous potential of RNA therapy as mentioned in early sections, there are only relatively few systems being tested in clinical trials. The safe and efficient delivery of powerful RNA molecules into target cells and organs is still a large obstacle. Developing synthetic non-toxic and effective delivery vehicles is of great interest and necessary for pushing RNA therapy into real application. Particularly, understanding the correlation between chemical structure and biological behavior is essential for the vector design. Currently, many delivery systems have their own targeting organs. Avoiding the passive aggregation and realizing targeted delivery is the end goal. This requires the novel design of vehicle-cargo interactions and specific recognition of target cells/organs. Additionally, building up a reliable relationship between experiments *in vitro* and *in vivo* would greatly speed up the development of gene delivery materials and the application of

RNA therapy. Although there is still a long way before RNA therapeutics get widely used in clinic, with fast development and continuous trials, we believe this powerful tool will eventually renovate our medicine and life.

1.10 References

- (1) Vranken, D. V.; Weiss, G., Introduction to Bioorganic Chemistry and Chemical Biology. *Garland Science*, **2013**.
- (2) Dunbar, C. E.; High, K. A.; Joun, J. K.; Kohn, D. B.; Ozawa, K.; Sadelain, M., Gene therapy comes of age. *Science* **2018**, 359 (6372), eaan4672.
- (3) Naldini, L., Gene therapy returns to centre stage. *Nature* **2015**, 526 (7573), 351-360.
- (4) Mulligan, R. C., The basic science of gene therapy. *Science* **1993**, 260 (5110), 926-932.
- (5) Friedmann, T., Progress toward human gene therapy. *Science* **1989**, 244 (4910), 1275-1281.
- (6) Sadelain, M.; Riviere, I.; Riddell, S., Therapeutic T cell engineering. *Nature* **2017**, 545, 423-431.
- (7) High, K. A.; Anguela, X. M., Adeno-associated viral vectors for the treatment of hemophilia. *Hum. Mol. Genet.* **2016**, 25, R36-R41.
- (8) Jenks, S., Gene therapy death – “everyone has to share in the guilt” *J. Natl. Cancer Inst.* **2000**, 92, 98-100.
- (9) Nienhuis, A. W.; Dunbar, C. E.; Sorrentino, B. P., Genotoxicity of retroviral integration in hematopoietic cells. *Mol. Ther.* **2006**, 13, 1031-1049.
- (10) Crooke, S. T.; Witztum, J. L.; Bennett, C. F.; Baker, B. F., RNA-Targeted Therapeutics. *Cell Metab.* **2018**, 27 (4), 714-739.
- (11) Lieberman, J., Tapping the RNA world for therapeutics. *Nat. Struct. Mol. Biol.* **2018**, 25 (5), 357-364.
- (12) Kowalski, P. S.; Rudra, A.; Miao, L.; Anderson, D. G., Delivering the Messenger: Advances in Technologies for Therapeutic mRNA Delivery. *Mol. Ther.* **2019**, 27(4), 710-728.
- (13) Kole, R.; Krainer, A. R.; Altman, S., RNA therapeutics: beyond RNA interference and antisense oligonucleotides. *Nature reviews. Drug discovery* **2012**, 11 (2), 125-140.
- (14) Gavrillo, K.; Saltzman, W. M., Therapeutic siRNA: principles, challenges, and strategies. *Yale J Biol. Med.* **2012**, 85 (2), 187-200.
- (15) Hsu, Patrick D.; Lander, Eric S.; Zhang, F., Development and Applications of CRISPR-Cas9 for Genome Engineering. *Cell* **2014**, 157 (6), 1262-1278.

- (16) Fire, A.; Xu, S.; Montgomery, M. K.; Kostas, S. A.; Driver, S. E.; Mello, C. C., Potent and specific genetic interference by double-stranded RNA in *Caenorhabditis elegans*. *Nature* **1998**, *391*, 806-811.
- (17) Dykxhoorn, D. M.; Novina, C. D.; Sharp, P. A., Killing the messenger: Short RNAs that silence gene expression. *Nat. Rev. Mol. Cell Biol.* **2003**, *4*, 457-467.
- (18) Wilson, R. C.; Doudna, J. A., Molecular mechanisms of RNA interference. *Annu. Rev. Biophys.* **2013**, *42*, 217-239.
- (19) Elbashir, S. M.; Lendeckel, W.; Tuschl, T., RNA interference is mediated by 21- and 22-nucleotide RNAs. *Genes Dev.* **2001**, *15*, 188-200.
- (20) Bernstein, E.; Caudy, A. A.; Hammond, S. M.; Hannon, G. J., Role for a bidentate ribonuclease in the initiation step of RNA interference. *Nature* **2001**, *409*, 363-366.
- (21) Hutvagner, G.; Zamore, P. D., A microRNA in a multiple-turnover RNAi enzyme complex. *Science* **2002**, *297* (5589), 2056-2060.
- (22) Meister G.; Tuschl, T. Mechanisms of gene silencing by double-stranded RNA. *Nature*, **2004**, *431*, 343-349.
- (23) Jinek M.; Doudna J. A., A three-dimensional view of the molecular machinery of RNA interference. *Nature* **2009**, *457* (7228), 405-412.
- (24) McManus, M. T.; Sharp, P. A., Gene silencing in mammals by small interfering RNAs. *Nature Rev. Genet.* **2002**, *3*, 737-747.
- (25) Pasquinelli, A. E.; Ruvkun, G., Control of developmental timing by micrornas and their targets. *Annu. Rev. Cell Dev. Biol.* **2002**, *18*, 495-513.
- (26) Lam, J. K.; Chow, M. Y.; Zhang, Y.; Leung, S. W., siRNA versus miRNA as therapeutics for gene silencing. *Mol. Ther. –Nucleic Acids* **2015**, *4*, e252.
- (27) Gavrilov, K.; Saltzman, W. M., Therapeutic siRNA: principles, challenges, and strategies. *Yale J Biol. Med.* **2012**, *85* (2), 187-200.
- (28) Wood, H., FDA approves patisiran to treat hereditary transthyretin amyloidosis. *Nat. Rev. Neurol.* **2018**, *14* (10), 570.
- (29) Kaczmarek, J. C.; Kowalski, P. S.; Anderson, D. G., Advances in the delivery of RNA therapeutics: from concept to clinical reality. *Genome Med* **2017**, *9* (1), 60.
- (30) Sahin, U.; Kariko, K.; Tureci, O., mRNA-based therapeutics--developing a new class of drugs. *Nat. Rev. Drug Discov.* **2014**, *13* (10), 759-780.
- (31) Josephson, N., The hemophilias and their clinical management. *Hematology Am. Soc. Hematol. Educ. Program* **2013**, *2013*, 261-267.
- (32) Bonne, G.; Barletta, M. R.; Varnous, S.; Becane, H.-M.; Hammouda, E.-H.; Merlini, L.; Muntoni, F.; Greenberg, C. R.; Gary, F.; Urtizberea, J.-A.; Duboc, D.; Fardeau, M.; Toniolo, D.; Schwartz, K., Mutations in the gene encoding lamin A/C cause autosomal dominant Emery–Dreifuss muscular dystrophy. *Nat. Genet.* **1999**, *21*, 285-288.

- (33) Leader, B.; Baca, Q. J.; Golan, D. E., Protein therapeutics: a summary and pharmacological classification. *Nat. Rev. Drug Discovery* **2008**, *7*, 21-39.
- (34) Warner, J.; Knopf, P.; Rich, A., A multiple ribosomal structure in protein synthesis. *Proc. Natl Acad. Sci. USA* **1963**, *49*, 122–129.
- (35) Hajj, K. A.; Whitehead, K. A., Tools for translation: non-viral materials for therapeutic mRNA delivery. *Nat. Rev. Mater.* **2017**, *2* (10), 17056.
- (36) Schlake, T.; Thess, A.; Fotin-Mleczek, M.; Kallen, K. J., Developing mRNA-vaccine technologies. *RNA Biol.* **2012**, *9* (11), 1319-1330.
- (37) Midoux, P.; Pichon, C., Lipid-based mRNA vaccine delivery systems. *Expert Rev. Vaccines* **2015**, *14*, 221–234.
- (38) Deering, R. P.; Kommareddy, S.; Ulmer, J. B.; Brito, L. A.; Geall, A. J., Nucleic acid vaccines: prospects for non-viral delivery of mRNA vaccines. *Expert Opin. Drug Deliv.* **2014**, *11* (6), 885-899.
- (39) Geall, A. J.; Verma, A.; Otten, G. R.; Shaw, C. A.; Hekele, A.; Banerjee, K.; Cu, Y.; Beard, C. W.; Brito, L. A.; Krucker, T.; O'Hagan, D. T.; Singh, M.; Mason, P. W.; Valiante, N. M.; Dormitzer, P. R.; Barnett, S. W.; Rappuoli, R.; Ulmer, J. B.; Mandl, C. W., Nonviral delivery of self-amplifying RNA vaccines. *Proc. Natl. Acad. Sci. U. S. A.* **2012**, *109* (36), 14604-14609.
- (40) Ortin J.; Parra, F., Structure and Function of RNA Replication. *Annu. Rev. Microbiol.* **2006**, *60*, 305-326.
- (41) Johansson, D. X.; Ljungberg, K.; Kakoulidou, M.; Liljeström, P., Intradermal Electroporation of Naked Replicon RNA Elicits Strong Immune Responses. *PLoS ONE* **2012**, *7*, e29732.
- (42) Pardi, N.; Parkhouse, K.; Kirkpatrick, E.; McMahon, M.; Zost, S. J.; Mui, B. L.; Tam, Y. K.; Kariko, K.; Barbosa, C. J.; Madden, T. D.; Hope, M. J.; Krammer, F.; Hensley, S. E.; Weissman, D., Nucleoside-modified mRNA immunization elicits influenza virus hemagglutinin stalk-specific antibodies. *Nat. Commun.* **2018**, *9*, 3361.
- (43) Richner, J. M.; Himansu, S.; Dowd, K. A.; Butler, S. L.; Salazar, V.; Fox, J. M.; Julander, J. G.; Tang, W. W.; Shresta, S.; Pierson, T. C.; Ciaramella, G.; Diamond, M. S., Modified mRNA vaccines protect against Zika virus infection. *Cell* **2017**, *168*, 1114-1125.
- (44) Stitz, L.; Vogel, A.; Schnee, M.; Voss, D.; Rauch, S.; Mutzke, T.; Ketterer, T.; Kramps, T.; Petsch, B. A thermostable messenger RNA based vaccine against rabies. *PLoS Neglected Trop. Dis.* **2017**, *11* (12), e0006108.
- (45) Oberli, M. A.; Reichmuth, A. M.; Dorkin, J. R.; Mitchell, M. J.; Fenton, O. S.; Jaklenec, A.; Anderson, D. G.; Langer, R.; Blankschtein, D., Lipid nanoparticle assisted mRNA delivery for potent cancer immunotherapy. *Nano Lett.* **2016**, *17*, 1326–1335.
- (46) Kalos, M.; June, C. H., Adoptive T cell transfer for cancer immunotherapy in the era of synthetic biology. *Immunity* **2013**, *39* (1), 49-60.
- (47) Maus, M.; Grupp, S. A.; Porter, D. L.; June, C. H., Antibody-modified T cells: CARs take the front seat for hematologic malignancies. *Blood* **2014**, *123*, 2625–2635.

- (48) Li, B.; Luo, X.; Dong, Y., Effects of Chemically Modified Messenger RNA on Protein Expression. *Bioconjugate chemistry* **2016**, 27 (3), 849-853.
- (49) Adli, M., The CRISPR tool kit for genome editing and beyond. *Nat. Commun.* **2018**, 9, 1911.
- (50) Horvath, P.; Barrangou, R., CRISPR/Cas, the Immune System of Bacteria and Archaea. *Science* **2010**, 327 (5962), 167-170.
- (51) Jiang, F.; Doudna, J. A., CRISPR-Cas9 structures and mechanisms. *Annu. Rev. Biophys.* **2017**, 6, 505-529.
- (52) Thurtle-Schmidt, D. M.; Lo, T. W., Molecular biology at the cutting edge: A review on CRISPR/CAS9 gene editing for undergraduates. *Biochem. Mol. Biol. Educ.* **2018**, 46 (2), 195-205.
- (53) Yin, H.; Kauffman, K. J.; Anderson, D. G., Delivery technologies for genome editing. *Nat. Rev. Drug Discovery* **2017**, 16 (6), 387-399.
- (54) Miller, J. B.; Zhang, S. Y.; Kos, P.; Xiong, H.; Zhou, K. J.; Perelman, S. S.; Zhu, H.; Siegwart, D. J., Non-Viral CRISPR/Cas Gene Editing In Vitro and In Vivo Enabled by Synthetic Nanoparticle Co-Delivery of Cas9 mRNA and sgRNA. *Angew. Chem. Int. Ed.* **2017**, 56 (4), 1059-1063.
- (55) Dowdy, S. F., Overcoming cellular barriers for RNA therapeutics. *Nat. Biotechnol.* **2017**, 35 (3), 222-229.
- (56) Sharova, L. V.; Sharov, A. A.; Nedorezov, T.; Piao, Y.; Shaik, N.; Ko, M. S. H., Database for mRNA HalfLife of 19 977 Genes Obtained by DNA Microarray Analysis of Pluripotent and Differentiating Mouse Embryonic Stem Cells. *DNA Res.* **2009**, 16 (1), 45-58.
- (57) Judge, A. D.; Sood, V.; Shaw, J. R.; Fang, D.; McClintock, K.; MacLachlan, I., Sequence-dependent stimulation of the mammalian innate immune response by synthetic siRNA. *Nat. Biotechnol.* **2005**, 23 (4), 457-462.
- (58) Behr, J. P., Synthetic Gene Transfer Vectors II: Back to the Future. *Acc. Chem. Res.* **2012**, 45, 980-984.
- (59) Emami, J., In vitro – in vivo correlation: from theory to applications. *J. Pharm. Pharmaceut. Sci.* **2006**, 9 (2), 31-51.
- (60) Mattison, K. W.; Dubin, P. L.; Brittain, I. J., Complex formation between bovine serum albumin and strong polyelectrolytes: Effect of polymer charge density. *J Phys Chem B* **1998**, 102 (19), 3830-3836.
- (61) Kranz, L. M.; Diken, M.; Haas, H.; Kreiter, S.; Loquai, C.; Reuter, K. C.; Meng, M.; Fritz, D.; Vascotto, F.; Hefesha, H.; Grunwitz, C.; Vormehr, M.; Husemann, Y.; Selmi, A.; Kuhn, A. N.; Buck, J.; Derhovanessian, E.; Rae, R.; Attig, S.; Diekmann, J.; Jabulowsky, R. A.; Heesch, S.; Hassel, J.; Langguth, P.; Grabbe, S.; Huber, C.; Tureci, O.; Sahin, U., Systemic RNA delivery to dendritic cells exploits antiviral defense for cancer immunotherapy. *Nature* **2016**, 534 (7607), 396-401.

- (62) Usman, W. M.; Pham, T. C.; Kwok, Y. Y.; Vu, L. T.; Ma, V.; Peng, B.; Chan, Y. S.; Wei, L.; Chin, S. M.; Azad, A.; He, A. B.; Leung, A. Y.; Yang, M.; Shyh-Chang, N.; Cho, W. C.; Shi, J.; Le, M. T., Efficient RNA drug delivery using red blood cell extracellular vesicles. *Nat. Commun.* **2018**, *9*, 2359.
- (63) Young, L. S.; Searle, P. F.; Onion, D.; Mautner, V., Viral gene therapy strategies: from basic science to clinical application. *J. Pathol.* **2006**, *208* (2), 299-318.
- (64) Davidson, B. L.; Breakefield, X. O., Viral vectors for gene delivery to the nervous system. *Nat. Rev. Neurosci.* **2003**, *4* (5), 353-364.
- (65) Greber, U. F.; Willetts, M.; Webster, P.; Helenius, A., Stepwise dismantling of adenovirus 2 during entry into cells. *Cell* **1993**, *75*, 477-486.
- (66) Colella, P.; Ronzitti, G.; Mingozzi, F., Emerging Issues in AAV-Mediated In Vivo Gene Therapy. *Mol. Ther-Meth. Clin. D.* **2018**, *8*, 87-104.
- (67) Yin, H.; Kanasty, R. L.; Eltoukhy, A. A.; Vegas, A. J.; Dorkin, J. R.; Anderson, D. G., Non-viral vectors for gene-based therapy. *Nat. Rev. Genet.* **2014**, *15* (8), 541-555.
- (68) Li, S. Y.; Yang, S. M.; Chen, G.; Li, X. D.; Chen, J.; Ma, Y. G.; Xu, H., Mechanism of Cellular Uptake, Localization and Cytotoxicity of Organic Nanoparticles. *J. Nanosci. Nanotechnol.* **2014**, *14* (5), 3292-3298.
- (69) Selby, L. I.; Cortez-Jugo, C. M.; Such, G. K.; Johnston, A. P. R., Nanoescapology: progress toward understanding the endosomal escape of polymeric nanoparticles. *Wiley Interdiscip Rev Nanomed Nanobiotechnol.* **2017**, *9* (5), e1452.
- (70) Resnier, P.; Montier, T.; Mathieu, V.; Benoit, J. P.; Passirani, C., A review of the current status of siRNA nanomedicines in the treatment of cancer. *Biomaterials* **2013**, *34* (27), 6429-6443.
- (71) Jobin, M. L.; Blanchet, M.; Henry, S.; Chaignepain, S.; Manigand, C.; Castano, S.; Lecomte, S.; Burlina, F.; Sagan, S.; Alves, I. D., The role of tryptophans on the cellular uptake and membrane interaction of arginine-rich cell penetrating peptides. *Biochim. Biophys. Acta* **2015**, *1848* (2), 593-602.
- (72) Pujals, S.; Giralt, E., Proline-rich, amphipathic cellpenetrating peptides. *Adv. Drug Delivery Rev.* **2008**, *60* (4-5), 473-484.
- (73) Varkouhi, A. K.; Scholte, M.; Storm, G.; Haisma, H. J., Endosomal escape pathways for delivery of biologicals. *J Control Release* **2011**, *151* (3), 220-228.
- (74) Cho, Y. W.; Kim, J. D.; Park, K., Polycation gene delivery systems: escape from endosomes to cytosol. *J Pharm. Pharmacol.* **2003**, *55* (6), 721-734.
- (75) Meng, Z.; Luan, L.; Kang, Z. Y.; Feng, S. L.; Meng, Q. B.; Liu, K. L., Histidine-enriched multifunctional peptide vectors with enhanced cellular uptake and endosomal escape for gene delivery. *J Mater Chem. B* **2017**, *5* (1), 74-84.
- (76) Akita, H.; Kudo, A.; Minoura, A.; Yamaguti, M.; Khalil, I. A.; Moriguchi, R.; Masuda, T.; Danev, R.; Nagayama, K.; Kogure, K.; Harashima, H., Multi-layered nanoparticles for penetrating the endosome and nuclear membrane via a step-wise membrane fusion process. *Biomaterials* **2009**, *30* (15), 2940-2949.

- (77) Nakase I.; Kobayashi S.; Futaki S., Endosomedisruptive peptides for improving cytosolic delivery of bioactive macromolecules. *Biopolymers* **2010**, *94*:763–770.
- (78) Seow, Y.; Wood, M. J., Biological gene delivery vehicles: beyond viral vectors. *Mol. Ther.* **2009**, *17* (5), 767-777.
- (79) Cullis, P. R.; Hope, M. J., Lipid Nanoparticle Systems for Enabling Gene Therapies. *Mol. Ther.* **2017**, *25* (7), 1467-1475.
- (80) Lonez, C.; Vandenbranden, M.; Ruyschaert, J. M., Cationic liposomal lipids: from gene carriers to cell signaling. *Prog. Lipid Res.* **2008**, *47*, 340–347.
- (81) Rietwyk, S.; Peer, D., Next-Generation Lipids in RNA Interference Therapeutics. *ACS Nano* **2017**, *11* (8), 7572-7586.
- (82) Sago, C. D.; Lokugamage, M. P.; Paunovska, K.; Vanover, D. A.; Monaco, C. M.; Shah, N. N.; Castro, M. G.; Anderson, S. E.; Rudoltz, T. G.; Lando, G. N.; Tiwari, P. M.; Kirschman, J. L.; Willett, N.; Jang, Y. C.; Santangelo, P. J.; Bryksin, A. V.; Dahlman, J. E., High-throughput in vivo screen of functional mRNA delivery identifies nanoparticles for endothelial cell gene editing. *Proc. Natl. Acad. Sci. U. S. A.* **2018**, *115*, E9944-E9952.
- (83) Lv, H.; Zhang, S.; Wang, B.; Cui, S.; Yan, J., Toxicity of cationic lipids and cationic polymers in gene delivery. *J Control Release* **2006**, *114* (1), 100-109.
- (84) Zhao, M.; Li, M.; Zhang, Z.; Gong, T.; Sun, X., Induction of HIV-1 gag specific immune responses by cationic micelles mediated delivery of gag mRNA. *Drug Deliv.* **2016**, *23*, 2596–2607.
- (85) Johnson, M. E.; Shon, J.; Guan, B. M.; Patterson, J. P.; Oldenhuis, N. J.; Eldredge, A. C.; Gianneschi, N. C.; Guan, Z., Fluorocarbon Modified Low-Molecular-Weight Polyethylenimine for siRNA Delivery. *Bioconjugate chemistry* **2016**, *27* (8), 1784-1788.
- (86) Baba, M.; Itaka, K.; Kondo, K.; Yamasoba, T.; Kataoka, K. Treatment of neurological disorders by introducing mRNA *in vivo* using polyplex nanomicelles. *J. Control. Release* **2015**, *201*, 41–48.
- (87) Ullah, I.; Muhammad, K.; Akpanyung, M.; Nejjari, A.; Neve, A. L.; Guo, J.; Feng, Y.; Shi, C., Bioreducible, hydrolytically degradable and targeting polymers for gene delivery. *Journal of Materials Chemistry B* **2017**, *5* (18), 3253-3276.
- (88) Luten, J.; van Nostrum, C. F.; De Smedt, S. C.; Hennink, W. E., Biodegradable polymers as non-viral carriers for plasmid DNA delivery. *J Control Release* **2008**, *126* (2), 97-110.
- (89) Oldenhuis, N. J.; Eldredge, A. C.; Burts, A. O.; Ryu, K. A.; Chung, J.; Johnson, M. E.; Guan, Z., Biodegradable Dendronized Polymers for Efficient mRNA Delivery. *ChemistrySelect* **2016**, *1* (15), 4413-4417.
- (90) Ou, M.; Xu, R.; Kim, S. H.; Bull, D. A.; Kim, S. W., A family of bioreducible poly(disulfide amine)s for gene delivery, *Biomaterials*, **2009**, *30* (29), 5804–5814.

- (91) Heller, J.; Barr, J.; Ng, S. Y.; Abdellauoi, K. S.; Gurny, R., Poly(ortho esters): synthesis, characterization, properties and uses. *Adv. Drug Deliv. Rev.* **2002**, *54*, 1015–1039.
- (92) McKinlay, C. J.; Vargas, J. R.; Blake, T. R.; Hardy, J. W.; Kanada, M.; Contag, C. H.; Wender, P. A.; Waymouth, R. M., Charge-altering releasable transporters (CARTs) for the delivery and release of mRNA in living animals. *P. Natl. Acad. Sci. U. S. A.* **2017**, *114* (4), E448-E456.
- (93) Bragonzi, A.; Boletta, A.; Biffi, A.; Muggia, A.; Sersale, G.; Cheng, S. H.; Bordignon, C.; Assael, B. M.; Conese, M., Comparison between cationic polymers and lipids in mediating systemic gene delivery to the lungs. *Gene Ther.* **1999**, *6*, 1995-2004.
- (94) Ahmed, M., Peptides, polypeptides and peptide-polymer hybrids as nucleic acid carriers. *Biomater. Sci.* **2017**, *5*, 2188-2211.
- (95) Guidotti, G.; Brambilla, L.; Rossi, D., Cell-Penetrating Peptides: From Basic Research to Clinics. *Trends Pharmacol Sci* **2017**, *38* (4), 406-424.
- (96) Copolovici, D. M.; Langel, K.; Eriste, E.; Langel, U., Cell-Penetrating Peptides: Design, Synthesis, and Applications. *ACS Nano*, **2014**, *8*, 1972-1994.
- (97) Frankel, A. D.; Pabo, C. O., Cellular Uptake of the Tat Protein from Human Immunodeficiency Virus. *Cell* **1988**, *55*, 1189–1193.
- (98) McKinlay, C. J.; Waymouth, R. M.; Wender, P. A., Cell-pepetrating, guanidinium-rich oligophosphoesters: effective and versatile molecular transporters for drug and probe delivery. *J. Am. Chem. Soc.* **2016**, *138*, 3510-3517.
- (99) Pooga, M.; Soomets, U.; Hallbrink, M.; Valkna, A.; Saar, K.; Rezaei, K.; Kahl, U.; Hao, J.; Xu, X.; Wiesenfeld-Hallin, Z.; Hokfelt, T.; Bartfai, T.; Langel, U. Cell penetrating PNA constructs regulate galanin receptor levels and modify pain transmission in vivo. *Nat. Biotechnol.* **1998**, *16*, 857–861.
- (100) Oehlke, J.; Scheller, A.; Wiesner, B.; Krause, E.; Beyermann, M.; Klauschenz, E.; Melzig, M.; Bienert, M. Cellular uptake of an alpha-helical amphipathic model peptide with the potential to deliver polar compounds into the cell interior non-endocytically. *Biochim. Biophys. Acta* **1998**, *1414*, 127–139.
- (101) Marks, J. R.; Placone, J.; Hristova, K.; Wimley, W. C. Spontaneous membrane-translocating peptides by orthogonal high-throughput screening. *J. Am. Chem. Soc.* **2011**, *133*, 8995–9004.
- (102) Aguilera, T. A.; Timmers, M. M.; Olson, E. S.; Jiang, T.; Tsien, R. Y., Systemic in vivo distribution of activatable cell penetrating peptides is superior to that of cell penetrating peptides. *Integr. Biol. (Camb.)* **2009**, *1*, 371–381.
- (103) Midoux, P.; Pichon, C.; Yaouanc, J. J.; Jaffres, P. A., Chemical vectors for gene delivery: a current review on polymers, peptides and lipids containing histidine or imidazole as nucleic acids carriers. *Br. J. Pharmacol.* **2009**, *157* (2), 166-178.
- (104) Jarver, P.; Mager, I.; Langel, U., In vivo biodistribution and efficacy of peptide mediated delivery. *Trends Pharmacol. Sci.* **2010**, *31*, 528–535.

- (105) Zeng, H.; Little, H. C.; Tiambeng, T. N.; Williams, G. A.; Guan, Z., Multifunctional dendronized peptide polymer platform for safe and effective siRNA delivery. *J. Am. Chem. Soc.* **2013**, *135* (13), 4962-4965.
- (106) Oldenhuis, N. J.; Eldredge, A. C.; Burts, A. O.; Ryu, K. A.; Chung, J.; Johnson, M. E.; Guan, Z., Biodegradable Dendronized Polymers for Efficient mRNA Delivery. *ChemistrySelect* **2016**, *1* (15), 4413-4417.
- (107) Zeng, H.; Johnson, M. E.; Oldenhuis, N. J.; Tiambeng, T. N.; Guan, Z., Structure Based Design of Dendritic Peptide Bolaamphiphiles for siRNA Delivery. *ACS Cent. Sci.* **2015**, *1* (6), 303-312.
- (108) Eldredge, A. C.; Johnson, M. E.; Oldenhuis, N. J.; Guan, Z., Focused Library Approach to Discover Discrete Dipeptide Bolaamphiphiles for siRNA Delivery. *Biomacromolecules* **2016**, *17* (10), 3138-3144.

Chapter 2: Multivalent Peptide-functionalized Bioreducible Polymers for Universal Delivery of Various RNAs

2.1 Introduction and Project Design

RNA-based therapeutics has emerged as an exciting new biotechnology platform to innovate protein therapies, develop next generation vaccines, and treat genetic diseases.¹⁻⁴ Compared to DNAs, RNAs are more versatile as therapeutic RNAs effect a diverse range of biological functions depending on their size and structure. For example, short interfering RNAs (siRNAs) are 20-25 base pairs (bp), rigid, and double-stranded, which can silence specific genes for disease treatments.⁵⁻⁶ On the other hand, messenger RNAs (mRNAs) are single-stranded and can vary from several hundred nucleotides (nts) to several thousand nucleotides. Therapeutic mRNAs are an emerging drug class for protein replacement therapy, cancer immunotherapy, and gene therapy.⁷⁻⁹ A special class of mRNA, called self-replicating or replicon mRNA, has remarkable large size ($\sim 10^4$ nt) and intricate secondary structure, which is highly promising for vaccination via inducing a prolonged immune response.¹⁰⁻¹¹ In addition, single guide RNA (sgRNA) with an intermediate length (~ 100 nts) can guide Cas9 nuclease protein to execute precise genome editing via Clustered Regularly Interspaced Short Palindromic Repeat (CRISPR)-Cas mechanisms.¹²

To achieve their therapeutic functions, RNAs must be safely and efficiently delivered into cells. Without proper delivery vehicles, naked RNAs are highly sensitive to nuclease degradation and can promote undesired immune response. Their large macromolecular sizes and high negative charges also prevent them from passively crossing the cell membrane.^{3,4,13} Despite the tremendous promise of RNA drugs, the general lack of safe and effective intracellular delivery vehicles has significantly hindered the clinical translation

and widespread application of RNA-based therapeutics.¹⁴⁻¹⁷ Furthermore, current delivery systems are usually designed for delivering one specific type of RNA cargo for each carrier. For general applicability, it is highly desirable to have a universal delivery system that can efficiently deliver all types of therapeutic RNAs of various structures and sizes to perform the diverse therapeutic functions. This would save research efforts in optimizing and identifying delivery vectors for each different RNA cargo and speed up the clinical translation of RNA therapies. Furthermore, a universal delivery vector allows for the potential to co-deliver multiple RNA species for advanced therapeutic applications and treatment of multiple pathways in a single formulation.

Broadly speaking, RNA delivery can be mediated by viral and non-viral vectors. Viral vectors are highly efficient delivery vehicles, however, they pose safety concerns related to immunogenicity and have limitations on cargo size, making them non-ideal candidates for a universal vector.¹⁸ These concerns have led to the development of a variety of synthetic non-viral delivery vectors over the past several decades, including lipids and lipid nanoparticles,¹⁹⁻²² polymers,²³⁻²⁹ dendrimers,³⁰⁻³² cell-penetrating peptides (CPP),³³⁻³⁴ and gold nanoparticles.³⁵⁻³⁶

An ideal RNA delivery vector should be biodegradable, bind RNA cargos favorably, facilitate cellular uptake and endosomal escape, and finally release the RNA molecules efficiently in the cytoplasm.^{13,37} Moreover, for a universal RNA delivery system for various applications, the vector needs to be nontoxic, scalable and tunable in order to match the diverse structures of various RNAs.³⁸⁻³⁹

With these criteria in mind, we designed a family of multivalent peptide-functionalized bio-reducible polymers (MPBP) as a universal vector system for safe and

efficient RNA delivery (**Figure 2.1**). In this system, a dicysteine unit is incorporated into each repeating unit of the polymer backbone to provide glutathione-triggered bioreducibility, ensuring low cytotoxicity and facilitating facile intracellular disassembly of polymer-RNA complexes to release the RNA cargo.^{27,40} L-lysine is used to introduce branched dendritic architectures to the polymer, providing convenient synthetic handles to graft functional peptides and other side chains to generate diverse multivalent architectures. Based on our previous studies,⁴¹⁻⁴⁴ a short, multifunctional peptide was designed to provide several important functional properties including electrostatic interactions for RNA complexation, enhanced cellular uptake, and efficient endosomal escape.

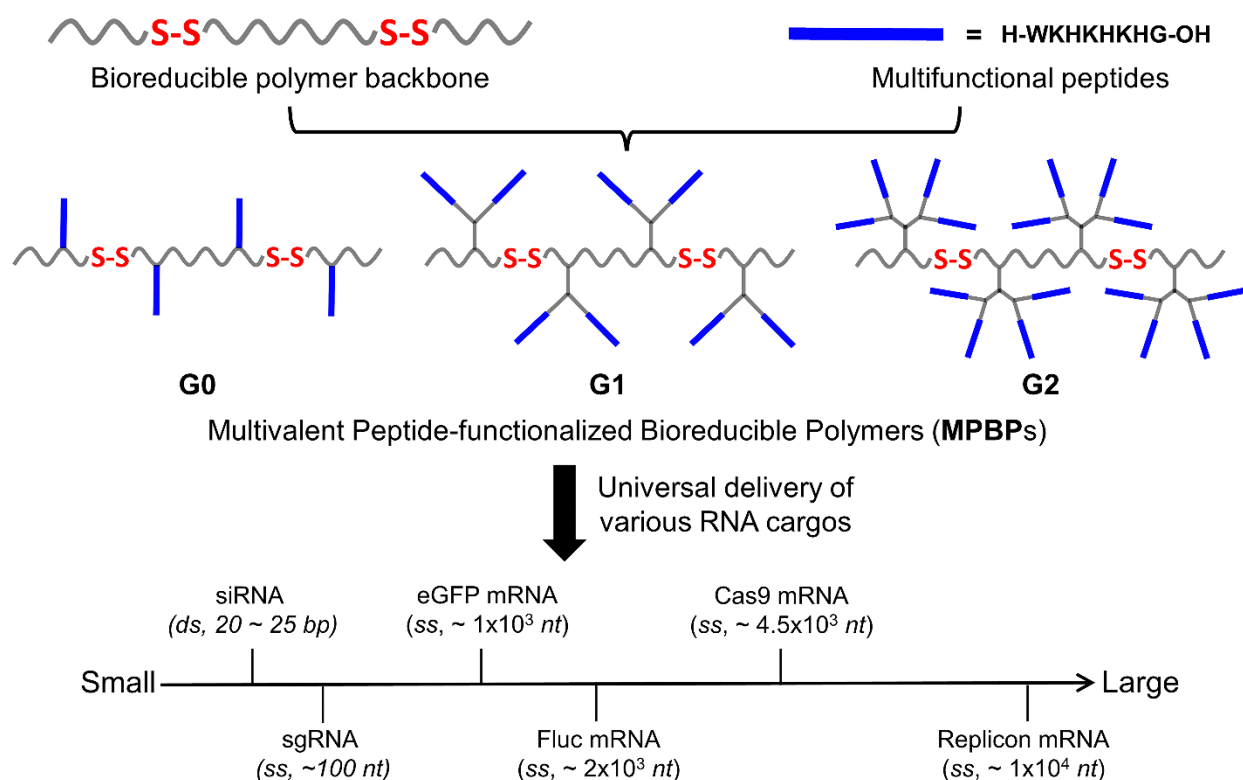


Figure 2.1 Concept of multivalent peptide-functionalized bioreducible polymer (MPBP) vectors for universal RNA delivery.

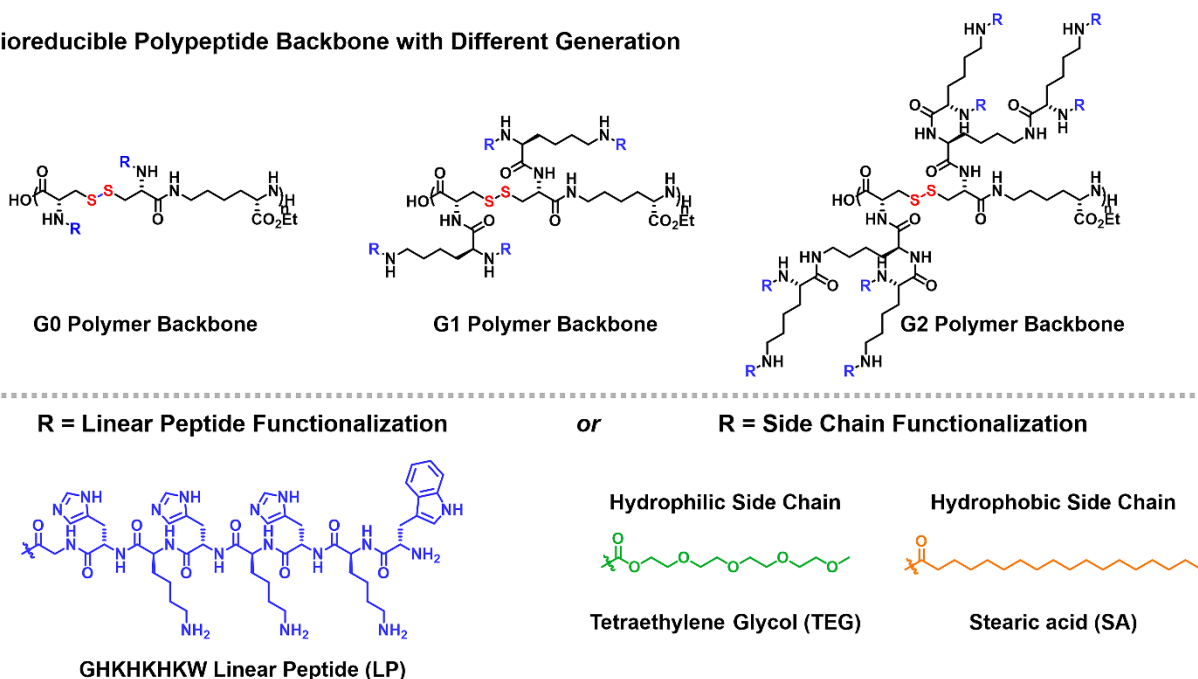
The **MPBP** system has several attractive features, including biocompatibility, high structural tunability, facile synthesis, and scalability. Furthermore, the multivalent presentation of our specially designed multifunctional peptide promotes RNA complexation, cellular uptake, and endosomal escape. Noticeably, through simple changes to the multivalent peptide functionalization we can tune the **MPBP** system to efficiently deliver many types of RNAs of drastically different lengths and structures to multiple cell lines. This includes the delivery of short double-stranded RNA such as siRNA (20-25 bp), sgRNA (100 nt), single-stranded mRNAs of various length (996 nt for eGFP mRNA, 1996 nt for Fluc mRNA, and 4521 nt for Cas9 mRNA), and very large single-stranded self-replicating (Replicon) RNA ($>10^4$ nt). In this article, we will describe the design, synthesis, and investigation of our new **MPBP** system for the successful delivery of various RNAs.

2.2 Design and Synthesis of MPBP

For the delivery of various RNAs with different size and structure, a small library of **MPBPs** with different polymer architectures and side chain functionalization was synthesized (**Figure 2.2**). First, following our previous work a polymer backbone composed of L-lysine – dicysteine repeating units was synthesized through simple step-growth polymerization of dicysteine and L-lysine using 1-ethyl-3-(3-dimethylaminopropyl)carbodiimide (EDC) as the coupling reagent (polymer M_n = 9.37 kDa, PDI = 2.08 by gel-permeation chromatography).⁴¹ Dicysteine was introduced into the polymer backbone to afford bioreducibility for facilitating intracellular disassembly of polymer-RNA complexes to release the RNA cargo in the cytoplasm. Onto the linear polymer backbone, different generations of L-lysine-based dendrons were then grown

through solution-phase peptide coupling. They will serve as the scaffolds to graft our designed multifunctional peptides and other side chains to obtain a small library of vectors.

Bioreducible Polypeptide Backbone with Different Generation



MPBP Library:

G0: G0-100LP, G0-20TEG-80LP, G0-50TEG-50LP, G0-20SA-80LP, G0-50SA-50LP

G1: G1-100LP, G1-20TEG-80LP, G1-50TEG-50LP, G1-20SA-80LP

G2: G2-100LP

Figure 2.2 A small library of **MPBPs** with different polymer architectures and side chain functionalization.

Based on our previous work of dendronized polypeptide (denpol) and bolaamphiphile (bola) based vectors,⁴¹⁻⁴⁴ we designed our multifunctional short peptides composed of three natural amino acids: L-histidine (His), L-lysine (Lys), and L-tryptophan (Trp). Previous studies by us^{41,43} and others⁴⁵ have shown that His moiety enhances endosomal escape through the buffering capacity provided by the pH-responsive nature of the imidazole ring. Lys units provide primary amines for sufficient cationic charges to bind RNA. Earlier studies have also shown that Trp incorporation improves RNA binding and

enhances the cellular uptake due to the intercalation of the indole ring.^{41,46} Whereas in our previous design His and Trp were *statistically* functionalized as individual amino acid moiety onto the periphery of Lys dendrons, in this work a *well-defined, discrete linear peptide* is designed to functionalize the dendrons. Using these three amino acids: His, Lys, and Trp, we initially synthesized several short peptides of various sequences and grafted these peptides onto the bioreducible polymer scaffolds, as prepared above. After some initial screening of various vectors with different peptide sequences (**Figure 2.3**), we chose H-WKHKHKHG-OH for our further studies.

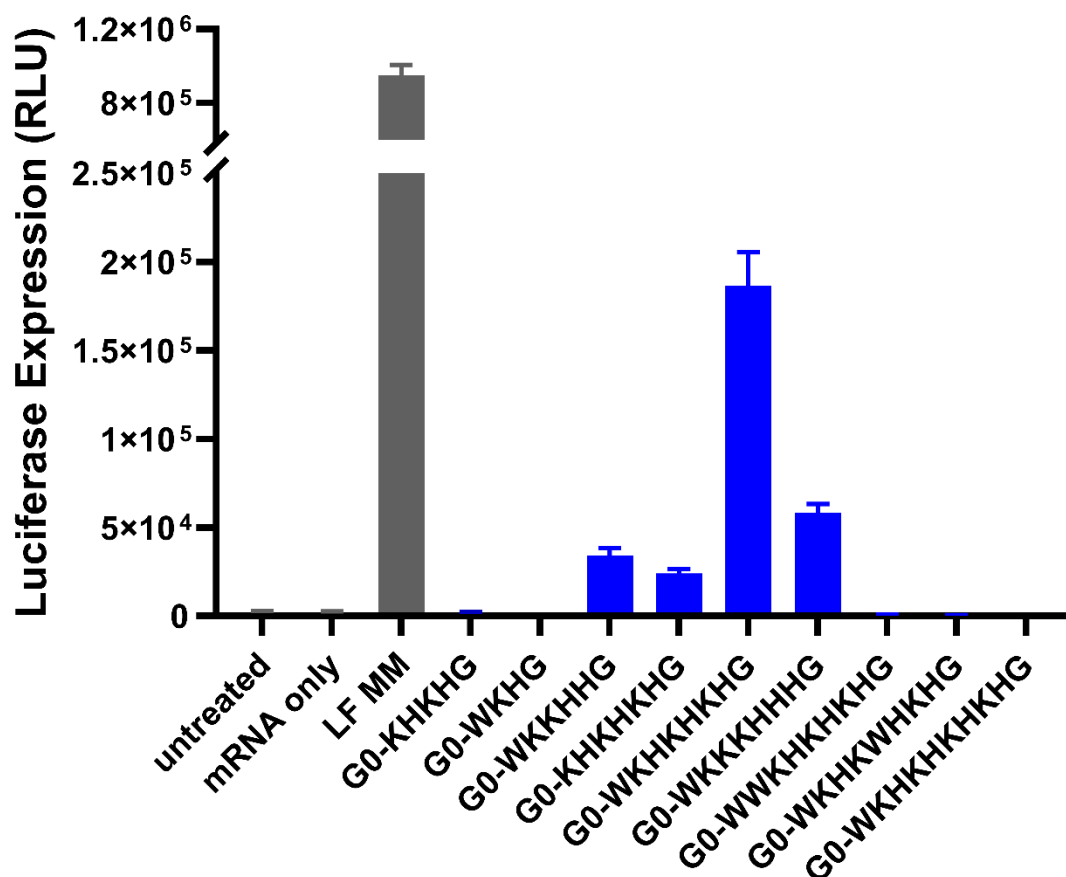


Figure 2.3 Initial Fluc mRNA delivery screening of different MPBPs functionalized with various linear peptides

In addition to peptide functionalization, a fraction of the MPBPs were also functionalized with either hydrophilic tetraethylene glycol (TEG) or hydrophobic stearic acid to tune the hydrophilicity and hydrophobicity of the vectors. TEG side chains were incorporated to prevent potential aggregation and increase serum stability,⁴² whereas stearic acid was added to promote the self-assembly and cell internalization of MPBP-RNA complexes.⁴⁷ The protected linear peptide Boc-WKHKHKHG-OH was synthesized through conventional solid-phase peptide synthesis⁴⁸ and coupled to the polypeptide backbone, with or without hydrophilic/hydrophobic side chains, to afford the final **MPBP** vectors (**Scheme 1, Section 2.12**). All details for the peptide and final MPBP synthesis can be found in **Section 2.12**. For simplicity, the **MPBPs** were named using the dendron generation and the functionalization components with the corresponding percentages. For example, **G1-20TEG-80LP** represents a **MPBP** polymer with first-generation lysine dendrons that were functionalized by 20 mol% TEG and 80 mol% linear peptides (LP).

2.3 Biophysical Study of MPBP-RNA Complexes

First, the binding affinity of the **MPBPs** to RNAs was evaluated via gel electrophoresis. The gel shift assays demonstrated that all **MPBPs** were able to completely bind both siRNA and mRNA at a primary amine/RNA phosphate (N/P) molar ratio of 5 (**Figure 2.4 - 2.5**).

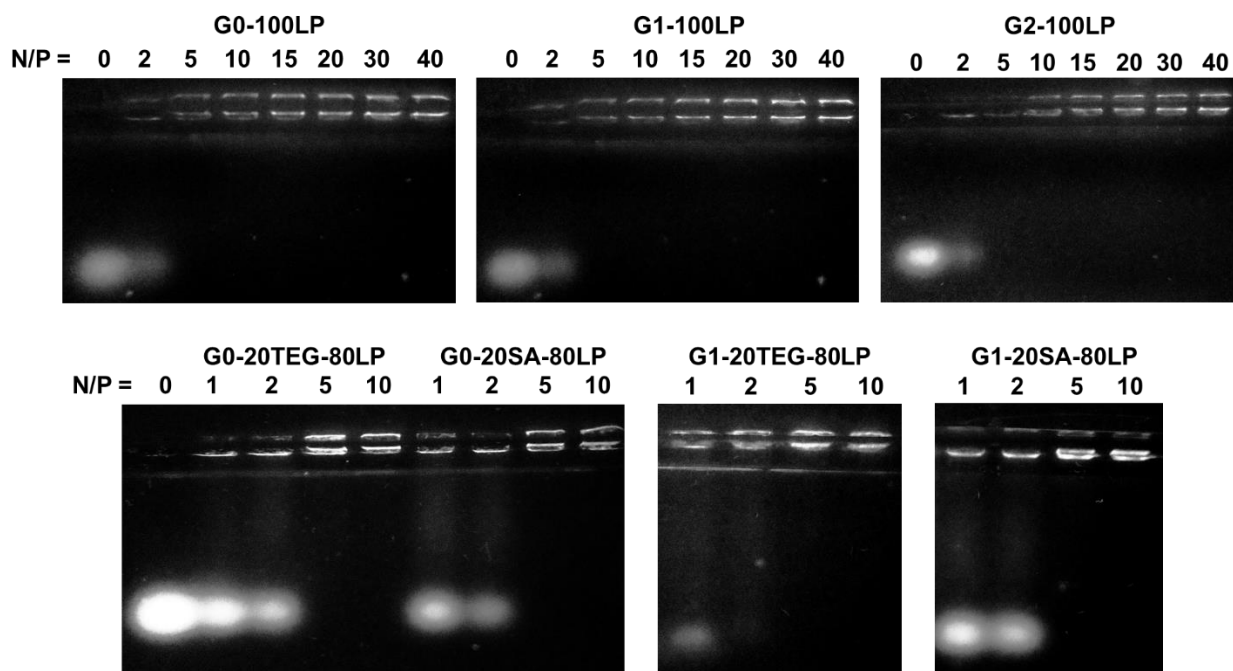


Figure 2.4 Gel electrophoresis study of **MPBP**-siRNA complexation. All vectors surveyed bound siRNA by N/P = 5.

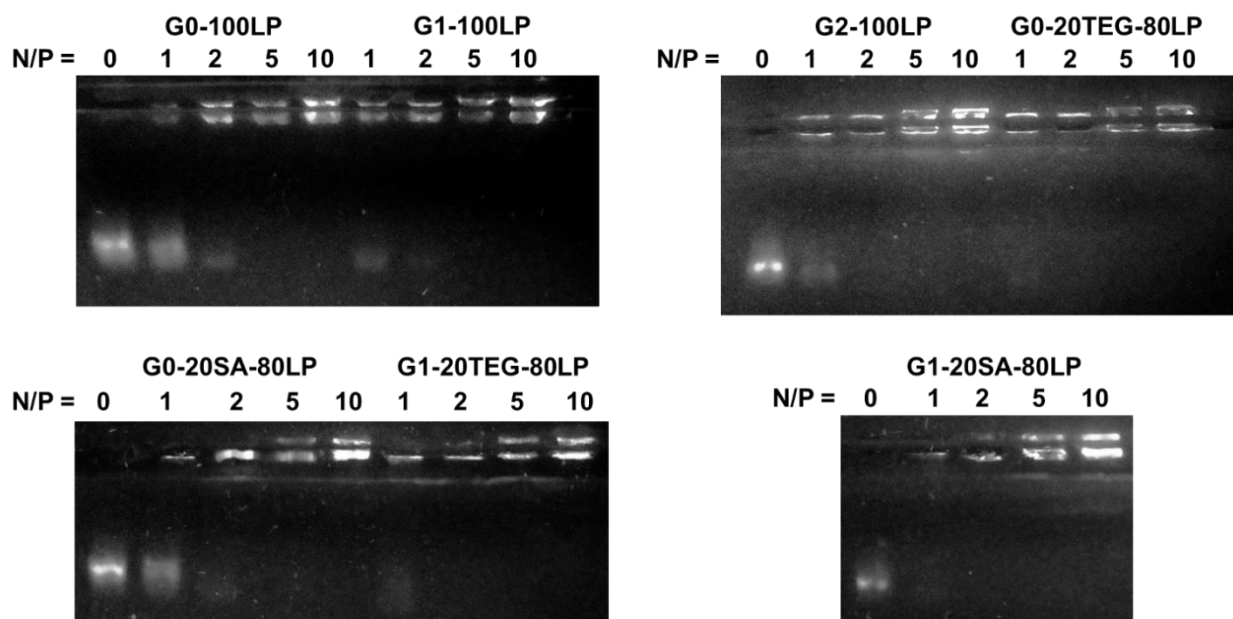


Figure 2.5 Gel electrophoresis study of **MPBP**-eGFP mRNA complexation. All vectors surveyed bound eGFP mRNA by N/P = 5.

RNAs, especially long mRNAs and Replicon RNAs, are very susceptible to degradation by RNases and need to be sufficiently protected for successful delivery.⁴⁹ After Fluc mRNA was complexed with the **MPBPs**, the nanoparticle complexes were incubated with 10% fetal bovine serum (FBS) for 20 minutes. FBS contains several compounds known to degrade RNA, including RNases. The complexes were then subjected to gel electrophoresis to determine the structural integrity of the RNA. Naked Fluc mRNA was fully degraded after FBS incubation, while Fluc mRNAs in **MPBP**-mRNA complexes remained bounded and intact after FBS incubation (**Figure 2.6A**). Furthermore, the dextran sulfate competitive binding study after FBS incubation showed that the RNAs from **MPBP**-RNA complexes were still intact, while the blank RNA was fully degraded (**Figure 2.6B**). These assays demonstrate that the **MPBPs** provide sufficient protection to the large Fluc mRNA molecules from RNases, a critical attribute for a successful delivery vector.

Dynamic light scattering (DLS) was then used to investigate the size and zeta potential of the **MPBP**-RNA nanoparticles. The DLS results showed that all **MPBPs** formed nanoparticles between 100 and 250 nm when complexed with either siRNA or mRNA (**Table 2.1 – 2.2, Figure 2.7 - 2.8**). Compared to **G0** series of vectors, **G1** and **G2** vectors condense RNAs into smaller nanoparticles with higher stability in buffer, presumably due to the increased multivalency and charge density per polymer repeating unit (**Figure 2.9**). TEM imaging of both **MPBP**-siRNA and **MPBP**-mRNA complexes showed spherical nanoparticles with diameters less than 100 nm in the dehydrated state (**Figure 2.10 – 2.11**).

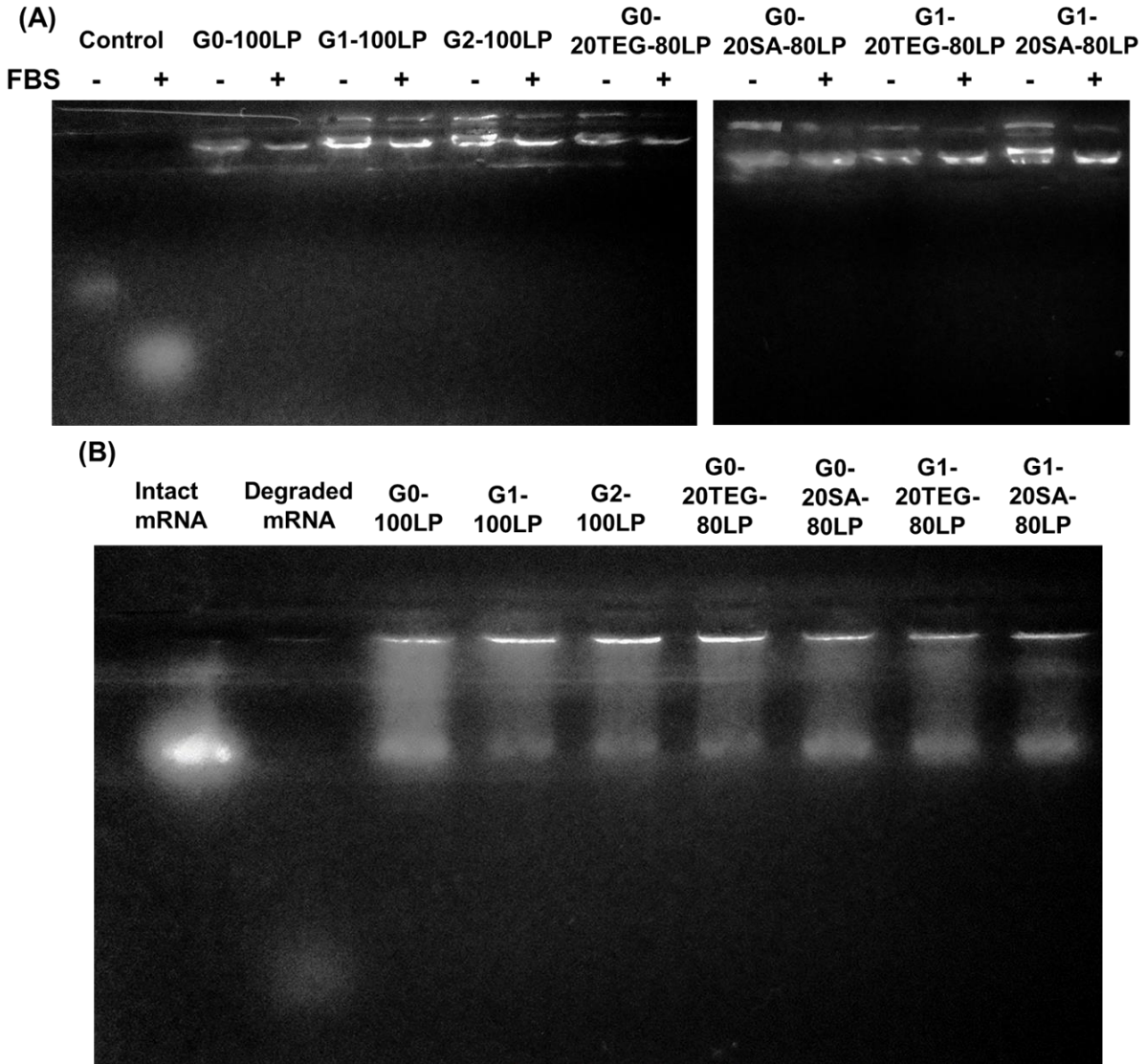


Figure 2.6 Gel electrophoresis study to determine mRNA degradation and protection. (A) Gel binding assays of **MPBP**-Fluc mRNA complexes (N/P = 10) with/without 10% FBS incubation (20 min). Naked mRNA was fully degraded after FBS incubation, while mRNAs in **MPBP**-mRNA complexes remained bounded and intact after FBS incubation. (B) Dextran sulfate competition (S/P = 80) with different **MPBP**-Fluc mRNA complexes (N/P = 10) after FBS incubation to release any bound RNA. The released RNAs from **MPBP**-mRNA complexes were still intact indicating that the **MPBP** protected the RNA from degradation, while the blank RNA was fully degraded.

Table 2.1 DLS measurements of size and Zeta potential of complexes between **MPBPs** and siRNA (N/P = 10, PBS buffer (pH = 7.4), [siRNA] = 150 nM). The Z-Average size is reported as an average value of 3 different measurements.

Sample	Z-Average Size (nm)	PDI	Zeta potential (mV)
G0-100LP	170±10	0.27	8.4
G1-100LP	140±14	0.14	28.2
G2-100LP	133±14	0.15	22.1
G0-20TEG-80LP	201±6	0.12	4.2
G0-20SA-80LP	198±9	0.17	5.4
G1-20TEG-80LP	186±6	0.15	17.1
G1-20SA-80LP	137±5	0.17	17.6

Table 2.2 DLS measurements of size and Zeta potential of complexes between **MPBPs** and Fluc mRNA (N/P = 10, PBS buffer (pH = 7.4), [mRNA] = 2 ng/μL). The Z-Average size is reported as an average value of 3 different measurements.

Sample	Z-Average Size (nm)	PDI	Zeta Potential (mV)
G0-100LP	245±11	0.06	26.5
G1-100LP	125±2	0.11	25.4
G2-100LP	128±2	0.12	28.0
G0-20TEG-80LP	245±13	0.08	28.2
G0-20SA-80LP	281±8	0.09	29.6
G1-20TEG-80LP	169±4	0.08	26.0
G1-20SA-80LP	138±3	0.12	28.4

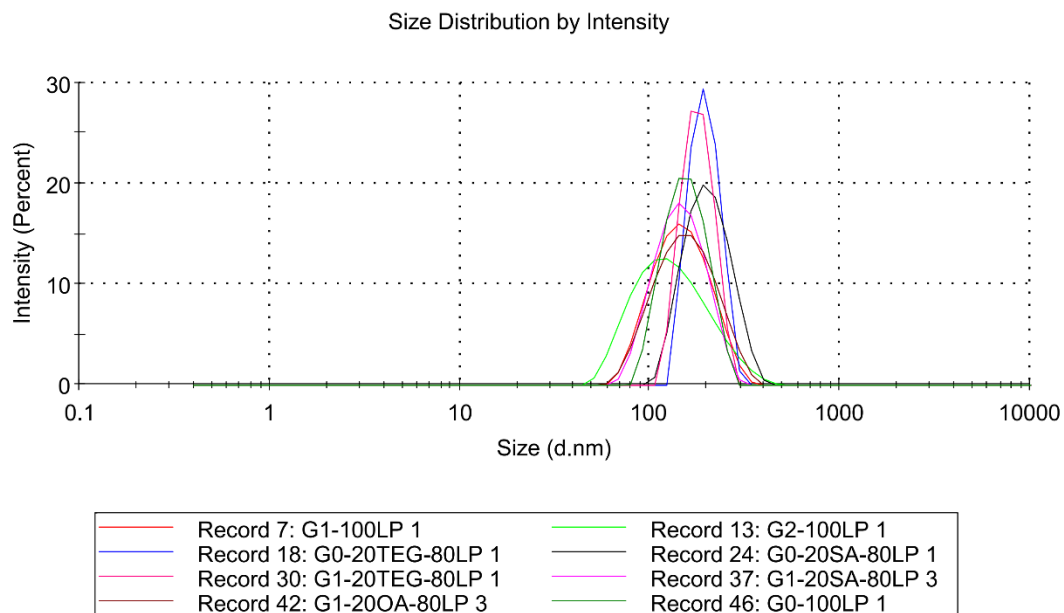


Figure 2.7 DLS measurement of different **MPBP**-siRNA complexes (N/P = 10, PBS buffer (pH = 7.4), [siRNA] = 150 nM).

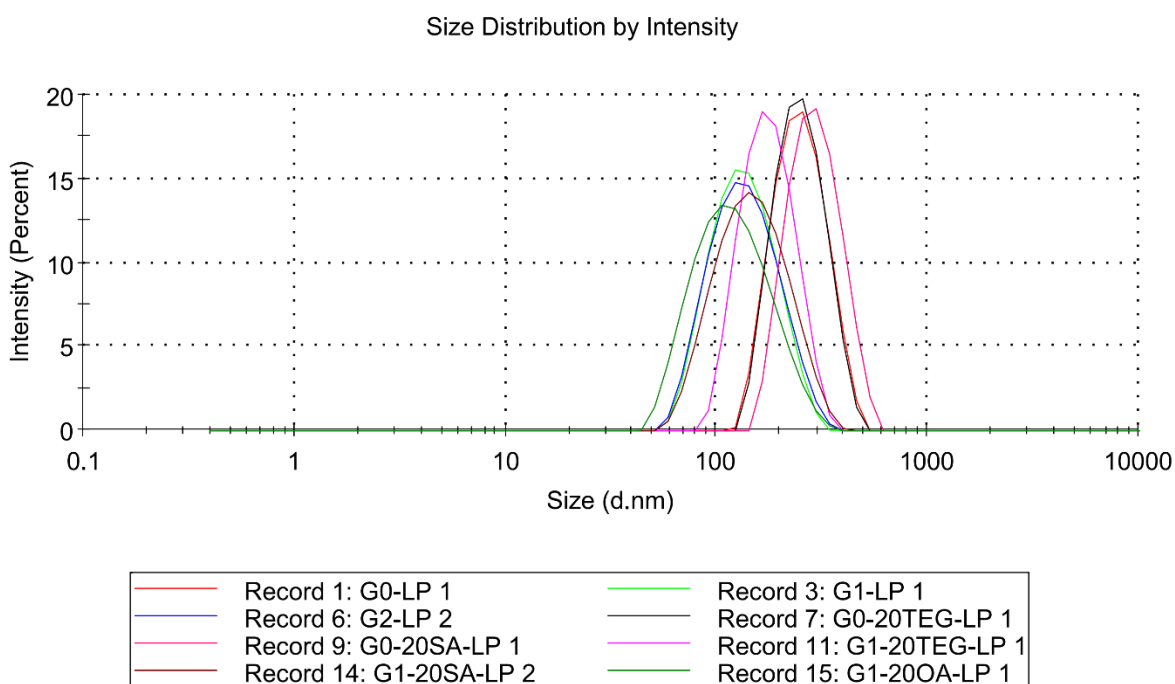


Figure 2.8 DLS measurement of different **MPBP**-Fluc mRNA complexes (N/P = 10, PBS buffer (pH = 7.4), [mRNA] = 2 ng/ μ L).

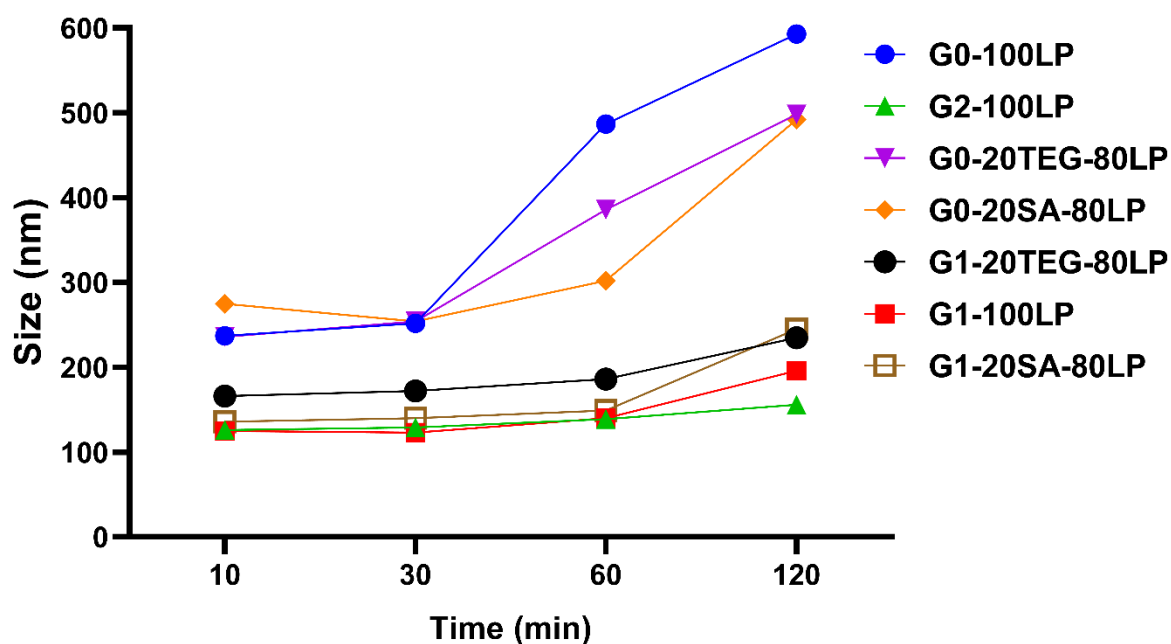


Figure 2.9 Stability of different **MPBP**-Fluc mRNA complexes in PBS buffer (pH = 7.4) as determined by DLS. All measurements reported as Z-average (nm).

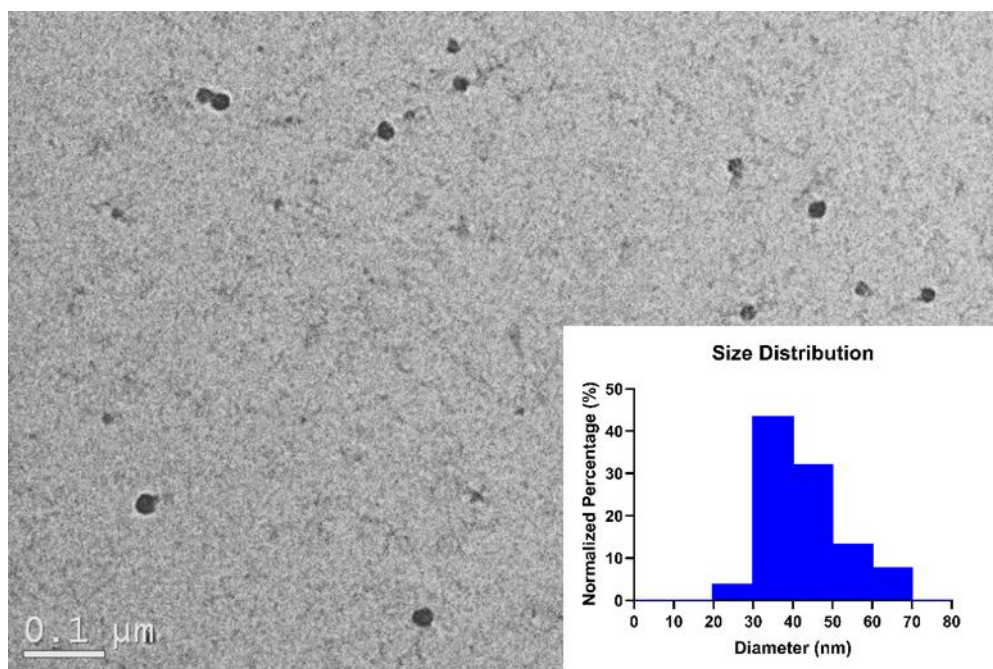


Figure 2.10 A representative stained TEM image of **G1-100LP**-siRNA complexes formed at N/P = 15. The size distribution was obtained by measuring the diameter of nanoparticles (n = 70).

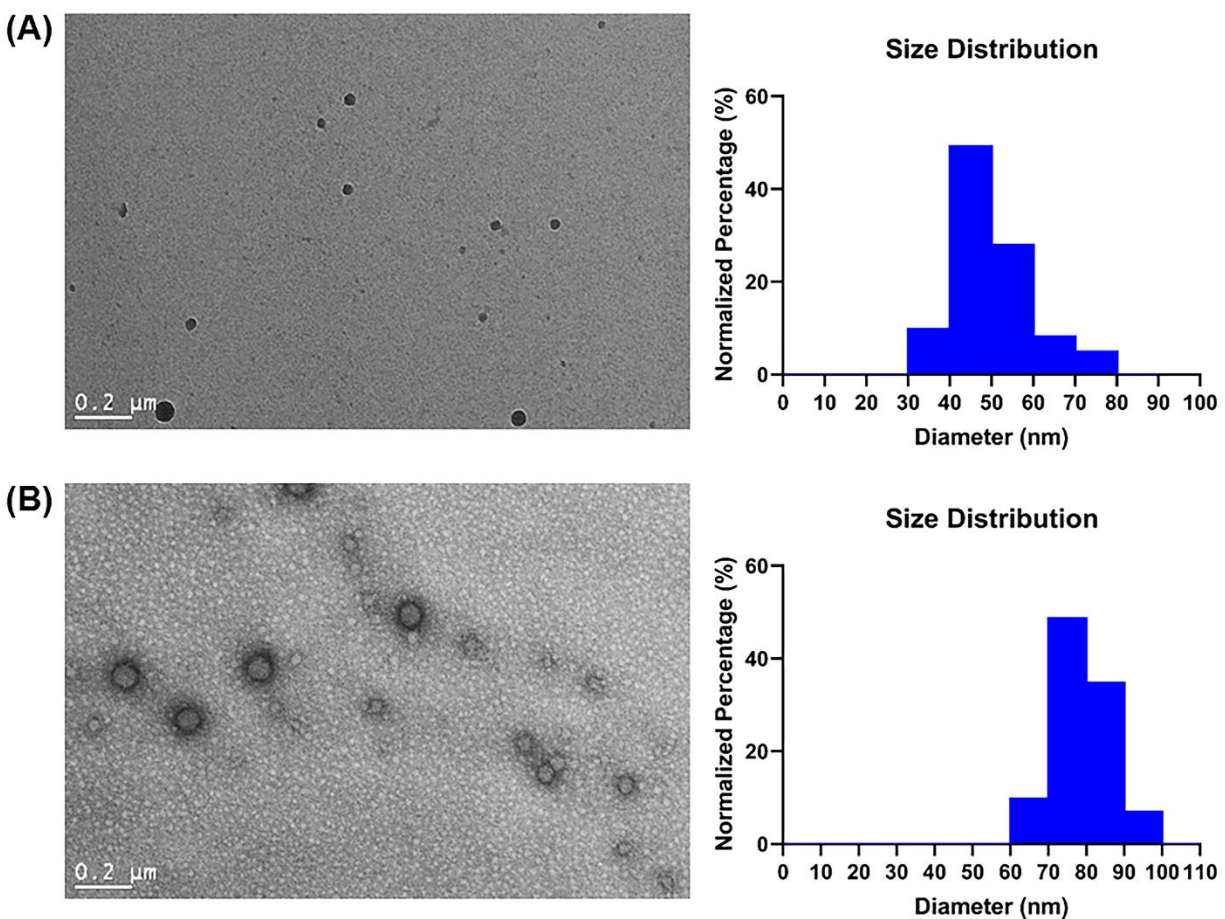


Figure 2.11 TEM images and size distribution ($n = 70$) of representative **MPBP**-RNA nanoparticle complexes stained with 2% wt uranyl acetate. (A) G0-100LP-siRNA complexes at $N/P = 10$. [siRNA] = $10 \mu\text{M}$. (B) G1-100LP-Fluc mRNA complexes at $N/P = 10$. [mRNA] = $0.1 \mu\text{g}/\mu\text{L}$.

2.4 siRNA Delivery

Next, the library of **MPBPs** was screened for siRNA delivery. siRNAs all have the same structure and similar size: ~ 20 -25 base pairs, rigid, and double-stranded.⁵⁰ Initially, we used a representative **MPBP**, **G0-100LP**, to identify the optimal conditions for siRNA transfection. For this purpose, anti-Luc siRNA was complexed with **G0-100LP** at various N/P ratios (3 – 80), transfected into the HEK-293 cells expressing firefly luciferase (Luc), and then assayed for luciferase activity after 48 h to determine the gene silencing (**Figure**

2.12). After identifying the optimal siRNA transfection conditions ([siRNA] = 60 nM, N/P = 12.5), we tested all **MPBPs** to determine the most effective vectors (**Figure 2.13**).

At the optimal siRNA transfection conditions, G0-series vectors, specifically **G0-100LP** and **G0-20SA-80LP**, knocked down luciferase expression by over 75%. Compared to a commercially available benchmark vector for siRNA transfection, Lipofectamine RNAiMAX, the **MPBPs** induced similar gene knockdown, but exhibited lower cytotoxicity. Noticeably, **G0-100LP** and **G0-20SA-80LP** exhibited high gene silencing at relatively low N/P ratios (N/P = 10 - 15) (**Figure 2.14**), in contrast to other synthetic vectors for siRNA delivery where higher N/P ratios are often required.^{28,41,43,51}

For potential *in vivo* applications, it is important to demonstrate successful transfection in the presence of serum. Transfections in the presence of serum provide several challenges as RNases in serum may degrade RNA molecules and the positively charged nanoparticles may aggregate with negatively charged proteins in serum.⁵²⁻⁵⁴ To investigate the serum compatibility of our **MPBP** system, transfections of **MPBP**-siRNA complexes were performed in OptiMEM containing 10% FBS (**Figure 2.15**). Compared to the transfections in serum-free media, higher N/P ratios were required for effective gene silencing in serum-containing conditions. Presumably at higher N/P ratios more stable nanoparticles were formed which could remain stable in serum-containing media. Several **MPBP** vectors (**G0-100LP**, **G0-20SA-80LP**, **G1-100LP**, **G1-20SA-80LP**) showed excellent gene silencing effect at their optimal N/P ratios, with similar or higher knock down efficiency compared to the Lipofectamine positive control.

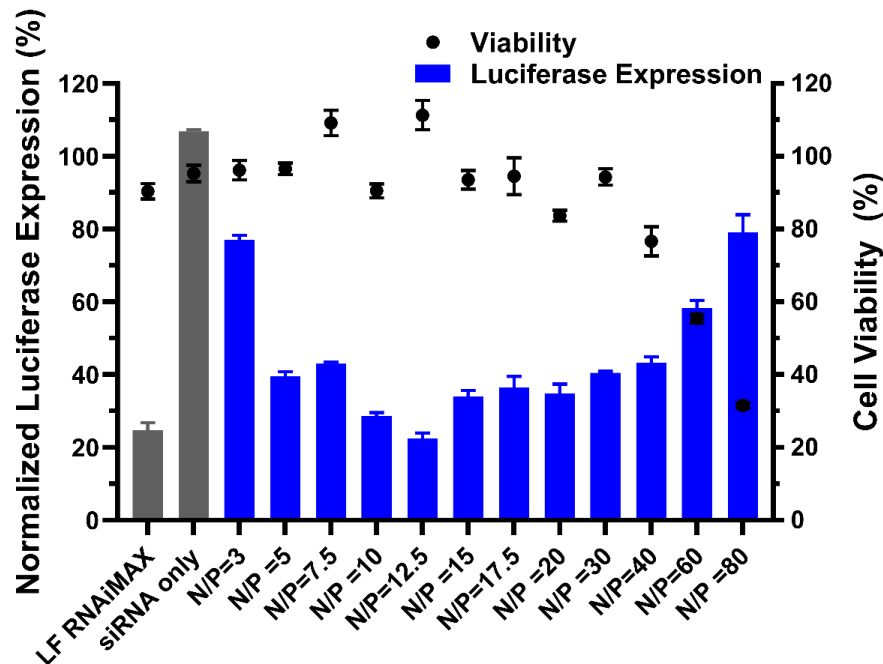


Figure 2.12 Transfection screening of **G0-100LP**-siRNA complexes at various N/P ratios (3 – 80) in firefly luciferase-expressing HEK-293 cells. [siRNA] = 60 nM.

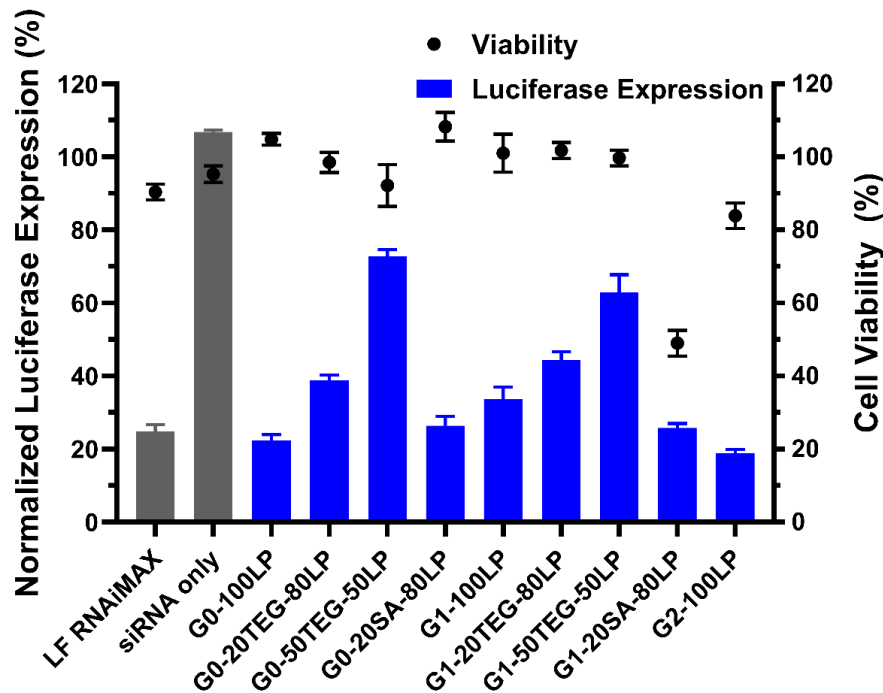


Figure 2.13 Gene silencing and cell viability results of different **MPBP**-siRNA complexes transfected to firefly luciferase-expressing HEK-293 cells. Cell viability was assessed by comparing luciferase expression in non-treated cells to cells treated with negative control siRNA-**MPBP** complex. In serum-free media, N/P = 12.5, [siRNA] = 60 nM.

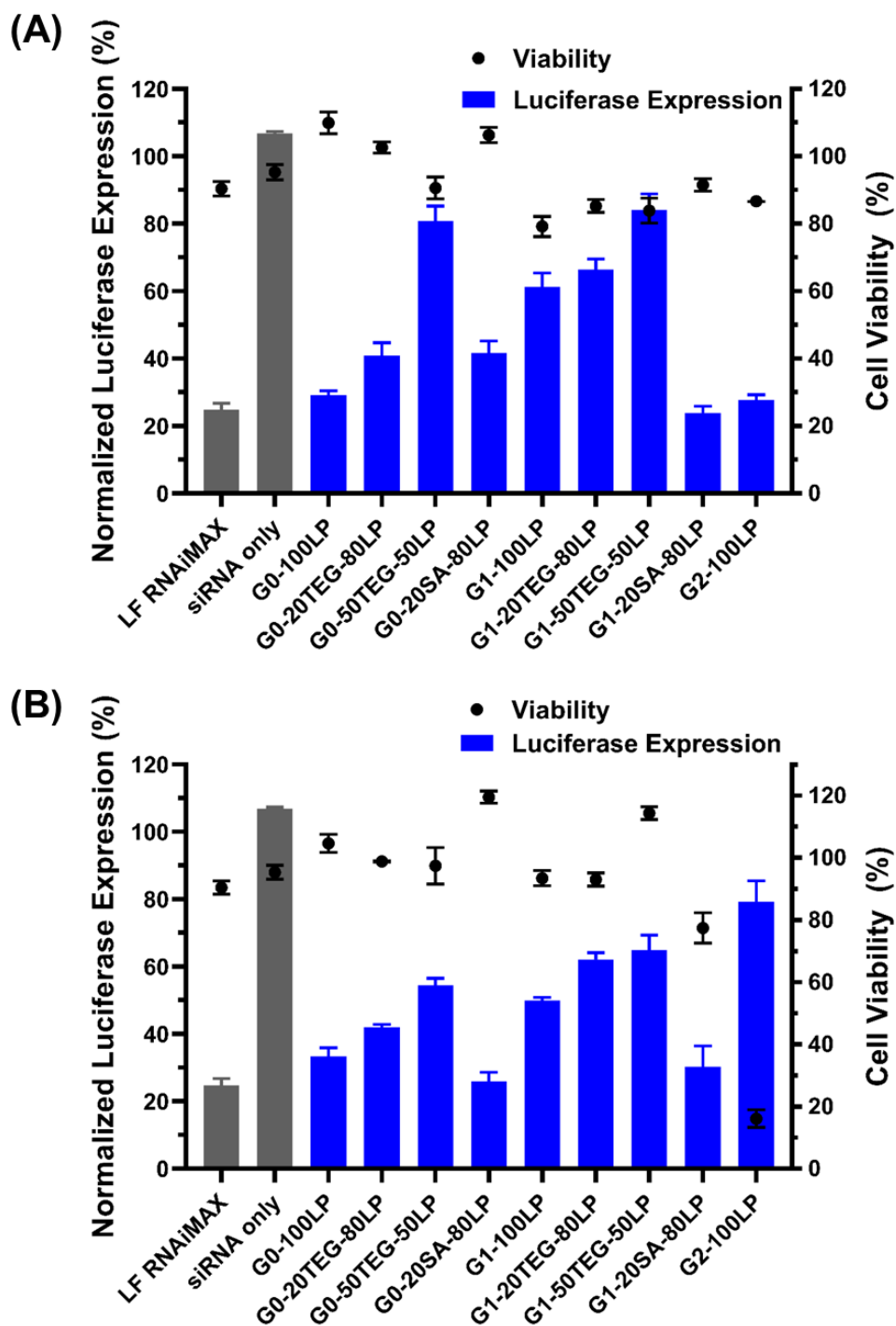


Figure 2.14 Transfection screening of different **MPBP**-siRNA complexes in firefly luciferase-expressing HEK-293 cells. Serum-free media. (A) N/P = 10, [siRNA] = 60 nM. (B) N/P = 15, [siRNA] = 60 nM.

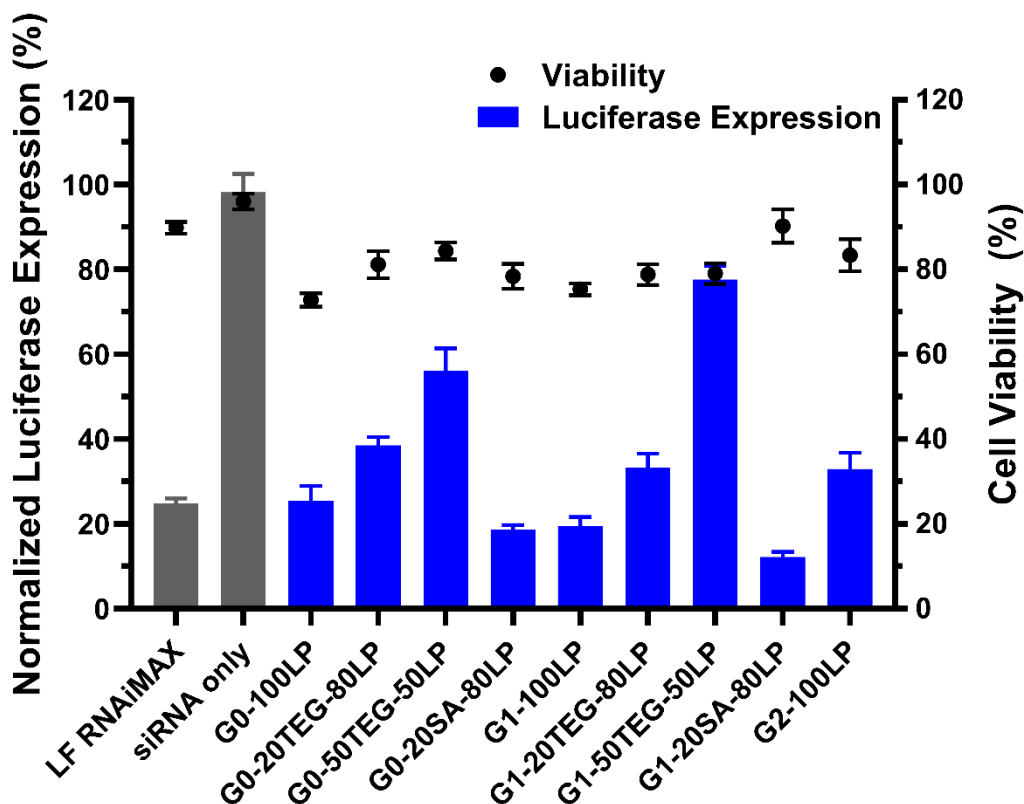


Figure 2.15 Gene silencing and cell viability results of different **MPBP**-siRNA complexes transfected to firefly luciferase-expressing HEK-293 cells. Cell viability was assessed by comparing luciferase expression in non-treated cells to cells treated with negative control siRNA-**MPBP** complex. In 10% FBS-containing media, N/P = 35 for **G0** series of vectors, N/P = 30 for **G1** series of vectors, N/P = 20 for **G2-100LP**, [siRNA] = 60 nM.

2.5 Fluc mRNA and eGFP mRNA Delivery.

After demonstrating the capability to deliver siRNA, **MPBPs** were further tested to deliver mRNAs of various sizes. Mammalian encoding mRNAs vary greatly in size, with a median length of 1.4 kb.⁵⁵ Compared to siRNAs, which all have similar size and structure, mRNAs vary dramatically in size and structure and are more susceptible to degradation.⁵⁶ Capitalizing the versatile architecture design, we investigated our **MPBPs** for universal delivery of mRNAs of varying length.

Initially, we tested the **MPBPs** for the delivery of Fluc mRNA, a 1996 nucleotide long single-stranded mRNA. To assay Fluc mRNA delivery, NIH 3T3 cells were treated with different **MPBP**-Fluc mRNA nanocomplexes. Lipofectamine MessengerMAX (LF MM) was used as a positive control and naked mRNA alone and untreated cells were used as negative controls. After 24 hours following transfection, the luciferase activity was assayed by an IVIS camera. To determine the optimal mRNA transfection conditions, **G0-100LP** and **G1-100LP** were used as representative vectors in our initial transfection screening (**Figure 2.16 - 2.17**). The luminescence was the greatest for G0-100LP at N/P = 10 and G1-100LP at N/P = 15. After identifying the optimized mRNA transfection conditions, we assayed all the vectors for Fluc mRNA delivery at their optimal N/P ratios (**Figure 2.18**). The vector **G1-100LP** performed significantly better than **G0-100LP**, with more than twice as much luminescence as compared to the positive control (LF MM). Two of the other vectors, **G0-20SA-80LP** and **G1-20TEG-80LP** also exhibited similar transfection efficacy as the positive control. Due to the significantly larger size and increased degradation instability of mRNA compared to siRNA, the vectors for mRNA delivery may require higher valency of linear peptide functionalization in order to form stable nanoparticles. We propose this is the reason why **G1-100LP** performs significantly better than **G0-100LP** in mRNA delivery.

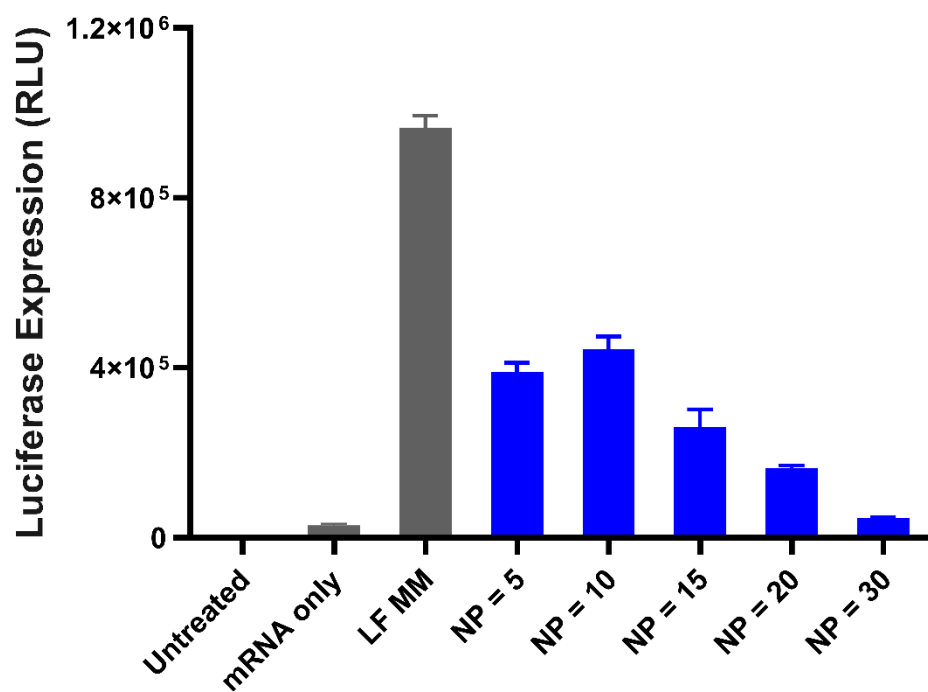


Figure 2.16 Transfection screening of G0-100LP-Fluc mRNA complexes in NIH 3T3 cells at various N/P ratios (5 – 30) (150 ng mRNA per well).

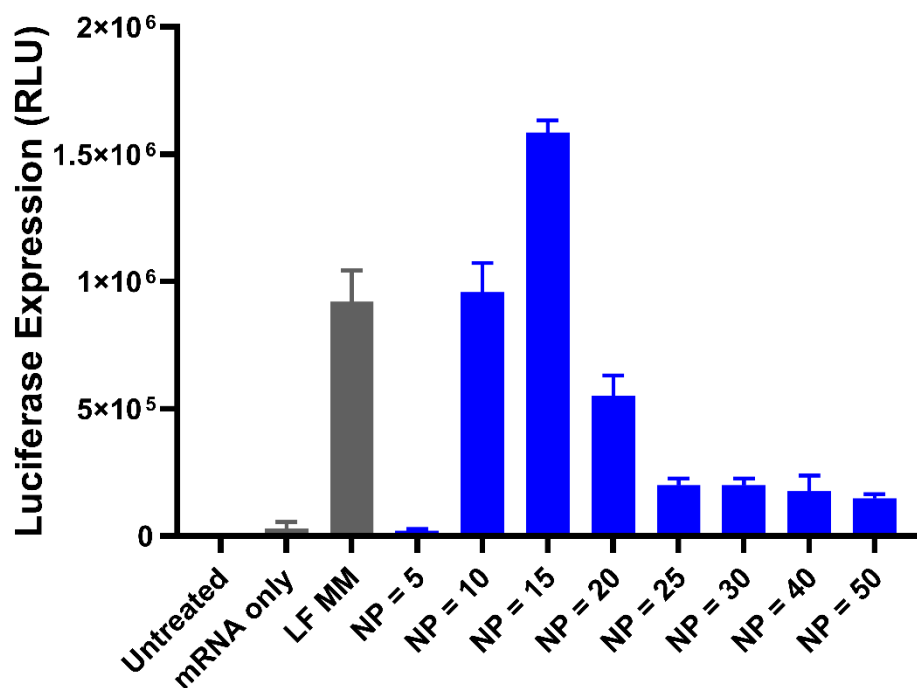


Figure 2.17 Transfection screening of G1-100LP-Fluc mRNA complexes in NIH 3T3 cells at various N/P ratios (5 – 50) (150 ng mRNA per well).

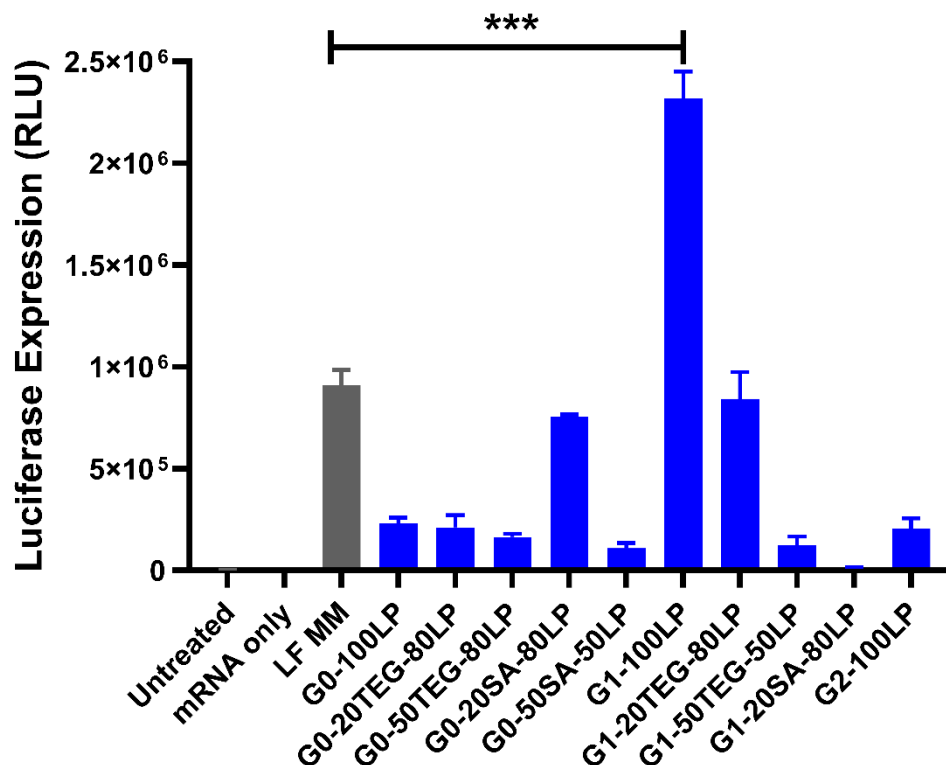


Figure 2.18 Fluc mRNA transfection using different **MPBPs** at their optimal N/P ratios in NIH 3T3 cells (150 ng mRNA per well). Results summary of transfections in serum-free media. N/P = 10 for **G0** series of vectors and N/P = 15 for **G1**, **G2** series of vectors. For RLU values, *** = $P < 0.001$ relative to LF MM.

Additionally, to demonstrate that the generality of **MPBPs** for delivery of mRNAs of varying sizes, we then investigated eGFP mRNA delivery. eGFP mRNA is roughly half the size of Fluc mRNA (996 nucleotides). To assay eGFP mRNA delivery efficacy, NIH 3T3 cells were transfected with **MPBP**-eGFP mRNA nanocomplexes and eGFP expression was measured 24 hours post-transfection via flow cytometry. Interestingly, the transfection results indicated that the best **MPBP** vector for luciferase delivery, **G1-100LP**, is also the most effective for delivering eGFP mRNA, with comparable protein expression level as the

positive control (LF MM) (**Figure 2.19**). These results demonstrate that the **MPBP** system is flexible and capable of delivering mRNAs of varying sizes.

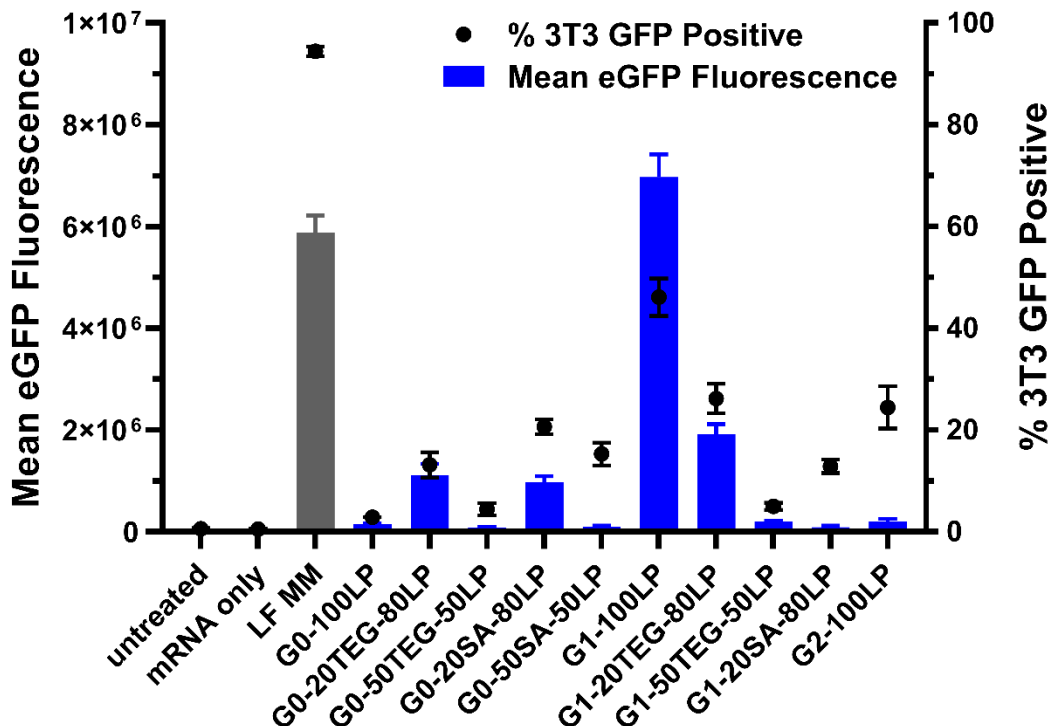


Figure 2.19 eGFP mRNA transfection using different **MPBPs** at their optimal N/P ratios in NIH 3T3 cells (150 ng mRNA per well). Results summary of transfections in serum-free media. N/P = 10 for **G0** series of vectors and N/P = 15 for **G1**, **G2** series of vectors.

Similar to siRNA delivery study, Fluc mRNA and eGFP mRNA transfections were also performed in media containing 10% FBS to assay the efficacy in the presence of serum (**Figure 2.20 - 2.21**). While LF MM delivery efficacy was substantially reduced in serum-containing conditions, our most effective vectors (**G1-100LP**, **G0-20SA-80LP**, and **G1-20TEG-80LP**) still maintain their high transfection efficacy in 10% FBS OptiMEM, outperforming LF MM by up to 240%.

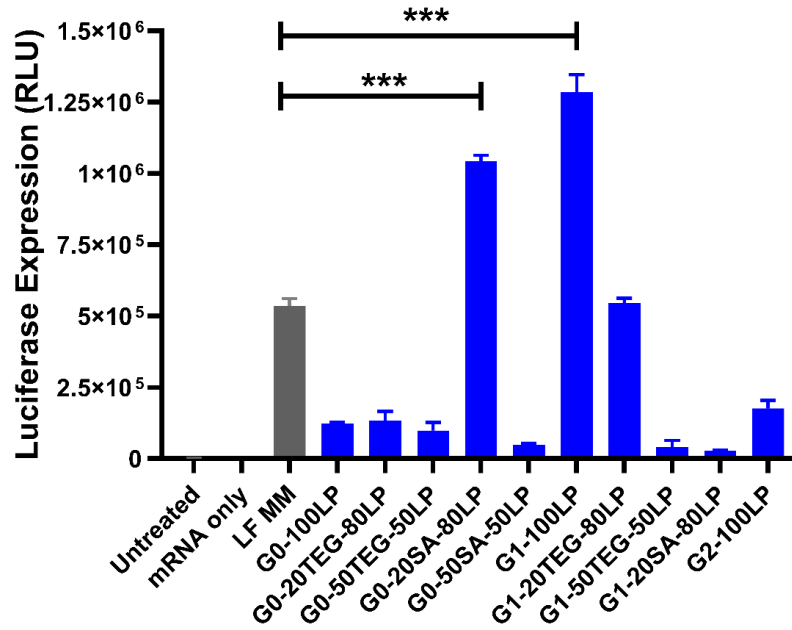


Figure 2.20 Fluc mRNA transfection using different **MPBPs** at their optimal N/P ratios in NIH 3T3 cells (150 ng mRNA per well). Results summary of transfections in 10% FBS-containing media. N/P = 50 for all vectors. For RLU values, *** = $P < 0.001$ relative to LF MM.

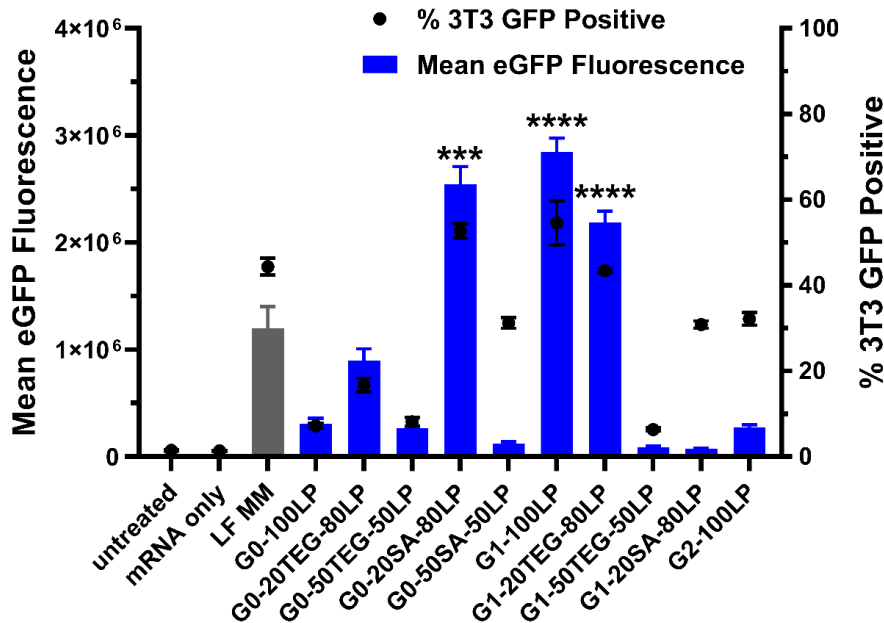


Figure 2.21 eGFP mRNA transfection using different **MPBPs** at their optimal N/P ratios in NIH 3T3 cells (150 ng mRNA per well). Results summary of transfections in 10% FBS-containing media. N/P = 50 for all vectors. For mean eGFP Fluorescence, *** = $P < 0.001$, **** = $P < 0.0001$ relative to LF MM.

In both serum-free media and 10% FBS-containing media, most of the vectors displayed minimal cytotoxicity as measured via lactate dehydrogenase (LDH) assay (**Figure 2.22**). The **G1** vectors with hydrophobic stearic acid functionalization exhibited slightly lower viability. Presumably, the attached long aliphatic chains may disrupt the cell membrane and induce toxicity.^{43,57} Higher toxicity was also observed for **G2** vector in both mRNA delivery and siRNA delivery, which presumably arises from the high positive charge density of the large **G2** dendrons.

2.6 Confocal Study of Cellular Uptake and Endosomal Escape

To gain insights on structure-function relationship for the **MPBPs**, confocal microscopy was employed to visualize the mRNA cellular internalization. Cells were transfected with Cy5-labelled Fluc mRNA and imaged using confocal microscopy to visualize the internalization of the **MPBP**-mRNA nanoparticles (**Figure 2.23**). Additionally, cellular uptake was quantified 4 hours post-transfection by flow cytometry (**Figure 2.24**). Most **MPBP**-mRNA complexes were internalized into the cells efficiently (over 70% Cy5-positive cells). Increased TEG incorporation decreased the mRNA cellular uptake, which explains why the siRNA and mRNA transfection efficacy decreased with the increasing amount of TEG functionalization. This observation agrees with previous studies showing that PEGylation generally reduces cell uptake of polyplexes.⁵⁸⁻⁵⁹ In contrast, as shown in both **G0**-series and **G1**-series **MPBPs**, incorporation of appropriate amount stearic acid enhanced cell internalization. Fatty acids have been shown to facilitate the cellular uptake through their favorable interactions with cell membrane.⁴⁷

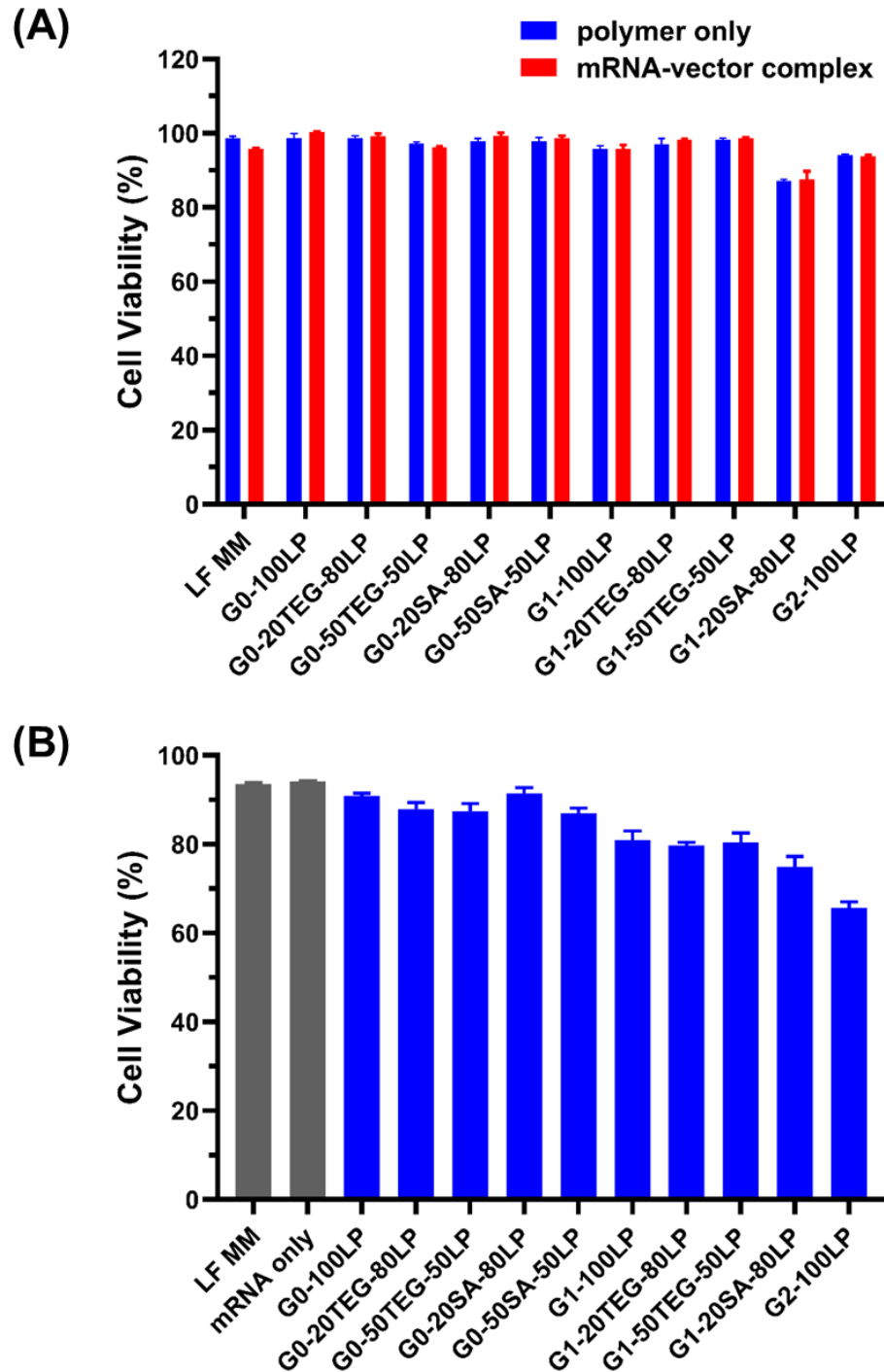


Figure 2.22 Cytotoxicity of the **MPBP** vectors against NIH 3T3 cells assayed using a LDH assay (150 ng Fluc mRNA per well). (A) Results summary of Fluc mRNA transfection in serum-free media, N/P = 10 for G0 series of vectors and N/P = 15 for G1, G2 series of vectors. (B) Results summary of Fluc mRNA transfection in 10% FBS-containing media, N/P = 50 for all vectors.

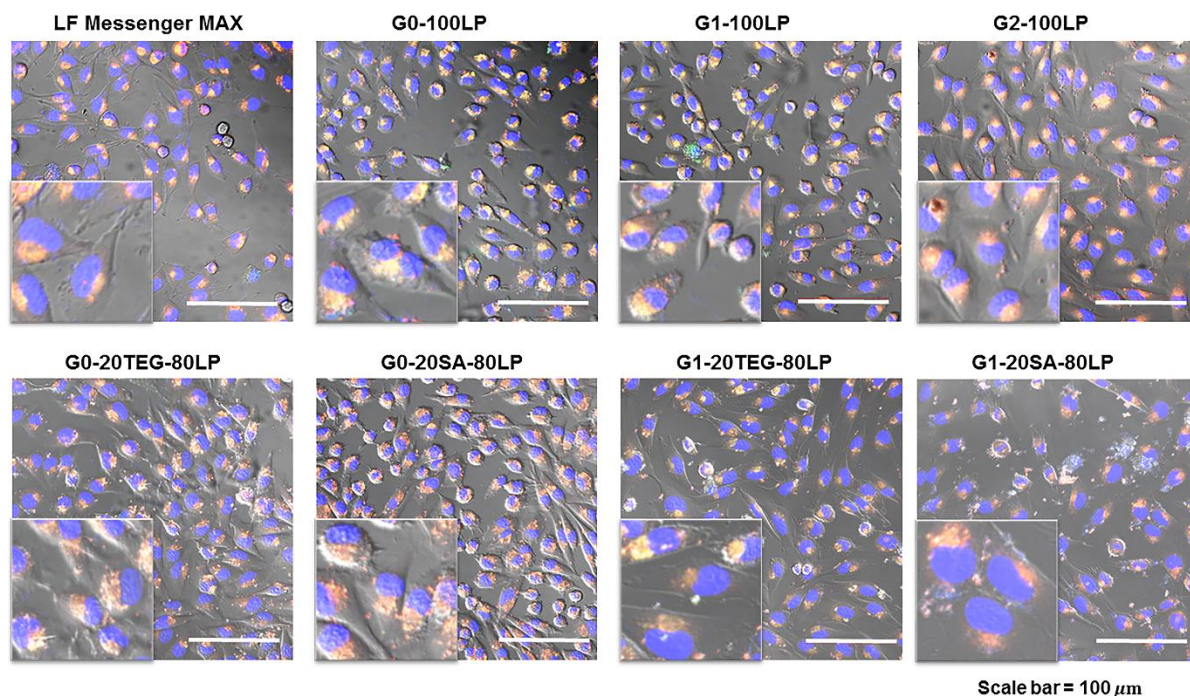


Figure 2.23 Cellular uptake of **MPBP**-Cy5 Fluc mRNA complexes as observed by confocal fluorescence microscopy. Confocal fluorescence images of NIH 3T3 cells 4 h post-transfection (nuclei were stained blue with Hoechst 33342 indicated in blue, lysosomes were stained with LysoTracker Deep Green indicated in green, Cy5 Fluc mRNA is indicated in red, all scale bars = 100 μ m). Zoomed in images are inserted for clear visualization of individual cells. Transfection conditions: 300 ng Cy5 Fluc mRNA per well, N/P = 15.

However, excess aliphatic chain functionalization may cause disruption to the cell membrane and induce toxicity as shown in our previous siRNA study (**Figure 2.13**) and LDH assay (**Figure 2.22**). The increased cytotoxicity of the **MPBPs** with high fatty acid content could cause the delivery deficiency of high generation **MPBPs** with stearic acid functionalization.

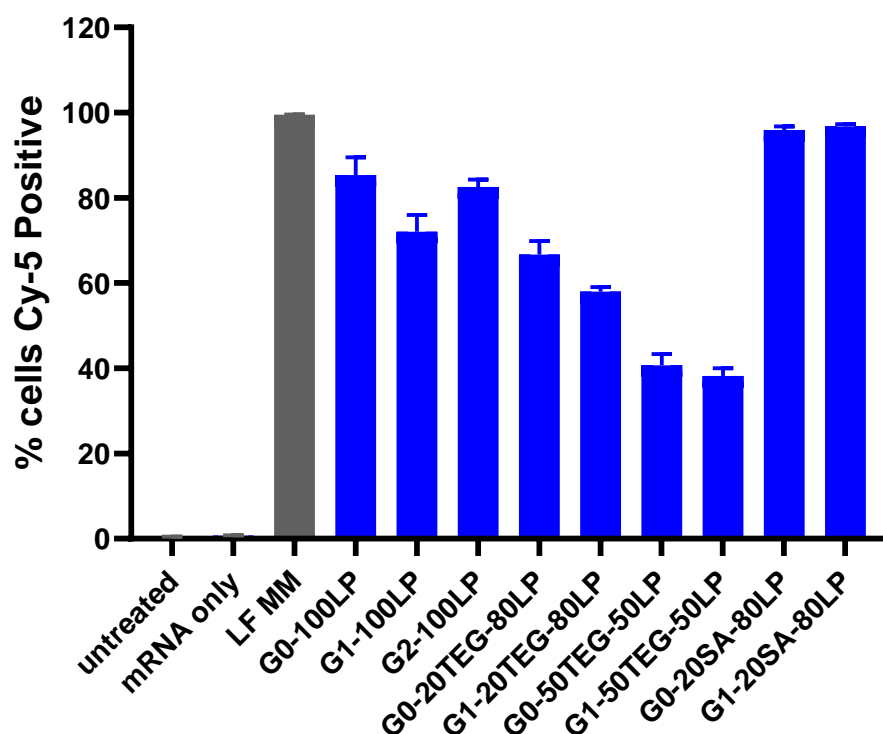


Figure 2.24 Cellular uptake of **MPBP-Cy5** Fluc mRNA complexes in NIH 3T3 cells quantified by flow cytometry. Fluorescence was measured 4 h post-transfection using a flow cytometer. Transfection conditions: 300 ng Cy5 Fluc mRNA per well, N/P = 15.

Furthermore, intracellular trafficking of nanoplexes was observed by confocal microscopy to gain insight on the endosomal escape efficiency of different **MPBP-eGFP** mRNA complexes (**Figure 2.25**). Endosomal escape was indicated by the absence of colocalization between Cy5-labelled eGFP mRNA, indicated in red, and LysoTracker Blue, indicated in green in the cytosol. Even though both **G1-100LP** and **G1-20SA-80LP** showed efficient cellular uptake after 4 h, **G1-100LP** exhibited much more efficient endosomal escape after 12 h. In the cells transfected by **G1-100LP-eGFP** mRNA complexes, dispersed Cy5-labelled eGFP mRNA was clearly observed and subsequent GFP expression was also detected (shown in blue in the figure) (**Figure 2.25A**).

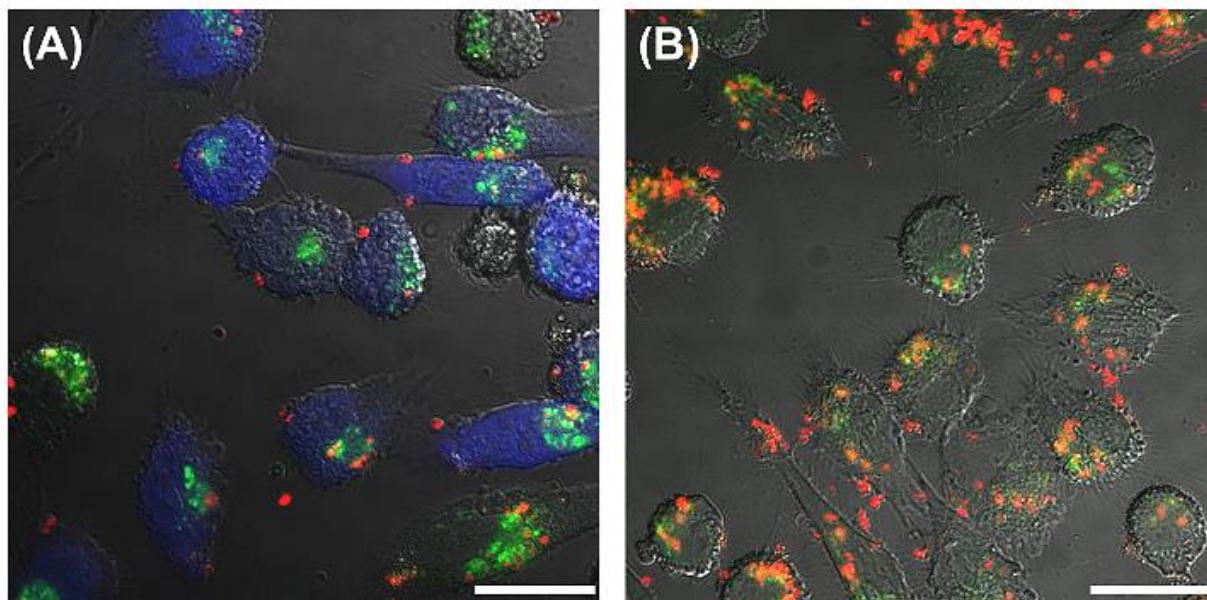


Figure 2.25 Endosomal escape by intracellular trafficking for **MPBP-Cy5 eGFP mRNA** complexes. Confocal fluorescence images of NIH 3T3 cells 12 h post-transfection of (A) **G1-100LP** and (B) **G1-20SA-80LP**. Lysosome was stained with LysoTracker Blue indicated in green, Cy5 eGFP mRNA is indicated in red, eGFP expression is indicated in blue, scale bars = 20 μ m. Transfection conditions: 300 ng Cy5 eGFP mRNA per well, N/P = 15.

In sharp contrast, substantial nanoparticle aggregation and eGFP mRNA-lysosome co-localization were observed inside the cells transfected by **G1-20SA-80LP**-eGFP mRNA complexes (**Figure 2.25B**). We believe the abundant hydrophobicity from excessive hydrocarbon side chains induces aggregation through hydrophobic interactions in the highly charged cell media. This aggregation may shield the proton sponge effect of imidazole moieties, which causes endosomal entrapment of large mRNA.⁶⁰⁻⁶¹ The higher delivery efficacy of **G1-100LP** can be attributed to the enhanced stability and endosomal escape compared to **G1-20SA-80LP**.

2.7 Replicon mRNA Delivery

Furthermore, we examined the **MPBP** vectors for replicon mRNA (RepRNA) delivery. Delivery of RepRNA is of great interest for the development of next generation vaccines.⁶² RepRNA is used in vaccines to express a protein antigen of interest in target cells to induce a prolonged immune responses, which increases the efficacy of the vaccines and reduces the need for booster shots.¹⁰⁻¹¹ Efficient delivery of RepRNA is extremely challenging due to its remarkable large size ($\sim 10^4$ nt) and complex secondary structure relative to other RNA species.⁶²⁻⁶⁴ The replicon mRNA expressing firefly luciferase was complexed with different **MPBPs** and then transfected into BHK cells (**Figure 2.26**).

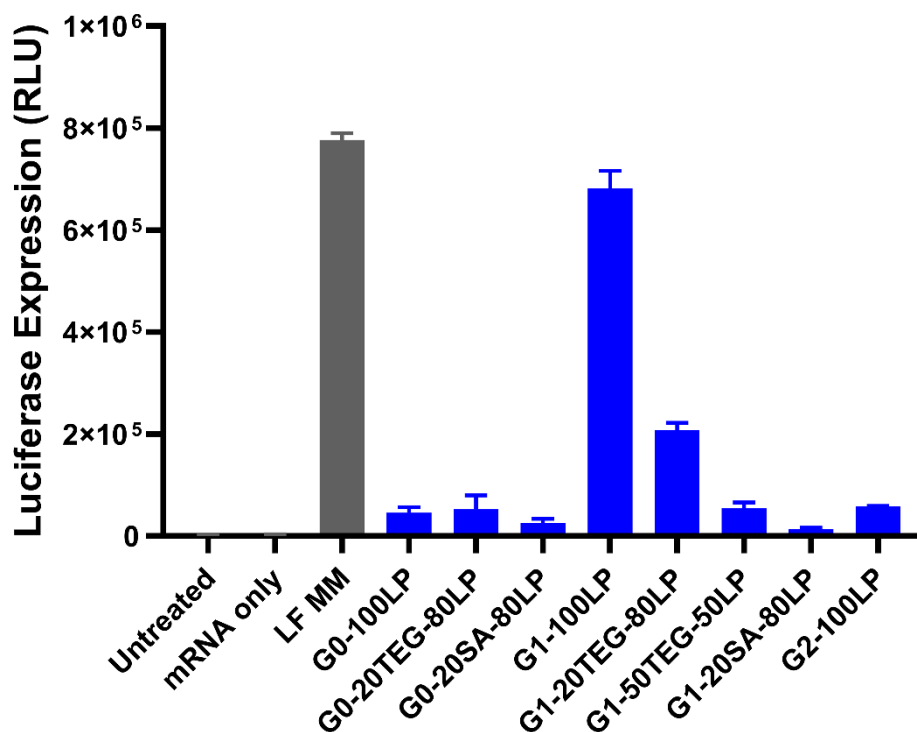


Figure 2.26 Replicon mRNA transfection of different **MPBPs** at their optimal N/P ratios (N/P = 10 for **G0** series of vectors and N/P = 15 for **G1**, **G2** series of vectors) in BHK cells (150 ng mRNA per well).

Our best vector, **G1-100LP**, was demonstrated to be able to deliver large replicon mRNA, with similar delivery efficiency as the positive control (LF MM) (**Figure 2.26**). Prolonged luciferase expression was observed 72 hours post-transfection, whereas regular Fluc mRNA transfection only provided transient luciferase expression after 24 hours post-transfection (**Figure 2.27**).

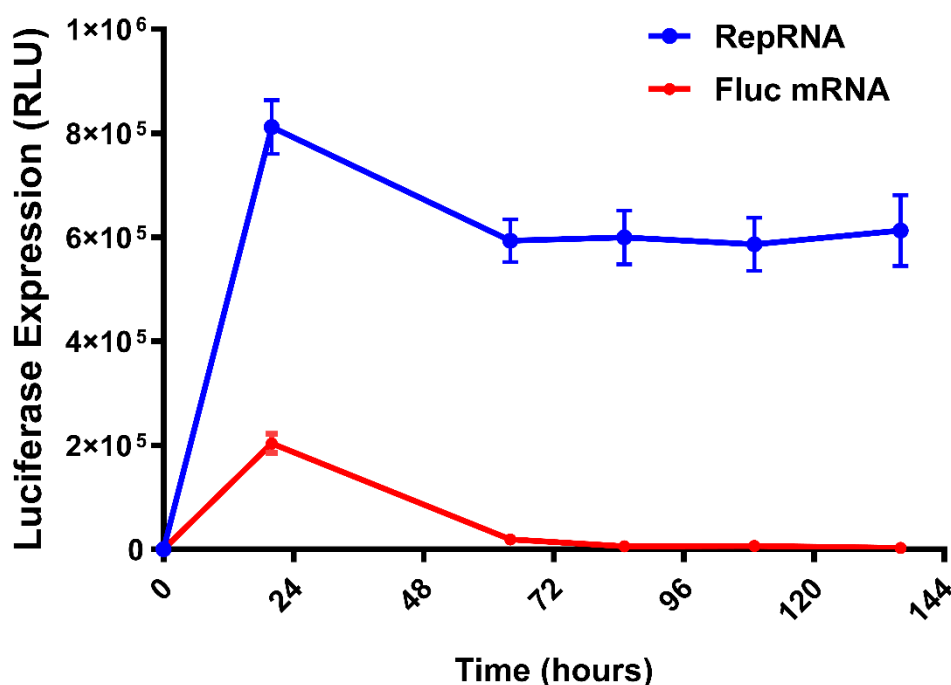


Figure 2.27 Comparison of luciferase expression between replicon mRNA delivery and regular Fluc mRNA delivery by **G0-100LP** at N/P = 10 (200 ng mRNA per well).

2.8 CRISPR-Cas9 Delivery

Over the past decade, the emergence of CRISPR technology has revolutionized the field of gene therapy by allowing for the permanent editing of faulty genes.^{12,65} However, the delivery of CRISPR-Cas9 machinery is extremely challenging, limiting its potential applications.^{17,66-67} There are three main methods to delivery CRISPR machinery:⁶⁸ delivery of DNA encoding CRISPR components,⁶⁹⁻⁷⁰ co-delivery of targeting sgRNA and mRNAs

encoding Cas9,^{22,71-72} and direct delivery of preformed Cas-ribonucleoproteins (RNP) particles.⁷³⁻⁷⁴ RNP delivery is hampered by the large size of the protein, causing poor delivery efficacy. Compared to DNA delivery, mRNA co-delivery of CRISPR components only produces transient Cas9 protein expression, reducing off-target effects and lowering cytotoxicity.⁷⁵⁻⁷⁶ RNA-based CRISPR-Cas9 editing requires the delivery of two components: an mRNA encoding Cas9 protein and a sgRNA for targeting the specific site of genome for editing. Upon cellular entry, Cas9 mRNA is translated to multiple copies of the Cas9 protein in the cytosol that then associate with the sgRNAs present to form active RNPs.⁷⁷ This method requires effective co-delivery of both large Cas9 mRNA and relatively short sgRNA. Because our **MPBP** system was successful for the delivery of both small RNA (siRNA) and large RNA (mRNA), we employed the **MPBP** system to address this difficult delivery challenge of CRISPR-Cas9 machinery.

For CRISPR-Cas9 delivery, we chose several vectors that demonstrated successful delivery of siRNA and mRNA. To assay the co-delivery of Cas9 mRNA and sgRNA, eGFP-expressing NIH 3T3 cells were treated with different RNA-**MPBP** nanocomplexes. In the co-delivery of Cas9 mRNA and sgRNA (sgRNA/Cas9 mRNA mass ratio ~ 10:1), large quantity of sgRNA is required to associate with abundant Cas9 protein from mRNA translation.^{22,71} After 24 hours, the media was changed to complete media and the cells were cultured for a further 5 days. On day 6 post-transfection, the cells were trypsinized and eGFP expression was determined via flow cytometry (**Figure 2.28A**). Importantly, the vectors with SA functionalization (**G0-20SA-80LP** and **G1-20SA-80LP**), which were most effective for siRNA delivery, showed potent gene editing efficacy of more than 60% (**Figure 2.28B**). The SA side chains incorporation promotes nanocomplex assembly and enhances cellular

uptake, which allows for high gene-editing efficiency. Compared to **G1-20SA-80LP**-mRNA transfection, the nanoparticle aggregation became less an issue in **G1-20SA-80LP**-siRNA transfection (**Figure 2.29**), presumably due to the significantly smaller RNA sizes and less positive charges on nanoparticle surfaces (**Table 2.1 - 2.2**). As sgRNA dominates in the co-delivery nanocomplex (sgRNA/Cas9 mRNA molar ratio $\sim 450:1$), the **MPBPs** which are effective for small RNA delivery are also the most effective for Cas9 mRNA/sgRNA co-delivery under this condition.

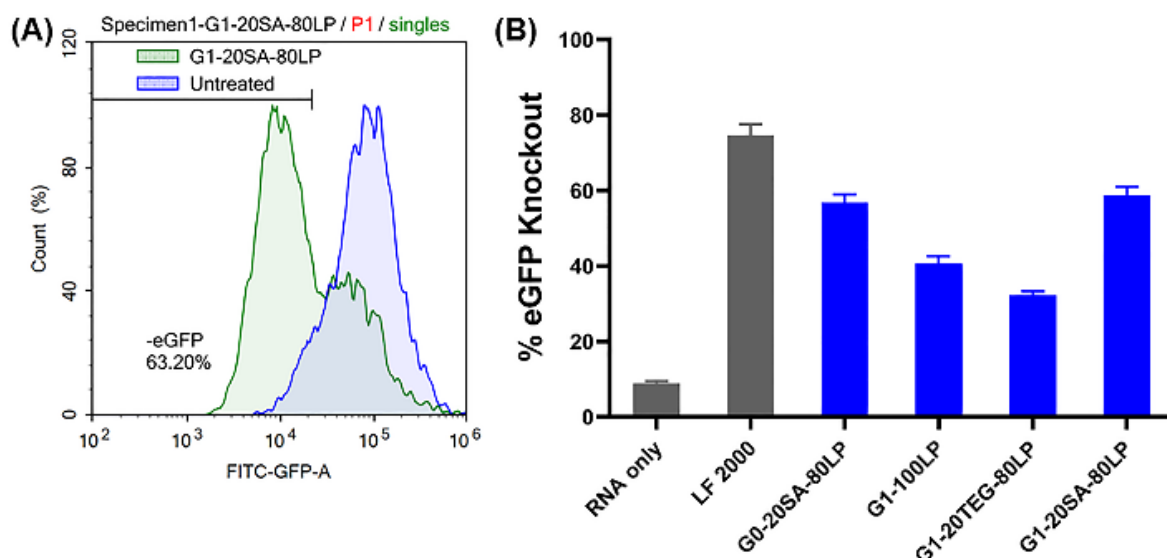


Figure 2.28 Transfection results of CRISPR-Cas9 delivery in eGFP-expressing 3T3 cells. (A) Representative flow cytometry plot for Cas9 mRNA/sgRNA co-delivery. (B) Results summary of Cas9 mRNA/sgRNA co-delivery in serum-free media. 5000 cells per well, 100 ng sgRNA and 10 ng mRNA per well. Transfections were performed in OptiMEM at an N/P = 30. Cells were analyzed via flow cytometry 6 days post transfection.

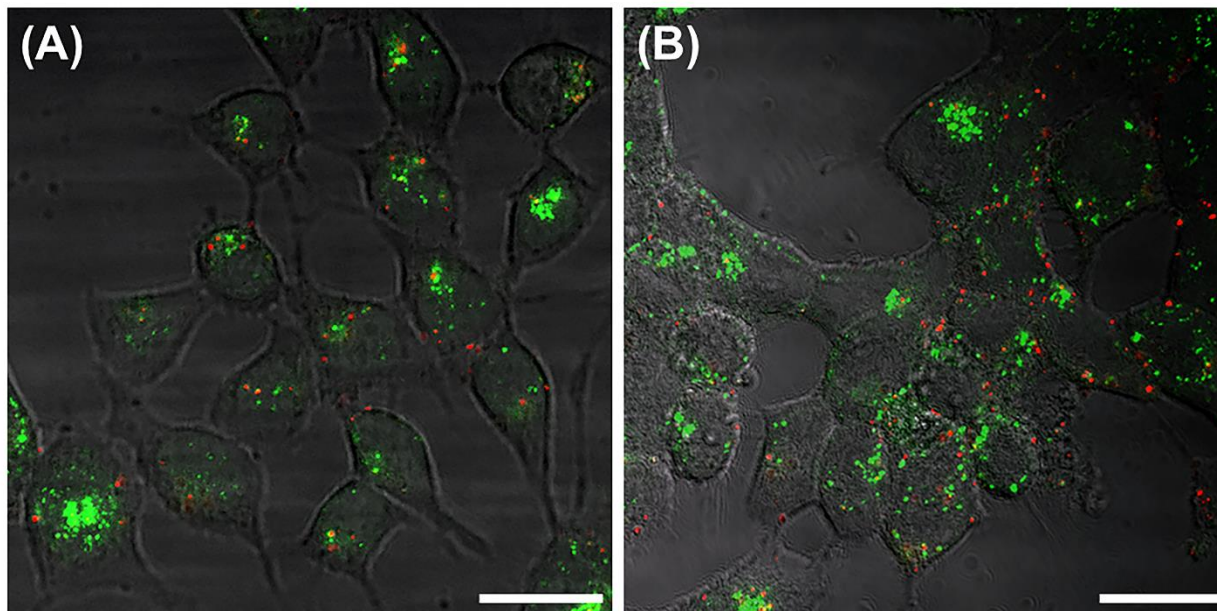


Figure 2.29 Endosomal escape by intracellular trafficking for **MPBP**-Cy5 siRNA complexes. Confocal fluorescence images of HEK-293T cells 24 h post-transfection of (A) G1-100LP and (B) G1-20SA-80LP. Lysosome was stained with LysoTracker Blue indicated in green, Cy5 negative control siRNA is indicated in red, scale bars = 20 μm . Transfection conditions: [siRNA] = 60 nM, N/P = 10.

2.9 Conclusions

In conclusion, we have developed a multivalent peptide-functionalized bio-reducible polymer (**MPBP**) system for universal, safe and efficient delivery of various RNAs of dramatically different sizes and structures efficiently to multiple cell lines. Benefitting from the structural diversity and facile synthesis, this delivery system is highly tunable, scalable and biodegradable. Vectors with high multivalency are required for the delivery of large RNAs because of their larger size and increased sensitivity to nuclease degradation. **G0-MPBPs** are most effective for siRNA delivery, whereas **G1** series of **MPBPs** are more effective for mRNA delivery. Although TEG enhances the colloidal stability, the TEG side chains also reduce cell internalization due to the increased hydrophilicity and reduction of charge density on the particle surface. Appropriate amount of hydrophobic side chains are

beneficial for nanoparticle assembly and cellular uptake, but excess aliphatic side chains induce aggregation, endosomal entrapment and high cytotoxicity. The high delivery efficiency and low cytotoxicity indicate that **MPBPs** are a promising family of vectors for universal RNA delivery. Further structural optimization of **MPBPs** as well as more biological studies including *in vivo* studies are currently underway in our laboratory.

2.10 Acknowledgement

I acknowledge Alex Eldredge for the help in CRISPR-Cas9 delivery experiments, Collin Hickey for the help in confocal imaging experiments, and Hurik Muradyan for the help in TEM imaging experiments.

2.11 References

- (1) Dunbar, C. E.; High, K. A.; Joung, J. K.; Kohn, D. B.; Ozawa, K.; Sadelain, M., Gene therapy comes of age. *Science* **2018**, 359 (6372), eaan4672.
- (2) Crooke, S. T.; Witztum, J. L.; Bennett, C. F.; Baker, B. F., RNA-Targeted Therapeutics. *Cell Metab.* **2018**, 27 (4), 714-739.
- (3) Lieberman, J., Tapping the RNA world for therapeutics. *Nat. Struct. Mol. Biol.* **2018**, 25 (5), 357-364.
- (4) Kowalski, P. S.; Rudra, A.; Miao, L.; Anderson, D. G., Delivering the Messenger: Advances in Technologies for Therapeutic mRNA Delivery. *Mol. Ther.* **2019**, 27(4), 710-728.
- (5) Castanotto, D.; Rossi, J. J., The promises and pitfalls of RNA interference-based therapeutics. *Nature* **2009**, 457, 426-433.
- (6) de Fougerolles, A.; Vornlocher, H.-P.; Maraganore, J.; Lieberman, J., Interfering with disease: a progress report on siRNA-based therapeutics. *Nat. Rev. Drug Discovery* **2007**, 6, 443-453.
- (7) Sahin, U.; Kariko, K.; Tureci, O., mRNA-based therapeutics--developing a new class of drugs. *Nat. Rev. Drug Discovery* **2014**, 13 (10), 759-780.
- (8) Kormann, M. S.; Hasenpusch, G.; Aneja, M. K.; Nica, G.; Flemmer, A. W.; Herber-Jonat, S.; Huppmann, M.; Mays, L. E.; Illenyi, M.; Schams, A.; Griesse, M.; Bittmann, I.; Handgretinger, R.; Hartl, D.; Rosenecker, J.; Rudolph, C., Expression of therapeutic

- proteins after delivery of chemically modified mRNA in mice. *Nat. Biotechnol.* **2011**, 29 (2), 154-157.
- (9) Zhong, Z.; Mc Cafferty, S.; Combes, F.; Huysmans, H.; De Temmerman, J.; Gitsels, A.; Vanrompay, D.; Portela Catani, J.; Sanders, N. N., mRNA therapeutics deliver a hopeful message. *Nano Today* **2018**, 23, 16-39.
 - (10) Johanning, F. W.; Conry, R. M.; LoBuglio, A. F.; Wright, M.; Sumerel, L. A.; Pike, M. J.; Curiel, D. T., A indbis virus mRNA polynucleotide vector achieves prolonged and high level heterologous gene expression in vivo. *Nucleic Acids Res.* **1995**, 23, 1495-1501.
 - (11) Johansson, D. X.; Ljungberg, K.; Kakoulidou, M.; Liljeström, P., Intradermal Electroporation of Naked Replicon RNA Elicits Strong Immune Responses. *PLoS ONE* **2012**, 7, e29732.
 - (12) Hsu, P. D.; Lander, E. S.; Zhang, F., Development and Applications of CRISPR-Cas9 for Genome Engineering. *Cell* **2014**, 157 (6), 1262-1278.
 - (13) Dowdy, S. F., Overcoming cellular barriers for RNA therapeutics. *Nat. Biotechnol.* **2017**, 35 (3), 222-229.
 - (14) Yin, H.; Kanasty, R. L.; Eltoukhy, A. A.; Vegas, A. J.; Dorkin, J. R.; Anderson, D. G., Non-viral vectors for gene-based therapy. *Nat. Rev. Genet.* **2014**, 15 (8), 541-555.
 - (15) Mitragotri, S.; Burke, P. A.; Langer, R., Overcoming the challenges in administering biopharmaceuticals: formulation and delivery strategies. *Nat. Rev. Drug Discovery* **2014**, 13 (9), 655-672.
 - (16) Nguyen, J.; Szoka, F. C., Nucleic Acid Delivery: The Missing Pieces of the Puzzle? *Acc. Chem. Res.* **2012**, 45, 1153-1162.
 - (17) Miller, J. B.; Siegwart, D. J., Design of synthetic materials for intracellular delivery of RNAs: From siRNA-mediated gene silencing to CRISPR/Cas gene editing. *Nano Res.* **2018**, 11 (10), 5310-5337.
 - (18) Schaffer, D. V.; Koerber, J. T.; Lim, K. I., Molecular engineering of viral gene delivery vehicles. *Annu. Rev. Biomed. Eng.* **2008**, 10, 169-194.
 - (19) Fenton, O. S.; Kauffman, K. J.; McClellan, R. L.; Appel, E. A.; Dorkin, J. R.; Tibbitt, M. W.; Heartlein, M. W.; DeRosa, F.; Langer, R.; Anderson, D. G., Bioinspired Alkenyl Amino Alcohol Ionizable Lipid Materials for Highly Potent In Vivo mRNA Delivery. *Adv. Mater.* **2016**, 28 (15), 2939-43.
 - (20) Sago, C. D.; Lokugamage, M. P.; Paunovska, K.; Vanover, D. A.; Monaco, C. M.; Shah, N. N.; Castro, M. G.; Anderson, S. E.; Rudoltz, T. G.; Lando, G. N.; Tiwari, P. M.; Kirschman, J. L.; Willett, N.; Jang, Y. C.; Santangelo, P. J.; Bryksin, A. V.; Dahlman, J. E., High-throughput in vivo screen of functional mRNA delivery identifies nanoparticles for endothelial cell gene editing. *Proc. Natl. Acad. Sci. U. S. A.* **2018**, 115 (48), E9944-E9952.
 - (21) Adams, D.; Gonzalez-Duarte, A.; O'Riordan, W. D.; Yang, C. -C.; Ueda, M.; Kristen, A. V.; Tournev, I.; Schmidt, H. H.; Coelho, T.; Berk, J. L.; Lin, K. -P.; Vita, G.; Attarian, S.;

- Plante-Bordeneuve, V.; Mezei, M. M.; Campistol, J. M.; Buades, J.; Brannagan III, T. H.; Kim, B. J.; Oh, J.; Parman, Y.; Sekijima, Y.; Hawkins, P. N.; Solomon, S. D.; Polydefkis, M.; Dyck, P. J.; Gandhi, P. J.; Goyal, S.; Chen, J.; Strahs, A. L.; Nochur, S. V.; Sweetser, M. T.; Grag, P. P.; Vaishnav, A. K.; Gollob, J. A.; Suhr, O. B., Patisiran, an RNAi Therapeutic, for Hereditary Transthyretin Amyloidosis. *N. Engl. J. Med.* **2018**, *379*, 11–21.
- (22) Miller, J. B.; Zhang, S.; Kos, P.; Xiong, H.; Zhou, K.; Perelman, S. S.; Zhu, H.; Siegwart, D. J., Non-Viral CRISPR/Cas Gene Editing In Vitro and In Vivo Enabled by Synthetic Nanoparticle Co-Delivery of Cas9 mRNA and sgRNA. *Angew. Chem. Int. Ed.* **2017**, *56* (4), 1059–1063.
- (23) Patel, A. K.; Kaczmarek, J. C.; Bose, S.; Kauffman, K. J.; Mir, F.; Heartlein, M. W.; DeRosa, F.; Langer, R.; Anderson, D. G., Inhaled Nanoformulated mRNA Polyplexes for Protein Production in Lung Epithelium. *Adv. Mater.* **2019**, *31* (8), 1805116.
- (24) Van Bruggen, C.; Hexum, J. K.; Tan, Z.; Dalal, R. J.; Reineke, T. M., Nonviral Gene Delivery with Cationic Glycopolymers. *Acc. Chem. Res.* **2019**, ASAP. DOI: 10.1021/acs.accounts.8b00665.
- (25) McKinlay, C. J.; Benner, N. L.; Haabeth, O. A.; Waymouth, R. M.; Wender, P. A., Enhanced mRNA delivery into lymphocytes enabled by lipid-varied libraries of charge-altering releasable transporters. *Proc. Natl. Acad. Sci. U. S. A.* **2018**, *115* (26), E5859–E5866.
- (26) Davis, M. E.; Zuckerman, J. E.; Choi, C. H.; Seligson, D.; Tolcher, A.; Alabi, C. A.; Yen, Y.; Heidel, J. D.; Ribas, A., Evidence of RNAi in humans from systemically administered siRNA via targeted nanoparticles. *Nature* **2010**, *464* (7291), 1067–1070.
- (27) Oupicky, D.; Li, J., Bio reducible polycations in nucleic acid delivery: past, present, and future trends. *Macromol. Biosci.* **2014**, *14* (7), 908–922.
- (28) Sizovs, A.; Song, X.; Waxham, M. N.; Jia, Y.; Feng, F.; Chen, J.; Wicker, A. C.; Xu, J.; Yu, Y.; Wang, J., Precisely Tunable Engineering of Sub-30 nm Monodisperse Oligonucleotide Nanoparticles. *J. Am. Chem. Soc.* **2014**, *136*, 234–240.
- (29) Uchida, H.; Itaka, K.; Uchida, S.; Ishii, T.; Suma, T.; Miyata, K.; Oba, M.; Nishiyama, N.; Kataoka, K., Synthetic Polyamines to Regulate mRNA Translation through the Preservative Binding of Eukaryotic Initiation Factor 4E to the Cap Structure. *J. Am. Chem. Soc.* **2016**, *138*, 1478–1481.
- (30) Khandare, J.; Calderon, M.; Dagia, N. M.; Haag, R., Multifunctional dendritic polymers in nanomedicine: opportunities and challenges. *Chem. Soc. Rev.* **2012**, *41* (7), 2824–2848.
- (31) Kurniasih, I. N.; Keilitz, J.; Haag, R., Dendritic nanocarriers based on hyperbranched polymers. *Chem. Soc. Rev.* **2015**, *44* (12), 4145–4164.
- (32) Yu, T.; Liu, X.; Bolcato-Bellemin, A.-L.; Wang, Y.; Liu, C.; Erbacher, P.; Qu, F.; Rocchi, P.; Behr, J.-P.; Peng, L., An Amphiphilic Dendrimer for Effective Delivery of Small Interfering RNA and Gene Silencing In Vitro and In Vivo. *Angew. Chem., Int. Ed.* **2012**, *51*, 8478–8484.

- (33) Guidotti, G.; Brambilla, L.; Rossi, D., Cell-Penetrating Peptides: From Basic Research to Clinics. *Trends Pharmacol. Sci.* **2017**, *38* (4), 406-424.
- (34) Copolovici, D. M.; Langel, K.; Eriste, E.; Langel, Ü., Cell-Penetrating Peptides: Design, Synthesis, and Applications. *ACS Nano*, **2014**, *8*, 1972-1994.
- (35) Kim, S. T.; Chompoosor, A.; Yeh, Y.-C.; Agasti, S. S.; Solfiell, D. J.; Rotello, V. M., Dendronized Gold Nanoparticles for siRNA Delivery. *Small* **2012**, *8*, 3253-3256.
- (36) Giljohann, D. A.; Seferos, D. S.; Prigodich, A. E.; Patel, P. C.; Mirkin, C. A., Gene Regulation with Polyvalent siRNA-Nanoparticle Conjugates. *J. Am. Chem. Soc.* **2009**, *131*, 2072-2073.
- (37) Behr, J. P., Synthetic Gene Transfer Vectors II: Back to the Future. *Acc. Chem. Res.* **2012**, *45*, 980-984.
- (38) Chen, G.; Ma, B.; Wang, Y.; Gong, S. A., Universal GSH-Responsive Nanoplatform for the Delivery of DNA, mRNA, and Cas9/sgRNA Ribonucleoprotein. *ACS Appl. Mater. Interfaces* **2018**, *10* (22), 18515-18523.
- (39) Read, M. L.; Singh, S.; Ahmed, Z.; Stevenson, M.; Briggs, S. S.; Oupicky, D.; Barrett, L. B.; Spice, R.; Kendall, M.; Berry, M.; Preece, J. A.; Logan, A.; Seymour, L. W., A versatile reducible polycation-based system for efficient delivery of a broad range of nucleic acids. *Nucleic Acids Res.* **2005**, *33* (9), e86.
- (40) Son, S.; Namgung, R.; Kim, J.; Singha, K.; Kim, W. J., Bioreducible Polymers for Gene Silencing and Delivery. *Acc. Chem. Res.* **2012**, *45*, 1100-1112.
- (41) Zeng, H.; Little, H. C.; Tiambeng, T. N.; Williams, G. A.; Guan, Z., Multifunctional dendronized peptide polymer platform for safe and effective siRNA delivery. *J. Am. Chem. Soc.* **2013**, *135* (13), 4962-4965.
- (42) Oldenhuis, N. J.; Eldredge, A. C.; Burts, A. O.; Ryu, K. A.; Chung, J.; Johnson, M. E.; Guan, Z., Biodegradable Dendronized Polymers for Efficient mRNA Delivery. *ChemistrySelect* **2016**, *1* (15), 4413-4417.
- (43) Zeng, H.; Johnson, M. E.; Oldenhuis, N. J.; Tiambeng, T. N.; Guan, Z., Structure-Based Design of Dendritic Peptide Bolaamphiphiles for siRNA Delivery. *ACS Cent. Sci.* **2015**, *1* (6), 303-312.
- (44) Eldredge, A. C.; Johnson, M. E.; Oldenhuis, N. J.; Guan, Z., Focused Library Approach to Discover Discrete Dipeptide Bolaamphiphiles for siRNA Delivery. *Biomacromolecules* **2016**, *17* (10), 3138-3144.
- (45) Midoux, P.; Pichon, C.; Yaouanc, J. J.; Jaffres, P. A., Chemical vectors for gene delivery: a current review on polymers, peptides and lipids containing histidine or imidazole as nucleic acids carriers. *Br. J. Pharmacol.* **2009**, *157* (2), 166-178.
- (46) Jobin, M. L.; Blanchet, M.; Henry, S.; Chaignepain, S.; Manigand, C.; Castano, S.; Lecomte, S.; Burlina, F.; Sagan, S.; Alves, I. D., The role of tryptophans on the cellular uptake and membrane interaction of arginine-rich cell penetrating peptides. *Biochim. Biophys. Acta* **2015**, *1848* (2), 593-602.

- (47) Pujals, S.; Giralt, E., Proline-rich amphipathic cell-penetrating peptides. *Adv. Drug Delivery Rev.* **2008**, *60* (4-5), 473-484.
- (48) Palomo, J. M., Solid-phase peptide synthesis: an overview focused on the preparation of biologically relevant peptides. *RSC Adv.* **2014**, *4* (62), 32658-32672.
- (49) Kormann, M. S.; Hasenpusch, G.; Aneja, M. K.; Nica, G.; Flemmer, A. W.; Herber-Jonat, S.; Huppmann, M.; Mays, L. E.; Illenyi, M.; Schams, A.; Griese, M.; Bittmann, I.; Handgretinger, R.; Hartl, D.; Rosenecker, J.; Rudolph, C., Expression of therapeutic proteins after delivery of chemically modified mRNA in mice. *Nat. Biotechnol.* **2011**, *29* (2), 154-157.
- (50) Fire, A.; Xu, S.; Montgomery, M. K.; Kostas S. A.; Driver, S. E.; Mello, C. C., Potent and sepecific genetic interference by double-stranded RNA in *Caenorhabditis elegans*. *Nature* **1998**, *391*, 806-811.
- (51) Sun, T. M.; Du, J. Z.; Yan, L. F.; Mao, H. Q.; Wang, J., Self-assembled biodegradable micellar nanoparticles of amphiphilic and cationic block copolymer for siRNA delivery. *Biomaterials* **2008**, *29* (32), 4348-4355.
- (52) Chuang, C. C.; Chang, C. W., Complexation of bio reducible cationic polymers with gold nanoparticles for improving stability in serum and application on nonviral gene delivery. *ACS Appl. Mater. Interfaces* **2015**, *7* (14), 7724-7731.
- (53) Zelphati, O.; Uyechi, L. S.; Barron, L. G.; Szoka, F. C. Jr., Effect of Serum Components on the Physico-Chemical Properties of Cationic Lipid/oligonucleotide Complexes and on their Interactions with Cells. *Biochim. Biophys. Acta* **1998**, *1390*, 119-133.
- (54) Li, S.; Tseng, W. C.; Stolz, D. B.; Wu, S. P.; Watkins, S. C.; Huang, L., Dynamic Changes in the Characteristics of Cationic Lipidic Vectors after Exposure to Mouse Serum: Implications for Intravenous Lipofection. *Gene Ther.* **1999**, *6*, 585-594.
- (55) Sommer, S. S.; Cohen, J. E., The Size Distributions of Proteins, mRNA, and Nuclear RNA. *J. Mol. Evol.* **1980**, *15*, 37-57.
- (56) Ross, J., mRNA Stability in Mammalian Cells. *Microbiol. Rev.* **1995**, *59* (3), 423-450.
- (57) Weltzien, H. U.; Arnold, B.; Reuther, R., Qunatitative studies on lysolecithin-mediated hemolysis. Use of ether-deoxylysolecithin analogs with varying aliphatic chain-lengths. *Biochim. Biophys. Acta* **1977**, *466* (3), 411-421.
- (58) Verhoef, J. J.; Anchordoquy, T. J., Questioning the Use of PEGylation for Drug Delivery. *Drug Delivery Transl. Res.* **2013**, *3* (6), 499-503.
- (59) Harvie, P.; Wong, F. M.; Bally, M. B., Use of Poly(ethylene glycol)-Lipid Conjugates to Regulate the Surface Attributes and Transfection Activity of Lipid-DNA Particles. *J. Pharm. Sci.* **2000**, *89* (5), 652-663.
- (60) Nelson, C. E.; Kintzing, J. R. Hanna, A.; Shannon, J. M.; Gupta, M. K.; Duvall, C. L., Balancing Cationic and Hydrophobic Content of PEGylated siRNA Polyplexes Enhances Endosome Escape, Stability, Blood Circulation Time, and Bioactivity *in Vivo*. *ACS Nano*, **2013**, *7*, 8870-8880.

- (61) Manganiello, M. J.; Cheng, C.; Convertine, A. J.; Bryers, J. D.; Stayton, P. S., Diblock copolymers with tunable pH transitions for gene delivery. *Biomaterials* **2012**, *33* (7), 2301-2309.
- (62) Geall, A. J.; Verma, A.; Otten, G. R.; Shaw, C. A.; Hekele, A.; Banerjee, K.; Cu, Y.; Beard, C. W.; Brito, L. A.; Krucker, T.; O'Hagan, D. T.; Singh, M.; Mason, P. W.; Valiante, N. M.; Dormitzer, P. R.; Barnett, S. W.; Rappuoli, R.; Ulmer, J. B.; Mandl, C. W., Nonviral delivery of self-amplifying RNA vaccines. *Proc. Natl. Acad. Sci. U. S. A.* **2012**, *109* (36), 14604-14609.
- (63) McCullough, K. C.; Bassi, I.; Milona, P.; Suter, R.; Thomann-Harwood, L.; Englezou, P.; Demoulins, T.; Ruggli, N., Self-replicating Replicon-RNA Delivery to Dendritic Cells by Chitosan-nanoparticles for Translation In Vitro and In Vivo. *Mol. Ther. --Nucleic Acids* **2014**, *3*, e173.
- (64) Demoulins, T.; Milona, P.; Englezou, P. C.; Ebensen, T.; Schulze, K.; Suter, R.; Pichon, C.; Midoux, P.; Guzman, C. A.; Ruggli, N.; McCullough, K. C., Polyethylenimine-based polyplex delivery of self-replicating RNA vaccines. *Nanomedicine* **2016**, *12* (3), 711-722.
- (65) Baylis, F.; McLeod, M., First-in-human Phase 1 CRISPR Gene Editing Cancer Trials: Are We Ready? *Curr. Gene Ther.* **2017**, *17* (4), 309-319.
- (66) Peng, R.; Lin, G.; Li, J., Potential pitfalls of CRISPR/Cas9-mediated genome editing. *FEBS Journal* **2016**, *283* (7), 1218-1231.
- (67) Jiang, C.; Mei, M.; Li, B.; Zhu, X. R.; Zu, W. H.; Tian, Y. J.; Wang, Q. N.; Guo, Y.; Dong, Y. Z.; Tan, X., A non-viral CRISPR/Cas9 delivery system for therapeutically targeting HBV DNA and *pcsk9* in vivo. *Cell Res.* **2017**, *27*, 440-443.
- (68) Luther, D. C.; Lee, Y. W.; Nagaraj, H.; Scaletti, F.; Rotello, V. M., Delivery approaches for CRISPR/Cas9 therapeutics in vivo: advances and challenges. *Expert Opin. Drug Delivery* **2018**, *15* (9), 905-913.
- (69) Platt, R. J.; Chen, S.; Zhou, Y.; Yim, M. J.; Swiech, L.; Kempton, H. R.; Dahlman, J. E.; Parnas, O.; Eisenhaure, T. M.; Jovanovic, M.; Graham, D. B.; Jhunjhunwala, S.; Heidenreich, M.; Xavier, R. J.; Langer, R.; Anderson, D. G.; Hacohen, N.; Regev, A.; Feng, G.; Sharp, P. A.; Zhang, F., CRISPR-Cas9 knock in mice for genome editing and cancer modeling. *Cell* **2014**, *159* (2), 440-455.
- (70) Li, L.; Song, L.; Liu, X.; Yang, X.; Li, X.; He, T.; Wang, N.; Yang, S.; Yu, C.; Yin, T.; Wen, Y.; He, Z.; Wei, X.; Su, W.; Wu, Q.; Yao, S.; Gong, C.; Wei, Y., Artificial Virus Delivers CRISPR-Cas9 System for Genome Editing of Cells in Mice. *ACS Nano* **2017**, *11* (1), 95-111.
- (71) Yin, H.; Song, C. Q.; Suresh, S.; Wu, Q.; Walsh, S.; Rhym, L. H.; Mintzer, E.; Bolukbasi, M. F.; Zhu, L. J.; Kauffman, K.; Mou, H.; Oberholzer, A.; Ding, J.; Kwan, S. Y.; Bogorad, R. L.; Zatspein, T.; Kotliansky, V.; Wolfe, S. A.; Xue, W.; Langer, R.; Anderson, D. G., Structure-guided chemical modification of guide RNA enables potent non-viral in vivo genome editing. *Nat. Biotechnol.* **2017**, *35* (12), 1179-1187.

- (72) Finn, J. D.; Smith, A. R.; Patel, M. C.; Shaw, L.; Youniss, M. R.; van Heteren, J.; Dirstine, T.; Ciullo, C.; Lescarbeau, R.; Seitzer, J.; Shah, R. R.; Shah, A.; Ling, D.; Growe, J.; Pink, M.; Rohde, E.; Wood, K. M.; Salomon, W. E.; Harrington, W. F.; Dombrowski, C.; Strapps, W. R.; Chang, Y.; Morrissey, D. V., A Single Administration of CRISPR/Cas9 Lipid Nanoparticles Achieves Robust and Persistent In Vivo Genome Editing. *Cell Rep.* **2018**, *22* (9), 2227-2235.
- (73) Mout, R.; Ray, M.; Yesilbag Tonga, G.; Lee, Y. W.; Tay, T.; Sasaki, K.; Rotello, V. M., Direct Cytosolic Delivery of CRISPR/Cas9-Ribonucleoprotein for Efficient Gene Editing. *ACS Nano* **2017**, *11* (3), 2452-2458.
- (74) Chang, J.; Chen, X.; Glass, Z.; Gao, F.; Mao, L.; Wang, M.; Xu, Q., Integrating Combinatorial Lipid Nanoparticle and Chemically Modified Protein for Intracellular Delivery and Genome Editing. *Acc. Chem. Res.* **2019**, *52* (3), 665-675.
- (75) Yin, H.; Kauffman, K. J.; Anderson, D. G., Delivery technologies for genome editing. *Nat. Rev. Drug Discovery* **2017**, *16* (6), 387-399.
- (76) Glass, Z.; Lee, M.; Li, Y.; Xu, Q., Engineering the Delivery System for CRISPR-Based Genome Editing. *Trends Biotechnol.* **2018**, *36* (2), 173-185.
- (77) Niu, Y.; Shen, B.; Cui, Y.; Chen, Y.; Wang, J.; Wang, L.; Kang, Y.; Zhao, X.; Si, W.; Li, W.; Xiang, A. P.; Zhou, J.; Guo, X.; Bi, Y.; Si, C.; Hu, B.; Dong, G.; Wang, H.; Zhou, Z.; Li, T.; Tan, T.; Pu, X.; Wang, F.; Ji, S.; Zhou, Q.; Huang, X.; Ji, W.; Sha, J., Generation of gene-modified cynomolgus monkey via Cas9/RNA-mediated gene targeting in one-cell embryos. *Cell* **2014**, *156* (4), 836-843.
- (78) Sanjana, N. E.; Shalem, O.; Zhang, F. Improved vectors and genome-wide libraries for CRISPR screening. *Nat. Methods* **2014**, *11* (8), 783-784.
- (79) Sancak, Y.; Peterson, T. R.; Shaul, Y. D.; Lindquist, R. A.; Thoreen, C. C.; Bar-Peled, L.; Sabatini, D. M. The Rag CTPases Bind Raptor and Mediate Amino Acid Signaling to mTORC1. *Science*, **2008**, *320*, 1496-1501.

2.12 Experimental

Materials. All commercially available chemicals were used without further purification unless otherwise noted. Protected amino acids were purchased from Advanced ChemTech (Louisville, KY) and Aroz Technologies, LLC. (Cincinnati, OH). Coupling reagents were purchased from GL Biochem Ltd. (Shanghai, China). All siRNA used in this study was purchased from Thermo Fischer Life Technologies with Silencer® Select negative control siRNA and Silencer® Select Custom siRNA used for gel assays, DLS measurements, and transfection studies. The sequences for the anti-Luc siRNA are: 5'-AGACUAUAAGAUUCAUCUTT-3' (sense) and 5'-AGAUUGAAUCUUAUAGUCUTG-3' (anti-sense). Mission® siRNA Fluorescent Universal Negative Control #1 Cyanine 5 was obtained from Sigma-Aldrich. CleanCap® eGFP mRNA (5moU), Fluc mRNA (5moU), Cyanine 5 Fluc mRNA (5moU), Cyanine 5 eGFP mRNA (5moU), and Cas9 mRNA (5moU-modified) were obtained from TriLink Biotechnologies (Sorrento Mesa, CA). Replicon mRNA was generously provided by Professor Darrell Irvine (Department of Biological Engineering, MIT). sgRNA was synthesized according to EnGen® sgRNA Synthesis Kit protocol. Lipofectamine RNAiMAX, Lipofectamine MessengerMAX, and Lipofectamine 2000 were purchased from Invitrogen (Carlsbad, CA) and used as positive controls following the manufacturer's protocol. Pierce™ LDH Cytotoxicity Assay Kit was purchased from Thermo Fisher (San Jose, CA). All reactions were performed using HPLC grade solvents unless otherwise noted. All water used in biological experiments was Nanopure water obtained from Barnstead Nanopure Diamond (Waltham, MA). Unmodified NIH 3T3 cells were a generous gift from Professor Young Jik Kwon (Department of Chemical Engineering, UC Irvine, CA). Firefly luciferase-expressing HEK cells were generously provided by Professor

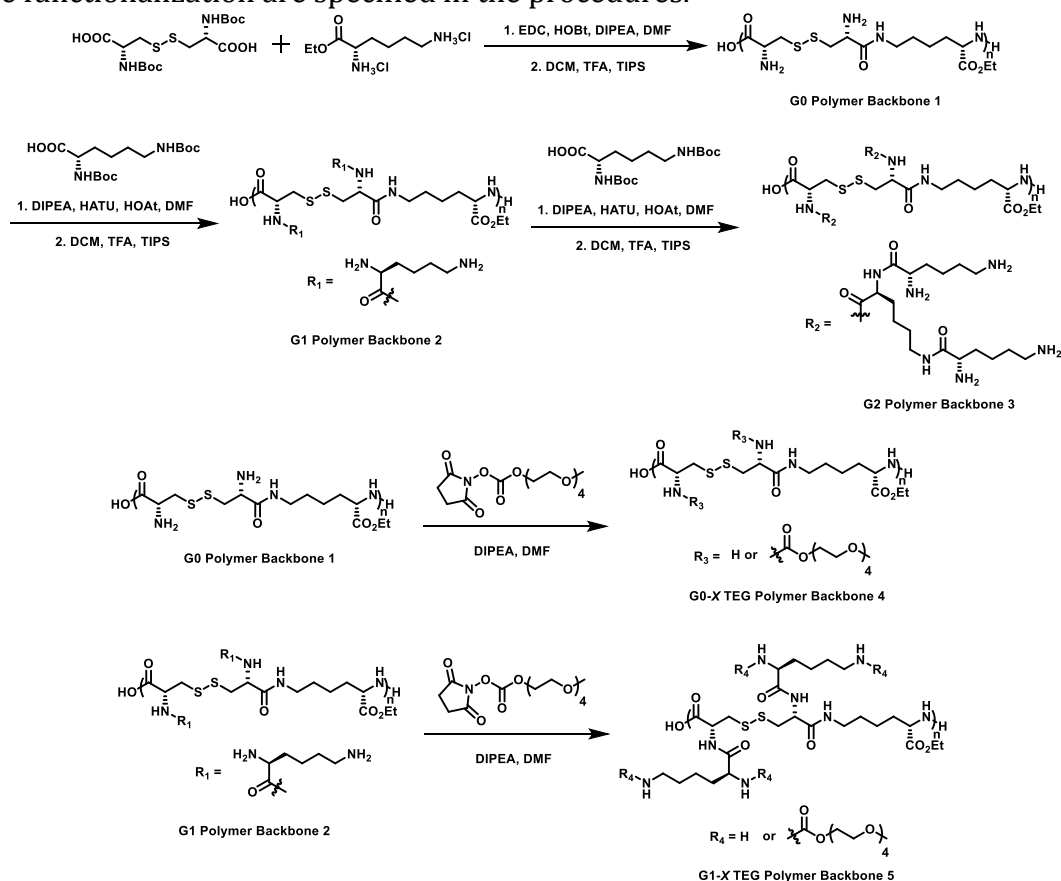
Jennifer Prescher (Department of Chemistry, UC Irvine, CA). GFP-expressing NIH 3T3 cells were obtained through lentiviral transduction.⁷⁸⁻⁷⁹ psPAX2 plasmid was a gift from Didier Trono (Addgene plasmid #12260; RRID: Addgene_12260), pMD2.G was a gift from Didier Trono (Addgene plasmid #12259; RRID: Addgene_12259), and pLJM1-EGFP was a gift from David Sabatini (Addgene plasmid #19319; RRID: Addgene_19319). Dulbecco's modified Eagle's medium (DMEM), fetal bovine serum (FBS), and OptiMEM were purchased from Invitrogen (Carlsbad, CA).

Instruments. Nuclear Magnetic Resonance (NMR) spectra were recorded on 500 MHz or 600 MHz Bruker spectrometers. Chemical shifts were reported in ppm. Coupling constants (J values) were reported in Hertz. ^1H NMR chemical shifts were referenced to D_2O ($\delta = 4.79$ ppm). The molecular weight and molecular weight distribution of the **MPBP** backbone was measured by gel permeation chromatography (GPC). GPC was performed on an Agilent 1100 SEC system using an OHpak SB-803 HQ column from Shodex. The molecular weight was determined with respect to poly(ethylene glycol) (PEG) S3 standards purchased from Aldrich. DMF with 0.1% LiBr (wt/v) was used as the eluent at a flow rate of 1.0 mL/min with column temperature at 45°C. The Z-average size and zeta potential of **MPBP**-RNA polyplexes were measured at 633 nm using Zetasizer (NanoZS) dynamic light scattering instrument (Malvern Instruments, Malvern, UK) at 25 °C with detection angle of 173°. The **MPBP**/RNA nanoparticles were visualized on a FEI/Philips CM-20 conventional TEM operated at an accelerating voltage of 200 kV. Confocal images were obtained using a Zeiss LSM 700 (Carl Zeiss AG, Oberkochen, Germany). Flow cytometry was performed on a BD ACCURI C6 flow cytometer (BD Biosciences, San Jose). Solid-phase peptide synthesis was

performed on a Protein Technologies PS3 synthesizer. Matrix assisted laser desorption ionization spectral data (MALDI) was obtained from the UC Irvine Mass Spectrometry Facility and collected with an AB SCIEX TOF/TOF 5800 System.

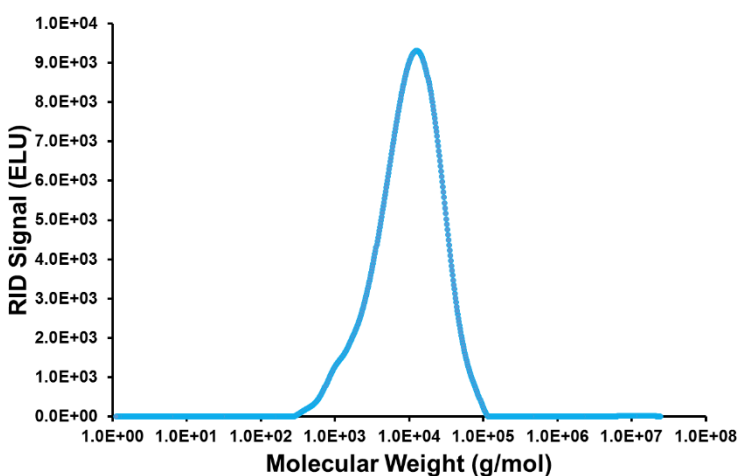
MPBP Vector Synthesis and Characterization

Scheme 2.1 Synthetic scheme for **MPBP** vectors. Amounts of TEG, SA, OA, and linear peptide functionalization are specified in the procedures.



G0 polymer backbone 1, **G1 polymer backbone 2**, **G2 polymer backbone 3**, and NHS-TEG-OMe were obtained according to previous literature.⁴¹⁻⁴² The functionalization percentage *X* and *Y* are determined based on the total amount of primary amines on different polymers. All yields given refer to isolated yields.

The deprotected **G0 polymer backbone 1** was characterized by analytical GPC with 0.1% LiBr in DMF as the eluent and poly(ethylene glycol) (PEG) standards were used as the reference. The result was shown below:



$$\begin{aligned} M_n &= 9.37 \times 10^3 \text{ g/mol} \\ M_w &= 1.95 \times 10^4 \text{ g/mol} \\ \text{PDI} &= 2.08 \end{aligned}$$

¹H NMR of the polymer samples used a 3 seconds d1 relaxation time to ensure chain relaxation and to help with resolution. Methanol, acetone and water were unable to be completely removed from the polymer samples. The integration ratios of ¹H NMR peaks are determined based on each repeating unit of the polymers. The integration of some peaks are not accurate due to the overlapping between sample signals and solvent signals.

Typical procedure for synthesis of **G0-X TEG polymer backbone 4**:

In a 25 mL round bottom flask equipped with a stir bar, **G0 polymer backbone 1** (1.0 equiv.) was dissolved in 5 mL of anhydrous DMF and DIPEA (2.0 equiv.) was added. The

reaction was cooled to 0 °C and the NHS-TEG-OMe was added in the corresponding amount of functionalization ratio X (0.4 equiv. for 20% and 1.0 equiv. for 50%). After 30 minutes, the ice bath was removed and the reaction mixture was stirred under nitrogen at room temperature overnight. After removal of the solvent under reduced pressure, the residue was dissolved in MeOH and purified via dialysis (MWCO = 6 – 8 kDa) against MeOH for 12 h. Then MeOH was removed *in vacuo* to give **G0- X TEG polymer backbone 4** as a colorless oil.

G0-20TEG polymer backbone (70% isolated yield): ^1H NMR (600 MHz, D_2O , 298 K, ppm): δ 4.43 – 4.16 (m, 6H), 3.78 – 3.63 (m, 6H), 3.39 (s, 1H), 3.29 – 3.02 (m, 6H), 1.90 – 1.41 (m, 6H), 1.29 – 1.27 (m, 3H).

G0-50TEG polymer backbone (65% isolated yield): ^1H NMR (600 MHz, D_2O , 298 K, ppm): δ 4.54 – 4.22 (m, 7H), 3.77 – 3.63 (m, 14H), 3.39 (s, 3H), 3.22 – 3.02 (m, 6H), 1.90 – 1.40 (m, 6H), 1.29 – 1.26 (m, 3H).

Typical procedure for synthesis of **G1- X TEG polymer backbone 5**:

In a 25 mL round bottom flask equipped with a stir bar, **G1 polymer backbone 2** (1.0 equiv.) was dissolved in 5 mL of anhydrous DMF and DIPEA (4.0 equiv.) was added. The reaction was cooled to 0 °C and the NHS-TEG-OMe was added in the corresponding amount of functionalization ratio X (0.8 equiv. for 20% and 2.0 equiv. for 50%). After 30 minutes, the ice bath was removed and the reaction mixture was stirred under nitrogen at room temperature overnight. After removal of the solvent under reduced pressure, the residue was dissolved in MeOH and purified via dialysis (MWCO = 6 – 8 kDa) against MeOH for 12

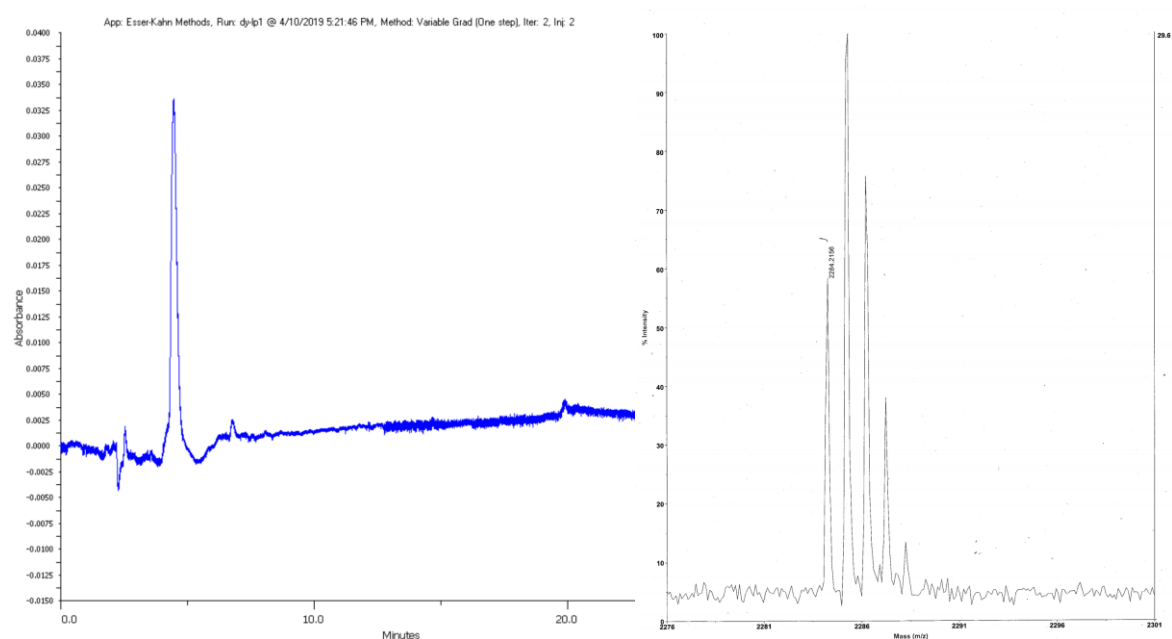
h. Then MeOH was removed *in vacuo* to give **G1-X TEG polymer backbone 5** as a colorless oil.

G1-20TEG polymer backbone (70% isolated yield): ^1H NMR (600 MHz, D_2O , 298 K, ppm): δ 4.64 – 4.03 (m, 9H), 3.76 – 3.63 (m, 11H), 3.39 (s, 2.4H), 3.21 – 3.00 (m, 10H), 1.92 – 1.34 (m, 18H), 1.27 (m, 3H).

G1-50TEG polymer backbone (68% isolated yield): ^1H NMR (600 MHz, D_2O , 298 K, ppm): δ 4.66 – 4.06 (m, 11H), 3.76 – 3.63 (m, 28H), 3.39 (s, 6H), 3.20 – 3.02 (m, 10H), 2.01 – 1.39 (m, 18H), 1.27 (m, 3H).

Protected linear peptide (Boc-WKHKHKHG-OH): 2-chlorotrityl chloride resin was first loaded with Fmoc-Gly-OH at the loading density of 0.484 mmol/g. Following the sequence of HKHKHKW, Gly-loaded resin (400 mg, 1.0 equiv., 0.194 mmol) was coupled with 3 different side-chain protected amino acids on a PS3 solid-phase peptide synthesizer. For each coupling step, one amino acid was added for reaction: Fmoc-His(Trt)-OH (601 mg, 5.0 equiv., 0.97 mmol), Fmoc-Lys(Boc)-OH (455 mg, 5.0 equiv., 0.97 mmol), or Boc-Trp(Boc)-OH (392 mg, 5.0 equiv., 0.97 mmol). HATU (332 mg, 4.5 equiv., 0.873 mmol) was utilized as coupling reagent and HOAt (119 mg, 4.5 equiv., 0.873 mmol) was included to suppress the possible epimerization. 20% collidine in DMF was used in the coupling reaction and 20% piperidine in DMF was used to deprotect the Fmoc group. After the synthesis was finished, the protected linear peptide was cleaved from the resin by using 20% hexafluoroisopropanol in anhydrous CH_2Cl_2 . After removal of the solvent under reduced pressure, the residue was obtained as a white solid to give 350 mg (79%) of **protected linear peptide (Boc-WKHKHKHG-OH)**. The synthesized linear peptide was purified by

C18 reverse-phase chromatography (MeOH as the eluent) and utilized for the following coupling reactions. MALDI-TOF MS m/z : 2284.2156 $[M+H]^+$.



G0-100LP 6: In a 20 mL scintillation vial, **G0 polymer backbone 1** (5.0 mg, 0.016 mmol), **protected linear peptide** (56 mg, 0.024 mmol), HATU (12.5 mg, 0.032 mmol) and HOAt (4.5 mg, 0.032 mmol) was dissolved in 2 mL anhydrous DMF. After DIPEA (14 μ L, 0.08 mmol) was added, the yellow reaction mixture was left to stir at room temperature overnight. The reaction mixture was then precipitated by adding the reaction solution into water. After centrifugation, the water was removed and the polymer was dissolved in a mixture of TFA (3.0 mL), CH_2Cl_2 (1.5 mL), anisole (1.5 mL) and TIPS (0.2 mL). The deprotection reaction mixture was stirred at room temperature for 6 h under nitrogen. After removal of the solvents under reduced pressure, the residue was dissolved in MeOH and then precipitated in diethyl ether. After centrifugation, the supernatant was discarded and the white precipitate was dissolved in MeOH and purified via dialysis (MWCO = 6 – 8

kDa) against MeOH for 24 h. Then MeOH was removed *in vacuo* to give 44 mg (82%) of **G0-100LP 6** (TFA salt) as a white solid. ¹H NMR (600 MHz, D₂O, 298 K, ppm): δ 8.63 – 8.58 (m, 6H), 7.54 – 7.50 (m, 4H), 7.30 – 7.13 (m, 12H), 4.59 – 4.02 (m, 21H), 3.80 – 3.74 (m, 2H), 3.23 – 3.14 (m, 17H), 3.06 – 2.94 (m, 17H), 1.83 – 1.24 (m, 45H).

G1-100LP 7: In a 20 mL scintillation vial, **G1 polymer backbone 2** (10.0 mg, 9.17×10^{-3} mmol), **protected linear peptide** (126 mg, 0.055 mmol), HATU (20.9 mg, 0.055 mmol) and HOAt (7.5 mg, 0.055 mmol) was dissolved in 2.5 mL anhydrous DMF. After DIPEA (34 μL, 0.19 mmol) was added, the reaction mixture was left to stir at room temperature overnight. The reaction mixture was then precipitated by adding the reaction solution into water. After centrifugation, the water was removed and the polymer was dissolved in a mixture of TFA (3.0 mL), CH₂Cl₂ (1.5 mL), anisole (1.5 mL) and TIPS (0.2 mL). The deprotection reaction mixture was stirred at room temperature for 6 h under nitrogen. After removal of the solvents under reduced pressure, the residue was dissolved in MeOH and then precipitated in diethyl ether. After centrifugation, the supernatant was discarded, and the white precipitate was dissolved in MeOH and purified via dialysis (MWCO = 6 – 8 kDa) against MeOH for 24 h. Then MeOH was removed *in vacuo* to give 47 mg (78%) of **G1-100LP 7** (TFA salt) as a white solid. ¹H NMR (600 MHz, D₂O, 298 K, ppm): δ 8.56 – 8.41 (m, 12H), 7.52 – 7.05 (m, 32H), 4.33 – 3.72 (m, 43H), 3.40 – 2.94 (m, 66H), 1.96 – 1.17 (m, 93H).

G2-100LP 8: In a 20 mL scintillation vial, **G2 polymer backbone 3** (10.0 mg, 4.85×10^{-3} mmol), **protected linear peptide** (124 mg, 0.054 mmol), HATU (20.0 mg, 0.052 mmol) and HOAt (7.1 mg, 0.052 mmol) was dissolved in 2.5 mL anhydrous DMF. After DIPEA (14 μL,

0.08 mmol) was added, the reaction mixture was left to stir at room temperature overnight. The reaction mixture was then precipitated by adding the reaction solution into water. After centrifugation, the water was removed and the polymer was dissolved in a mixture of TFA (3.0 mL), CH₂Cl₂ (1.5 mL), anisole (1.5 mL) and TIPS (0.2 mL). The deprotection reaction mixture was stirred at room temperature for 6 h under nitrogen. After removal of the solvents under reduced pressure, the residue was dissolved in MeOH and then precipitated in diethyl ether. After centrifugation, the supernatant was discarded, and the white precipitate was dissolved in MeOH and purified via dialysis (MWCO = 6 – 8 kDa) against MeOH for 24 h. Then MeOH was removed *in vacuo* to give 39 mg (61%) of **G2-100LP 8** (TFA salt) as a white solid. ¹H NMR (600 MHz, D₂O, 298 K, ppm): δ 8.57 – 8.43 (m, 24H), 7.53 – 7.06 (m, 64H), 4.33 – 3.65 (m, 83H), 3.24 – 2.94 (m, 130H), 1.72 – 1.26 (m, 189H).

Typical procedure for synthesis of **G0-X TEG-Y LP 9**:

In a 20 mL scintillation vial, **G0-X TEG polymer backbone 4** (1.0 equiv.), **protected linear peptide** (quantity determined by the functionalization ratio *Y*, 1.6 equiv. for 80% and 1.0 equiv. for 50%), HATU (1.6 equiv. for 80% and 1.0 equiv. for 50%) and HOAt (1.6 equiv. for 80% and 1.0 equiv. for 50%) was dissolved in 2 mL anhydrous DMF. After DIPEA (3.2 equiv. for 80% and 2.0 equiv. for 50%) was added, the yellow reaction mixture was left to stir at room temperature overnight. The reaction mixture was then precipitated by adding the reaction solution into water. After centrifugation, the water was removed and the polymer was dissolved in a mixture of TFA (3.0 mL), CH₂Cl₂ (1.5 mL), anisole (1.5 mL) and TIPS (0.2 mL). The deprotection reaction mixture was stirred at room temperature for 6 h

under nitrogen. After removal of the solvents under reduced pressure, the residue was dissolved in MeOH and then precipitated in diethyl ether. After centrifugation, the supernatant was discarded, and the white precipitate was dissolved in MeOH and purified via dialysis (MWCO = 6 – 8 kDa) against MeOH for 24 h. Then MeOH was removed *in vacuo* to give **G0-X TEG-Y LP 9** (TFA salt) as a white solid.

G0-20TEG-80LP (75% isolated yield): ^1H NMR (600 MHz, D_2O , 298 K, ppm): δ 8.58 – 8.39 (m, 5H), 7.55 – 7.06 (m, 13H), 4.68 – 4.61 (m, 2H), 4.35 – 3.99 (m, 11H), 3.83 – 3.59 (m, 6H), 3.41 – 2.96 (m, 30H), 1.75 – 1.17 (m, 38H).

G0-50TEG-50LP (71% isolated yield): ^1H NMR (600 MHz, D_2O , 298 K, ppm): δ 8.46 – 8.12 (m, 3H), 7.54 – 7.06 (m, 8H), 4.64 – 3.98 (m, 20H), 3.73 – 3.59 (m, 13H), 3.20 – 2.94 (m, 23H), 1.72 – 1.21 (m, 27H).

Typical procedure for synthesis of **G1-X TEG-Y LP 10**:

In a 20 mL scintillation vial, **G1-X TEG polymer backbone 5** (1.0 equiv.), **protected linear peptide** (quantity determined by the functionalization ratio *Y*, 3.2 equiv. for 80% and 2.0 equiv. for 50%), HATU (3.2 equiv. for 80% and 2.0 equiv. for 50%) and HOAt (3.2 equiv. for 80% and 2.0 equiv. for 50%) was dissolved in 2 mL anhydrous DMF. After DIPEA (6.4 equiv. for 80% and 4.0 equiv. for 50%) was added, the yellow reaction mixture was left to stir at room temperature overnight. The reaction mixture was then precipitated by adding the reaction solution into water. After centrifugation, the water was removed and the polymer was dissolved in a mixture of TFA (3.0 mL), CH_2Cl_2 (1.5 mL), anisole (1.5 mL) and TIPS (0.2 mL). The deprotection reaction mixture was stirred at room temperature for 6 h under nitrogen. After removal of the solvents under reduced pressure, the residue was

dissolved in MeOH and then precipitated in diethyl ether. After centrifugation, the supernatant was discarded, and the white precipitate was dissolved in MeOH and purified via dialysis (MWCO = 6 – 8 kDa) against MeOH for 24 h. Then MeOH was removed *in vacuo* to give **G1-X TEG-Y LP 10** (TFA salt) as a white solid.

G1-20TEG-80LP (72% isolated yield): ^1H NMR (600 MHz, D_2O , 298 K, ppm): δ 8.54 – 8.24 (m, 10H), 7.53 – 7.06 (m, 26H), 4.66 – 4.60 (m, 2H), 4.33 – 4.13 (m, 22H), 4.01 – 3.64 (m, 24H), 3.40 – 2.94 (m, 57H), 1.86 – 1.20 (m, 73H).

G1-50TEG-50LP (68% isolated yield): ^1H NMR (600 MHz, D_2O , 298 K, ppm): δ 8.52 – 8.28 (m, 6H), 7.54 – 7.05 (m, 16H), 4.67 – 4.60 (m, 1H), 4.33 – 3.86 (m, 17H), 3.74 – 3.59 (m, 34H), 3.41 – 2.95 (m, 40H), 1.74 – 1.23 (m, 60H).

Typical procedure for synthesis of **G0-X SA-Y LP 11**:

In a 20 mL scintillation vial, **G0 polymer backbone 1** (1.0 equiv.), stearic acid (quantity determined by the functionalization ratio *X*, 0.4 equiv. for 20% and 1.0 equiv. for 50%), **protected linear peptide** (quantity determined by the functionalization ratio *Y*, 1.6 equiv. for 80% and 1.0 equiv. for 50%), HATU (2.0 equiv.) and HOAt (2.0 equiv.) was dissolved in 2 mL anhydrous DMF. After DIPEA (4.0 equiv.) was added, the yellow reaction mixture was left to stir at room temperature overnight. The reaction mixture was then precipitated by adding the reaction solution into water. After centrifugation, the water was removed and the polymer was dissolved in a mixture of TFA (3.0 mL), CH_2Cl_2 (1.5 mL), anisole (1.5 mL) and TIPS (0.2 mL). The deprotection reaction mixture was stirred at room temperature for 6 h under nitrogen. After removal of the solvents under reduced pressure, the residue was dissolved in MeOH and then precipitated in diethyl ether. After centrifugation, the

supernatant was discarded, and the white precipitate was dissolved in MeOH and purified via dialysis (MWCO = 6 – 8 kDa) against MeOH for 24 h. Then MeOH was removed *in vacuo* to give **G0-X SA-Y LP 11** (TFA salt) as a white solid.

G0-20SA-80LP (63% isolated yield): ¹H NMR (600 MHz, D₂O, 298 K, ppm): δ 8.49 – 8.14 (m, 5H), 7.55 – 7.06 (m, 13H), 4.66 – 4.58 (m, 3H), 4.32 – 3.98 (m, 10H), 3.81 – 3.71 (m, 2H), 3.41 – 2.94 (m, 29H), 2.03 – 1.23 (m, 50H).

G0-50SA-50LP (52% isolated yield): ¹H NMR (600 MHz, D₂O, 298 K, ppm): δ 8.44 – 8.00 (m, 3H), 7.55 – 7.01 (m, 8H), 4.66 – 4.57 (m, 2H), 4.35 – 3.96 (m, 8H), 3.81 – 3.69 (m, 1H), 3.39 – 2.94 (m, 20H), 2.04 – 1.23 (m, 40H).

Typical procedure for synthesis of **G1-X SA-Y LP 12**:

In a 20 mL scintillation vial, **G1 polymer backbone 2** (1.0 equiv.), stearic acid (quantity determined by the functionalization ratio X, 0.8 equiv. for 20% and 2.0 equiv. for 50%), **protected linear peptide** (quantity determined by the functionalization ratio Y, 3.2 equiv. for 80% and 2.0 equiv. for 50%), HATU (4.0 equiv.) and HOAt (4.0 equiv.) was dissolved in 2 mL anhydrous DMF. After DIPEA (8.0 equiv.) was added, the yellow reaction mixture was left to stir at room temperature overnight. The reaction mixture was then precipitated by adding the reaction solution into water. After centrifugation, the water was removed and the polymer was dissolved in a mixture of TFA (3.0 mL), CH₂Cl₂ (1.5 mL), anisole (1.5 mL) and TIPS (0.2 mL). The deprotection reaction mixture was stirred at room temperature for 6 h under nitrogen. After removal of the solvents under reduced pressure, the residue was dissolved in MeOH and then precipitated in diethyl ether. After centrifugation, the supernatant was discarded and the white precipitate was dissolved in MeOH and purified

via dialysis (MWCO = 6 – 8 kDa) against MeOH for 24 h. Then MeOH was removed *in vacuo* to give **G1-X SA-Y LP 12** (TFA salt) as a white solid.

G1-20SA-80LP (64% isolated yield): ^1H NMR (600 MHz, D_2O , 298 K, ppm): δ 8.51 – 8.04 (m, 10H), 7.55 – 7.01 (m, 26H), 4.66 – 4.54 (m, 6H), 4.33 – 4.25 (m, 28H), 3.81 – 3.66 (m, 2H), 3.40 – 2.95 (m, 55H), 1.93 – 1.27 (m, 104H).

MPBP/RNA Binding Study

Gel electrophoresis

The binding of siRNA or mRNA to **MPBPs** was studied by agarose gel electrophoresis. Both siRNA/mRNA and **MPBPs** were diluted with 10 mM pH 7.4 phosphate buffer. Different amount of **MPBP** solutions (10 mg/mL) were added to 5.0 μL 5 μM siRNA solution or 1.0 μL 0.5 $\mu\text{g}/\mu\text{L}$ mRNA solution to achieve different N/P ratio (the molar ratio of primary amine groups from **MPBPs** and phosphate groups from siRNA/mRNA, imidazole groups of histidine residues not counted because they are not protonated at pH 7.4). The same buffer was added to adjust the final volume to 10.0 μL , followed by 10 min incubation at room temperature. 2 μL 6X RNA loading dye was added to each sample and 10 μL of the mixture was loaded to each well in 1% agarose gel with 1X GelRed dye. The electrophoresis was run in TBE buffer (pH 7.9) at 60 V for 90 min and the gel was visualized under a UV transilluminator. Related results are shown in **Figure 2.4** and **2.5**.

Gel electrophoresis study of mRNA protection

(1) Following the aforementioned protocol, different **MPBPs** were complexed with Fluc mRNA at N/P = 10 with duplicate. Two naked mRNA solutions were used as controls. To

one copy of each **MPBP**-mRNA complex solution and naked mRNA solutions, 10% FBS (v/v) was added. The solutions were left to stand for 20 minutes at room temperature. The other copy of each **MPBP**-mRNA complex solution and naked mRNA solutions were used as negative controls. All solutions were subjected to agarose gel electrophoresis to examine the integrity of mRNA. As shown in **Figure 2.6A**, naked mRNA was fully degraded into small species after FBS incubation, while no small species were detected from all **MPBP**-mRNA complex solutions.

(2) Following the aforementioned protocol, different **MPBPs** were complexed with Fluc mRNA at N/P = 10 and 10% FBS (v/v) was added to each complex solution. The solutions were left to stand for 20 minutes at room temperature. 7 μ L dextran sulfate (0.017 M) solution was added to each complex to achieve S/P = 80 (the molar ratio of sulfate groups from DS and phosphate groups from mRNA) and incubated for 5 minutes. The samples were then subjected to agarose gel electrophoresis under the aforementioned condition. As shown in **Figure 2.6B**, naked mRNA was fully degraded into small species after FBS incubation, while the RNA released from **MPBP**-RNA complexes was still intact.

DLS measurements

The size and zeta potential of **MPBP**-siRNA or **MPBP**-mRNA complexes were measured at 633 nm using Zetasizer (NanoZS) dynamic light scattering instrument (Malvern Instruments, Malvern, UK) at 25 °C with detection angle of 173°. Both **MPBP** and siRNA/mRNA were diluted in nanopure water, followed by brief vortexing. After 10 min incubation at room temperature, DLS measurement was taken. The solution was then

diluted with 600 μ L PBS and subjected to zeta-potential measurement. At least three measurements were taken for each sample and the mean Z-average values were reported.

TEM characterization

MPBP-siRNA and **MPBP**-mRNA complexes were prepared in ddH₂O by following aforementioned protocol. For siRNA complexation, N/P =10 and [siRNA] = 10 μ M. For mRNA complexation, N/P = 10 and [mRNA] = 0.1 μ g/ μ L. The solution was vortexed and incubated at room temperature for 10 minutes before imaging. 8 μ L sample solution was placed on a TEM grid (Ted Pella, Copper Formvar/Carbon, 200 mesh) and let stand for 1 min. The solution was blotted away with a filter paper, while 15 μ L 2% Uranyl Acetate solution was pipetted on to the grid. After 1 min, the staining process was repeated with another 15 μ L 2% Uranyl Acetate solution. All the solution was removed by a filter paper and the grid was left air dry overnight before imaging. Images were obtained on a FEI/Philips CM-20 conventional TEM operated at an accelerating voltage of 200 kV.

Biological Studies

siRNA transfections

(1) Vector-siRNA complex preparation

The TFA-salts of the various **MPBPs** were stored at -20 ° C as 10 mg/ml solutions in RNase free water and prior to complexation the vectors, along with all buffers, were allowed to reach room temperature. Both negative control and targeted siRNA were diluted to 1.5 μ M with RNase free water. The diluted siRNA was further diluted with OptiMEM and complexed with the appropriate amount of vector solution required to achieve the desired

N/P ratio. The complex solutions were prepared at 5X the desired final concentration (60 nM) and with a final volume of 60 μ L. 20 μ L of the complex solution with 300 nM siRNA was added to each well containing 80 μ L of OptiMEM to give a transfection media with 60 nM siRNA. Lipofectamine RNAiMAX was used as a positive control and prepared as instructed in the product manual.

(2) Transfection in luciferase-expressing HEK-293 cells

Transfections were performed in triplicate in a cell culture treated clear-bottom 96-well plate (Corning). After passaging, the cells were plated in 96-well plates so that they were 40~50% confluent at the time of transfection. The 5X vector-siRNA complexes were prepared using the aforementioned protocol. The culture media was switched to 80 μ L OptiMEM (with or without 10% FBS) per well and 20 μ L of the complex solution was added to each well. The cells were cultured for 48 hours prior to analysis.

(3) Transfection analysis in luciferase-expressing HEK-293 cells

After 48 hours of incubation post-transfection, the culture media was removed and replaced with 100 μ L of a 150 μ g/mL solution of firefly D-luciferin in FluoroBrite™ DMEM. Without any further treatment, the cells were incubated at 37 °C for 5 minutes after which they were imaged using an IVIS lumina II camera. The normalized luciferase knockdown was determined by comparing the overall luminescence of the samples treated with complexes containing anti-luc siRNA to those treated with complexes containing negative control siRNA.

mRNA transfections

(1) Vector-mRNA complex preparation

Before performing the mRNA transfections, the area was sterilized with bleach and RNase ZAP (Ambion), and special care was taken to use RNase free products when handling the mRNA. Lipofectamine MessengerMAX was used as a positive control and prepared as instructed in the product manual. The mRNA was thawed and diluted to a concentration of 0.05 $\mu\text{g}/\mu\text{L}$ with OptiMEM. Appropriate amount of vector solution was added to achieve the desired N/P ratio and the mixture was mixed by pipetting up and down 10 times. Finally, the mixture is diluted to 60 μL with OptiMEM so that 20 μL of the complex solution will contain 150 ng of mRNA. Then 1 μL of Insulin-Transferrin-Selenium (100X) was added. The mixture was then incubated at room temperature for 5 minutes.

(2) Transfection in NIH 3T3 cells and BHK cells

Transfections were performed in triplicate in a cell culture treated clear-bottom 96-well plate (Corning). After passaging, the cells were plated in 96-well plates so that they were 60~70% confluent at the time of transfection. The vector-mRNA complex solutions were prepared using the aforementioned protocol. The culture media was switched to 80 μL OptiMEM (with or without 10% FBS) per well and 20 μL of the complex solution was added to each well. The cells were cultured for 24 hours prior to analysis.

(3) Transfection analysis in Fluc mRNA or Replicon mRNA (expressing Fluc) transfected cells

24 hours post-transfection, the culture media was removed and replaced with 100 μ L of a 150 μ g/mL solution of firefly D-luciferin in FluoroBrite™ DMEM. Without any further treatment, the cells were incubated at 37 °C for 5 minutes after which they were imaged using an IVIS lumina II camera and the luminescence was determined.

(4) Transfection analysis in eGFP mRNA or Cy5-labelled mRNA transfected cells via flow cytometry.

24 hours post-transfection, the culture media was removed and replaced with 30 μ L trypsin and incubated at 37 °C for 5 minutes. 70 μ L of complete media were added to the plate and the cells were transferred to a 96-well non-cell treated plate for flow cytometry. Fluorescence of the transfected cells was measured on a Becton-Dickinson LSR II flow cytometer with argon ion excitation laser. 5000 events were recorded per sample and each value reported is the average of 3 samples.

CRISPR-Cas9 delivery

(1) Vector-RNA (Cas9 mRNA & sgRNA) complex preparation

Before performing the mRNA/sgRNA transfections, the area was sterilized with bleach and RNase ZAP (Ambion), and special care was taken to use RNase free products when handling the mRNA. Lipofectamine 2000 was used as a positive control and prepared as instructed in the product manual. The mRNA and sgRNA were thawed and diluted to a concentration of 0.05 μ g/ μ L with OptiMEM. Appropriate amount of vector solution was added to achieve

the desired N/P ratio and the mixture was mixed by pipetting up and down 10 times. Finally, the mixture is diluted to 60 μ L with OptiMEM so that 20 μ L of the complex solution will contain 100 ng of sgRNA and 10 ng of Cas9 mRNA. The mixture was then incubated at room temperature for 5 minutes.

(2) Transfection in eGFP-expressing NIH 3T3 cells

Transfections were performed in triplicate in a cell culture treated clear-bottom 96-well plate (Corning). After passaging, the cells were plated in 96-well plates so that they were 50% confluent at the time of transfection. The vector-mRNA complex solutions were prepared using the aforementioned protocol. The culture media was switched to 80 μ L OptiMEM per well and 20 μ L of the complex solution was added to each well. After 24 hours, the media was changed to complete media and the cells were cultured for a further 5 days. The cells were analyzed on day 6 via flow cytometry.

(3) Flow cytometry analysis

After 6 days of incubation post-transfection, the culture media was removed and replaced with 30 μ L trypsin and incubated at 37 °C for 5 minutes. 70 μ L of complete media were added to the plate and the cells were transferred to a 96-well non-cell treated plate for flow cytometry. Fluorescence of the transfected cells was measured on a Becton-Dickinson LSR II flow cytometer with argon ion excitation laser.

LDH cytotoxicity assay

NIH 3T3 cells seeded in a 96-well plate were treated with **MPBP**-mRNA complexes at an N/P ratio of 15 (serum-free media) or N/P ratio of 50 (10% FBS-containing media), formulated as specified above. After 24 h incubation with the nanoparticle complexes, 50 μ L of the supernatant was taken and cytotoxicity was measured using a Pierce™ LDH Cytotoxicity Assay Kit (ThermoFisher) as directed in the manual. Related results are shown in **Figure 2.22**.

Confocal microscopy studies

(1) Confocal laser microscopy was used to track Cy5-labelled mRNA in the transfected cells. Unmodified NIH 3T3 cells were seeded at a density of 15000 cells/well on an 8-well chamber slide (Lab-Tek, Rochester, NY, polylysine treated) 24 h prior to transfection. Cy5-labeled mRNA was complexed with different **MPBPs** at an N/P of 15 and transfected to the cells under the aforementioned conditions. Confocal fluorescence microscopy was performed 4 h or 12 h post-transfection. The nucleus was stained with 1 μ g/mL solution of Hoechst 33342. The endosome was stained with 75 nM LysoTracker® Green or Blue probes (200 μ L per well).

(2) Confocal laser microscopy was also used to track Cy5-labelled negative control siRNA in the transfected cells. HEK-293T cells were seeded at a density of 10000 cells/well on an 8-well chamber slide (Lab-Tek, Rochester, NY, polylysine treated) 24 h prior to transfection. Cy5-labeled siRNA was complexed with different **MPBPs** at an N/P of 10 and transfected to the cells under the aforementioned conditions. Confocal fluorescence microscopy was

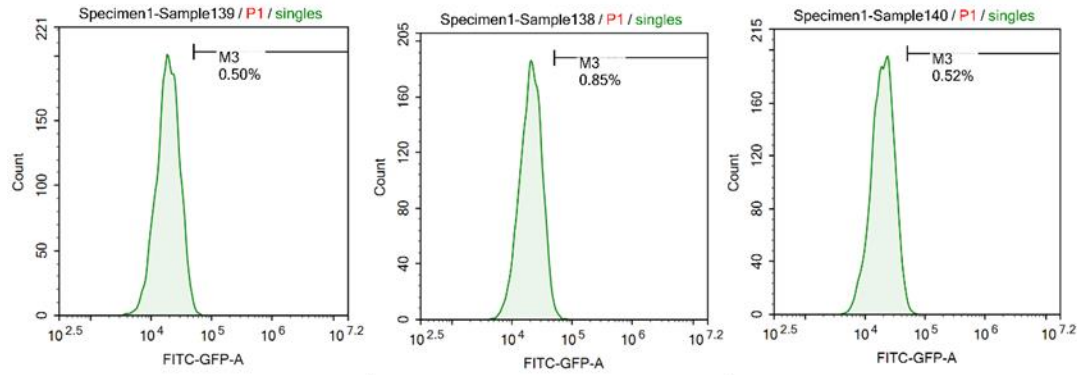
performed 24 h post-transfection. The endosome was stained with 75 nM LysoTracker® Blue probes (200 µL per well).

(3) All confocal images were acquired using a Zeiss LSM 700 inverted laser-scanning confocal microscope. A 20X plan apochromatic numerical aperture of 0.8 DIC II objective was used for cellular uptake imaging experiments. A 63X oil objective was used for endosomal escape imaging experiments. A 639 nm laser and a 606-700 nm band-pass filter were used to obtain the images of Cy5-labelled mRNA. A 405 nm laser and a 400-498 nm band-pass filter were used to obtain the images of the Hoechst 33342 counter-stained nuclei. The fluorescent images were scanned separately and overlaid together with the differential interference contrast image (DIC). The cells were scanned as a z-stack of two-dimensional images (1024×1024 pixels) and an image cutting approximately through the middle of the cellular height was selected to present the intracellular RNA localization.

2.13 Flow cytometry Output

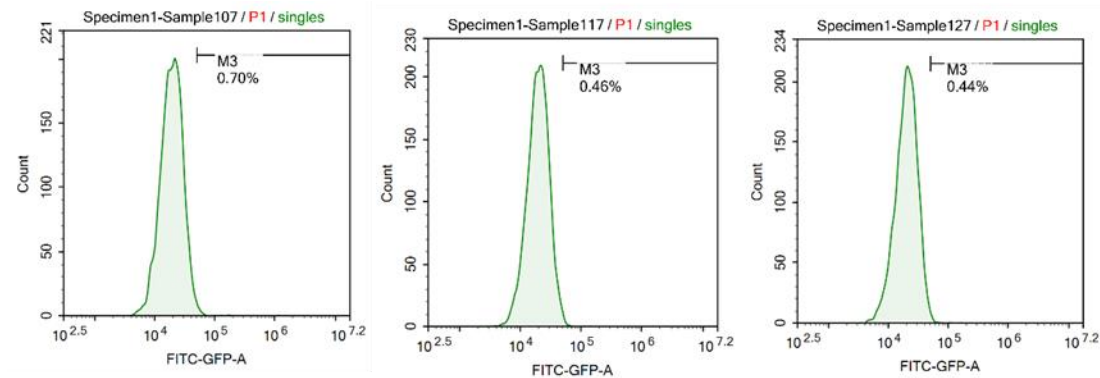
(1) eGFP mRNA transfection in serum-free media

Untreated



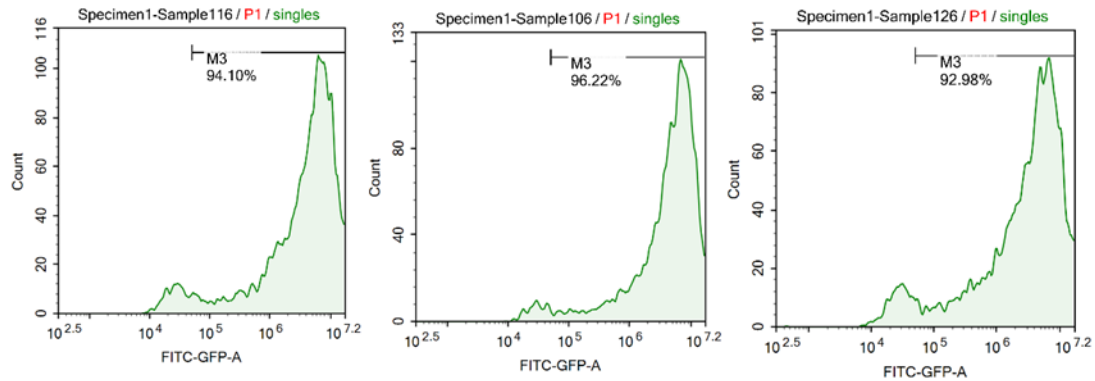
Sample	Count	% of All	Mean FITC-GFP
1	5000	0.50	22410
2	5000	0.85	20908
3	5000	0.52	21544

mRNA only



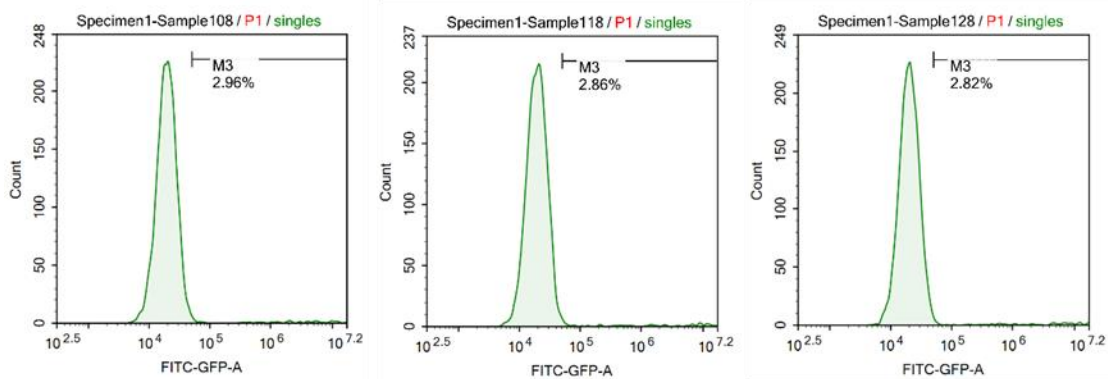
Sample	Count	% of All	Mean FITC-GFP
1	5000	0.70	21356
2	5000	0.46	21457
3	5000	0.44	22012

LF MM



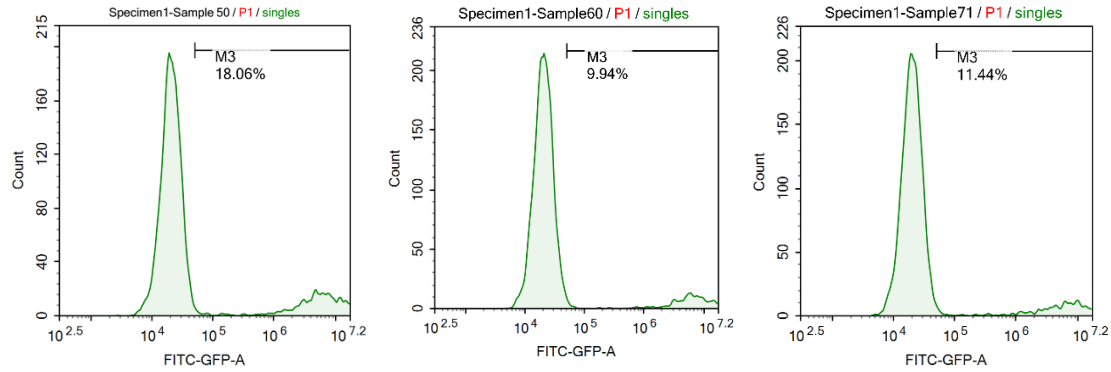
Sample	Count	% of All	Mean FITC-GFP
1	5000	94.10	6324327
2	5000	96.22	6092067
3	5000	92.98	5234940

G0-100LP



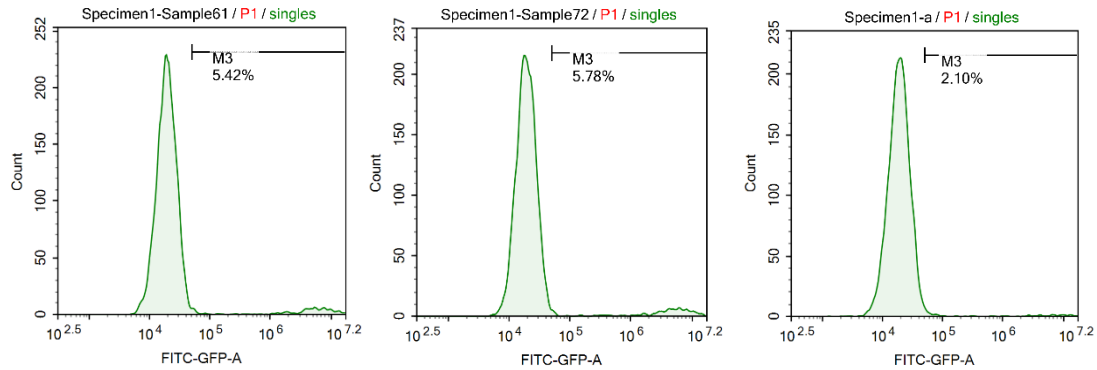
Sample	Count	% of All	Mean FITC-GFP
1	5000	2.96	143835
2	5000	2.86	156423
3	5000	2.82	161359

G0-20TEG-80LP



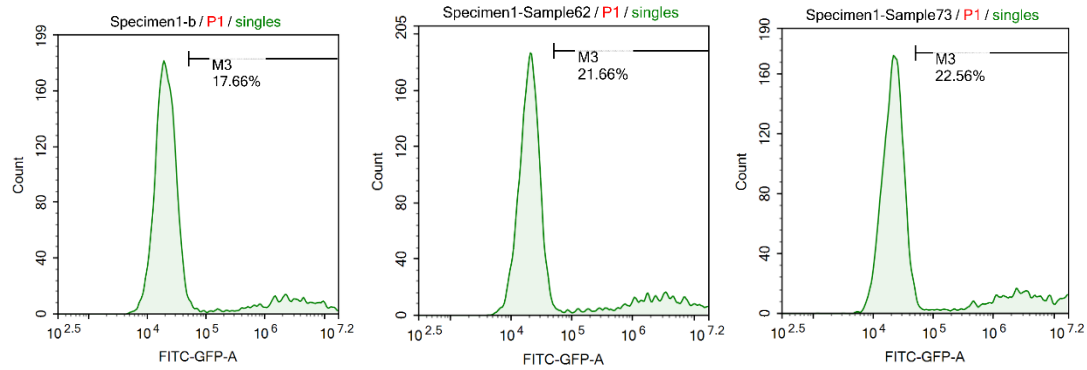
Sample	Count	% of All	Mean FITC-GFP
1	5000	18.06	1563883
2	5000	9.94	822601
3	5000	11.44	939790

G0-50TEG-50LP



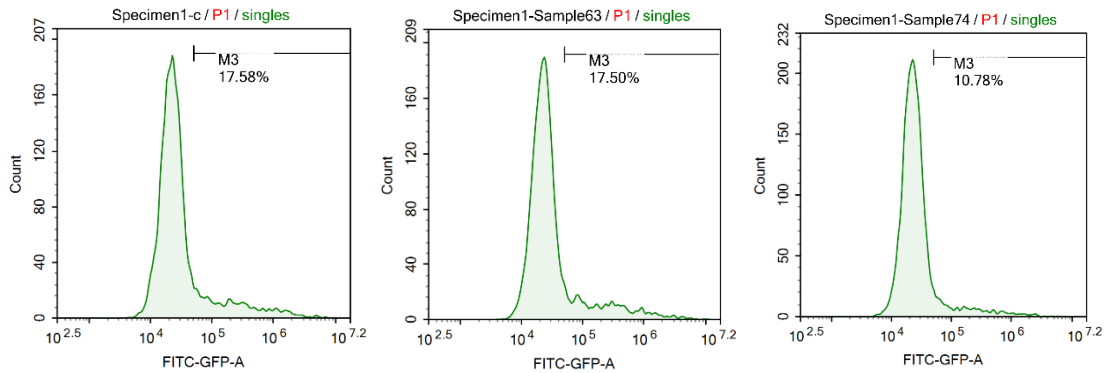
Sample	Count	% of All	Mean FITC-GFP
1	5000	5.42	61233
2	5000	5.78	80527
3	5000	2.10	121996

G0-20SA-80LP



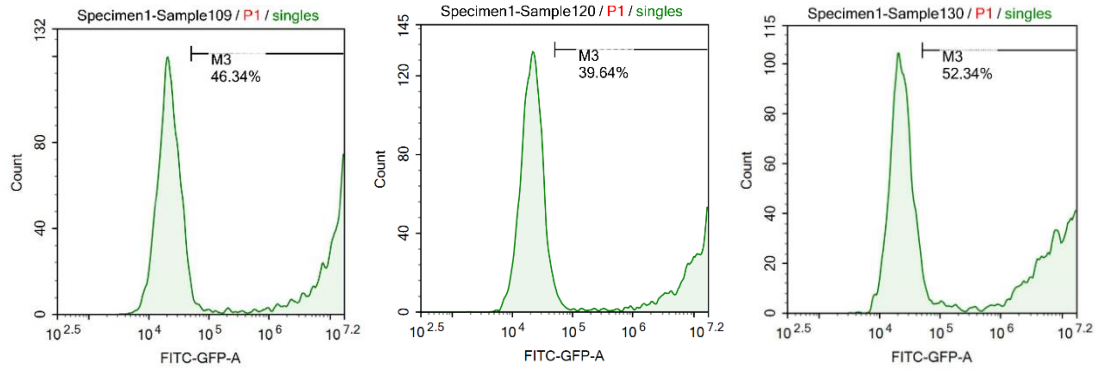
Sample	Count	% of All	Mean FITC-GFP
1	5000	17.66	756082
2	5000	21.66	1000737
3	5000	22.56	1161848

G0-50SA-50LP



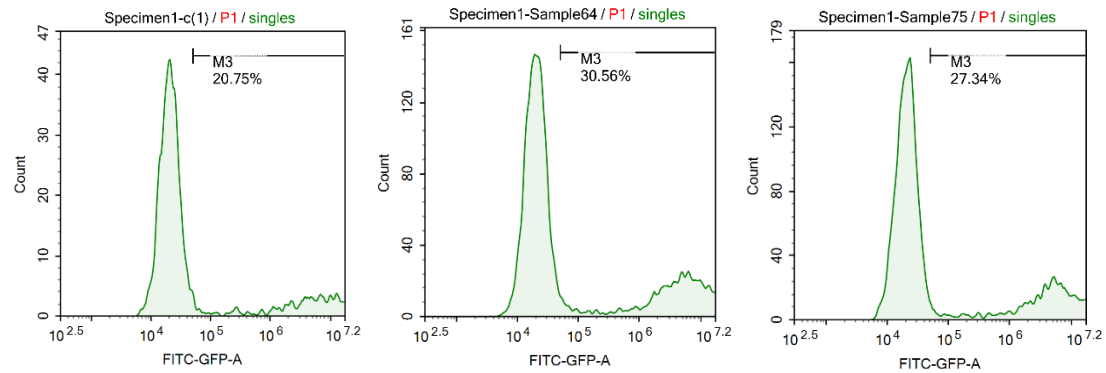
Sample	Count	% of All	Mean FITC-GFP
1	5000	17.58	116702
2	5000	17.50	123622
3	5000	10.78	70883

G1-100LP



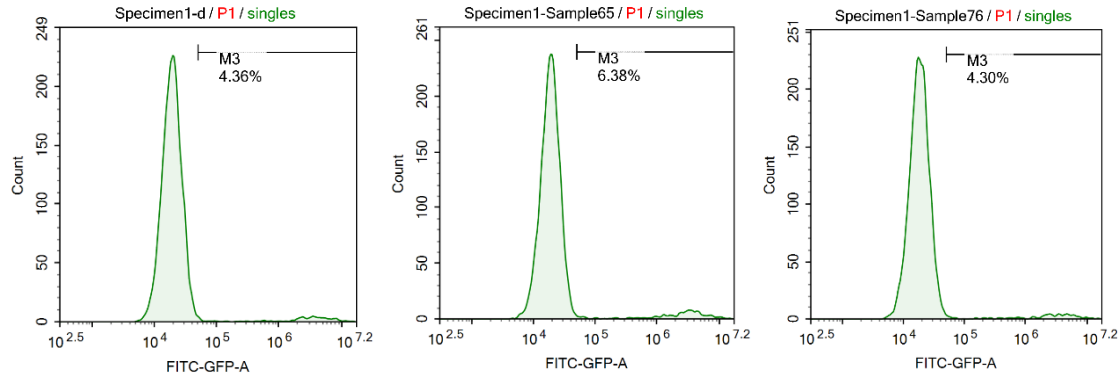
Sample	Count	% of All	Mean FITC-GFP
1	5000	46.34	7240389
2	5000	39.64	6094296
3	5000	52.34	7575724

G1-20TEG-80LP



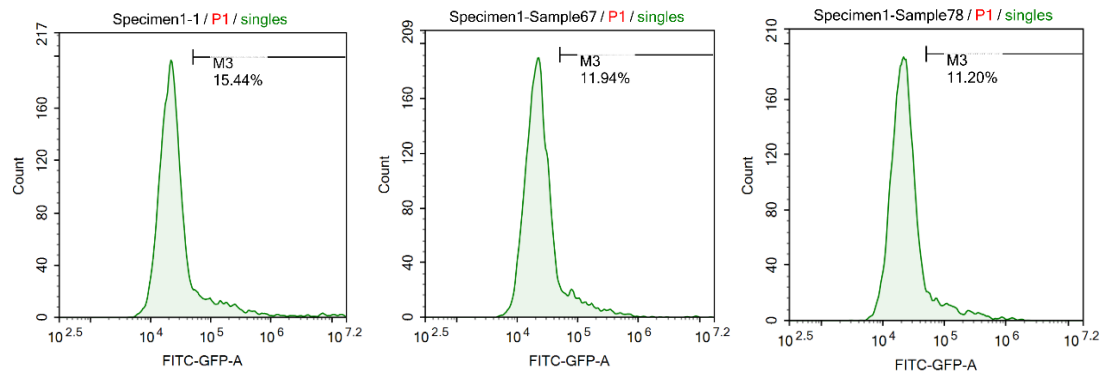
Sample	Count	% of All	Mean FITC-GFP
1	5000	20.75	1537838
2	5000	30.56	2214018
3	5000	27.34	1996336

G1-50TEG-50LP



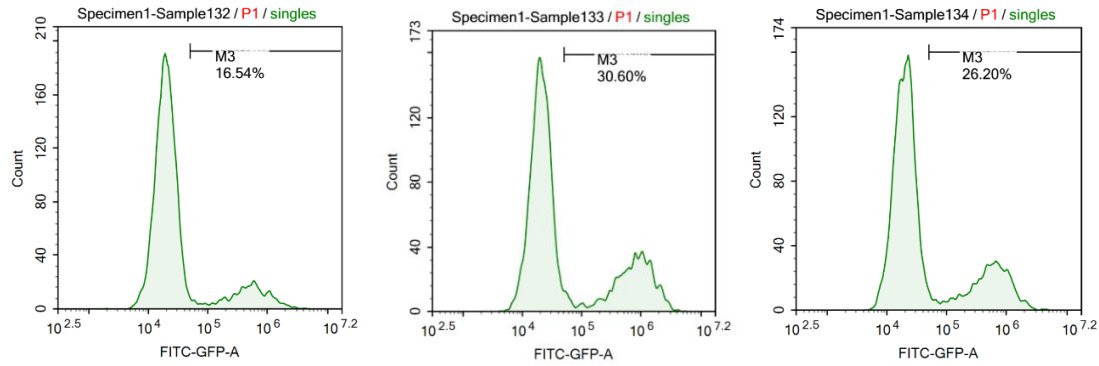
Sample	Count	% of All	Mean FITC-GFP
1	5000	4.36	188241
2	5000	6.38	247591
3	5000	4.30	168589

G1-20SA-80LP



Sample	Count	% of All	Mean FITC-GFP
1	5000	15.44	152264
2	5000	11.94	74424
3	5000	11.20	42282

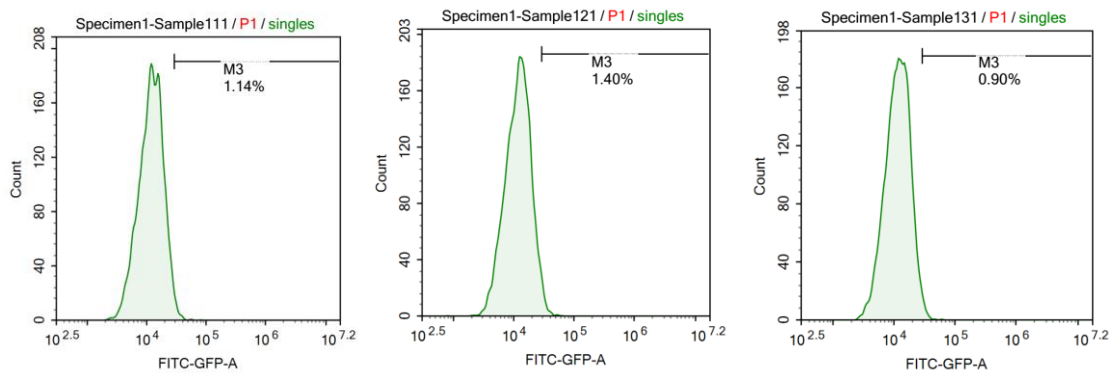
G2-100LP



Sample	Count	% of All	Mean FITC-GFP
1	5000	16.54	122083
2	5000	30.60	293665
3	5000	26.20	190229

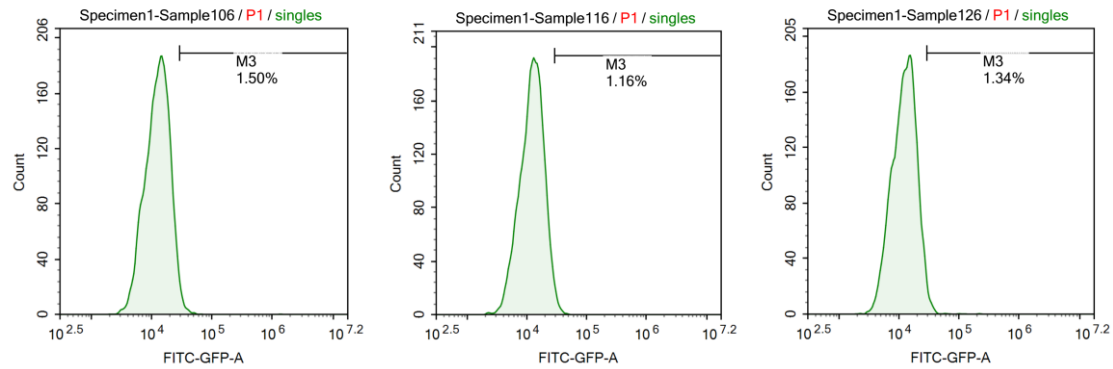
(2) eGFP mRNA transfection in 10% FBS-containing media

Untreated



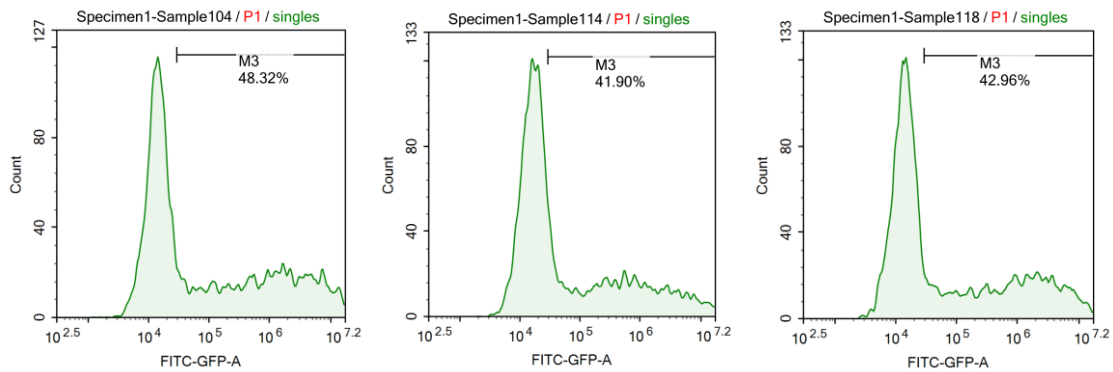
Sample	Count	% of All	Mean FITC-GFP
1	5000	1.14	18735
2	5000	1.40	13250
3	5000	0.90	12835

mRNA only



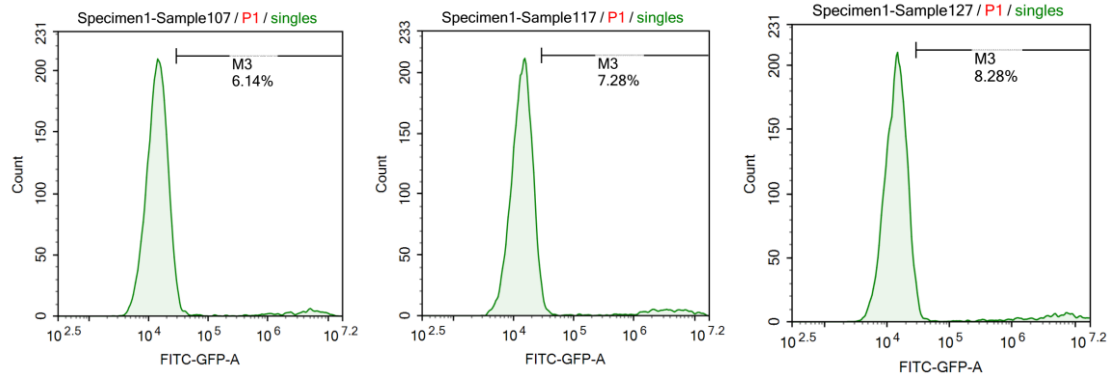
Sample	Count	% of All	Mean FITC-GFP
1	5000	1.50	14210
2	5000	1.16	13471
3	5000	1.34	13791

LF MM



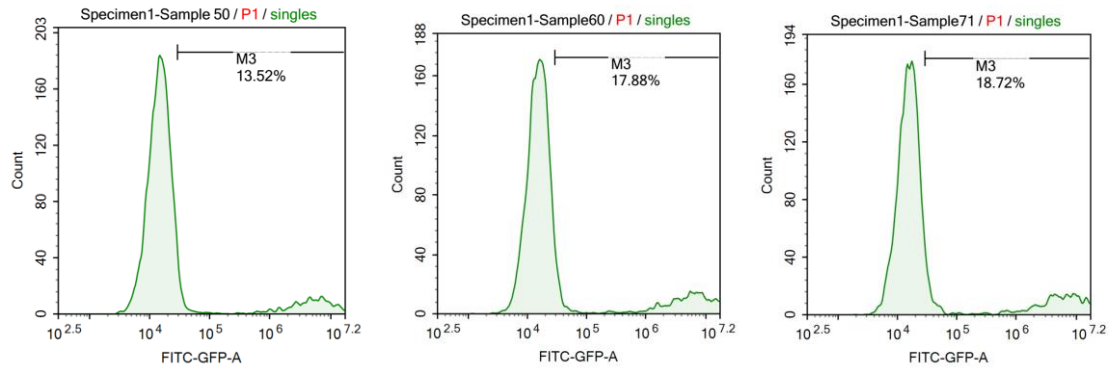
Sample	Count	% of All	Mean FITC-GFP
1	5000	48.32	1582084
2	5000	41.90	893936
3	5000	42.96	1126860

G0-100LP



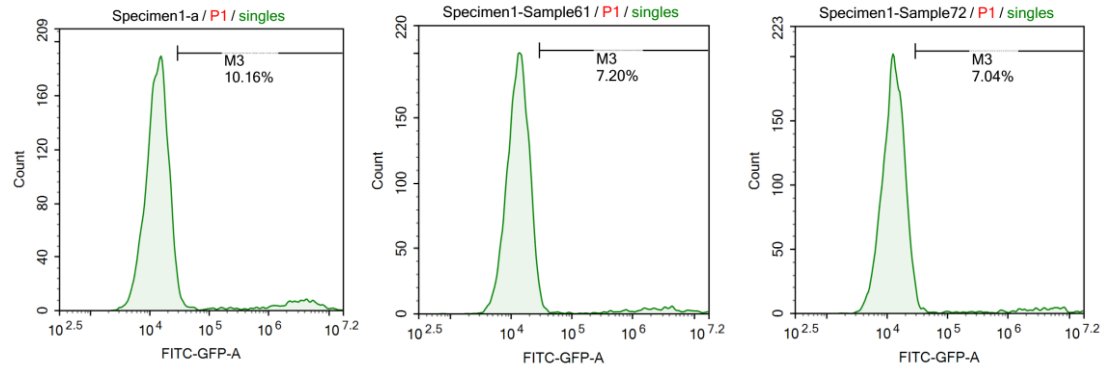
Sample	Count	% of All	Mean FITC-GFP
1	5000	6.14	225490
2	5000	7.28	297331
3	5000	8.28	400630

G0-20TEG-80LP



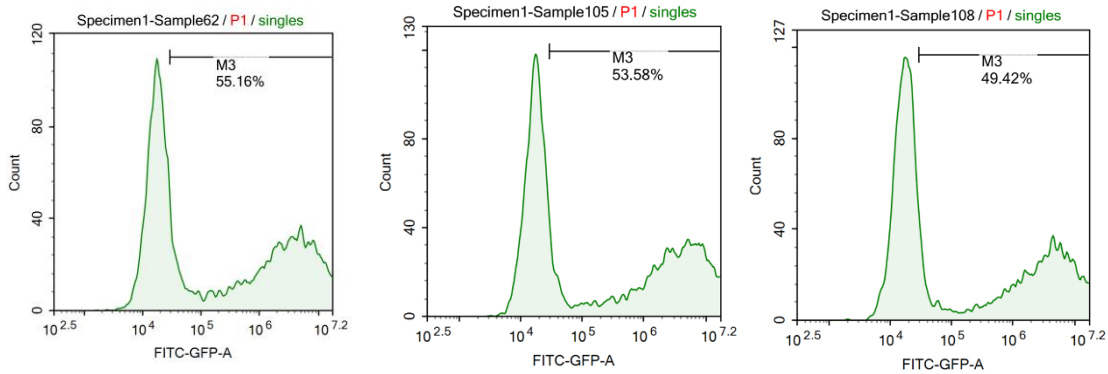
Sample	Count	% of All	Mean FITC-GFP
1	5000	13.52	685989
2	5000	17.88	958579
3	5000	18.72	1049797

G0-50TEG-50LP



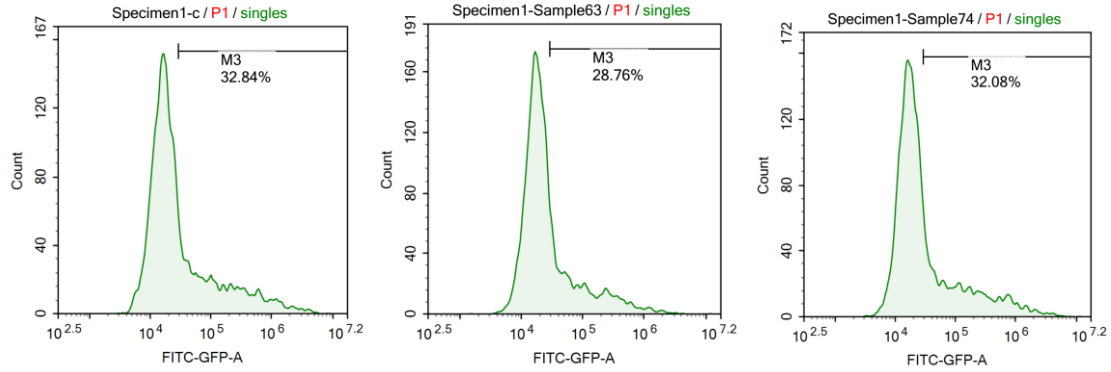
Sample	Count	% of All	Mean FITC-GFP
1	5000	10.16	298567
2	5000	7.20	235771
3	5000	7.04	261280

G0-20SA-80LP



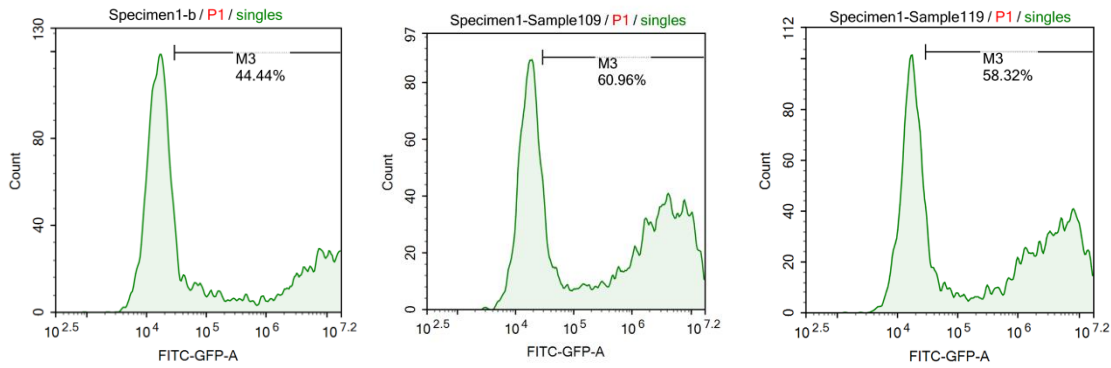
Sample	Count	% of All	Mean FITC-GFP
1	5000	55.16	2268149
2	5000	53.58	2836431
3	5000	49.42	2532842

G0-50SA-50LP



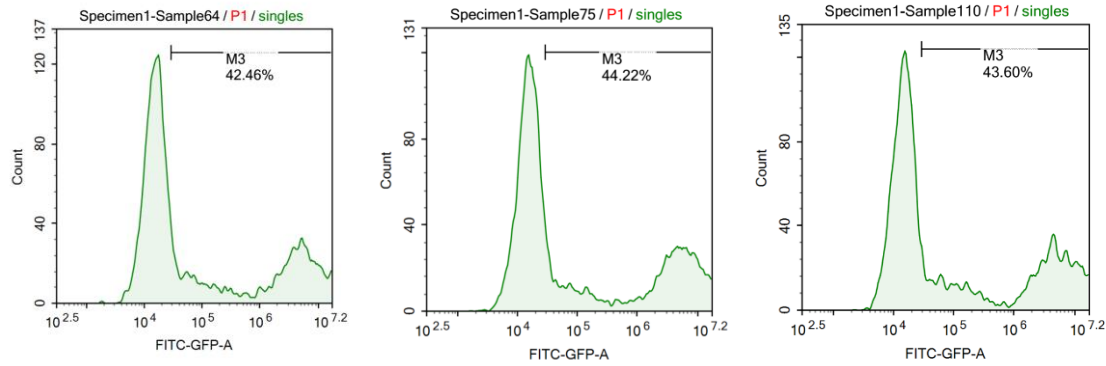
Sample	Count	% of All	Mean FITC-GFP
1	5000	32.84	143484
2	5000	28.76	81912
3	5000	32.08	137334

G1-100LP



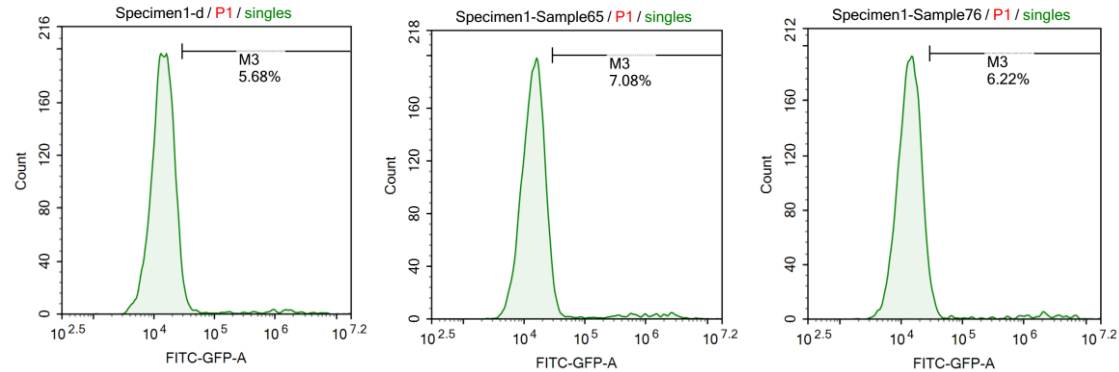
Sample	Count	% of All	Mean FITC-GFP
1	5000	44.44	3077175
2	5000	60.96	2631080
3	5000	58.32	2831390

G1-20TEG-80LP



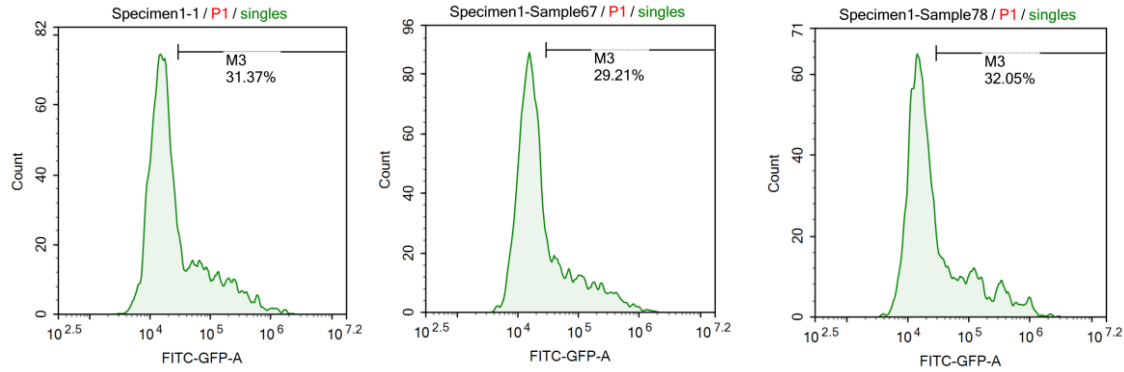
Sample	Count	% of All	Mean FITC-GFP
1	5000	42.46	2075207
2	5000	44.22	2084895
3	5000	43.60	2398933

G1-50TEG-50LP



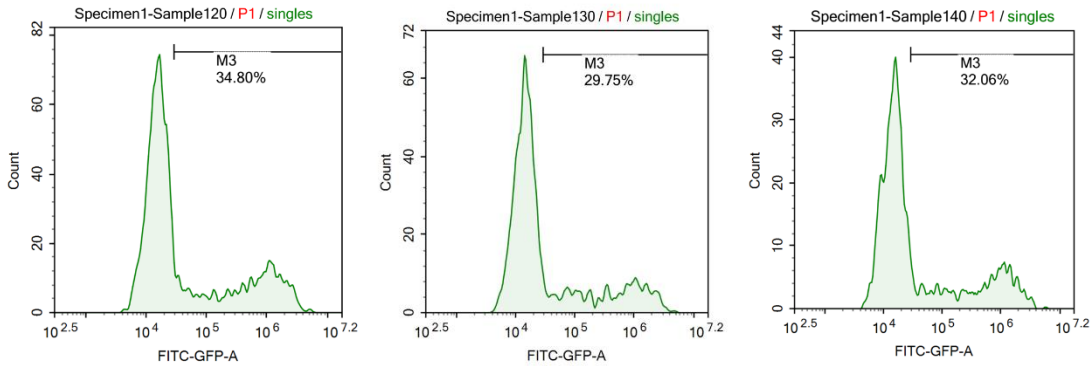
Sample	Count	% of All	Mean FITC-GFP
1	5000	5.68	71726
2	5000	7.08	88078
3	5000	6.22	107803

G1-20SA-80LP



Sample	Count	% of All	Mean FITC-GFP
1	5000	31.37	72255
2	5000	29.21	63708
3	5000	32.05	85301

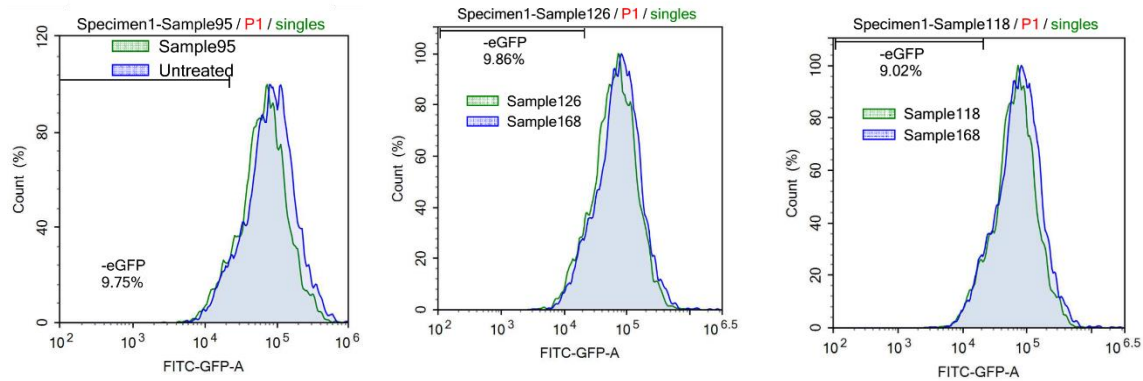
G2-100LP



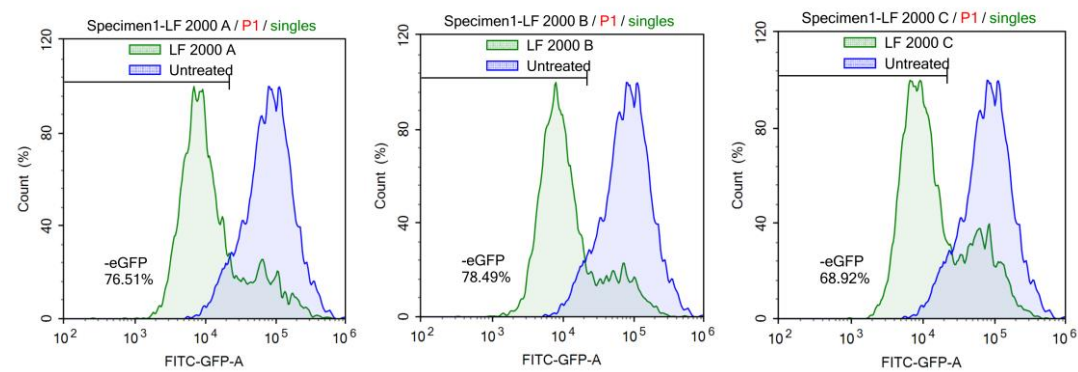
Sample	Count	% of All	Mean FITC-GFP
1	5000	34.80	316001
2	5000	29.75	240382
3	5000	32.06	268352

(3) Co-delivery of Cas9 mRNA and sgRNA

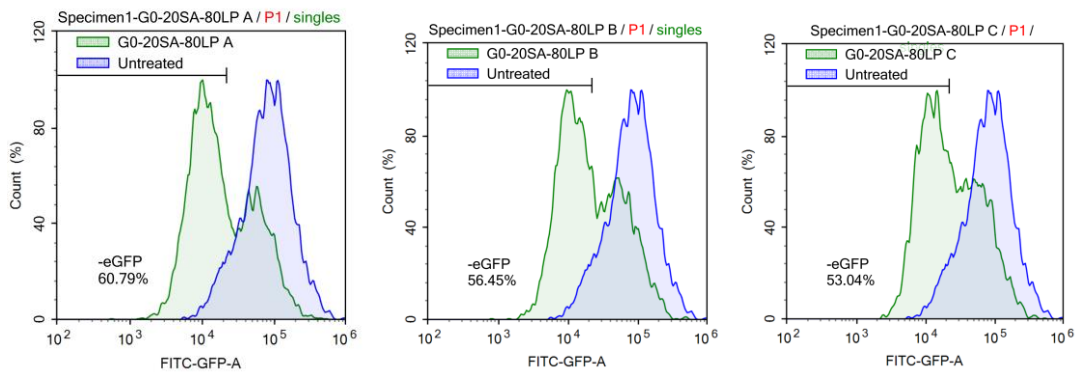
Cas9 mRNA/sgRNA only



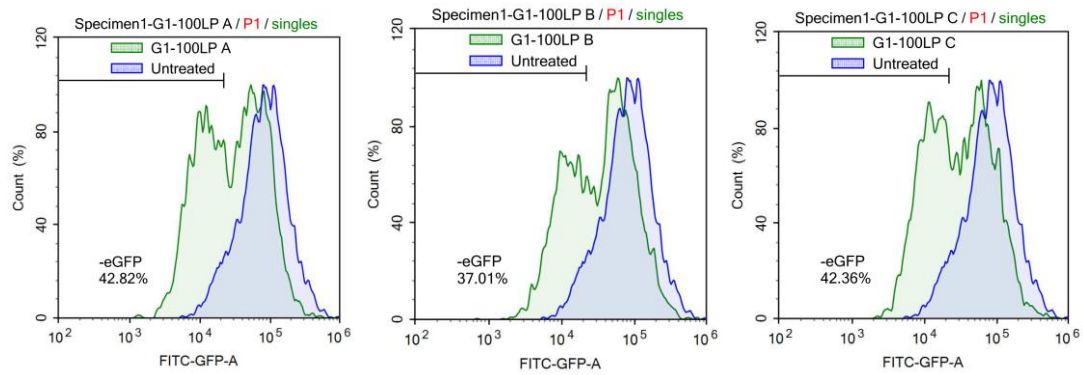
LF 2000



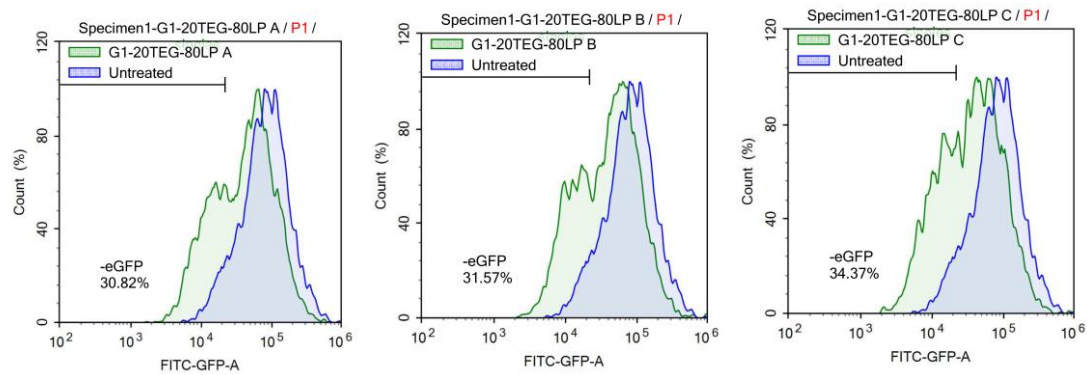
G0-20SA-80LP



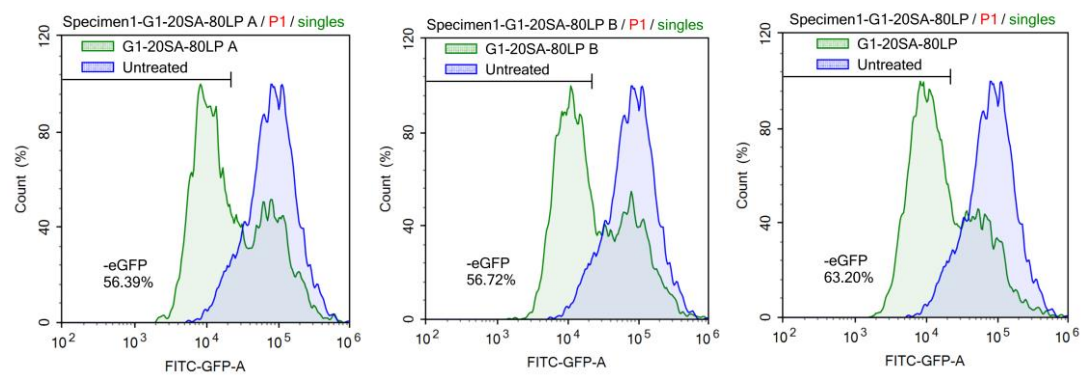
G1-100LP



G1-20TEG-80LP

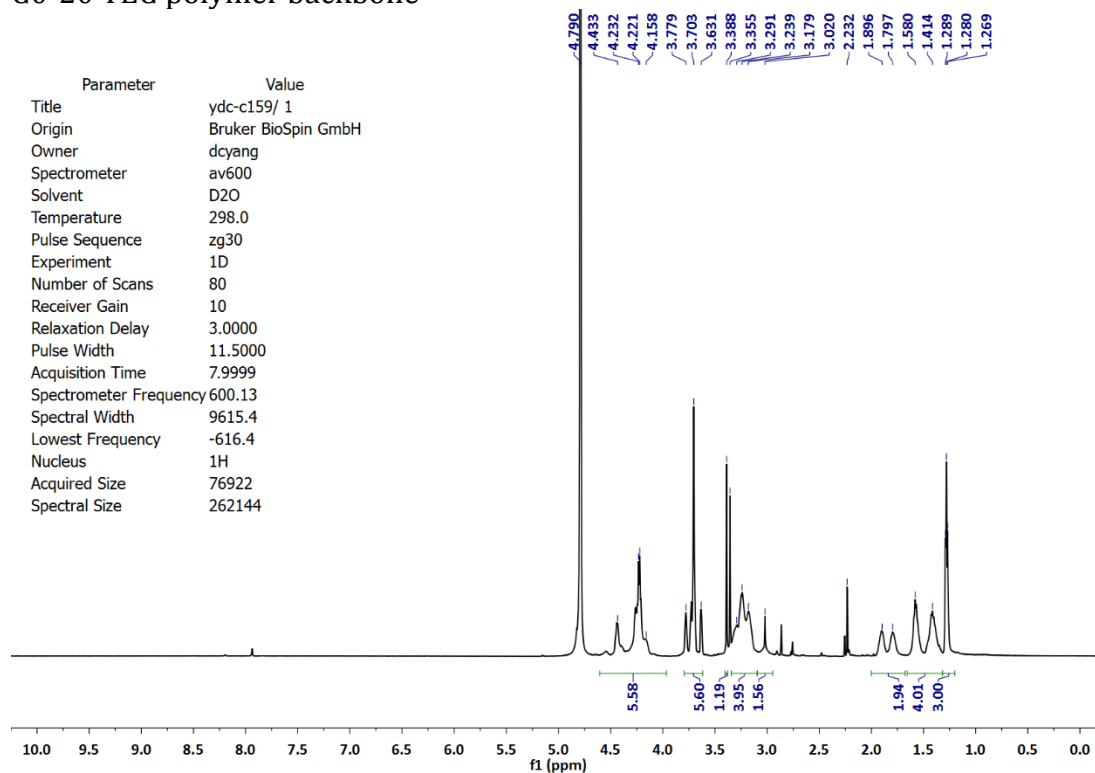


G1-20SA-80LP

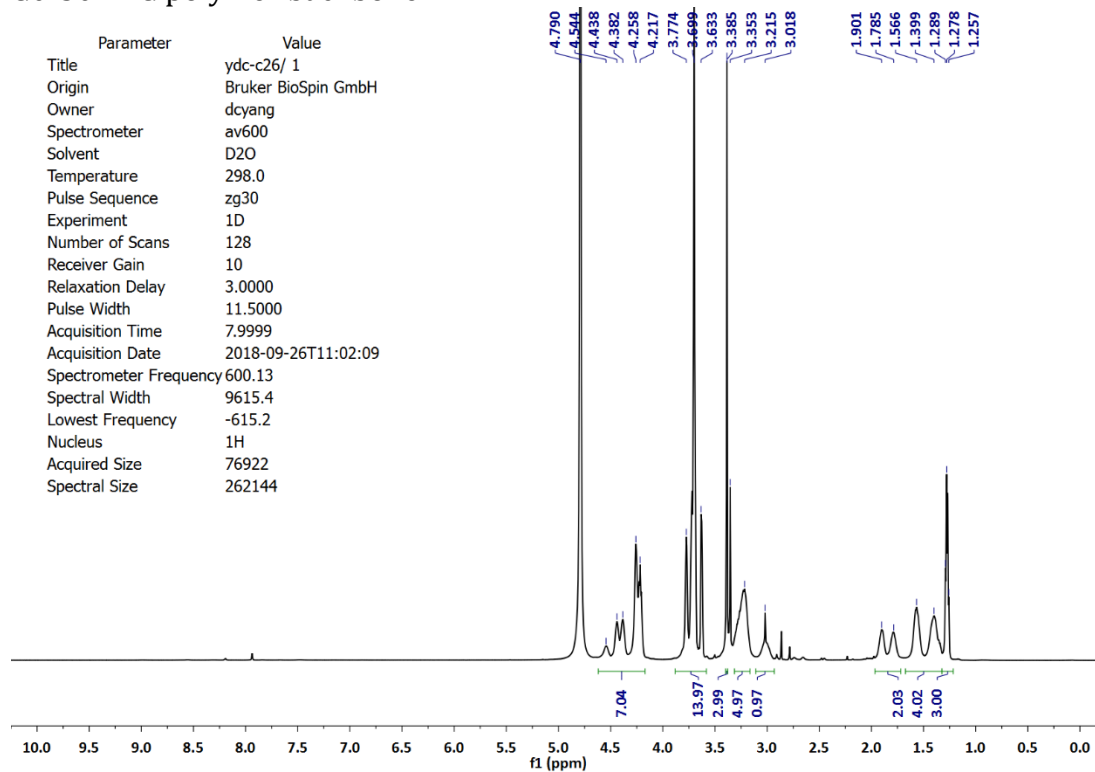


2.14 ¹H NMR Spectra

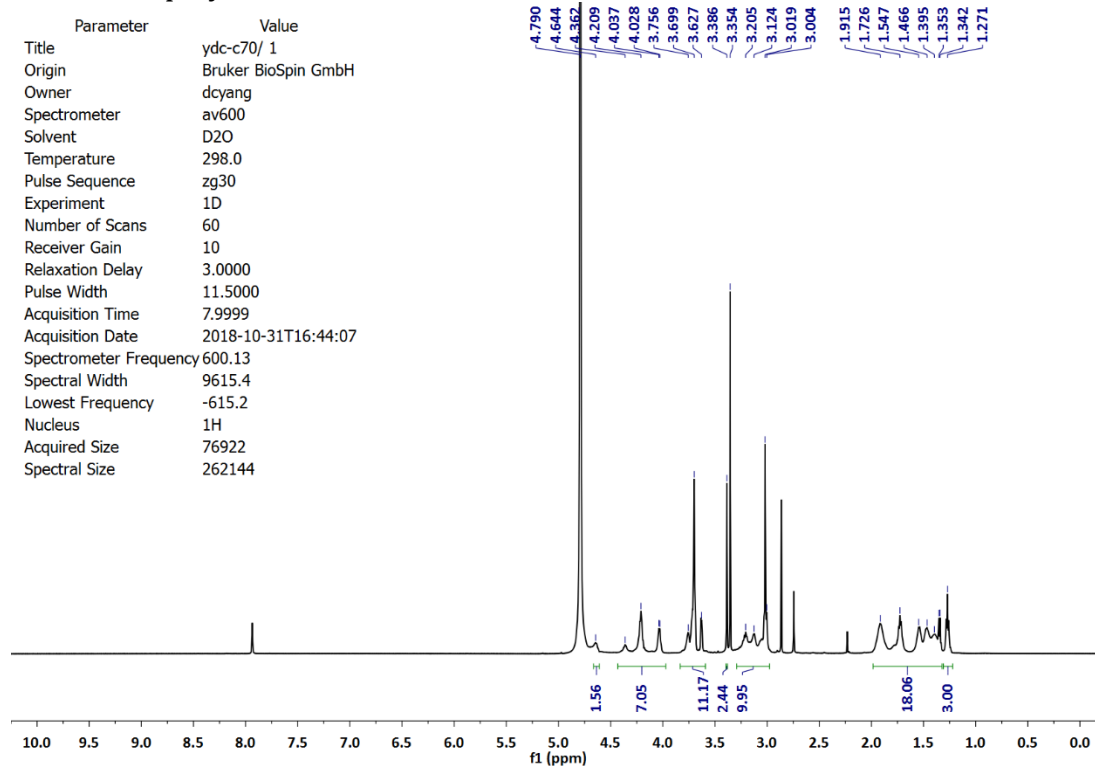
G0-20 TEG polymer backbone



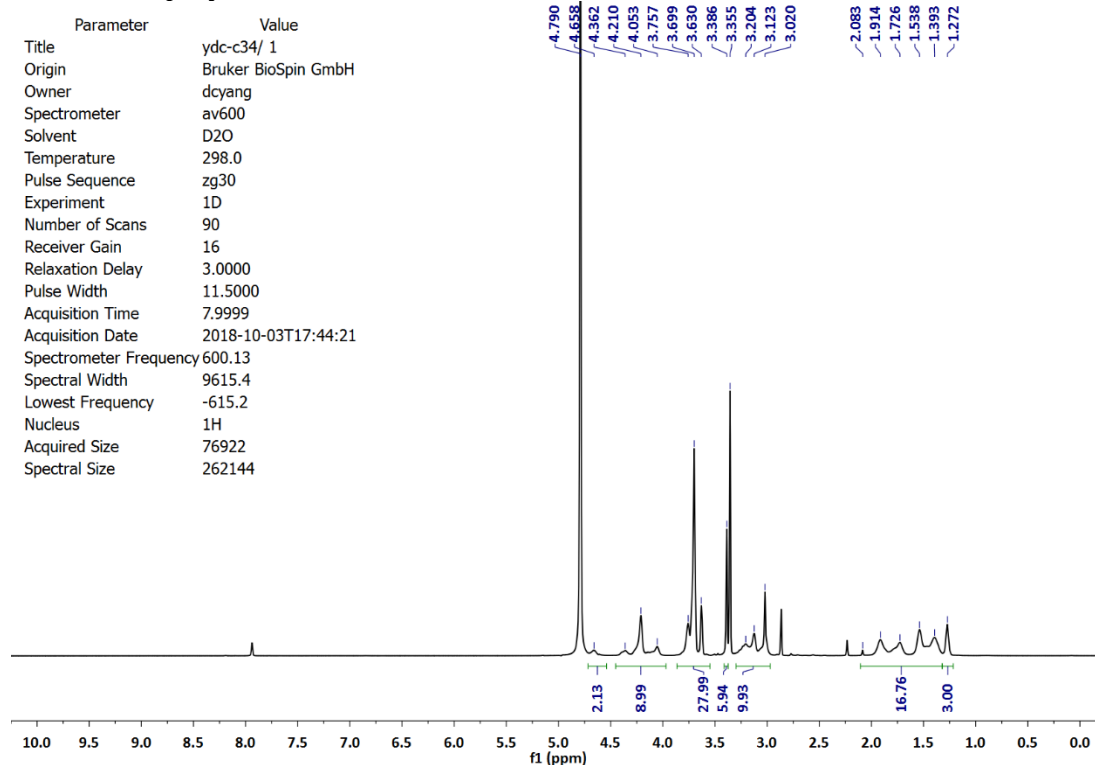
G0-50 TEG polymer backbone



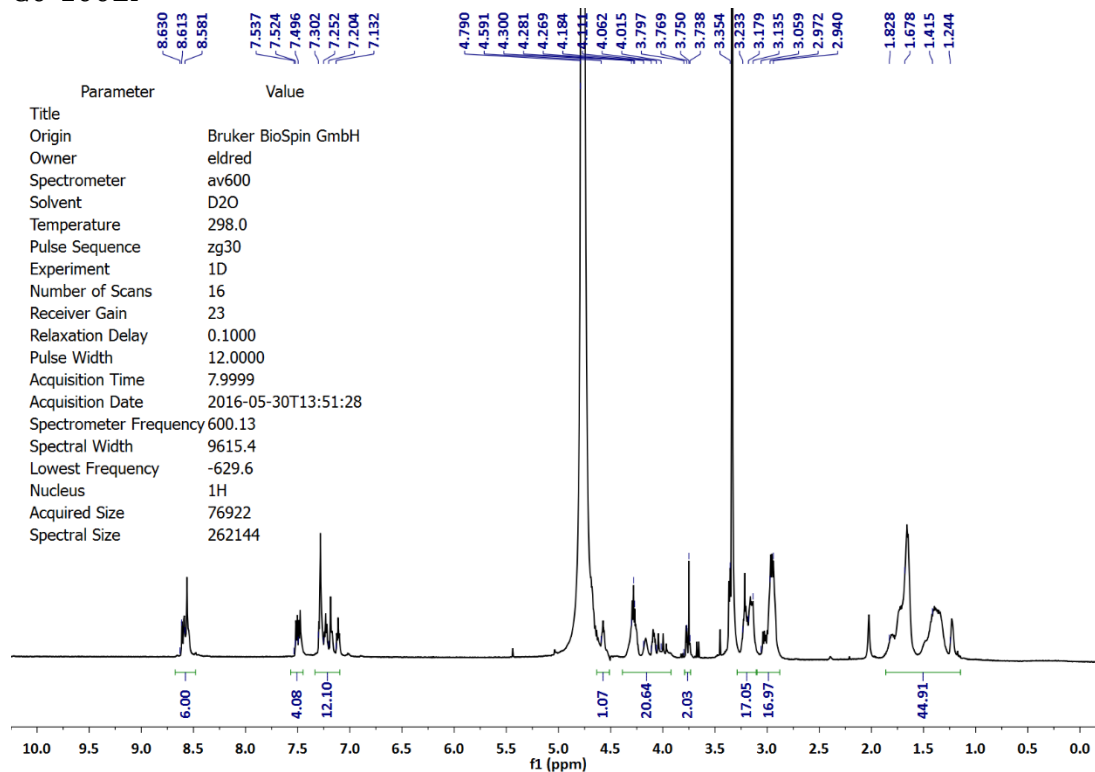
G1-20 TEG polymer backbone



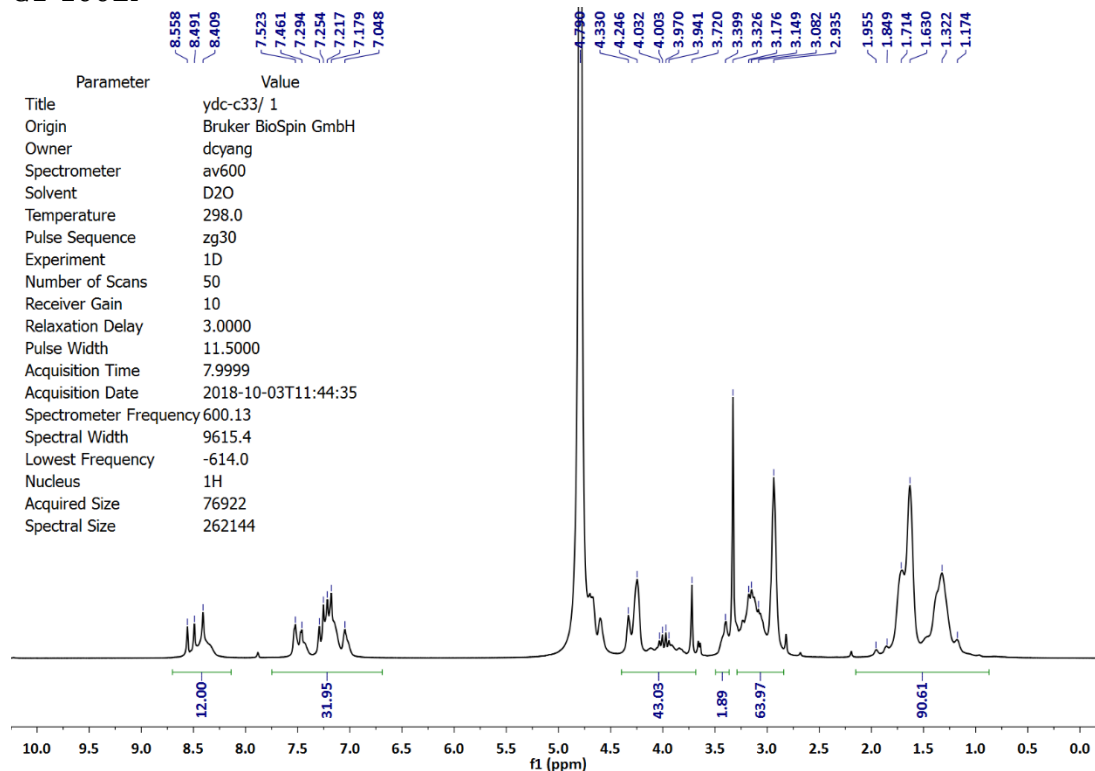
G1-50 TEG polymer backbone



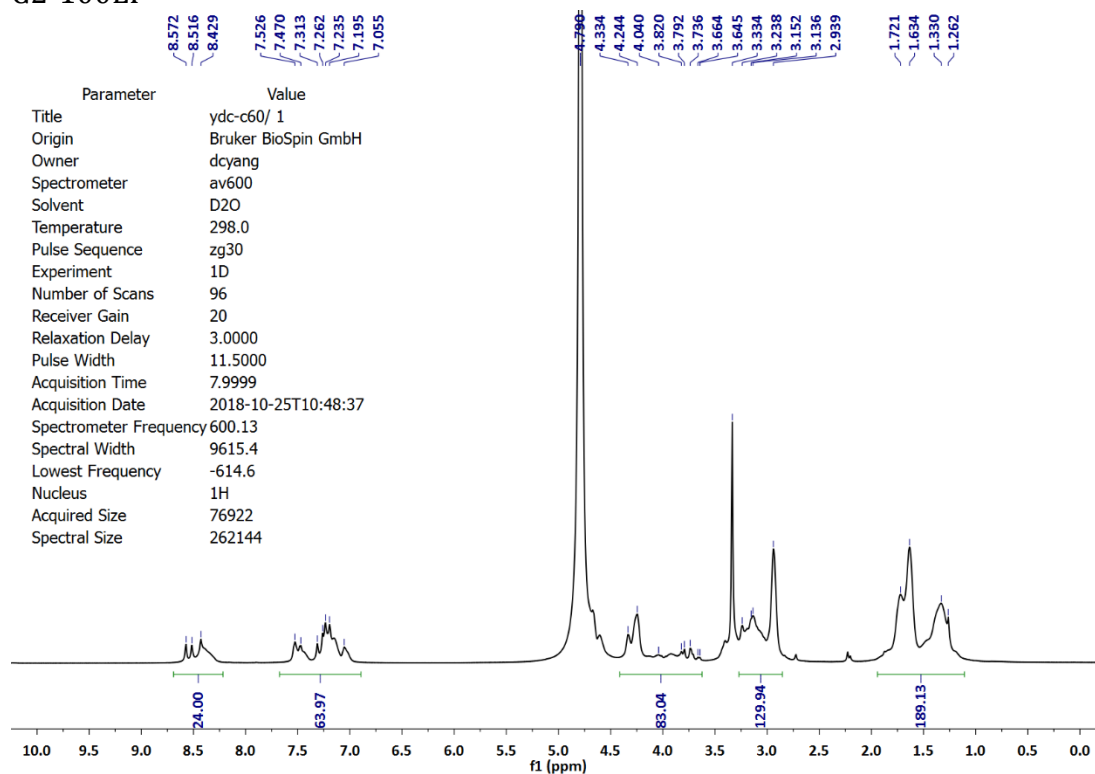
G0-100LP



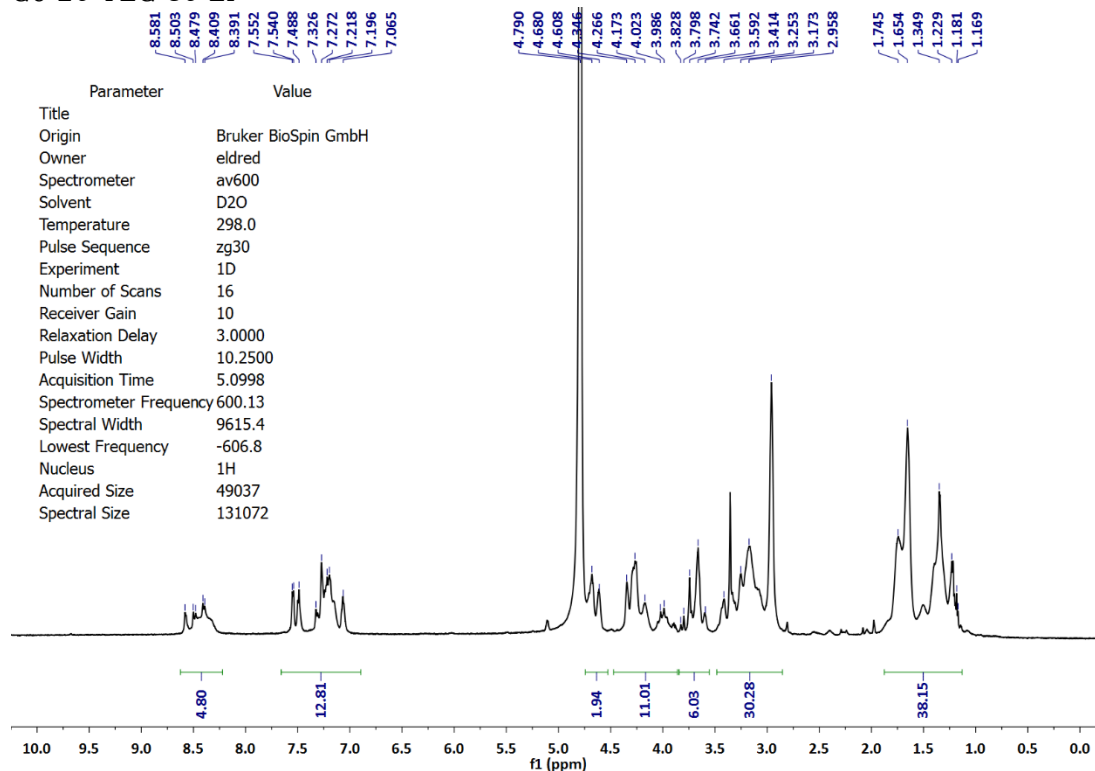
G1-100LP



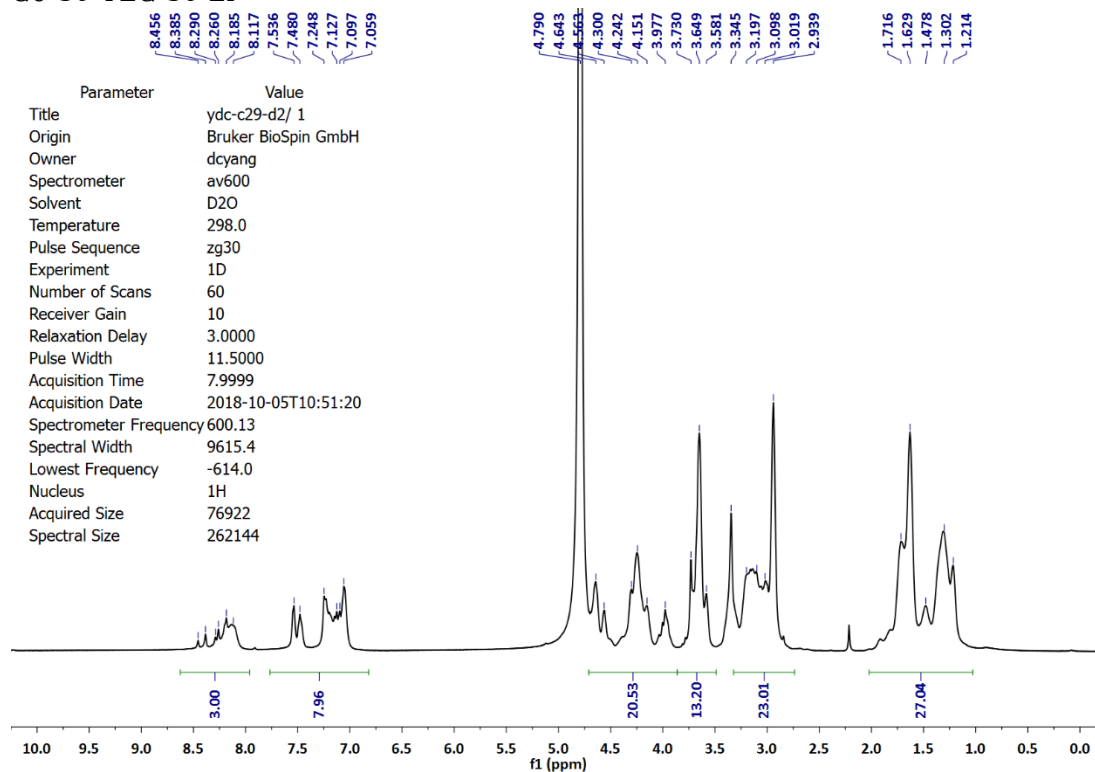
G2-100LP



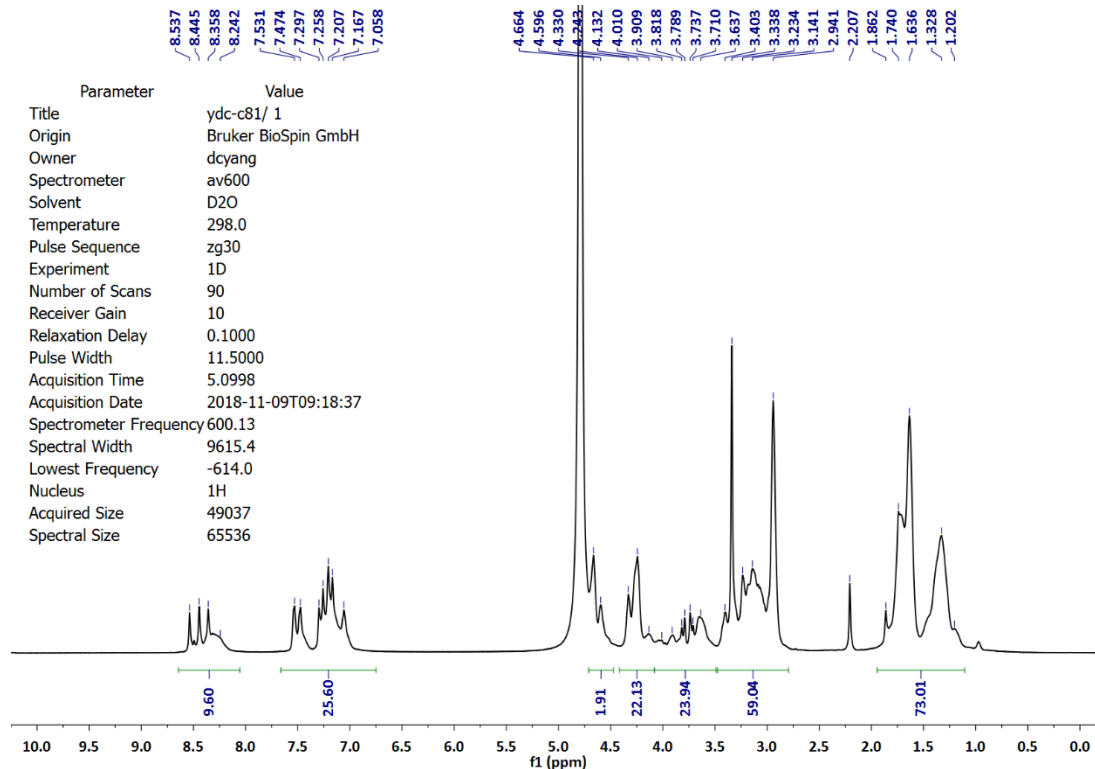
G0-20 TEG-80 LP



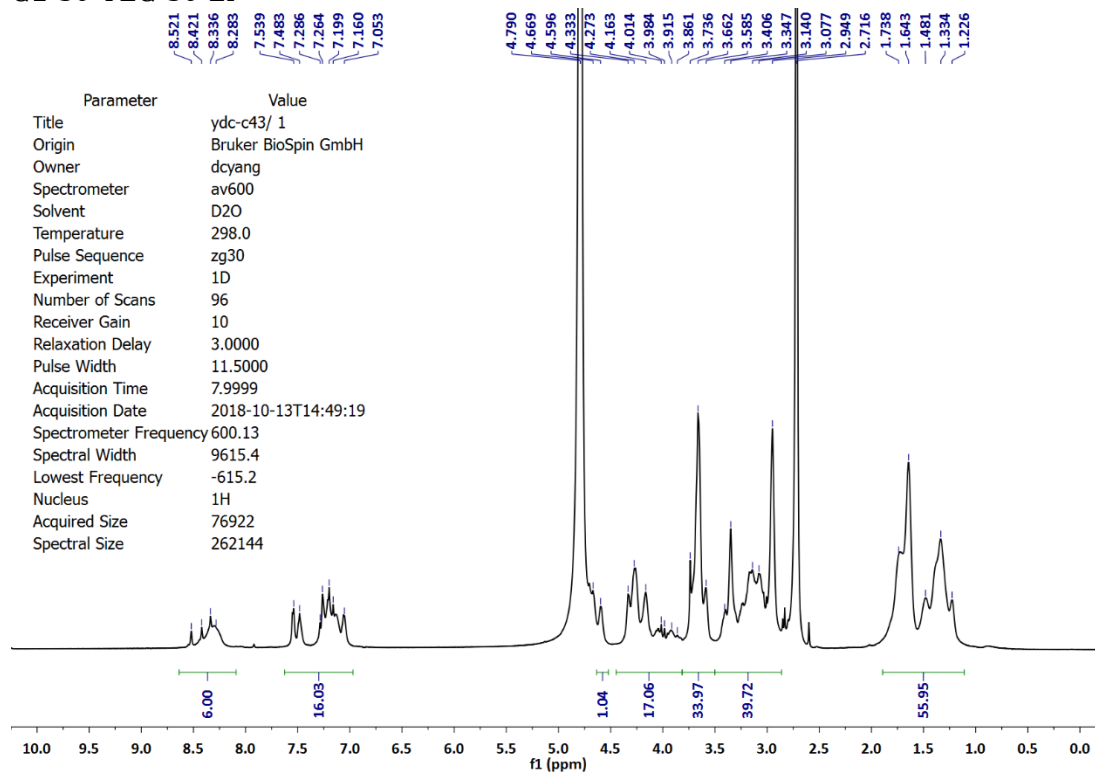
G0-50 TEG-50 LP



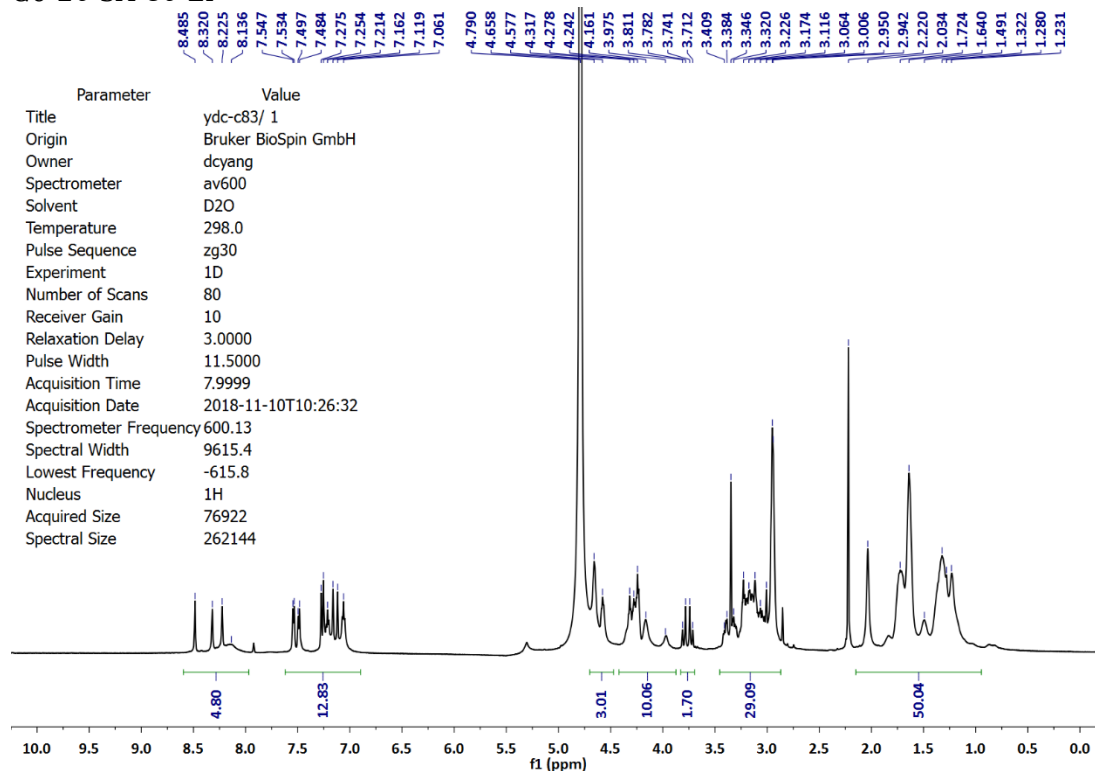
G1-20 TEG-80 LP



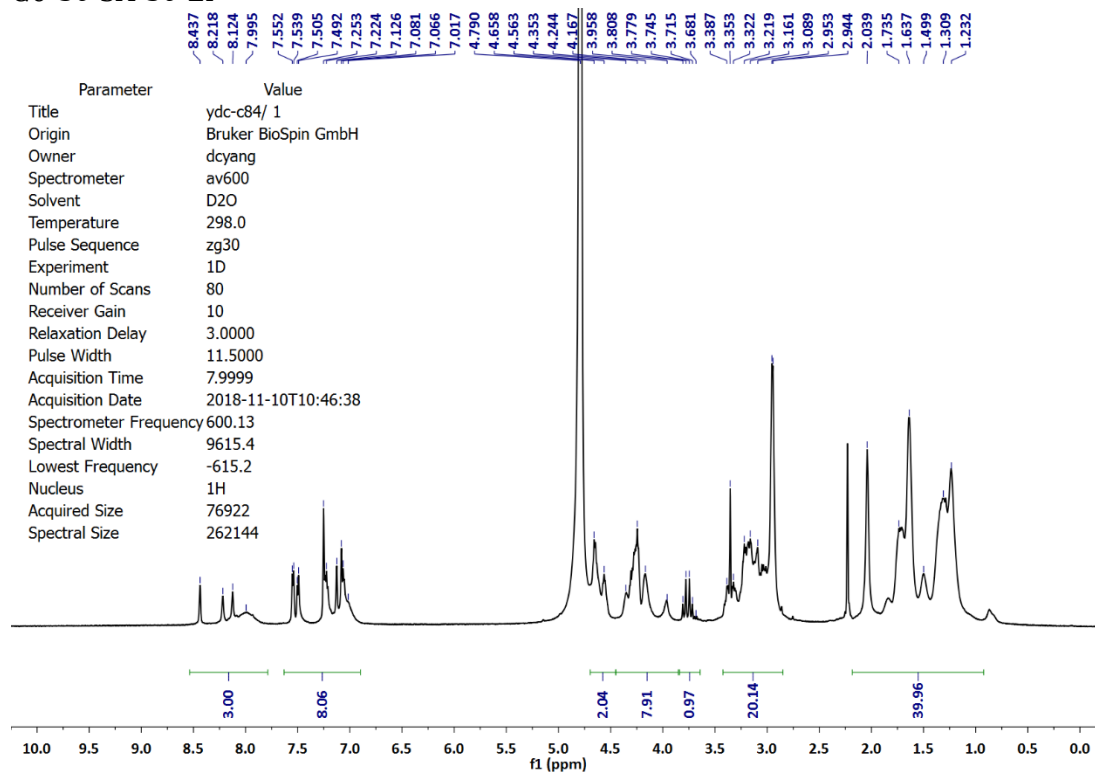
G1-50 TEG-50 LP



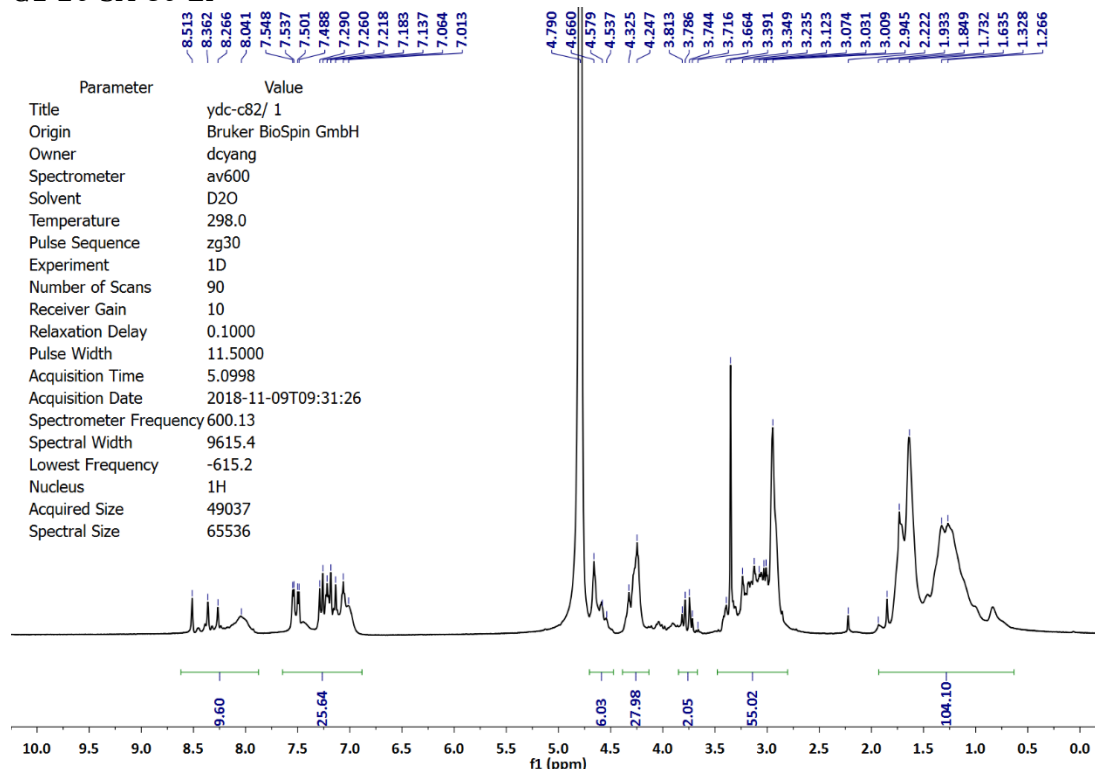
G0-20 SA-80 LP



G0-50 SA-50 LP



G1-20 SA-80 LP



Chapter 3: Peptide-functionalized Bio reducible Amphiphilic Vectors for siRNA Delivery

3.1 Introduction and Project Design

As introduced in **Section 1.2**, RNAi technology holds tremendous potential for therapeutic treatments.¹⁻³ However, the wide application of RNAi therapeutics has been greatly hampered by the lack of safe and efficient delivery methods.⁴⁻⁵ Due to the immunogenicity and size limitation of viral vectors,⁶ there is a large demand for the development of novel non-viral synthetic vectors for siRNA delivery. More importantly, a systematic study to elucidate the structure-property relationships is highly preferred to improve the rational design of synthetic vectors.

Guan lab recently developed a novel family of bolaamphiphiles for safe and effective siRNA delivery (**Section 1.8**).⁷⁻⁸ Besides delivering siRNA into conventional HEK and 3T3 cell lines, our lab realized efficient siRNA delivery into adipocytes by using the same bolaamphiphile system.⁹ Adipose tissue plays an important role in the development of obesity and obesity-associated diseases. Successful siRNA delivery in adipocytes provides the opportunity of gene therapy for obesity treatment.¹⁰⁻¹¹

The aforementioned siRNA delivery system mainly benefits from the unique structure design of 'bolaamphiphile': the hydrophobic core and two hydrophilic dendritic head groups. However, the dendritic head groups are statistically functionalized by different amino acids, which introduces heterogeneity in the vector structure. Further study of this system with dipeptide functionalization confirmed that the peptide head groups play multiple roles in siRNA delivery,⁸ including RNA complexation, facilitating cellular uptake, and enhancing endosomal escape. Moreover, according to numerous

studies about cell-penetrating peptides (**Section 1.7**),¹²⁻¹³ peptide functionalization can not only promote the interaction between vectors and cell membrane but also offer the possibility to realize targeting delivery.

In this work, a family of peptide-functionalized bio reducible amphiphilic vectors (**PBAV**) was systematically developed and studied, aiming to further explore the roles of different hydrophobic cores and hydrophilic peptide head groups in siRNA delivery.

3.2 Design and Synthesis of PBAV

Inspired by our previous dendritic bolaamphiphile system (**Section 1.8**),⁷⁻⁸ we designed a series of novel peptide-functionalized bio reducible amphiphilic vectors (**PBAV**) for effective siRNA delivery (**Figure 3.1**). Instead of using statistically functionalized lysine dendrons in the amphiphilic structure, we utilized short linear peptides as the hydrophilic head groups. This can reduce the structural heterogeneity of the delivery vectors and guide us to further explore the correlation between chemical structure and biological function. Additionally, as shown for some cell-penetrating peptide system, peptides can form secondary structures which promote the interaction between delivery vectors and cell membrane.¹²⁻¹⁵

Therefore, short linear peptide head groups were conjugated onto different hydrophobic cores through conventional amide-coupling chemistry, affording different peptide-functionalized bolaamphiphiles and monoamphiphiles. Both fluorocarbon core and hydrocarbon core were incorporated into these two systems in order to study the influence of different hydrophobicity.¹⁶⁻¹⁷ Bio reducible disulfide linkages were also incorporated to

link the hydrophobic cores and hydrophilic head groups, aiming to provide stimuli-responsive activity in the cytoplasm and enhance biocompatibility.¹⁸

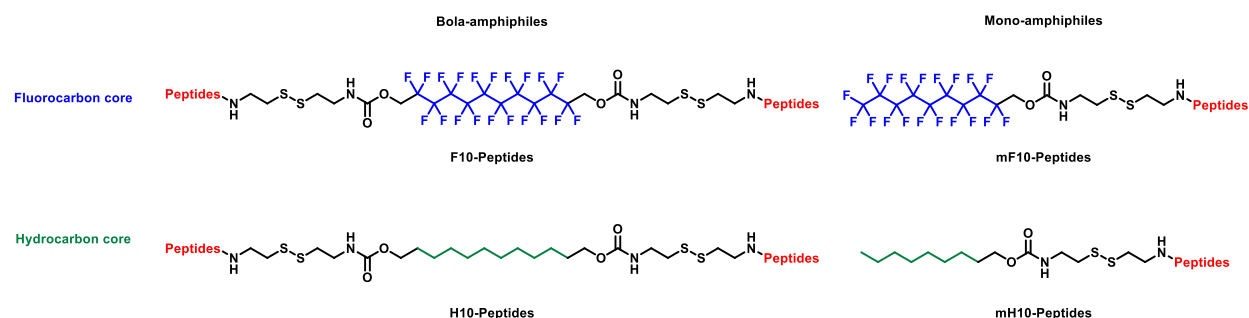


Figure 3.1 The designed library of **PBAVs** with different hydrophobic cores and peptide-functionalization.

Similar to the peptide design of **MPBP** vectors described in Chapter 2, three amino acids, L-histidine (His), L-lysine (Lys), and L-tryptophan (Trp), were utilized to construct the functional peptides. His is used to provide buffering capacity which is essential for promoting endosomal escape.¹⁹ Protonated primary amines on Lys can provide cationic charges to complex with negatively charged siRNA cargos. Trp is incorporated to improve RNA binding through the intercalation of the indole ring.²⁰ It is also known that Trp can provide favorable hydrophobic interaction with cell membrane which promotes cellular uptake.²¹ Furthermore, in order to study the influence of individual amino acid and peptide sequences, different short linear peptides were designed, synthesized, and utilized to functionalize the hydrophobic cores (**Table 3.1**). First, four units of cationic charges, offered by three Lys side chains and one N-terminal primary amine, were introduced in each peptide. This was designed to mimic the +4 charges in our previous bolaamphiphile system.⁷ Second, alternative peptide sequences, which could possibly generate peptide secondary structure, were designed to compare with block peptide sequences. In addition,

in order to further study the function of Trp, peptides with different Trp position (internal position and terminal position) and existence were constructed.

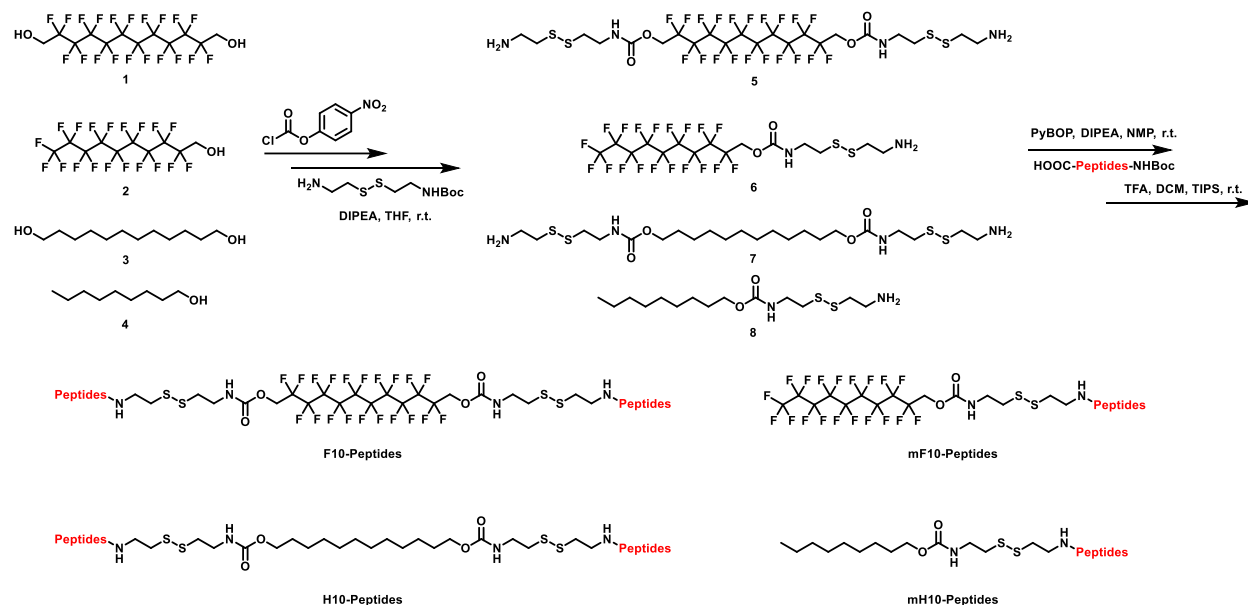
Table 3.1 Chemical structures of **PBAV** library with different hydrophobic cores and peptide-functionalization. √ indicates completed synthesis, characterization, and full study. — indicates that the vectors were skipped for study due to the insufficient delivery efficacy for hydrocarbon vectors.

Peptide Sequence	Bola-F10	Mono-F10	Bola-H10	Mono-H10
GHHHKKKW	√	√	√	√
GHKHKHKW	√	√	√	√
GWHHHKKK	√	√	—	—
GWHKHKHK	√	√	—	—
GHHHKKK	√	√	—	—
GHKHKHK	√	√	—	—

The synthetic route of the designed **PBAVs** is shown in **Scheme 3.1**. After activated by 4-nitrobenzyl chloroformate, the fluorocarbon or hydrocarbon alcohols were conjugated to mono-Boc protected cystamine through a carbonate linker, affording four types of hydrophobic cores (hydrocarbon and fluorocarbon, monoamphile and bolaamphiphile) with disulfide handles. On the other hand, functional linear peptides were synthesized via well-established solid phase peptide synthesis.²² After cleavage from the resin, the side-chain protected peptides were coupled with the obtained hydrophobic cores. Then a global deprotection was performed to remove all protection groups. The final products were purified via C18 reverse phase column and characterized by analytical HPLC and MALDI-MS (**Section 3.7**). For simplicity, the **PBAVs** were named using the hydrophobic cores with the sequences of functional peptides (from C-terminus to N-terminus). For instance, **F10-GHHHKKKW** represents a F10 core with GHHHKKKW

peptide functionalization on both sides. **mH10-GHKHKHKW** represents a mH10 core with a single functionalization of GHKHKHKW peptide.

Scheme 3.1 Synthetic route to PBAVs.



3.3 Biophysical Study of PBAV-siRNA Complexes

Several vectors were chosen as representative examples to study the complexation between **PBAV** and siRNA. Gel electrophoresis study showed that both fluorocarbon and hydrocarbon bolaamphiphiles can bind to siRNA completely starting from N/P (the ratio between primary amines on the vectors and phosphates on the RNA cargos) = 5 (**Figure 3.2**). However, monoamphiphiles showed much less binding affinity to siRNA cargo (**Figure 3.2**), possibly due to the lower density of cationic charges. Further DLS study exhibited that fluorocarbon bolaamphiphiles and monoamphiphiles can form relatively small nanoparticle complexes (around 200 nm) with siRNA, whereas the siRNA complexes formed by hydrocarbon bolaamphiphiles and monoamphiphiles are 100 nm larger (**Table**

3.2). This enhanced nanoparticle assembly induced by fluorocarbon effect is consistent with previous reports.^{7,16-17,23}

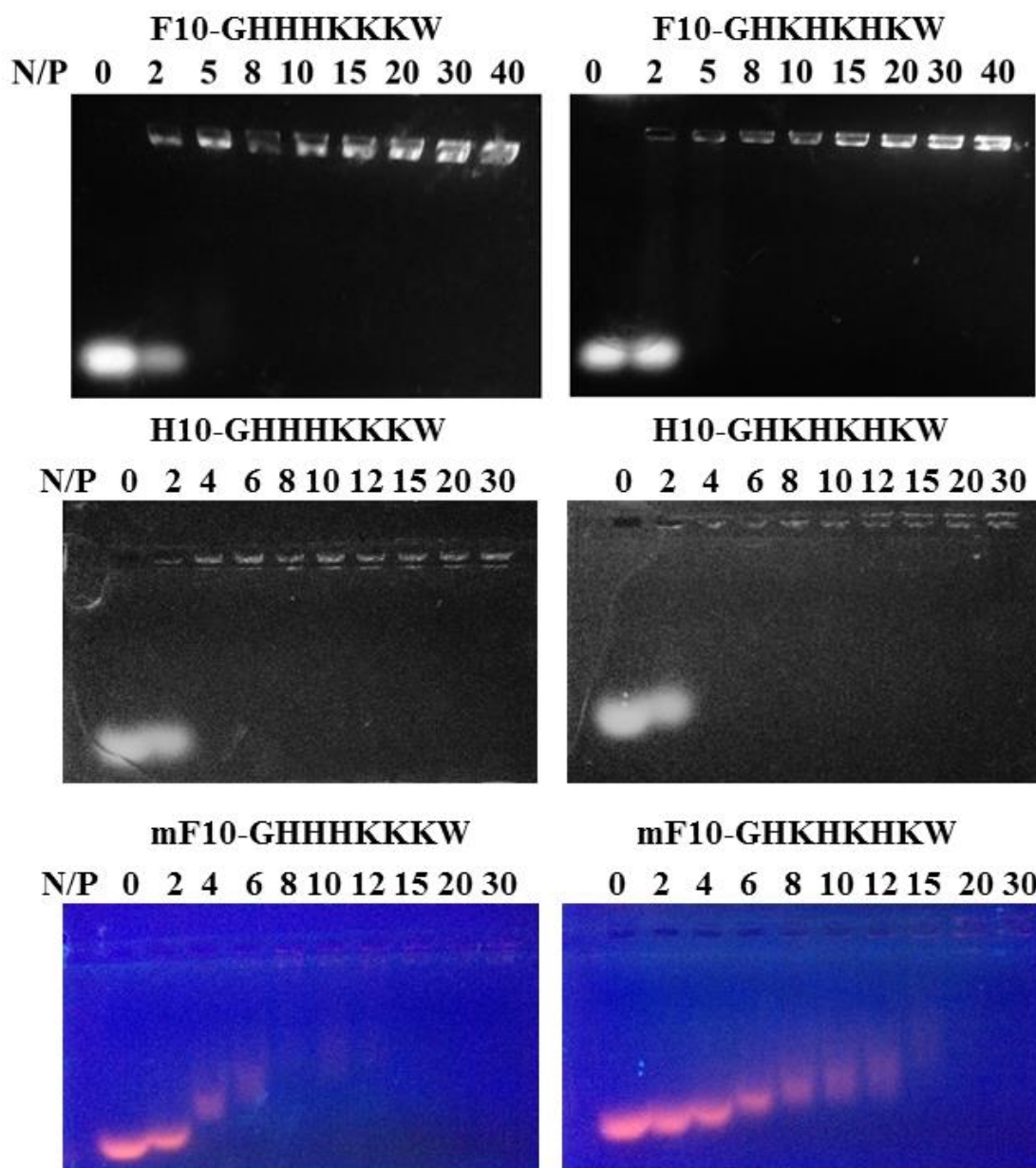


Figure 3.2 Gel electrophoresis study of PBAV-siRNA complexation. **F10-HHHKKKW**, **F10-HKHKHKW**, **H10-GHHHKKKW**, **H10-GHKHKHKW**, **mF10-GHHHKKKW**, and **mF10-GHKHKHKW** were chosen as representative vectors for complexation study.

The nanoparticle complexes were stable in both complexation media (low salt PBS buffer) and transfection media (OptiMEM). In OptiMEM, **F10-GHHHKKKW**-siRNA complexes are generally 100 nm larger than **F10-GHKHKHKW**-siRNA complexes, which may due to the partial aggregation induced by the block of positive charges in **F10-GHHHKKKW** vector. In contrast, alternative peptide sequence can space out cationic charges on the protonated primary amines, affording smaller nanoparticles with higher stability.

Table 3.2 Nanoparticle sizes of **PBAV**-siRNA complexes determined by DLS. The particles were tested in two different media, low salt PBS buffer (LSPBS) and transfection media (OptiMEM). The results were presented as Z-average size in diameter (nm) and PDI in brackets. N/P = 30.

Time (min)	6	12	18	24	30
F10-GHHHKKKW/ LSPBS	237.7 (0.445)	129.8 (0.477)	201.9 (0.384)	173.0 (0.389)	196.8 (0.469)
F10-GHKHKHKW/ LSPBS	226.2 (0.378)	195.1 (0.372)	197.1 (0.364)	199.3 (0.364)	210.7 (0.355)
F10-GHHHKKKW/ OptiMEM	266.0 (0.313)	310.5 (0.487)	293.0 (0.426)	396.5 (0.400)	374.3 (0.535)
F10-GHKHKHKW/ OptiMEM	183.2 (0.300)	200.2 (0.370)	202.6 (0.379)	177.9 (0.273)	178.6 (0.275)
mF10-GHHHKKKW/ LSPBS	141.0 (0.317)	150.5 (0.259)	172.2 (0.197)	178.1 (0.241)	166.7 (0.251)
mF10-GHKHKHKW/ LSPBS	148.5 (0.237)	149.7 (0.176)	167.0 (0.325)	172.2 (0.208)	186.9 (0.205)
H10-GHHHKKKW/ LSPBS	200.1 (0.381)	220.9 (0.008)	261.1 (0.274)	289.1 (0.349)	294.3 (0.305)
H10-GHKHKHKW/ LSPBS	193.7 (0.035)	218.5 (0.103)	225.2 (0.102)	252.3 (0.011)	258.6 (0.071)
mH10-GHHHKKKW/ LSPBS	293.8 (0.610)	318.7 (0.137)	311.8 (0.056)	330.6 (0.021)	390.8 (0.106)
mH10-GHKHKHKW/ LSPBS	210.1 (0.060)	299.0 (0.020)	316.4 (0.004)	314.7 (0.048)	302.8 (0.190)

3.4 siRNA Delivery

The library of **PBAVs** was screened for siRNA delivery. Specifically, anti-Luc siRNA was complexed with different vectors at various N/P ratios, transfected into the HEK-293

cells expressing firefly luciferase (Luc), and then assayed for luciferase activity after 48 h to determine the gene silencing. Lipofectamine RNAiMAX was used as positive controls in the siRNA delivery experiments. First, several bolaamphiphiles and monoamphiphiles with fluorocarbon/hydrocarbon cores were used as representative examples to identify the optimal conditions (siRNA concentration and N/P ratio) for siRNA transfection (**Figure 3.3-3.4**).

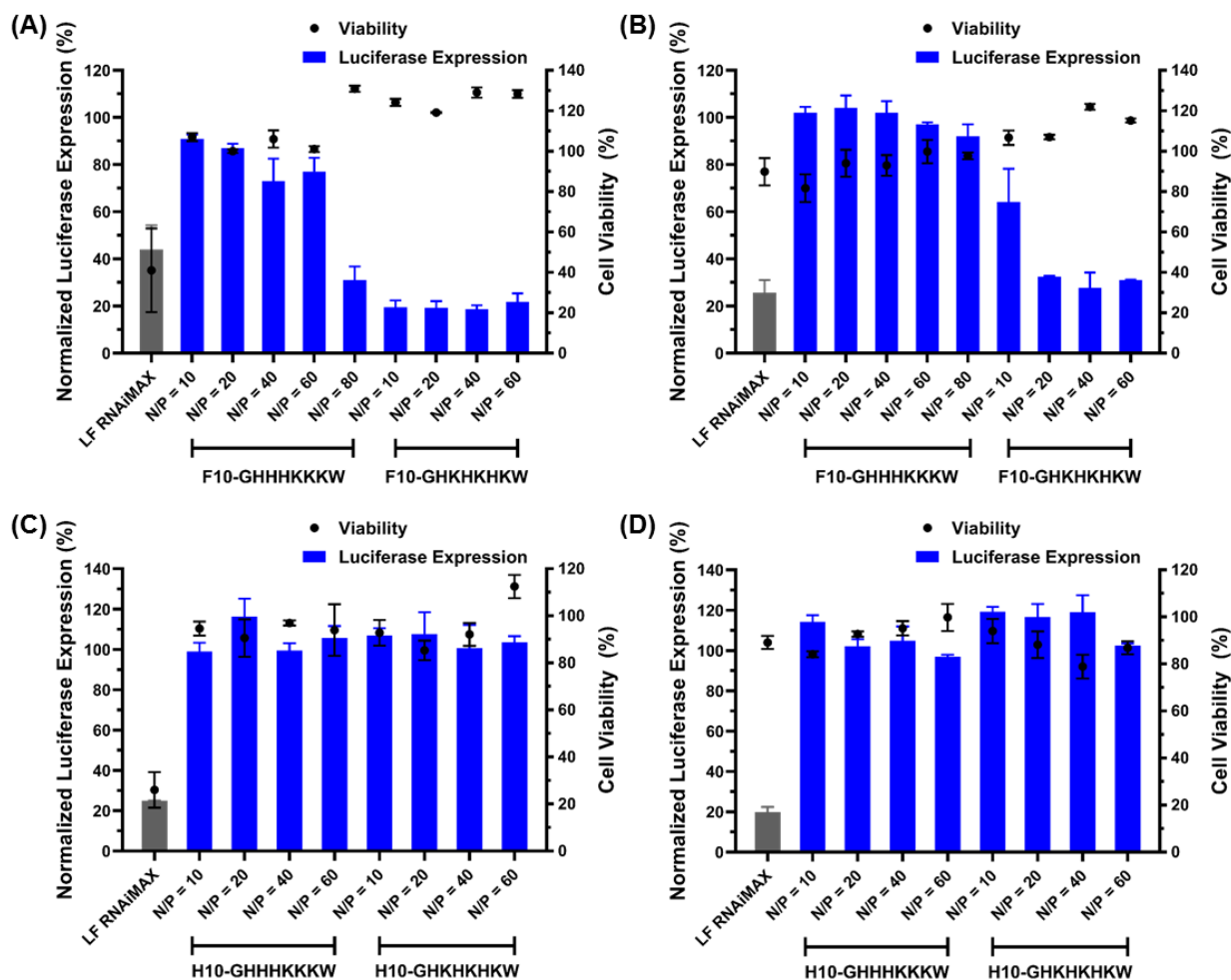


Figure 3.3 Gene silencing and cell viability results of representative bolaamphiphile-siRNA complexes transfected to firefly luciferase-expressing HEK-293 cells in serum-free media. Cell viability was assessed by comparing luciferase expression in non-treated cells to cells treated with negative control siRNA-**PBAV** complexes. (A) Fluorocarbon bolaamphiphiles, [siRNA] = 20 nM. (B) Fluorocarbon bolaamphiphiles, [siRNA] = 10 nM. (C) Hydrocarbon bolaamphiphiles, [siRNA] = 20 nM. (D) Hydrocarbon bolaamphiphiles, [siRNA] = 10 nM.

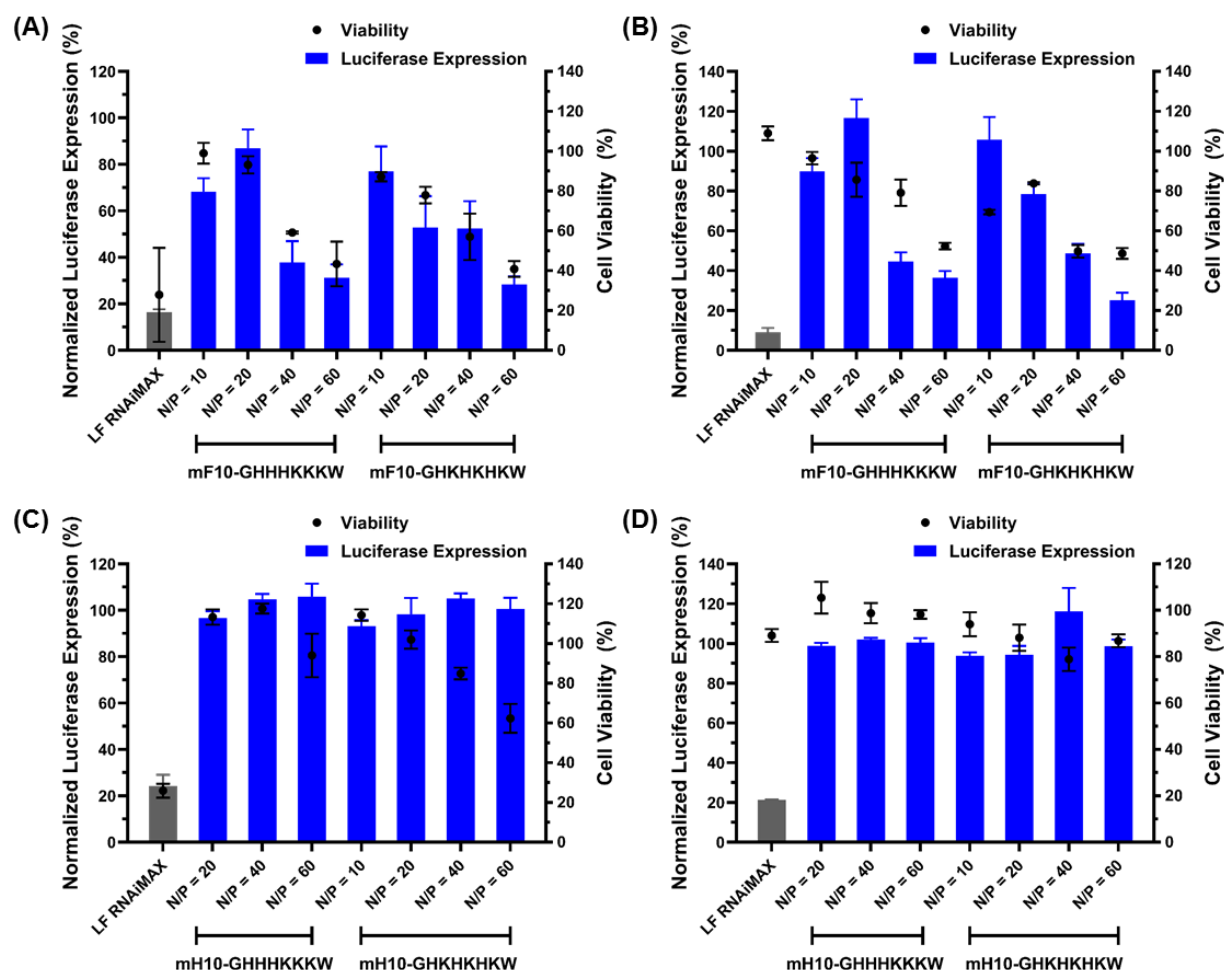


Figure 3.4 Gene silencing and cell viability results of representative monoamphiphile-siRNA complexes transfected to firefly luciferase-expressing HEK-293 cells in serum-free media. Cell viability was assessed by comparing luciferase expression in non-treated cells to cells treated with negative control siRNA-**PBAV** complexes. (A) Fluorocarbon monoamphiphiles, [siRNA] = 20 nM. (B) Fluorocarbon monoamphiphiles, [siRNA] = 10 nM. (C) Hydrocarbon monoamphiphiles, [siRNA] = 20 nM. (D) Hydrocarbon monoamphiphiles, [siRNA] = 10 nM.

As shown in the results, generally fluorocarbon-containing vectors induced higher gene knockdown than hydrocarbon-containing vectors (**Figure 3.3 A, B vs C, D, Figure 3.4 A, B vs C, D**). We believe this is due to the smaller nanoparticle size generated from fluorocarbon assembly, which promotes cellular uptake. Additionally, monoamphiphiles exhibited significantly higher toxicity (lower viability) than bolaamphiphiles (**Figure 3.3-**

3.4). This phenomenon is consistent with our previous report,⁷ which may due to the insertion of monoamphiphiles into cell membrane.²⁴ Moreover, it is interesting that **F10-GHKHKHKW** showed significantly higher gene silencing compared to **F10-GHHHKKKW**, which indicated that the aggregation induced by blocks of cationic charges prohibited efficient siRNA delivery.

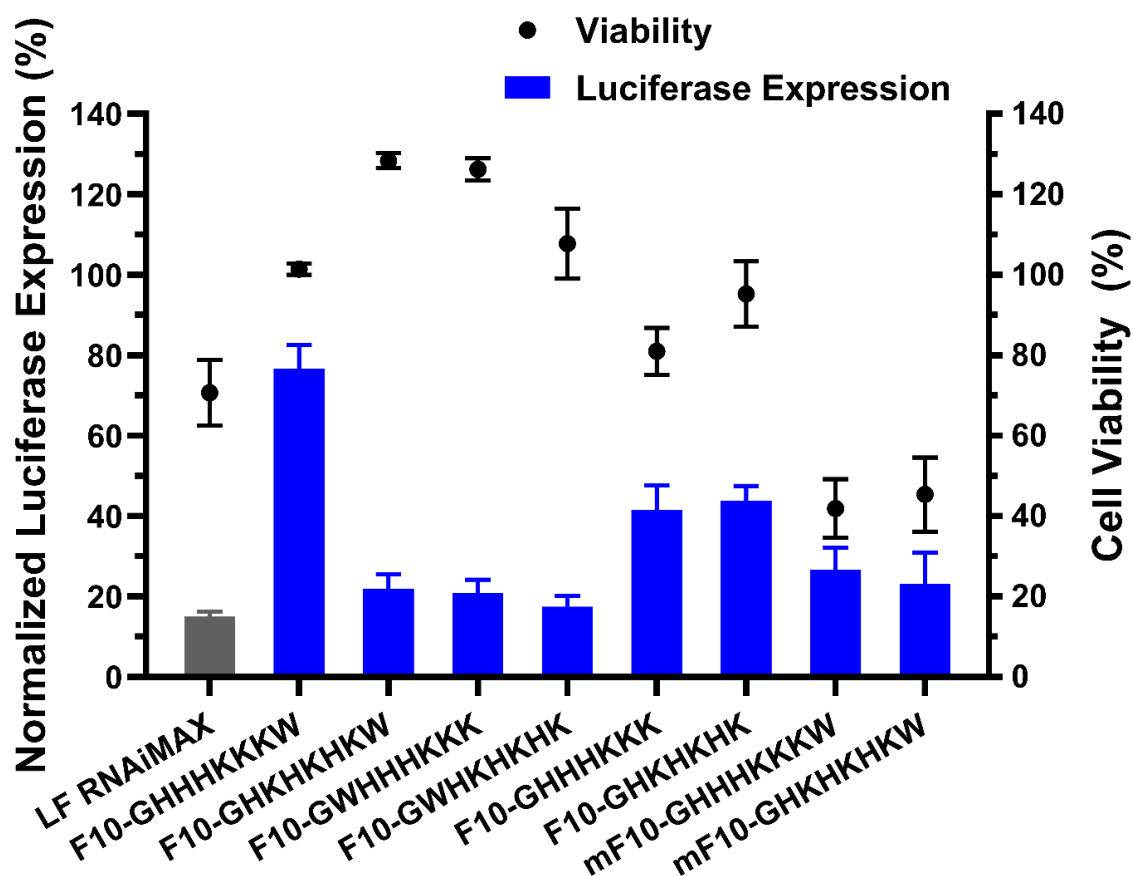


Figure 3.5 Gene silencing and cell viability results of fluorocarbon **PBAV**s-siRNA complexes transfected to firefly luciferase-expressing HEK-293 cells in serum-free media. Cell viability was assessed by comparing luciferase expression in non-treated cells to cells treated with negative control siRNA-**PBAV** complexes. N/P = 60, [siRNA] = 20 nM.

After identifying the optimal transfection conditions (N/P = 60, [siRNA] = 20 nM), we screened all fluorocarbon-containing bolaamphiphiles and monoamphiphiles for siRNA delivery (**Figure 3.5**). The result showed that several vectors, including **F10-GHKHKHKW**,

F10-GWHHHKKK, and **F10-GWHKHKHK**, induced over 75% gene knockdown after siRNA transfection. The incorporation of Trp is essential to achieve the high gene silencing efficacy while the location of Trp in the peptide sequences did not make significant differences. Again, monoamphiphiles with all peptide sequences exhibited much higher toxicity than bolaamphiphiles, especially in high N/P ratios and high siRNA concentrations.

In addition, we systematically screened all bolaamphiphiles and monoamphiphiles with fluorocarbon cores for siRNA delivery under different siRNA concentrations and N/P ratios (**Figure 3.6-3.7**).

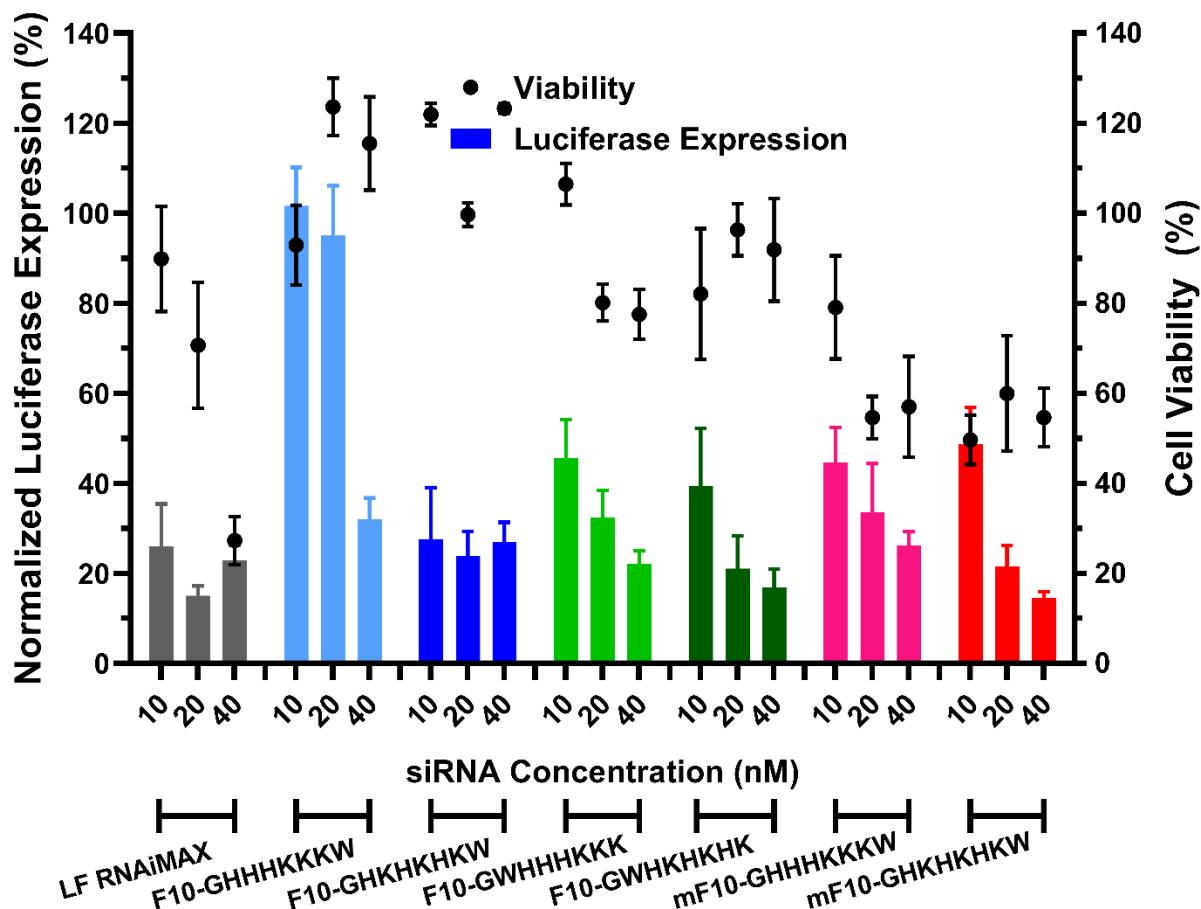


Figure 3.6 Gene silencing and cell viability results of fluorocarbon **PBAVs**-siRNA complexes transfected to firefly luciferase-expressing HEK-293 cells under different siRNA concentrations. N/P = 40. Cell viability was assessed by comparing luciferase expression in non-treated cells to cells treated with negative control siRNA-**PBAV** complexes.

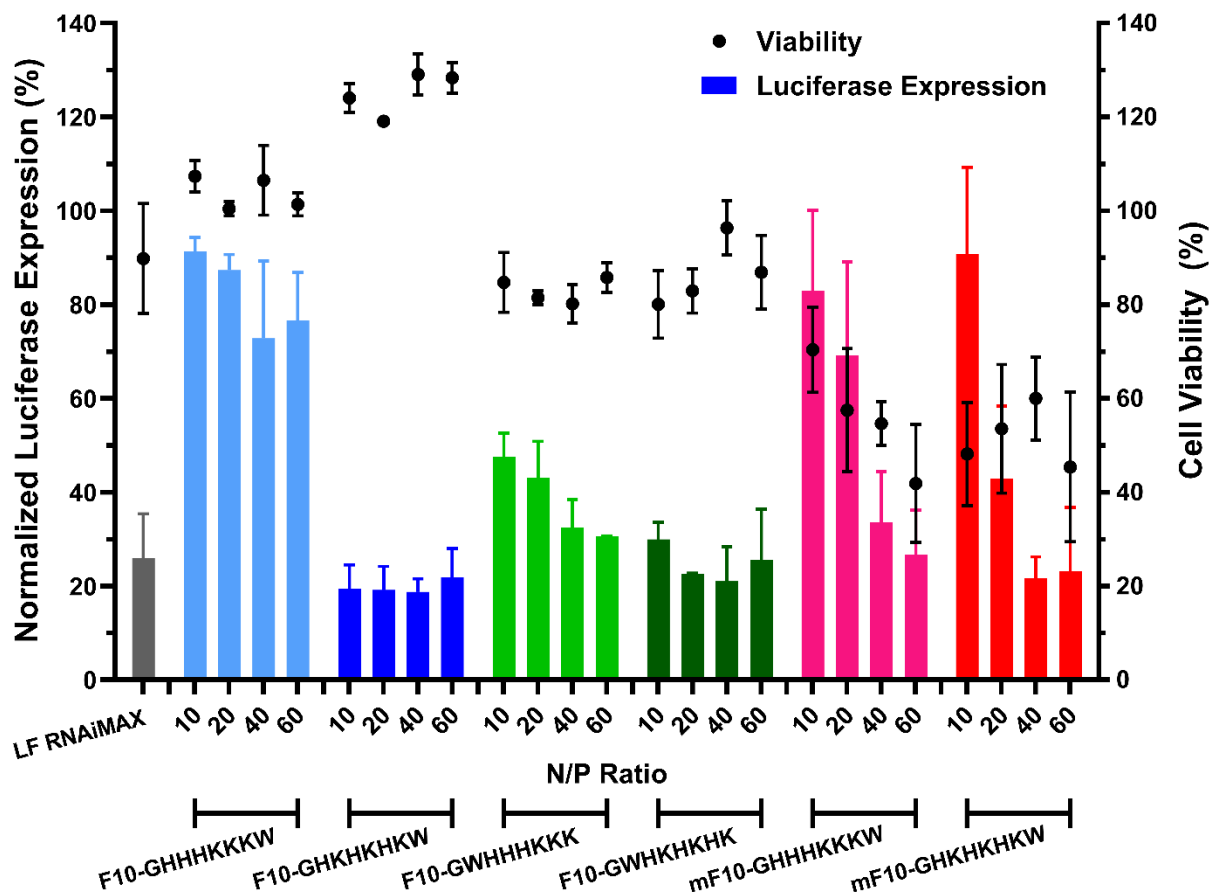


Figure 3.7 Gene silencing and cell viability results of fluorocarbon **PBAVs**-siRNA complexes transfected to firefly luciferase-expressing HEK-293 cells at different N/P ratios. Cell viability was assessed by comparing luciferase expression in non-treated cells to cells treated with negative control siRNA-**PBAV** complexes. [siRNA] = 20 nM.

The positive control, LF RNAiMAX, brought significant cytotoxicity when siRNA concentration increased to 20 nM. Our best vector, **F10-GHKHKHKW**, was able to induce prominent gene silencing (~80%) at relatively low siRNA concentration (10 nM) and low N/P ratio (N/P = 10). In comparison, other fluorocarbon-containing bolaamphiphiles and monoamphiphiles required higher siRNA concentration and N/P ratio.⁷ However, low viability and high toxicity were often observed when increasing these two components in the transfection experiments. This phenomenon is especially distinct for monoamphiphiles.

In order to determine the effective concentration of our best fluorocarbon bolaamphiphiles, we did concentration-dependent siRNA transfection studies (**Figure 3.8**). The most effective vector, **F10-GHKHKHKW**, demonstrated highly efficient transfection with an IC_{50} value of 6.0 nM. Another fluorocarbon bolaamphiphile, **F10-GWHKHKHK**, also exhibited efficient gene knockdown with an IC_{50} of 12.0 nM.

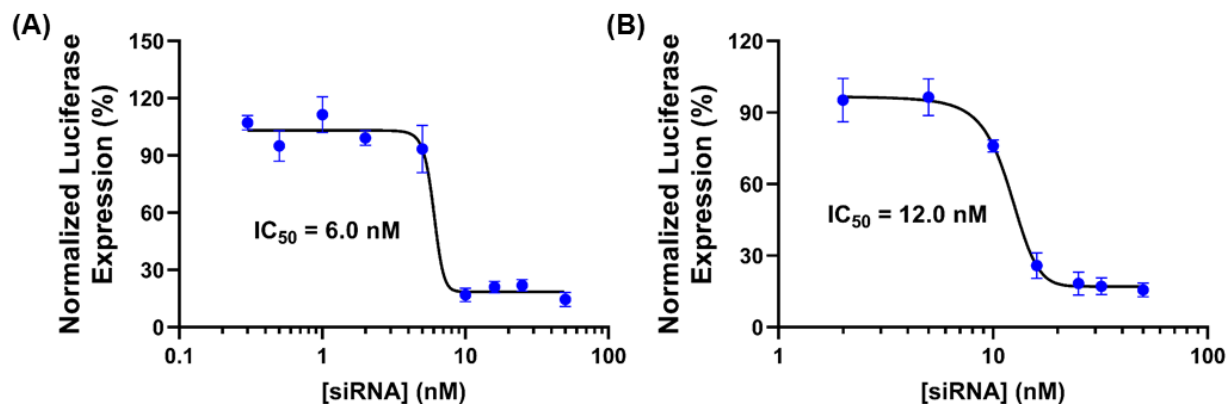


Figure 3.8 Concentration-dependent siRNA transfection studies of effective fluorocarbon bolaamphiphiles in firefly luciferase-expressing HEK-293 cells. N/P = 40 for all vectors. (A) **F10-GHKHKHKW**. (B) **F10-GWHKHKHK**.

To further investigate the toxicity of monoamphiphiles, we performed concentration-dependent transfections with different fluorocarbon monoamphiphile-siRNA complexes (**Figure 3.9**). LC_{50} (lethal concentration) values were calculated according to the obtained results. In general, all monoamphiphiles started inducing obvious toxicity (cell viability < 70%) from low concentrations (15 – 25 nM). Additionally, vectors with blocks of lysines showed higher toxicity than vectors with alternative peptide sequences. This may be due to the aggregation generated between cationic charge blocks and negatively-charged proteins in the transfection media.

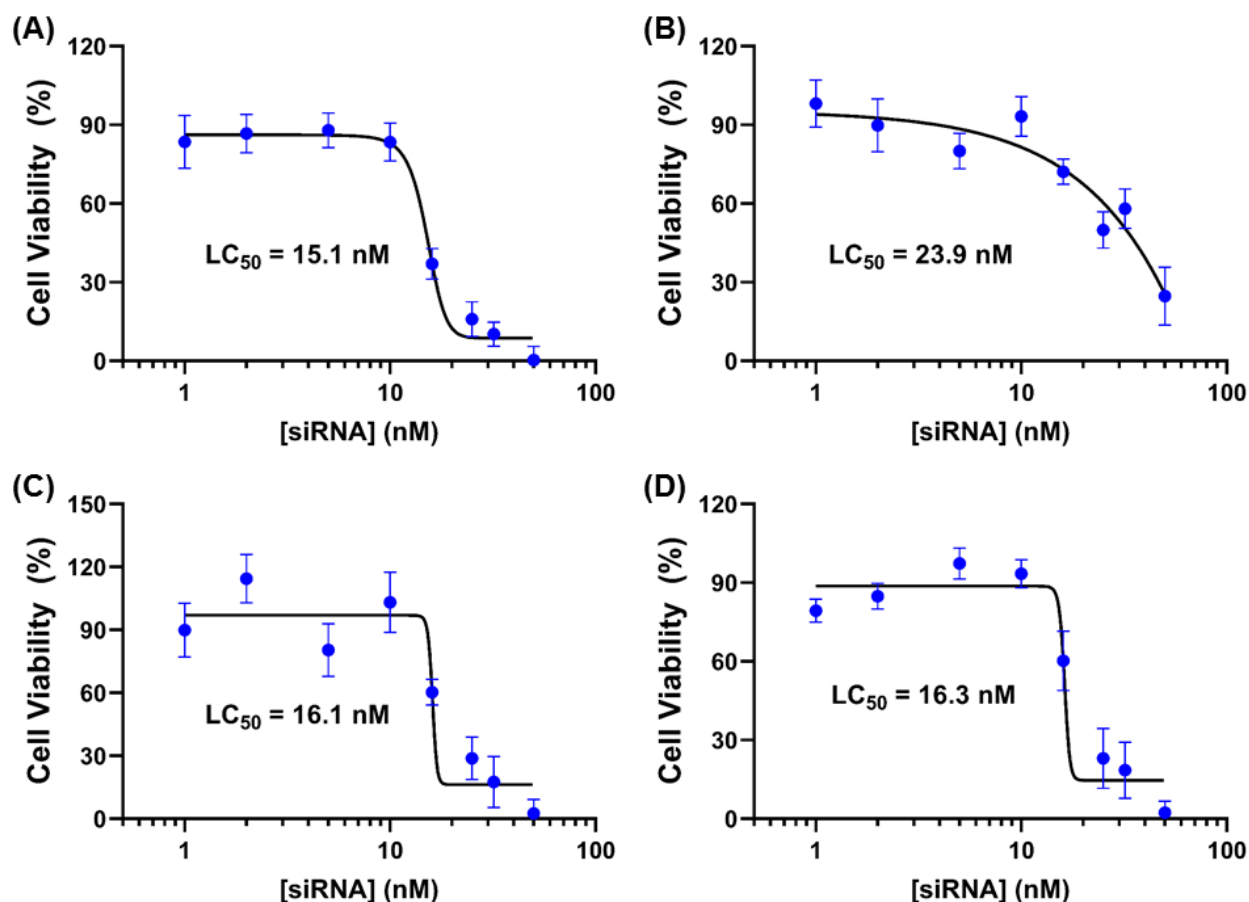


Figure 3.9 Concentration-dependent cell viability studies of fluorocarbon monoamphiphile-siRNA complexes in firefly luciferase-expressing HEK-293 cells. N/P = 40 for all vectors. (A) **mF10-GHHHKKKW**. (B) **mF10-GHKHKHKW**. (C) **mF10-GWHHHKKK**. (D) **mF10-GWHKHKHK**.

To gain some insight of the differences between peptides with block sequences and peptides with alternative sequences, we used circular dichroism (CD) spectroscopy to investigate the possible secondary structures generated from our linear peptides. Both H-WKKKHHHG-OH peptide and H-WKHKHKHW-OH peptide were deprotected, purified, and subjected to CD spectroscopy (**Figure 3.10**). Both peptides showed typical disordered structures without secondary structure formation. We believe this was still due to the short peptide length which is insufficient to form α -helix or β -sheet structures.

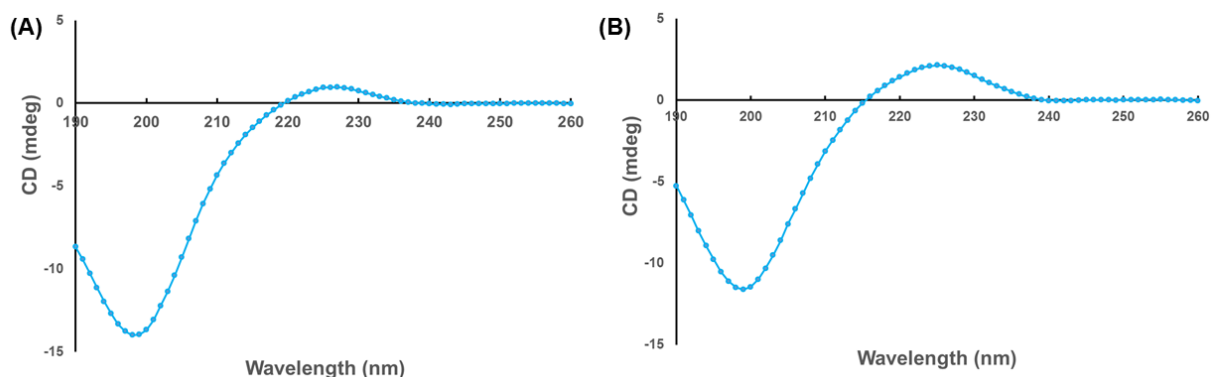


Figure 3.10 Circular dichroism spectra of deprotected linear peptides. (A) H-WKKKHHHG-OH. (B) H-WKHKHKHG-OH.

3.5 Conclusions

In summary, we successfully designed, synthesized, and investigated a family of peptide-functionalized bio-reducible amphiphilic vectors for efficient siRNA delivery. The structure of bolaamphiphile is essential for the effective siRNA transfection whereas monoamphiphiles induce significant toxicity from cell membrane insertion. Fluorocarbon core is important to provide hydrophobicity and promote nanoparticle assembly between vectors and siRNA cargos. For the design of functional peptides, His, Lys, and Trp are critical to afford buffering capacity for endosomal escape, cationic charges for siRNA complexation, and membrane interaction for cellular uptake, respectively. Peptides with alternative sequences are beneficial for efficient delivery as it prevents aggregation generated between cationic charge blocks and anionic charged phosphates/serum proteins. The high transfection efficiency and high biocompatibility suggest the peptide-functionalized fluorocarbon bolaamphiphiles are promising candidates for siRNA delivery. Further structural optimization of this system and *in vivo* study are currently being conducted in our laboratory.

3.6 References

- (1) Gavrilov, K.; Saltzman, W. M., Therapeutic siRNA: principles, challenges, and strategies. *Yale J Biol. Med.* **2012**, *85* (2), 187-200.
- (2) de Fougerolles, A.; Vornlocher, H.-P.; Maraganore, J.; Lieberman, J., Interfering with disease: a progress report on siRNA-based therapeutics. *Nat. Rev. Drug Discovery* **2007**, *6*, 443-453.
- (3) Castanotto, D.; Rossi, J. J., The promises and pitfalls of RNAinterference-based therapeutics. *Nature* **2009**, *457*, 426-433.
- (4) Whitehead, K. A.; Langer, R.; Anderson, D. G., Knocking down barriers: advances in siRNA delivery. *Nat. Rev. Drug Discovery* **2009**, *8*, 129-138.
- (5) Mitragotri, S.; Burke, P. A.; Langer, R., Overcoming the challenges in administering biopharmaceuticals: formulation and delivery strategies. *Nat. Rev. Drug Discovery* **2014**, *13*, 655-672.
- (6) Colella, P.; Ronzitti, G.; Mingozzi, F., Emerging Issues in AAV-Mediated In Vivo Gene Therapy. *Mol. Ther-Meth. Clin. D.* **2018**, *8*, 87-104.
- (7) Zeng, H.; Johnson, M. E.; Oldenhuis, N. J.; Tiambeng, T. N.; Guan, Z., Structure Based Design of Dendritic Peptide Bolaamphiphiles for siRNA Delivery. *ACS Cent. Sci.* **2015**, *1* (6), 303-312.
- (8) Eldredge, A. C.; Johnson, M. E.; Oldenhuis, N. J.; Guan, Z., Focused Library Approach to Discover Discrete Dipeptide Bolaamphiphiles for siRNA Delivery. *Biomacromolecules* **2016**, *17* (10), 3138-3144.
- (9) Eldredge, A. C.; Johnson, M. E.; Cao, Y.; Zhang, L.; Zhao, C.; Liu, Z.; Yang, Q.; Guan, Z., Dendritic peptide bolaamphiphiles for siRNA delivery to primary adipocytes. *Biomaterials* **2018**, *178*, 458-466.
- (10) Won, Y.-W.; Adhikary, P. P.; Lim, K. S.; Kim, H. J.; Kim, J. K.; Kim, Y.-H., Oligopeptide complex for targeted non-viral gene delivery to adipocytes. *Nat. Mater.* **2014**, *13* (12), 1157-1164.
- (11) Lee, M. J.; Pickering, R. T.; Puri, V., Prolonged efficiency of siRNA-mediated gene silencing in primary cultures of human preadipocytes and adipocytes. *Obesity* **2014**, *22* (4), 1064-1069.
- (12) Guidotti, G.; Brambilla, L.; Rossi, D., Cell-Penetrating Peptides: From Basic Research to Clinics. *Trends Pharmacol. Sci.* **2017**, *38* (4), 406-424.
- (13) Copolovici, D. M.; Langel, K.; Eriste, E.; Langel, U., Cell-Penetrating Peptides: Design, Synthesis, and Applications. *ACS Nano*, **2014**, *8*, 1972-1994.
- (14) Hoyer, J.; Neundorff, I., Peptide vectors for the nonviral delivery of nucleic acids. *Acc. Chem. Res.* **2012**, *45*, 1048-1056.
- (15) Kang, Z.; Meng, Q.; Liu, K. Peptide-based gene delivery vectors. *J. Mater. Chem. B.* **2019**, *7*, 1824-1841.

- (16) Saito, H.; Shinoda, W.; Mikami, M., Fluorination effects on structure and dynamics of phospholipid bilayer: A molecular dynamics study. *Chem. Phys. Lett.* **2009**, *468*, 260-263.
- (17) Dafik, L.; Kalsani, V.; Leung, A. K. L.; Kumar, K., Fluorinated Lipid Constructs Permit Facile Passage of Molecular Cargo into Living Cells. *J. Am. Chem. Soc.* **2009**, *131*, 12091-12093.
- (18) Son, S.; Namgung, R.; Kim, J.; Singha, K.; Kim, W. J., Bio reducible Polymers for Gene Silencing and Delivery. *Acc. Chem. Res.* **2012**, *45*, 1100-1112.
- (19) Midoux, P.; Pichon, C.; Yaouanc, J. J.; Jaffres, P. A., Chemical vectors for gene delivery: a current review on polymers, peptides and lipids containing histidine or imidazole as nucleic acids carriers. *Br. J. Pharmacol.* **2009**, *157* (2), 166-178.
- (20) Jobin, M. L.; Blanchet, M.; Henry, S.; Chaignepain, S.; Manigand, C.; Castano, S.; Lecomte, S.; Burlina, F.; Sagan, S.; Alves, I. D., The role of tryptophans on the cellular uptake and membrane interaction of arginine-rich cell penetrating peptides. *Biochim. Biophys. Acta* **2015**, *1848* (2), 593-602.
- (21) Wimley, W. C.; White, S. H., Experimentally determined hydrophobicity scale for proteins at membrane interfaces. *Nat. Struct. Biol.* **1996**, *3*, 842-848.
- (22) Palomo, J. M., Solid-phase peptide synthesis: an overview focused on the preparation of biologically relevant peptides. *RSC Adv.* **2014**, *4* (62), 32658-32672.
- (23) Saito, H.; Shinoda, W.; Mikami, M., Enhanced Hydrophobicity of Fluorinated Lipid Bilayer: A Molecular Dynamics Study. *J. Phys. Chem. B*, **2008**, *112*, 11305-11309.
- (24) Marie, E.; Sagan, S.; Cribier, S.; Tribet, C., Amphiphilic macromolecules on cell membranes: from protective layers to controlled permeabilization. *J. Membrane Biol.* **2014**, *247*, 861-881.

3.7 Experimental

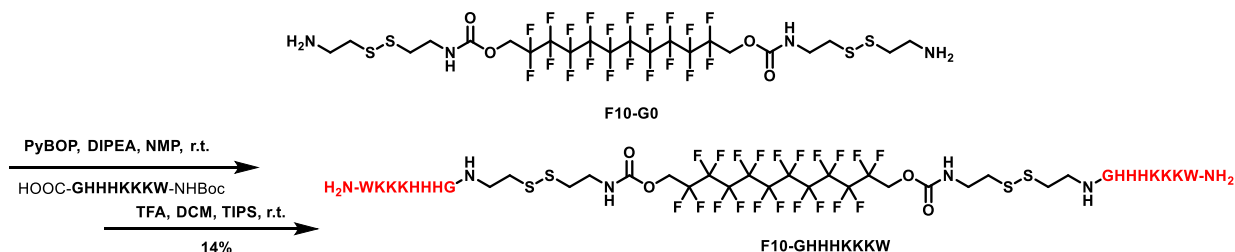
Materials. All commercially available chemicals were used without further purification unless otherwise noted. Protected amino acids were purchased from Advanced ChemTech (Louisville, KY) and Aroz Technologies, LLC. (Cincinnati, OH). Coupling reagents were purchased from GL Biochem Ltd. (Shanghai, China). All siRNA used in this study was purchased from Thermo Fischer Life Technologies with Silencer® Select negative control siRNA and Silencer® Select Custom siRNA used for gel assays, DLS measurements, and transfection studies. The sequences for the anti-Luc siRNA are: 5'-AGACUAUAAGAUUCAUCUTT-3' (sense) and 5'-AGAUUGAAUCUUAUAGUCUTG-3' (anti-sense). All reactions were performed using HPLC grade solvents unless otherwise noted. All water used in biological experiments was Nanopure water obtained from Barnstead Nanopure Diamond (Waltham, MA). Firefly luciferase-expressing HEK cells were generously provided by Professor Jennifer Prescher (Department of Chemistry, UC Irvine, CA). Dulbecco's modified Eagle's medium (DMEM), fetal bovine serum (FBS), and OptiMEM were purchased from Invitrogen (Carlsbad, CA).

Instruments. Nuclear Magnetic Resonance (NMR) spectra were recorded on 500 MHz or 600 MHz Bruker spectrometers. Chemical shifts were reported in ppm. Coupling constants (J values) were reported in Hertz. ^1H NMR chemical shifts were referenced to D_2O ($\delta = 4.79$ ppm). The Z-average size and zeta potential of **PBAV**-siRNA complexes were measured at 633 nm using Zetasizer (NanoZS) dynamic light scattering instrument (Malvern Instruments, Malvern, UK) at 25 °C with detection angle of 173°. Solid-phase peptide synthesis was performed on a Protein Technologies PS3 synthesizer. CD measurements

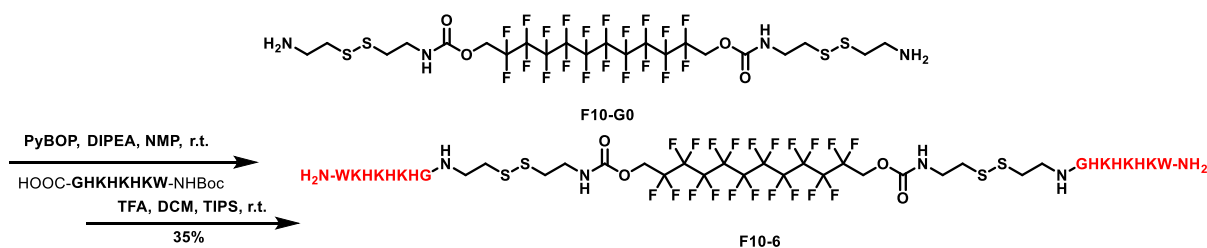
were performed on a Jasco J-810 spectropolarimeter (163-900 nm). Mass spectral data (ES-MS) was obtained from the UC Irvine Mass Spectrometry Facility and collected with a Micromass LCT spectrometer. Matrix assisted laser desorption ionization spectral data (MALDI) was obtained from the UC Irvine Mass Spectrometry Facility and collected with an AB SCIEX TOF/TOF 5800 System.

PBAV Vector Synthesis and Characterization

Protected linear peptides: 2-chlorotrityl chloride resin was first loaded with Fmoc-Gly-OH at the loading density of 0.484 mmol/g. Following different peptide sequences, Gly-loaded resin (400 mg, 1.0 equiv., 0.194 mmol) was coupled with 3 different side-chain protected amino acids on a PS3 solid-phase peptide synthesizer. For each coupling step, one amino acid was added for reaction: Fmoc-His(Trt)-OH (601 mg, 5.0 equiv., 0.97 mmol), Fmoc-Lys(Boc)-OH (455 mg, 5.0 equiv., 0.97 mmol), or Boc-Trp(Boc)-OH (392 mg, 5.0 equiv., 0.97 mmol). HATU (332 mg, 4.5 equiv., 0.873 mmol) was utilized as coupling reagent and HOAt (119 mg, 4.5 equiv., 0.873 mmol) was included to suppress the possible epimerization. 20% collidine in DMF was used in the coupling reaction and 20% piperidine in DMF was used to deprotect the Fmoc group. After the synthesis was finished, the protected linear peptide was cleaved from the resin by using 20% hexafluoroisopropanol in anhydrous CH_2Cl_2 . After removal of the solvent under reduced pressure, the residue was obtained as a white solid to give **protected linear peptides**. The purity of synthesized linear peptide was checked by ESI-MS and the peptides were utilized for the subsequent coupling reactions without further purification.

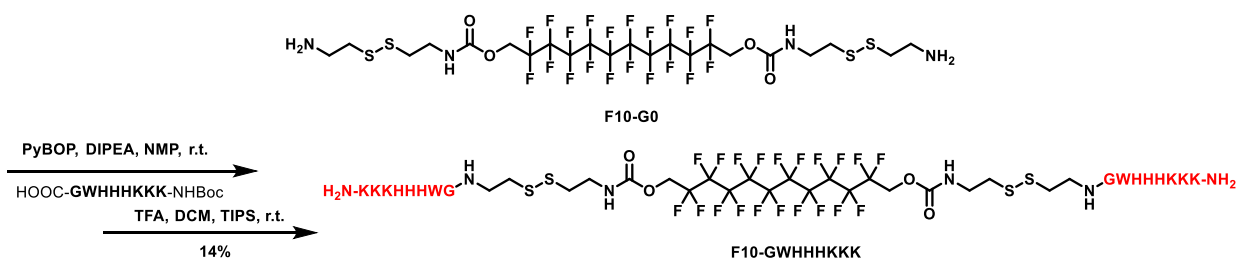


A solution of F10-G0 core (13.8 mg, 1.20×10^{-2} mmol), Boc-protected peptide (HOOC-GHHHKKKW-NHBoc) (68.8 mg, 3.01×10^{-2} mmol), PyBOP (21.9 mg, 4.21×10^{-2} mmol), and DIPEA (18.8 μ L, 1.08×10^{-1} mmol) in NMP (300 μ L) was stirred at room temperature for 24 h. The protected linear peptide vector was precipitated in an excess amount of deionized water. After removing water completely, the solid was dissolved in 1.5 mL TFA, 1.5 mL DCM, 1.5 mL anisole and 0.5 mL TIPS. After stirring overnight, the solvent was removed in vacuo, the resulting solid was redissolved in MeOH and precipitated in Et₂O. The residue was further purified by C18 reverse phase column (eluent: H₂O/MeCN) to give **F10-GHHHKKKW** as a white solid (5 mg, 14%). HRMS (MALDI-TOF) *m/z* Calcd for C₁₂₀H₁₆₆F₂₀N₄₀O₂₀S₄: 2995.18; Found: 2995.8391 [M]⁺.

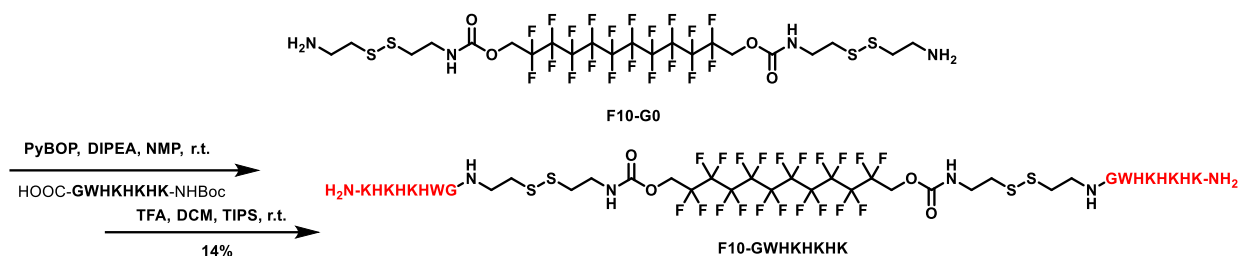


A solution of F10-G0 (13.3 mg, 1.16×10^{-2} mmol), Boc-protected peptide (HOOC-GHKHKHKW-NHBoc) (66.3 mg, 2.90×10^{-2} mmol), PyBOP (21.1 mg, 4.06×10^{-2} mmol), and DIPEA (18.2 μ L, 1.04×10^{-1} mmol) in NMP (300 μ L) was stirred at room temperature for 24 h. The protected linear peptide vector was precipitated in an excess amount of

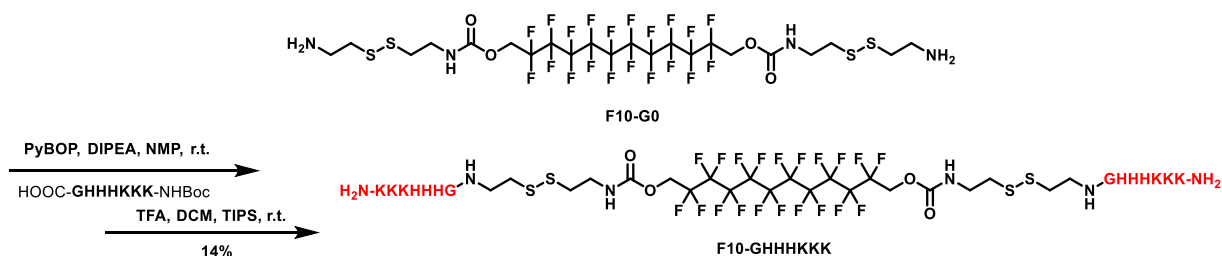
deionized water. After removing water completely, the solid was dissolved in 1.5 mL TFA, 1.5 mL DCM, 1.5 mL anisole and 0.5 mL TIPS. After stirring overnight, the solvent was removed in *vacuo*, the resulting solid was redissolved in MeOH and precipitated in Et₂O. The residue was further purified by C18 reverse phase column (eluent: H₂O/MeCN) to give **F10-GHKHKHKW** as a white solid (7 mg, 35%). *m/z* Calcd for C₁₂₀H₁₆₆F₂₀N₄₀O₂₀S₄: 2995.18; Found: 2994.9382 [M]⁺.



A solution of F10-G0 core (12.0 mg, 1.07×10^{-2} mmol), Boc-protected peptide (HOOC-GWHHHKKK-NHBoc) (61.0 mg, 2.67×10^{-2} mmol), PyBOP (19.0 mg, 3.75×10^{-2} mmol), and DIPEA (17.0 μ L, 9.63×10^{-2} mmol) in NMP (200 μ L) was stirred at room temperature for 24 h. The protected linear peptide vector was precipitated in an excess amount of deionized water. After removing water completely, the solid was dissolved in 1.5 mL TFA, 1.5 mL DCM, 1.5 mL anisole and 0.5 mL TIPS. After stirring overnight, the solvent was removed in *vacuo*, the resulting solid was redissolved in MeOH and precipitated in Et₂O. The residue was further purified by C18 reverse phase column (eluent: H₂O/MeCN) to give **F10-GWHHHKKK** as a white solid (4.7 mg, 13%). HRMS (MALDI-TOF) *m/z* Calcd for C₁₂₀H₁₆₆F₂₀N₄₀O₂₀S₄: 2995.18; Found: 2994.8860 [M]⁺.

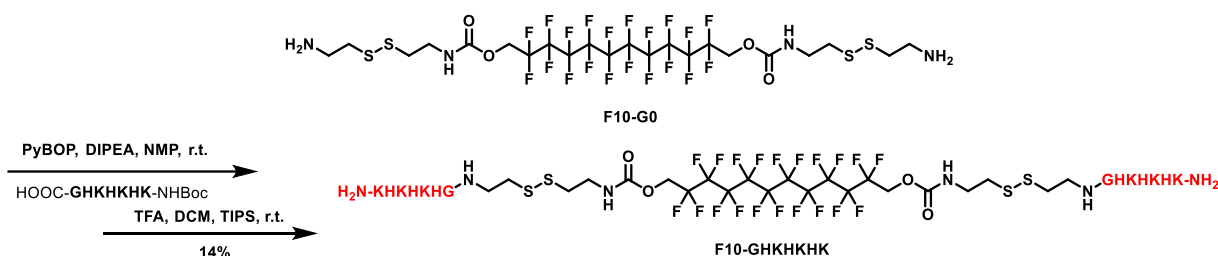


A solution of F10-G0 core (10.0 mg, 9.16×10^{-3} mmol), Boc-protected peptide (HOOC-GWHKHKHK-NHBoc) (52.3 mg, 2.29×10^{-2} mmol), PyBOP (16.7 mg, 3.21×10^{-2} mmol), and DIPEA (14.3 μ L, 8.24×10^{-2} mmol) in NMP (200 μ L) was stirred at room temperature for 24 h. The protected linear peptide vector was precipitated in an excess amount of deionized water. After removing water completely, the solid was dissolved in 1.5 mL TFA, 1.5 mL DCM, 1.5 mL anisole and 0.5 mL TIPS. After stirring overnight, the solvent was removed in *vacuo*, the resulting solid was redissolved in MeOH and precipitated in Et₂O. The residue was further purified by C18 reverse phase column (eluent: H₂O/MeCN) to give **F10-GWHKHKHK** as a white solid (4.8 mg, 13%). HRMS (MALDI-TOF) *m/z* Calcd for C₁₂₀H₁₆₆F₂₀N₄₀O₂₀S₄: 2995.18; Found: 2995.1829 [M]⁺.

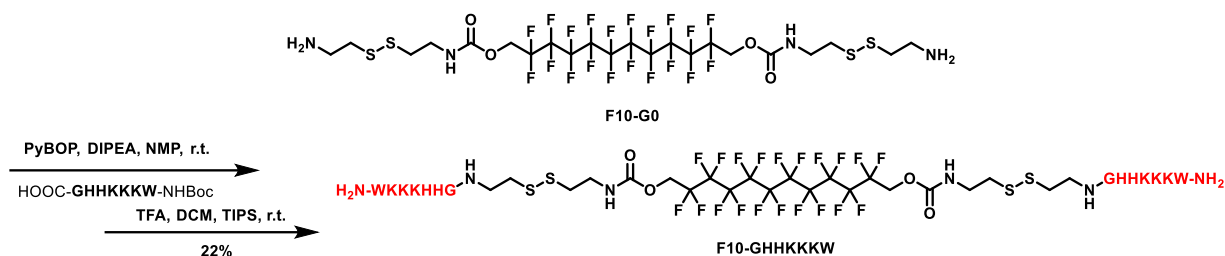


A solution of F10-G0 core (12.0 mg, 1.02×10^{-2} mmol), Boc-protected peptide (HOOC-GHHHKKK-NHBoc) (51.0 mg, 2.55×10^{-2} mmol), PyBOP (19.0 mg, 3.57×10^{-2} mmol), and DIPEA (16.0 μ L, 9.18×10^{-2} mmol) in NMP (200 μ L) was stirred at room temperature for 24 h. The protected linear peptide vector was precipitated in an excess

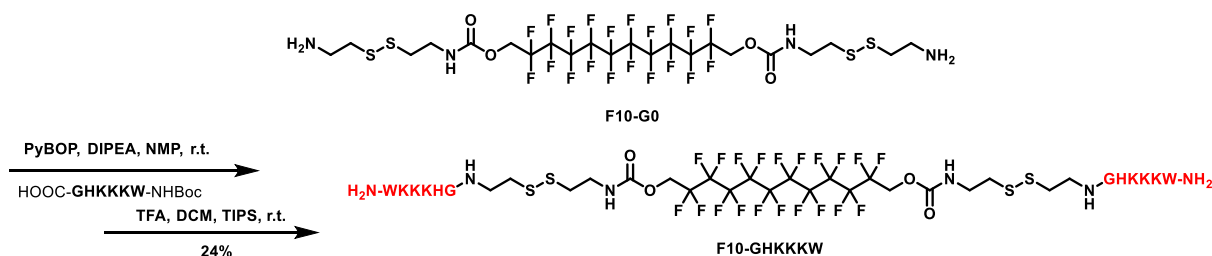
amount of deionized water. After removing water completely, the solid was dissolved in 1.5 mL TFA, 1.5 mL DCM, 1.5 mL anisole and 0.5 mL TIPS. After stirring overnight, the solvent was removed in *vacuo*, the resulting solid was redissolved in MeOH and precipitated in Et₂O. The residue was further purified by C18 reverse phase column (eluent: H₂O/MeCN) to give **F10-GHHHKKK** as a white solid (5.3 mg, 20%). HRMS (MALDI-TOF) *m/z* Calcd for C₉₈H₁₄₆F₂₀N₃₆O₁₈S₄: 2623.02; Found: 2623.5552 [M]⁺.



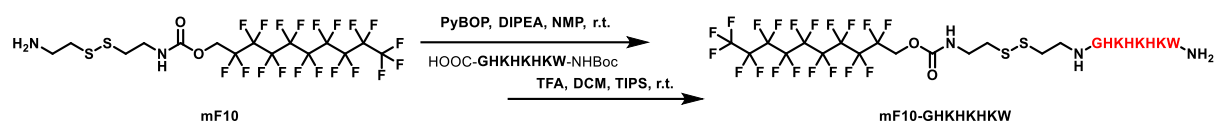
A solution of F10-G0 core (7.0 mg, 6.10×10^{-3} mmol), Boc-protected peptide (HOOC-GHKHKHK-NHBoc) (30.0 mg, 1.50×10^{-2} mmol), PyBOP (11.0 mg, 2.11×10^{-2} mmol), and DIPEA (9.0 μ L, 5.16×10^{-2} mmol) in NMP (200 μ L) was stirred at room temperature for 24 h. The protected linear peptide vector was precipitated in an excess amount of deionized water. After removing water completely, the solid was dissolved in 1.5 mL TFA, 1.5 mL DCM, 1.5 mL anisole and 0.5 mL TIPS. After stirring overnight, the solvent was removed in *vacuo*, the resulting solid was redissolved in MeOH and precipitated in Et₂O. The residue was further purified by C18 reverse phase column (eluent: H₂O/MeCN) to give **F10-GHKHKHK** as a white solid (3.4 mg, 21%). HRMS (MALDI-TOF) *m/z* Calcd for C₉₈H₁₄₆F₂₀N₃₆O₁₈S₄: 2623.02; Found: 2623.6265 [M]⁺.



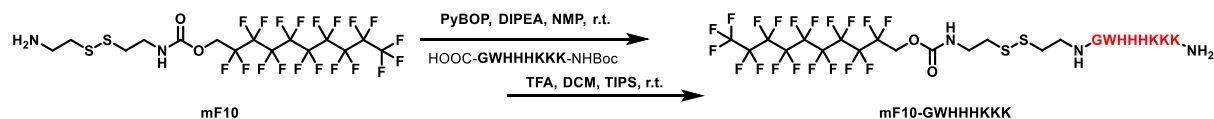
A solution of F10-G0 core (24.9 mg, 2.17×10^{-2} mmol), Boc-protected peptide (HOOC-GHHKKKW-NHBoc) (124.0 mg, 6.52×10^{-2} mmol), PyBOP (45.2 mg, 8.69×10^{-2} mmol), and DIPEA (37.8 μ L, 2.17×10^{-1} mmol) in NMP (200 μ L) was stirred at room temperature for 24 h. The protected linear peptide vector was precipitated in an excess amount of deionized water. After removing water completely, the solid was dissolved in 1.5 mL TFA, 1.5 mL DCM, 1.5 mL anisole and 0.5 mL TIPS. After stirring overnight, the solvent was removed in *vacuo*, the resulting solid was redissolved in MeOH and precipitated in Et₂O. The residue was further purified by C18 reverse phase column (eluent: H₂O/MeCN) to give **F10-GHHKKKW** as a white solid (12.9 mg, 22%). HRMS (MALDI-TOF) *m/z* Calcd for C₁₀₈H₁₅₂F₂₀N₃₄O₁₈S₄: 2722.06; Found: 2721.8289 [M]⁺.



A solution of F10-G0 core (22.0 mg, 1.92×10^{-2} mmol), Boc-protected peptide (HOOC-GHKKKW-NHBoc) (87.9 mg, 5.76×10^{-2} mmol), PyBOP (40.0 mg, 7.68×10^{-2} mmol), and DIPEA (33.5 μ L, 1.92×10^{-1} mmol) in NMP (200 μ L) was stirred at room temperature for 24 h. The protected linear peptide vector was precipitated in an excess

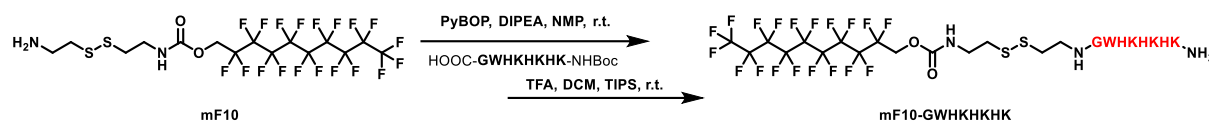


A solution of mF10-G0 core (17.4 mg, 2.20×10^{-2} mmol), Boc-protected peptide (HOOC-GHKHKHKW-NHBoc) (75.0 mg, 3.30×10^{-2} mmol), PyBOP (23.0 mg, 4.40×10^{-2} mmol), and DIPEA (19.0 μL , 1.10×10^{-1} mmol) in NMP (300 μL) was stirred at room temperature for 24 h. The protected linear peptide vector was precipitated in an excess amount of deionized water. After removing water completely, the solid was dissolved in 1.5 mL TFA, 1.5 mL DCM, 1.5 mL anisole and 0.5 mL TIPS. After stirring overnight, the solvent was removed in *vacuo*, the resulting solid was redissolved in MeOH and precipitated in Et₂O. The residue was further purified by C18 reverse phase column (eluent: H₂O/MeCN) to give **mF10-GHKHKHKW** as a white solid (5.8 mg, 15%). HRMS (MALDI-TOF) *m/z* Calcd for C₆₄H₈₃F₁₉N₂₀O₁₀S₂: 1717.59; Found: 1717.3539 [M]⁺.

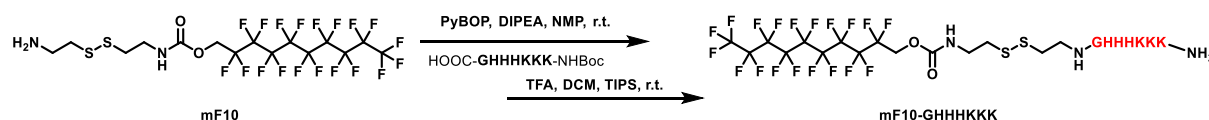


A solution of mF10-G0 core (16.8 mg, 2.13×10^{-2} mmol), Boc-protected peptide (HOOC-GWHHHKKK-NHBoc) (72.9 mg, 3.19×10^{-2} mmol), PyBOP (22.0 mg, 4.26×10^{-2} mmol), and DIPEA (18.6 μL , 1.07×10^{-1} mmol) in NMP (300 μL) was stirred at room temperature for 24 h. The protected linear peptide vector was precipitated in an excess amount of deionized water. After removing water completely, the solid was dissolved in 1.5 mL TFA, 1.5 mL DCM, 1.5 mL anisole and 0.5 mL TIPS. After stirring overnight, the solvent was removed in *vacuo*, the resulting solid was redissolved in MeOH and precipitated in Et₂O. The residue was further purified by C18 reverse phase column (eluent: H₂O/MeCN) to

give **mF10-GWHHHKKK** as a white solid (4.6 mg, 13%). HRMS (MALDI-TOF) m/z Calcd for $C_{64}H_{83}F_{19}N_{20}O_{10}S_2$: 1717.59; Found: 1717.5122 $[M]^+$.

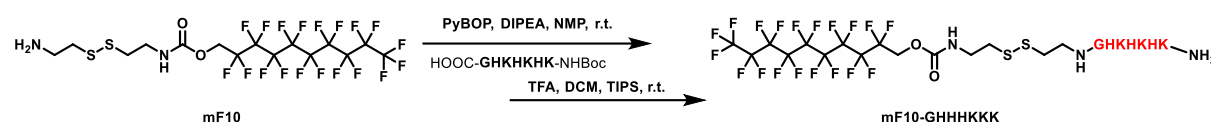


A solution of mF10-G0 core (15.6 mg, 1.97×10^{-2} mmol), Boc-protected peptide (HOOC-GWHKKHKHK-NHBoc) (67.5 mg, 2.95×10^{-2} mmol), PyBOP (20.5 mg, 3.94×10^{-2} mmol), and DIPEA (17.1 μ L, 9.85×10^{-2} mmol) in NMP (300 μ L) was stirred at room temperature for 24 h. The protected linear peptide vector was precipitated in an excess amount of deionized water. After removing water completely, the solid was dissolved in 1.5 mL TFA, 1.5 mL DCM, 1.5 mL anisole and 0.5 mL TIPS. After stirring overnight, the solvent was removed in *vacuo*, the resulting solid was redissolved in MeOH and precipitated in Et₂O. The residue was further purified by C18 reverse phase column (eluent: H₂O/MeCN) to give **mF10-GWHKKHKHK** as a white solid (14.5 mg, 43%). HRMS (MALDI-TOF) m/z Calcd for $C_{64}H_{83}F_{19}N_{20}O_{10}S_2$: 1717.59; Found: 1717.5231 $[M]^+$.

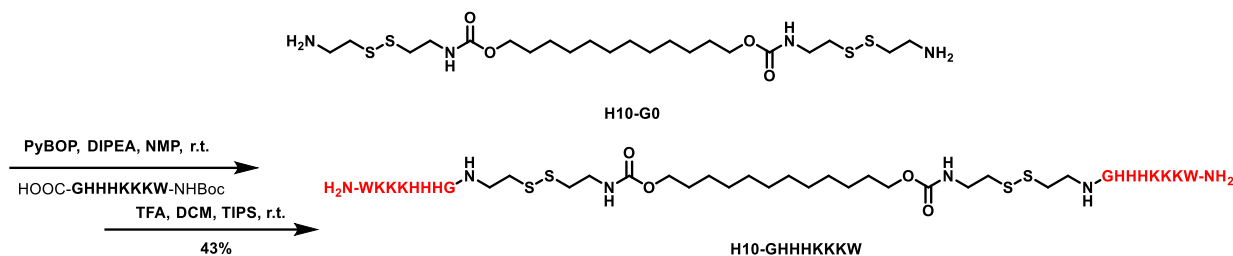


A solution of mF10-G0 core (16.8 mg, 2.12×10^{-2} mmol), Boc-protected peptide (HOOC-GHHHHKKK-NHBoc) (63.5 mg, 3.18×10^{-2} mmol), PyBOP (22.0 mg, 4.24×10^{-2} mmol), and DIPEA (18.5 μ L, 1.06×10^{-1} mmol) in NMP (300 μ L) was stirred at room temperature for 24 h. The protected linear peptide vector was precipitated in an excess amount of deionized water. After removing water completely, the solid was dissolved in 1.5

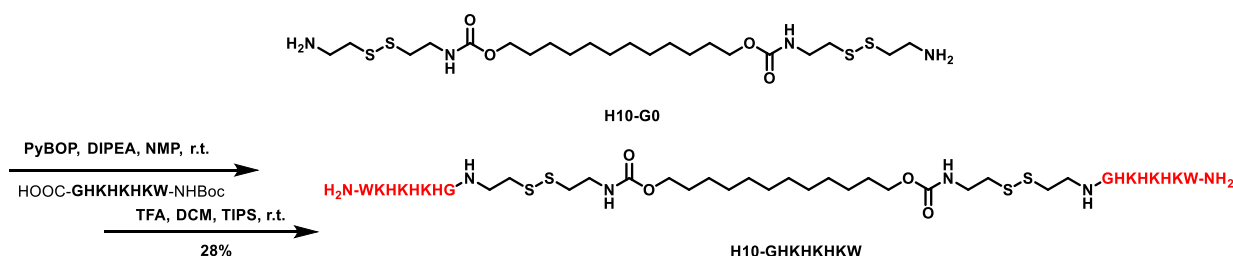
mL TFA, 1.5 mL DCM, 1.5 mL anisole and 0.5 mL TIPS. After stirring overnight, the solvent was removed in *vacuo*, the resulting solid was redissolved in MeOH and precipitated in Et₂O. The residue was further purified by C18 reverse phase column (eluent: H₂O/MeCN) to give **mF10-GHHHKKK** as a white solid (9.1 mg, 28%). HRMS (MALDI-TOF) *m/z* Calcd for C₅₃H₇₃F₁₉N₁₈O₉S₂: 1531.37; Found: 1531.3429 [M]⁺.



A solution of mF10-G0 core (16.7 mg, 2.11×10^{-2} mmol), Boc-protected peptide (HOOC-GHKHKHK-NHBoc) (63.4 mg, 3.17×10^{-2} mmol), PyBOP (22.0 mg, 4.24×10^{-2} mmol), and DIPEA (18.5 μ L, 1.06×10^{-1} mmol) in NMP (300 μ L) was stirred at room temperature for 24 h. The protected linear peptide vector was precipitated in an excess amount of deionized water. After removing water completely, the solid was dissolved in 1.5 mL TFA, 1.5 mL DCM, 1.5 mL anisole and 0.5 mL TIPS. After stirring overnight, the solvent was removed in *vacuo*, the resulting solid was redissolved in MeOH and precipitated in Et₂O. The residue was further purified by C18 reverse phase column (eluent: H₂O/MeCN) to give **mF10-GHKHKHK** as a white solid (8.9 mg, 28%). HRMS (MALDI-TOF) *m/z* Calcd for C₅₃H₇₃F₁₉N₁₈O₉S₂: 1531.37; Found: 1531.3319 [M]⁺.

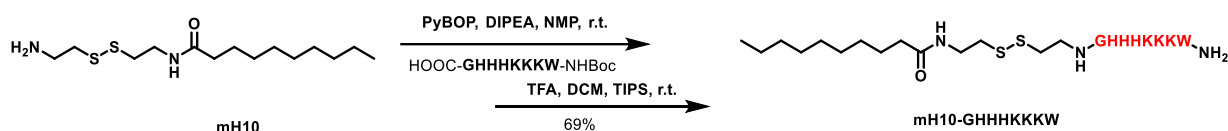


A solution of H10-G0 core (5.8 mg, 7.41×10^{-3} mmol), Boc-protected peptide (HOOC-GHHHKKKW-NHBoc) (50.8 mg, 2.22×10^{-2} mmol), PyBOP (15.4 mg, 2.96×10^{-2} mmol), and DIPEA (13.0 μ L, 7.41×10^{-2} mmol) in NMP (200 μ L) was stirred at room temperature for 24 h. The protected linear peptide vector was precipitated in an excess amount of deionized water. After removing water completely, the solid was dissolved in 1.5 mL TFA, 1.5 mL DCM, 1.5 mL anisole and 0.5 mL TIPS. After stirring overnight, the solvent was removed in *vacuo*, the resulting solid was redissolved in MeOH and precipitated in Et₂O. The residue was further purified by C18 reverse phase column (eluent: H₂O/MeCN) to give **H10-GHHHKKKW** as a white solid (8.4 mg, 43%). HRMS (MALDI-TOF) *m/z* Calcd for C₁₂₀H₁₈₆N₄₀O₂₀S₄: 2636.37; Found: 2636.1006 [M]⁺.

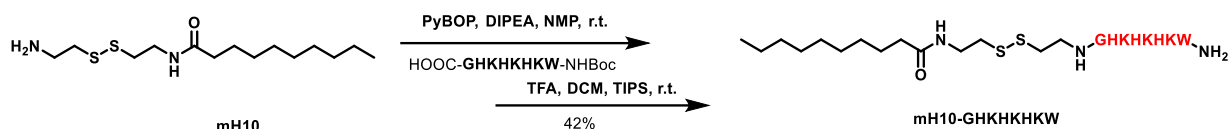


A solution of H10-G0 core (7.4 mg, 9.42×10^{-3} mmol), Boc-protected peptide (HOOC-GHHHKKKW-NHBoc) (64.6 mg, 2.83×10^{-2} mmol), PyBOP (19.6 mg, 3.77×10^{-2} mmol), and DIPEA (16.0 μ L, 9.42×10^{-2} mmol) in NMP (200 μ L) was stirred at room temperature for 24 h. The protected linear peptide vector was precipitated in an excess

amount of deionized water. After removing water completely, the solid was dissolved in 1.5 mL TFA, 1.5 mL DCM, 1.5 mL anisole and 0.5 mL TIPS. After stirring overnight, the solvent was removed in *vacuo*, the resulting solid was redissolved in MeOH and precipitated in Et₂O. The residue was further purified by C18 reverse phase column (eluent: H₂O/MeCN) to give **H10-GHKHKHKW** as a white solid (5.5 mg, 28%). HRMS (MALDI-TOF) *m/z* Calcd for C₁₂₀H₁₈₆N₄₀O₂₀S₄: 2636.37; Found: 2636.1255 [M]⁺.



A solution of mH10-G0 core (8.9 mg, 2.12×10^{-2} mmol), Boc-protected peptide (HOOC-GHHHKKKW-NHBoc) (72.5 mg, 3.17×10^{-2} mmol), PyBOP (22.1 mg, 4.24×10^{-2} mmol), and DIPEA (18.5 μ L, 1.04×10^{-1} mmol) in NMP (300 μ L) was stirred at room temperature for 24 h. The protected linear peptide vector was precipitated in an excess amount of deionized water. After removing water completely, the solid was dissolved in 1.5 mL TFA, 1.5 mL DCM, 1.5 mL anisole and 0.5 mL TIPS. After stirring overnight, the solvent was removed in *vacuo*, the resulting solid was redissolved in MeOH and precipitated in Et₂O. The residue was further purified by C18 reverse phase column (eluent: H₂O/MeCN) to give **mH10-GHHHKKKW** as a white solid (19.7 mg, 69%). HRMS (MALDI-TOF) *m/z* Calcd for C₆₃H₁₀₀N₂₀O₉S₂: 1344.74; Found: 1345.6091 [M+H]⁺.



A solution of mH10-G0 core (11.2 mg, 2.66×10^{-2} mmol), Boc-protected peptide (HOOC-GHHHKKKW-NHBoc) (91.3 mg, 3.99×10^{-2} mmol), PyBOP (27.7 mg, 5.32×10^{-2} mmol), and DIPEA (18.5 μL , 1.04×10^{-1} mmol) in NMP (300 μL) was stirred at room temperature for 24 h. The protected linear peptide vector was precipitated in an excess amount of deionized water. After removing water completely, the solid was dissolved in 1.5 mL TFA, 1.5 mL DCM, 1.5 mL anisole and 0.5 mL TIPS. After stirring overnight, the solvent was removed in *vacuo*, the resulting solid was redissolved in MeOH and precipitated in Et₂O. The residue was further purified by C18 reverse phase column (eluent: H₂O/MeCN) to give **mH10-GHKHKHKW** as a white solid (12.1 mg, 42%). HRMS (MALDI-TOF) *m/z* Calcd for C₆₃H₁₀₀N₂₀O₉S₂: 1344.74; Found: 1345.4943 [M+H]⁺.

Gel electrophoresis

The binding of siRNA to **PBAVs** was studied by agarose gel electrophoresis. Both siRNA and **PBAVs** were diluted with 10 mM pH 7.4 phosphate buffer. Different amount of **PBAV** solutions (10 mg/mL) were added to 5.0 μL 5 μM siRNA solution to achieve different N/P ratio (the molar ratio of primary amine groups from **PBAVs** and phosphate groups from siRNA, imidazole groups of histidine residues not counted because they are not protonated at pH 7.4). The same buffer was added to adjust the final volume to 10.0 μL , followed by 10 min incubation at room temperature. 2 μL 6X RNA loading dye was added to each sample and 10 μL of the mixture was loaded to each well in 1% agarose gel with 1X GelRed dye.

The electrophoresis was run in TBE buffer (pH 7.9) at 60 V for 90 min and the gel was visualized under a UV transilluminator. Related results are shown in **Figure 3.2**.

DLS measurements

The size of **PBAV**-siRNA complexes were measured at 633 nm using Zetasizer (NanoZS) dynamic light scattering instrument (Malvern Instruments, Malvern, UK) at 25 °C with detection angle of 173°. Both **PBAV** and siRNA were diluted in nanopure water, followed by brief vortexing. After 10 min incubation at room temperature, DLS measurement was taken. At least three measurements were taken for each sample and the mean Z-average values were reported.

siRNA transfections

(1) Vector-siRNA complex preparation

The TFA-salts of the various **PBAVs** were stored at -20 ° C as 10 mg/ml solutions in RNase free water and prior to complexation the vectors, along with all buffers, were allowed to reach room temperature. Both negative control and targeted siRNA were diluted to 1.5 µM with RNase free water. The diluted siRNA was further diluted with OptiMEM and complexed with the appropriate amount of vector solution required to achieve the desired N/P ratio. The complex solutions were prepared at 5X the desired final concentration (60 nM) and with a final volume of 60 µL. 20 µL of the complex solution with 300 nM siRNA was added to each well containing 80 µL of OptiMEM to give a transfection media with 60 nM siRNA. Lipofectamine RNAiMAX was used as a positive control and prepared as instructed in the product manual.

(2) Transfection in luciferase-expressing HEK-293 cells

Transfections were performed in triplicate in a cell culture treated clear-bottom 96-well plate (Corning). After passaging, the cells were plated in 96-well plates so that they were 40~50% confluent at the time of transfection. The 5X vector-siRNA complexes were prepared using the aforementioned protocol. The culture media was switched to 80 μ L OptiMEM (with or without 10% FBS) per well and 20 μ L of the complex solution was added to each well. The cells were cultured for 48 hours prior to analysis.

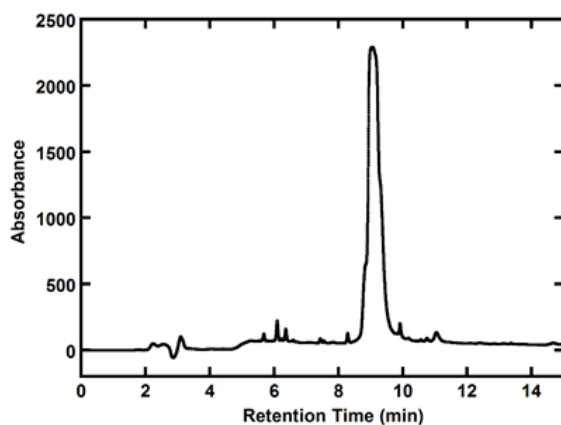
(3) Transfection analysis in luciferase-expressing HEK-293 cells

After 48 hours of incubation post-transfection, the culture media was removed and replaced with 100 μ L of a 150 μ g/mL solution of firefly D-luciferin in FluoroBrite™ DMEM. Without any further treatment, the cells were incubated at 37 °C for 5 minutes after which they were imaged using an IVIS lumina II camera. The normalized luciferase knockdown was determined by comparing the overall luminescence of the samples treated with complexes containing anti-luc siRNA to those treated with complexes containing negative control siRNA.

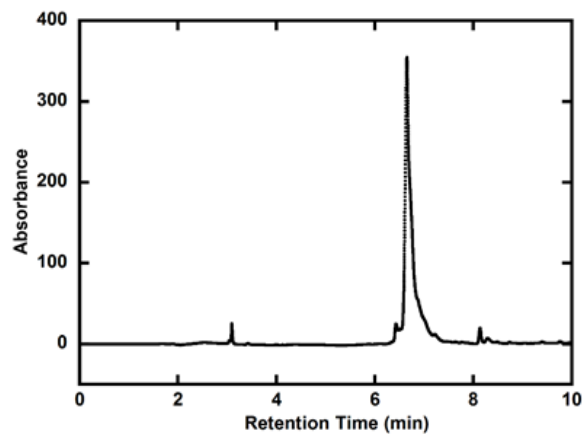
3.8 HPLC Traces and MALDI-MS Spectra

Representative HPLC Traces

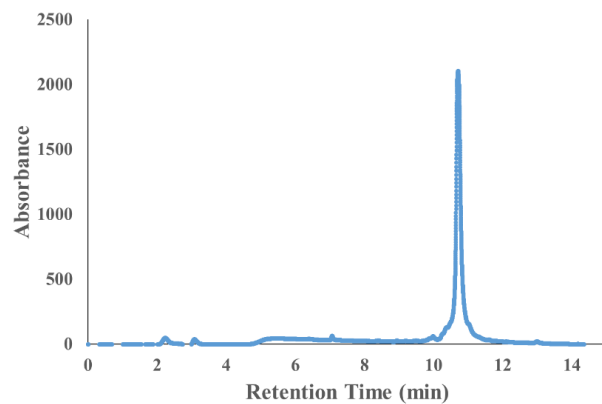
F10-GHHHKKKW



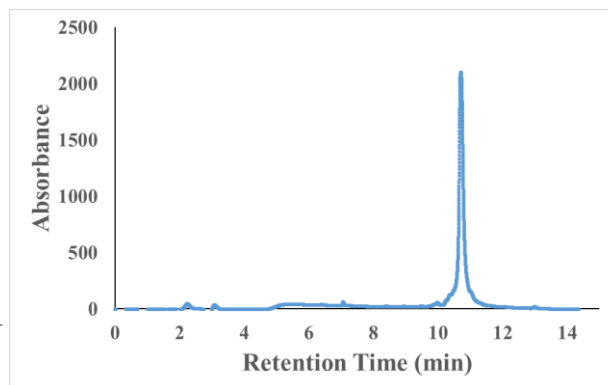
F10-GHKHKHKW



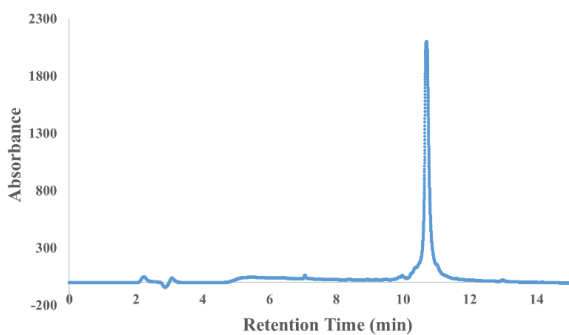
F10-GWHHHKKK



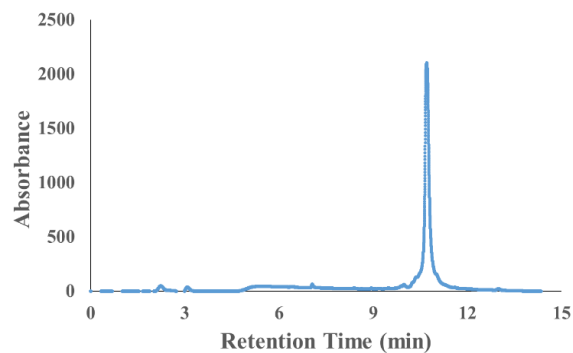
F10-GWHKHKHK



F10-GHHHKKK

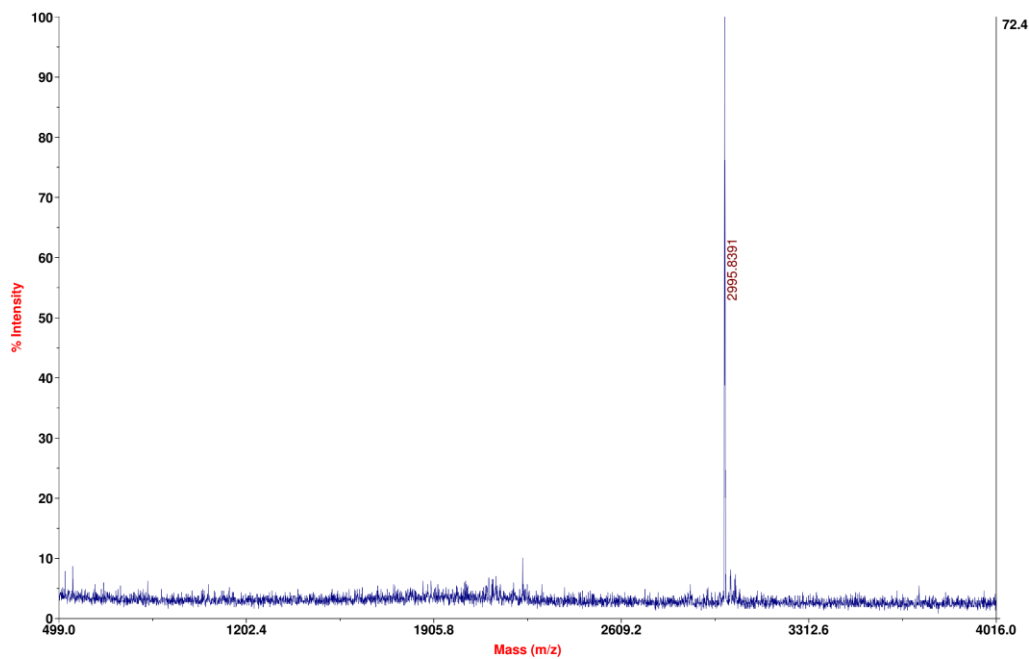


F10-GHKHKHK

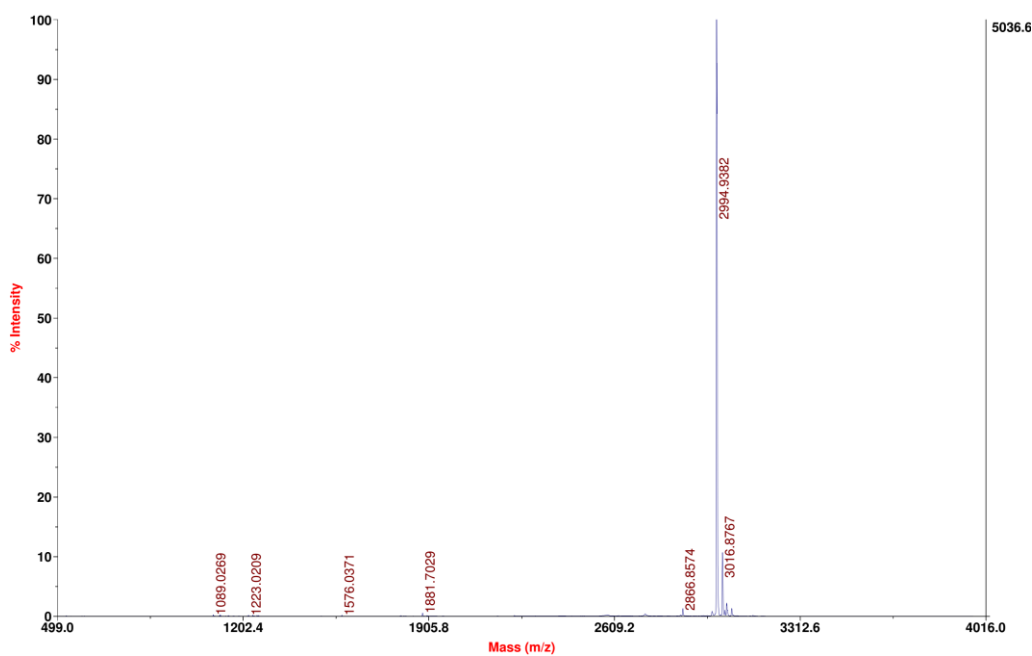


MALDI-MS Spectra

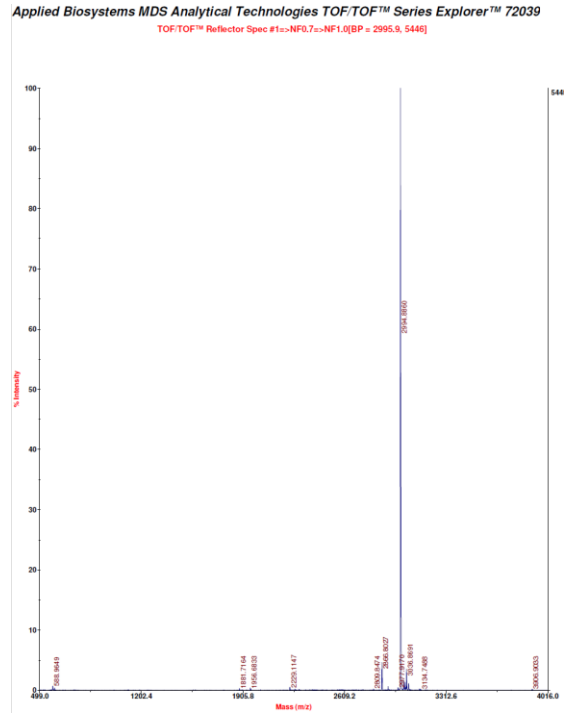
F10-GHHHKKKW



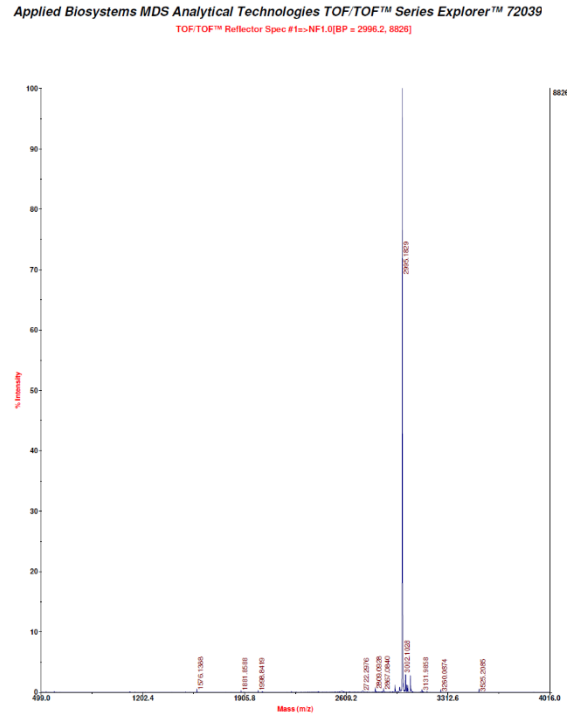
F10-GHKHKHKW



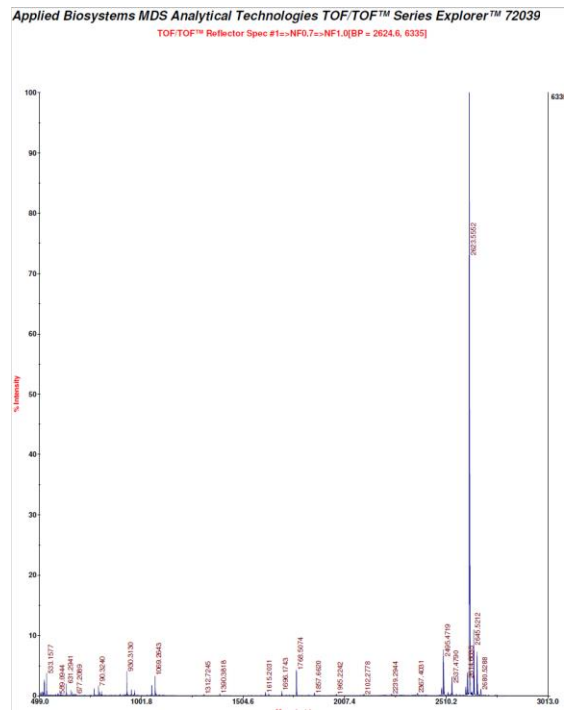
F10-GWHHHKKK



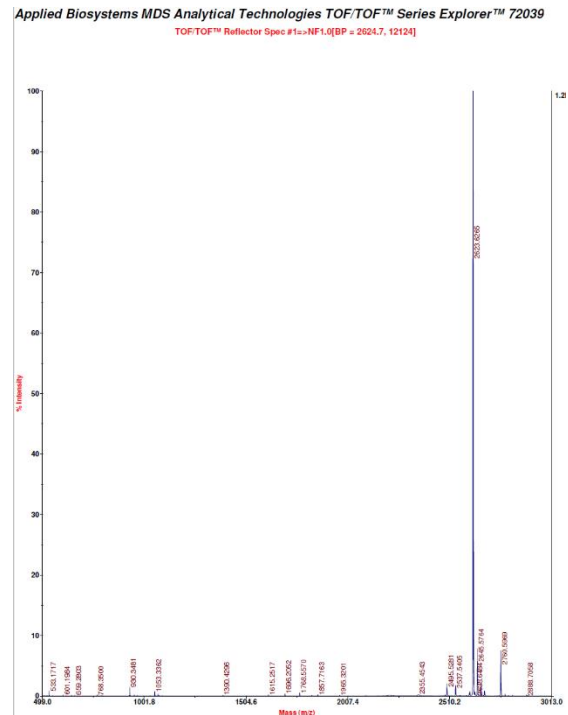
F10-GWHKHKHK



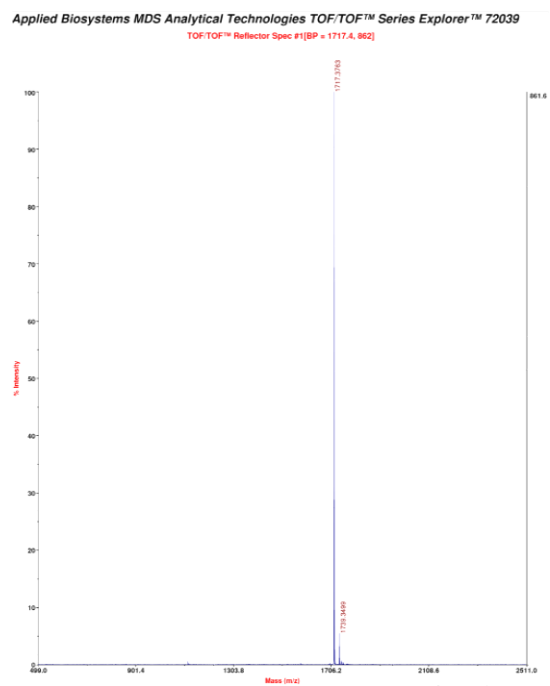
F10-GHHHKKK



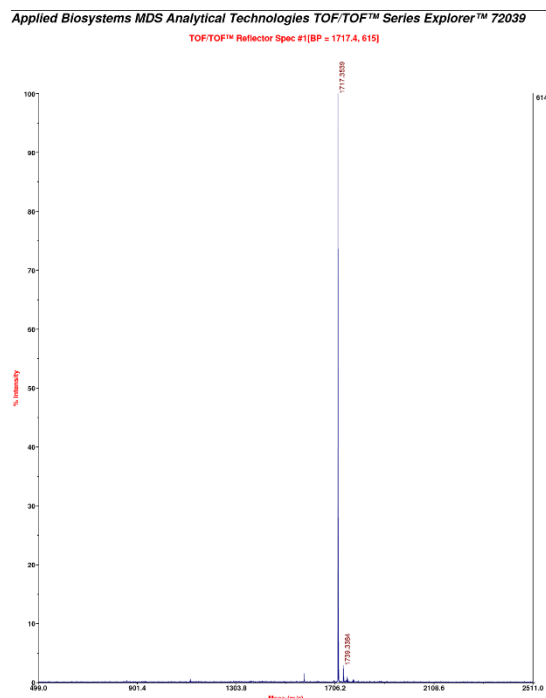
F10-GHKHKHK



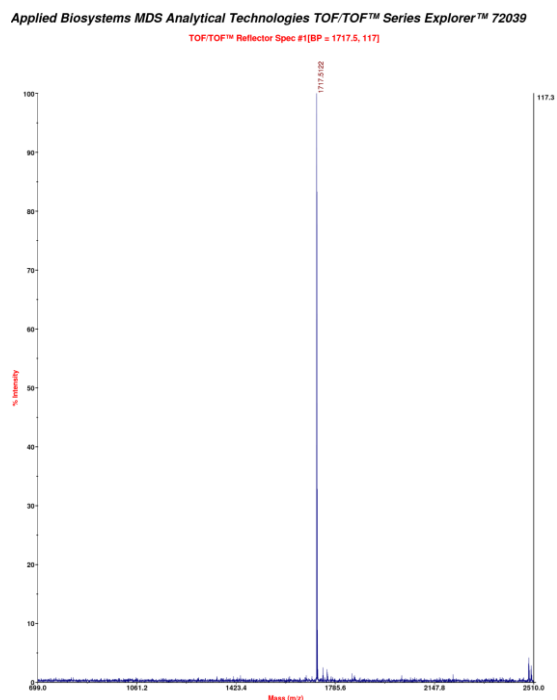
mF10-GHHHKKKW



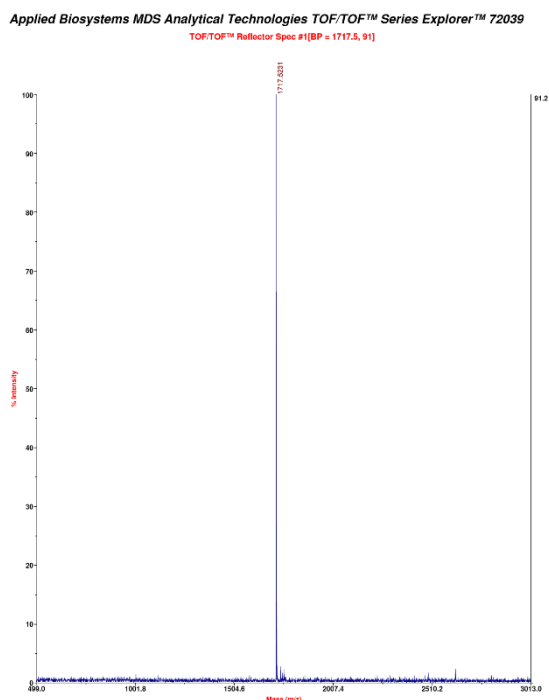
mF10-GHKHKHKW



mF10-GWHHHKKK

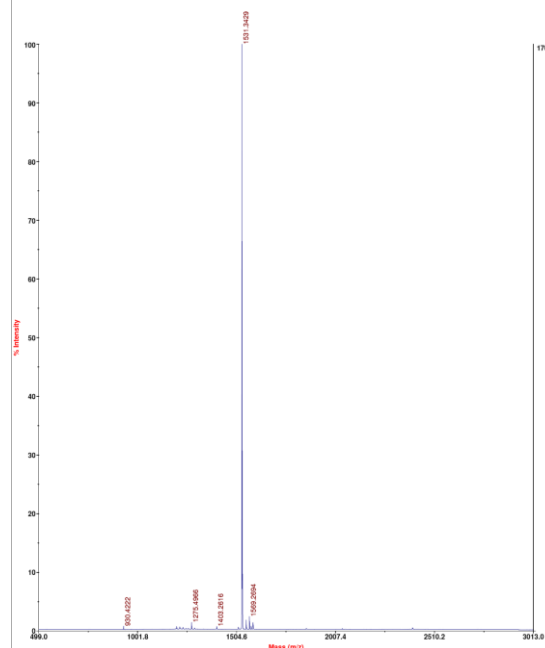


mF10-GWHKHKHK



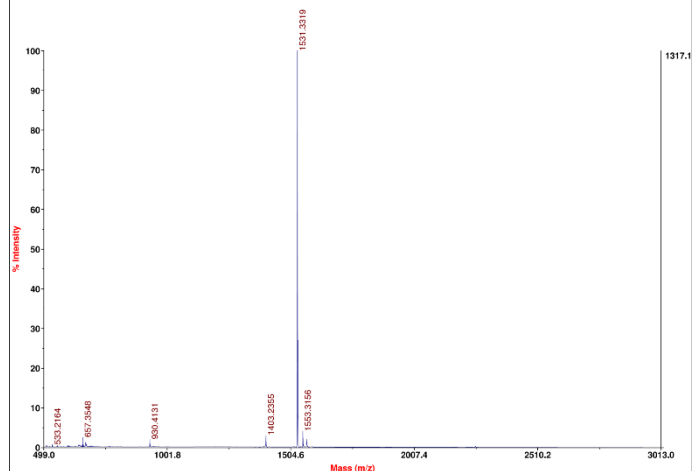
mF10-GHHHKKK

Applied Biosystems MDS Analytical Technologies TOF/TOF™ Series Explorer™ 72039
TOF/TOF™ Reflector Spec #1=>NF0.7=>NF0.9=>NF1.0=>NR(2.00)>>RSM5000(BP = 1531.4, 1703)



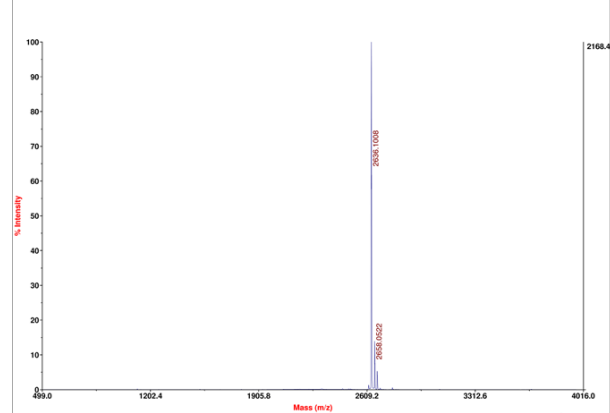
mF10-GHKHKHK

Applied Biosystems MDS Analytical Technologies TOF/TOF™ Series Explorer™ 72039
TOF/TOF™ Reflector Spec #1=>NR(2.00)>>RSM5000=>NR(2.00)>>SM5(BP = 1531.3, 1317)



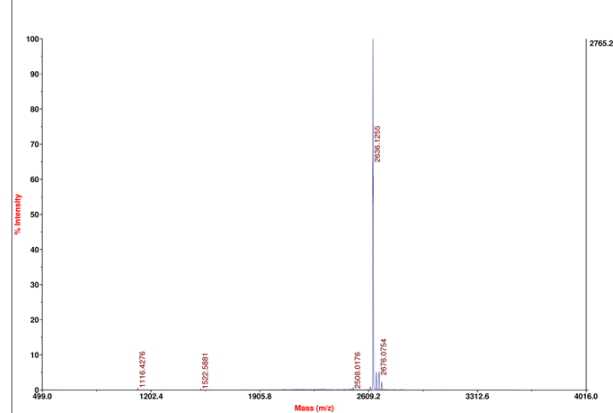
H10-GHHHKKKW

Applied Biosystems MDS Analytical Technologies TOF/TOF™ Series Explorer™ 72039
TOF/TOF™ Reflector Spec #1=>NF0.7=>RSM5000=>SM5=>NR(2.00)(BP = 2637.1, 2168)

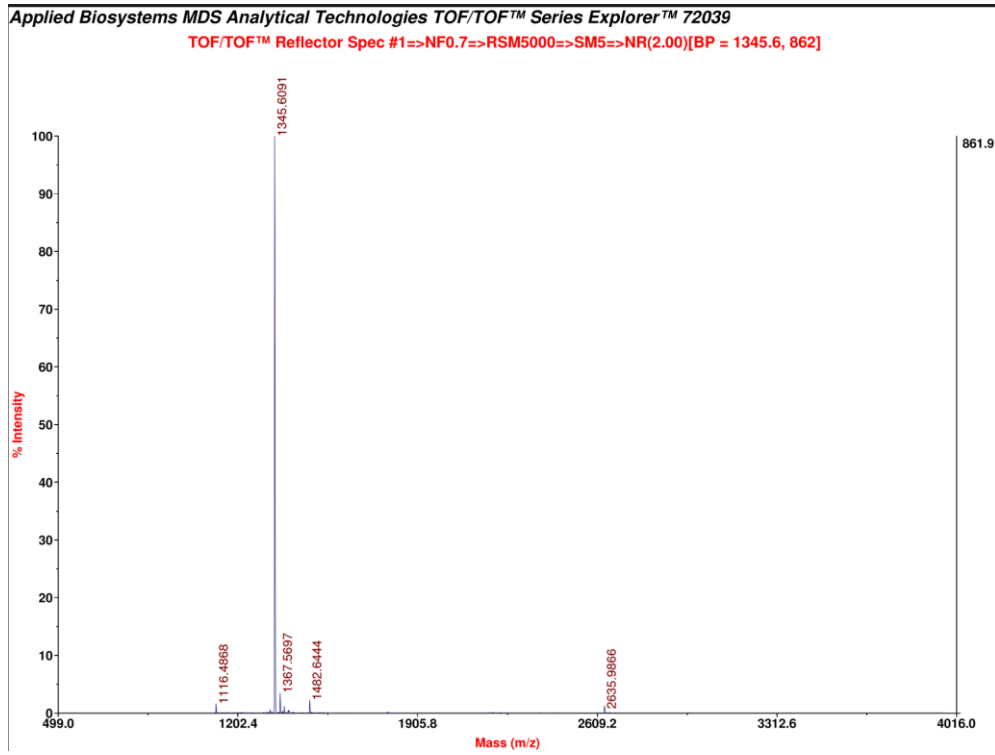


H10-GHKHKHKW

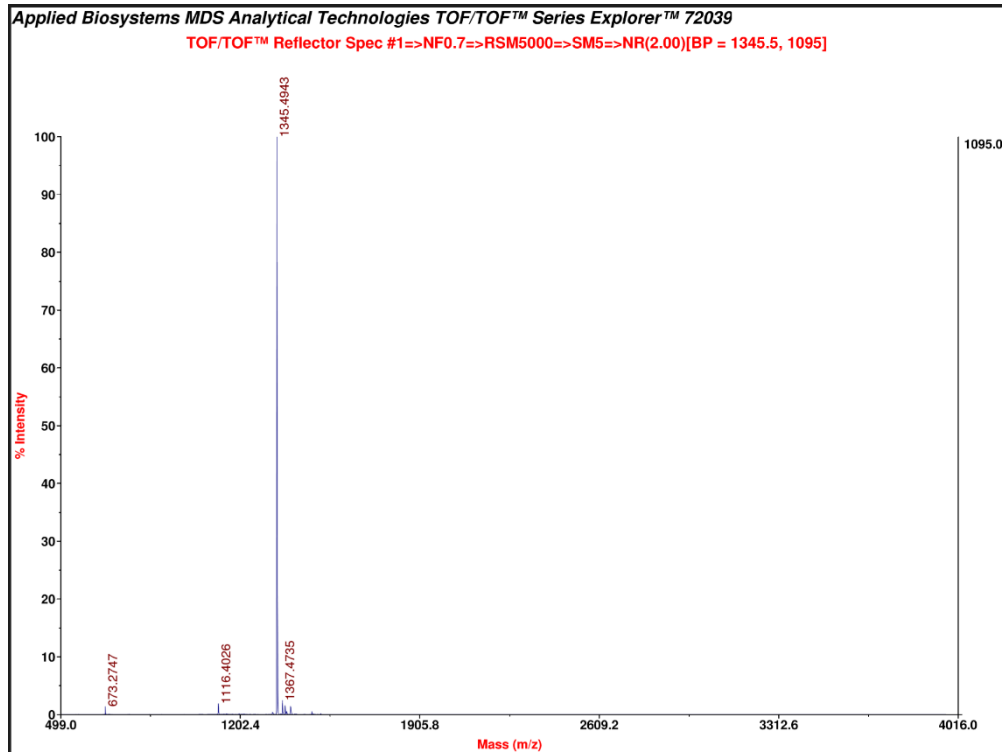
Applied Biosystems MDS Analytical Technologies TOF/TOF™ Series Explorer™ 72039
TOF/TOF™ Reflector Spec #1=>NF0.7=>RSM5000=>NR(2.00)>>SM5(BP = 2637.2, 2765)



mH10-GHHHKKKW



mH10-GHKHKHKW



Chapter 4: Poly(thymine)-functionalized Bioreducible Polymers for mRNA Delivery

4.1 Introduction and Project Design

As introduced in **Section 1.3**, mRNA therapeutics has emerged as a powerful novel technology and it holds great promise in revolutionize protein replacement therapies, immunotherapy, and the treatment of genetic diseases.¹⁻³ However, the lack of safe and efficient mRNA delivery vehicle still hinders the widespread application of mRNA technology.⁴⁻⁵ As described in **Section 1.5**, the ideal mRNA delivery material needs to bind mRNA cargos favorably, promote cellular uptake and endosomal escape, and release mRNA efficiently in the cytoplasm.⁶⁻⁷ Moreover, compared to siRNA, mRNA is generally more sensitive to RNase degradation due to the long single-stranded structure.⁶ Therefore, delivery vehicles must be able to effectively protect mRNAs during the delivery processes. Among all the common non-viral mRNA delivery systems (**Section 1.7**), the great majority of synthetic vectors bind to RNA cargos through electrostatic interaction. The delivery vectors are often positively charged, interacting with negatively charged RNA molecules and forming nanoparticle complexes. However, the abundant cationic charges can bring several side effects. First, the cationic vectors can also interact with anionic serum proteins, which generates aggregation and cytotoxicity.⁸ In addition, the zeta potential of formed nanoparticle complexes are often positive due to the excess cationic vectors, which triggers immune response and brings disuniform bio-distribution *in vivo*. For instance, it has been shown that positively charged particles are prone to accumulate in the lung and spleen.⁹

In this chapter, we attempted a novel delivery system which combined different mechanisms for mRNA complexation and nanoparticle formation. mRNA is usually single-

stranded and consists of ribonucleotides which are linked by phosphodiester bonds. A typical human protein coding mRNA includes several regions: 5'-cap, 5'-untranslated region, coding sequence, 3'-untranslated region, and 3'-poly(adenosine) (poly-A) tail (**Figure 4.1A – 4.1B**).¹⁰ Interestingly, this poly-A tail is a structural homology which is shared by almost all functional mRNAs. It is a long chain (100 – 250 nucleotides) of adenine nucleotides and plays essential role in mRNA function. The poly-A tail has been demonstrated to increase the stability of mRNA and prevent degradation.¹¹ In addition, it allows the mature mRNA molecule to be exported from the nucleus after transcription and translated into a protein by ribosomes in the cytoplasm.¹¹⁻¹³ Moreover, several studies have shown that the poly-A tail binds to poly-A binding proteins in the ribosome, which facilitates mRNA translation and protein production.¹⁴⁻¹⁵

Due to the unique poly-A tail structure of mRNA, we decided to introduce the poly(thymine)-poly(adenine) base-pairing into our vehicle design (**Figure 4.1C**). Poly(thymine) probes have been utilized to detect and image poly(A) RNAs.¹⁶⁻¹⁷ Through introducing poly(thymine) units into regular cationic polymeric vectors, we can construct the specific binding motif for mRNA delivery. The base-pairing between poly-T and poly-A will serve as initial templates for further vector-mRNA complexation facilitated by charge interactions, which may enhance binding affinity, condense nanoparticle size, and reduce cationic charges on the particle surface. The smaller nanoparticle size and less positive zeta potential are highly preferable for promoting endocytosis, elongating circulation time, and reduce cytotoxicity.¹⁸

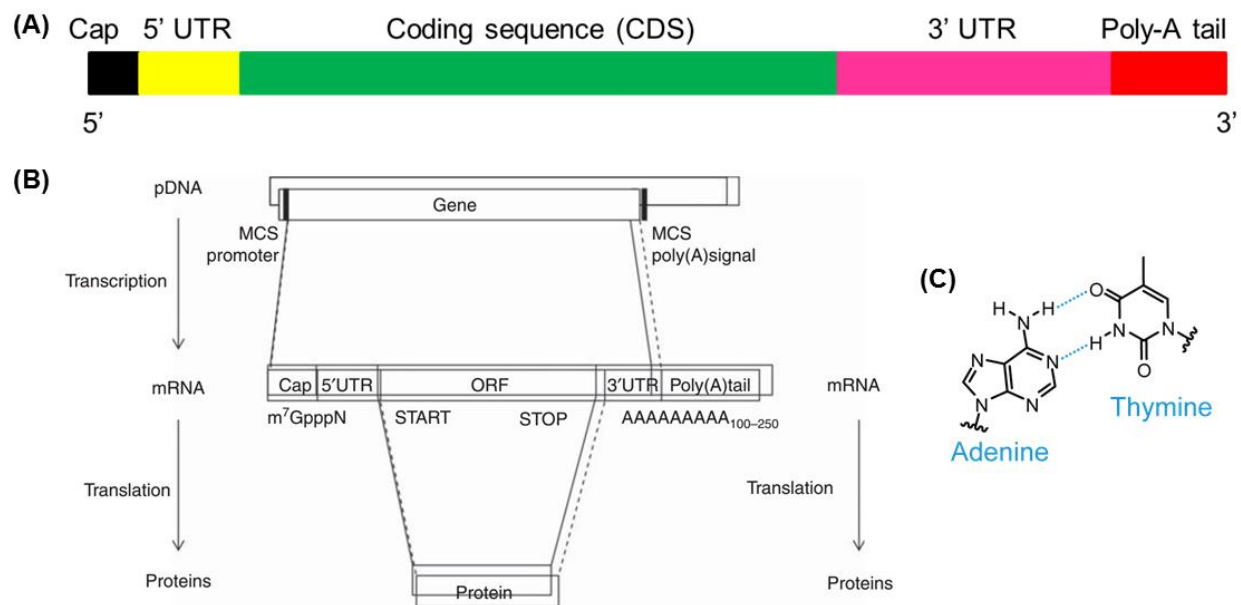


Figure 4.1 The general eukaryotic mRNA structure and hydrogen binding between adenine and thymine. (A) The structure of a typical eukaryotic mRNA. (B) pDNA-mediated gene transfer and mRNA-mediated gene transfer. Adapted and reprinted from Ref.¹⁰ (C) Hydrogen binding interactions between adenine and thymine.

To demonstrate this hypothesis, our initial trial was to functionalize gold nanoparticles with oligo poly(thymine) DNA. The poly(thymine) DNA-functionalized gold nanoparticles are able to bind with mRNA cargos after thermal annealing. But they showed minimal mRNA delivery efficacy in the subsequent transfection assays, possibly due to low cellular uptake efficiency induced by negative charges on the particle surface. The charge repulsion between anionic gold nanoparticles and anionic phosphate lipid in the cell membrane inhibited cell internalization (**Chapter 1, Section 1.6**).

Therefore, we decided to use peptide nucleic acid (PNA) to introduce poly(thymine) in the following study. PNA is a family of DNA/RNA analogues in which the sugar-phosphate backbone is replaced by pseudo-peptide backbone (**Figure 4.2A**).¹⁹ Typically, the backbone of PNA is acyclic, achiral, and neutral. PNA can bind to complementary

nucleic acids in both antiparallel Watson-Crick mode and parallel Hoogsteen mode, providing a much stronger binding affinity than DNA-DNA base matching (**Figure 4.2B**).²⁰ Since the neutral PNA backbone does not generate charge repulsion with DNA/RNA, the DNA/RNA-PNA binding is usually stable in the environment of different ionic strength. PNA has been demonstrated as a powerful biomolecular tool in the molecular genetic diagnostics with a large variety of applications, including the usage as antigene agent, antisense agent, and biosensors.²¹⁻²²

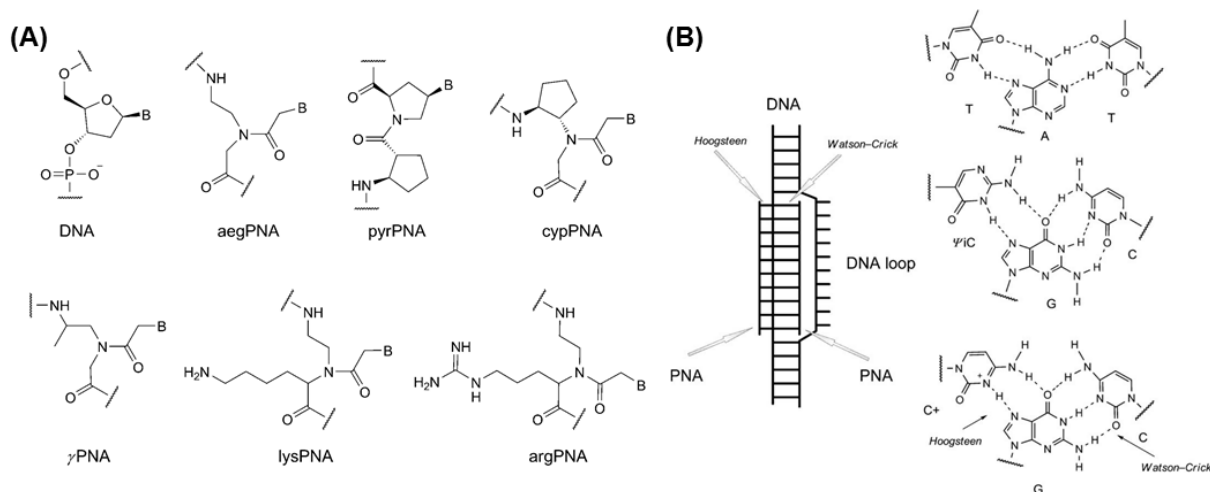


Figure 4.2 (A) Chemical structures of DNA and PNA analogues. (B) Triple base pairing between different PNA and DNA. Adapted and reprinted from Ref.²⁰

In this work, we designed a family of poly(thymine) peptide nucleic acid-functionalized bio-reducible polymers (**PTBP**) for mRNA delivery (**Figure 4.3**). The bio-reducible polymer backbone in this study is the same as the polymer backbone in **MPBP** system introduced in Chapter 2. Dicycysteine units are incorporated to provide glutathione-triggered intracellular disassembly and ensure high biocompatibility.²³ The polymer backbone is functionalized by two components: poly(thymine) oligo peptide nucleic acid (poly-T PNA) and short linear functional peptide. Different amounts of poly-T PNAs were

introduced into the **PTBP** system to bind with poly-A tails on mRNAs. This is designed to serve as initial templates for further ionic complexation. Another component is a short linear functional peptide which has been discussed in **MPBP** system (Chapter 2). Histidine (His), lysine (Lys), and tryptophan (Trp) were used to construct the peptide (H-WKHKHKHG-OH). His enhances endosomal escape through increasing buffering capacity and Lys provides cationic charge for further coulombic complexation.²⁴ In the meantime, terminal Trp improves RNA binding and cellular uptake.²⁵ We propose a two-step process to realize the templated vector-mRNA complexation for **PTBP** system. First, the **PTBP** vector was complexed with mRNA cargo at high ionic strength media, which suppressed the electrostatic interaction. The A-T interaction would direct the vector and mRNA to form templates. Then after reducing the media ionic strength, cationic-anionic charge interaction would dominate and further condense the complexes into small nanoparticles.

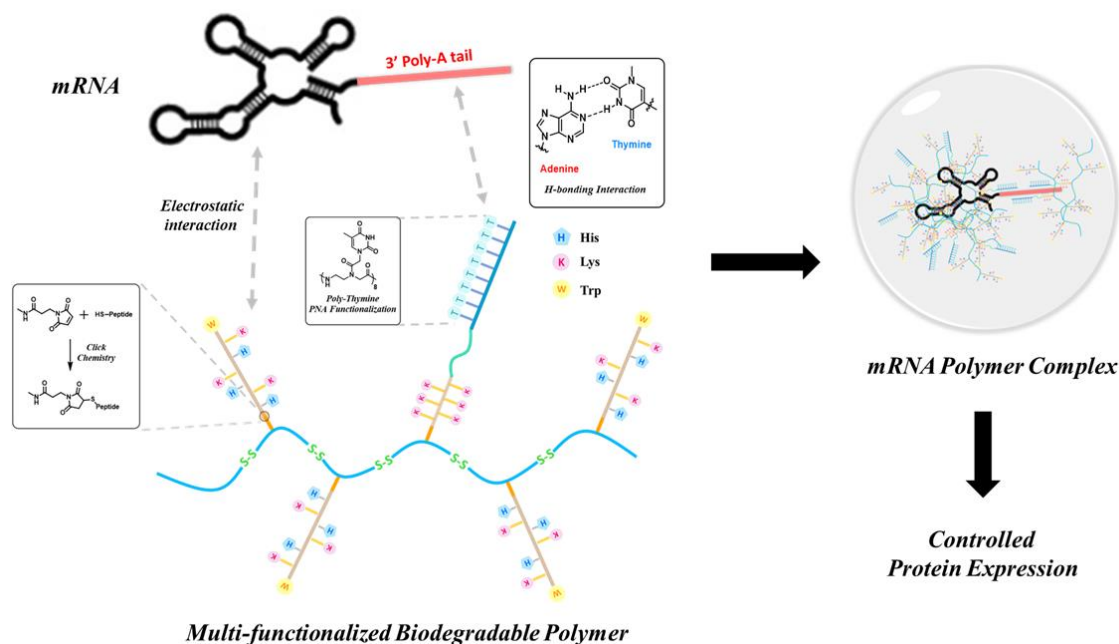
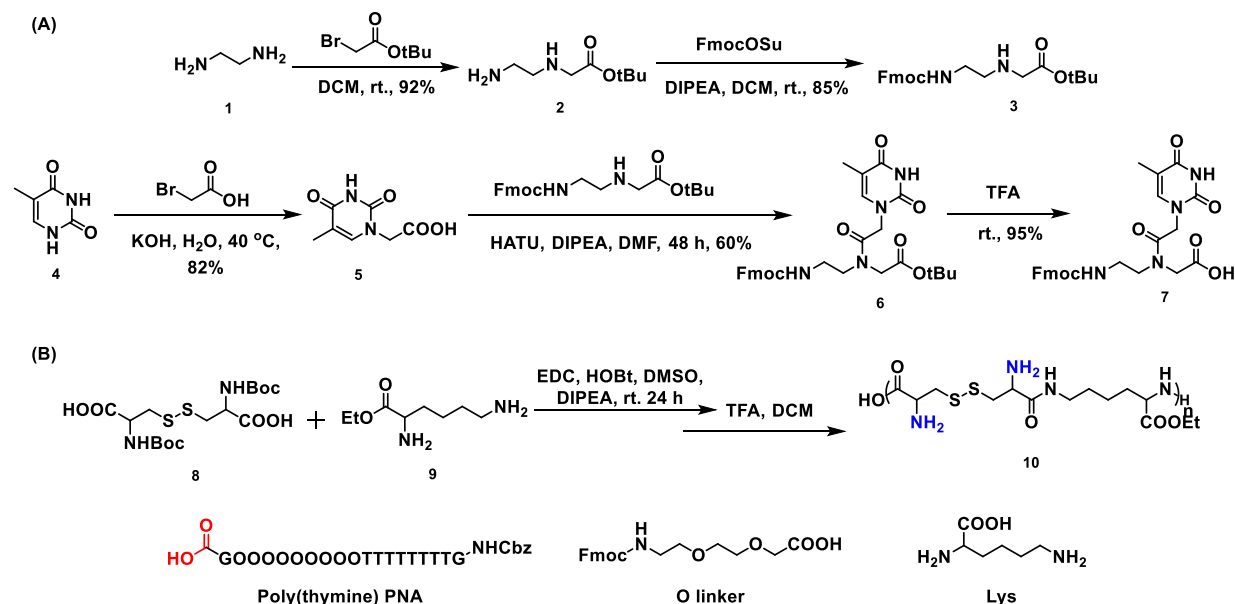


Figure 4.3 The design of poly(thymine)-functionalized bioreducible polymers (**PTBP**) for mRNA delivery.

4.2 Design and Synthesis of PTBP

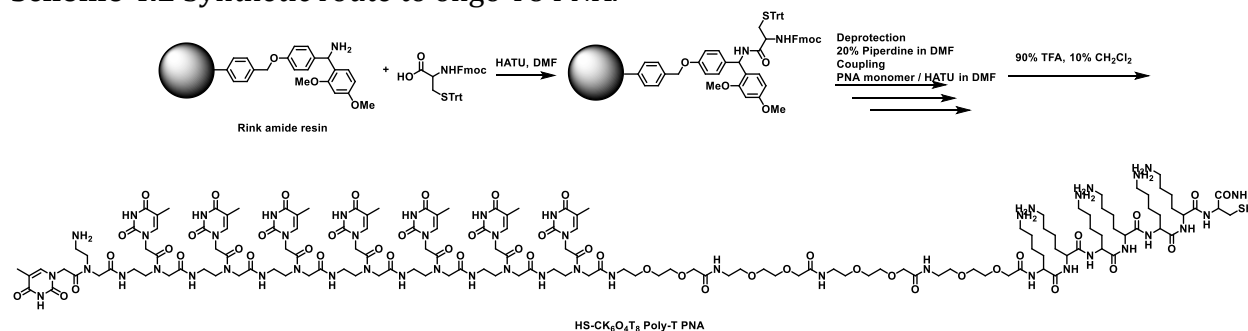
First, the thymine-containing PNA monomer and **PTBP** polymer backbone were synthesized by following the established protocol (**Scheme 4.1**).²⁶⁻²⁷ The synthesis of poly-T PNA was performed through conventional solid-phase peptide synthesis.²⁸ Oligo poly-T PNA is a synthetic challenging due to the poor solubility.²⁹ Ethylene glycol linker (O linker) and lysine were incorporated into the PNA sequence to enhance the solubility which is crucial for the subsequent polymer functionalization. Noticeably, all side chains and N-terminus of poly-T PNA need to be fully protected in order to avoid cross-reactions in the following amide coupling process. Unfortunately, even though substantial O linker units were incorporated into the poly-T PNA sequence, the poor solubility still hindered the subsequent polymer functionalization. Lys units need to be deprotected to expose primary amines in order to enhance solubility. Therefore, we changed our PNA design and functionalization strategy.

Scheme 4.1 Synthetic route to PNA monomer and PTBP backbone. (A) Synthetic route to poly-T PNA monomer (B) Synthetic route to **PTBP** backbone and the structure of poly-T PNA.



After initial binding strength calculation, oligo T8 PNA was chosen in our **PTBP** study. In order to ensure good PNA solubility for the following purification and functionalization reaction, several Lys units and O linker units were incorporated into the PNA sequence. After loading *L*-cysteine (Cys) as the first amino acid onto rink amide resin, we performed our PNA synthesis through traditional solid phase peptide synthesis (**Scheme 4.2**). In the last step, high concentration of trifluoroacetic acid (TFA) was used to cleave the peptide from the resin, as well as deprotect all of the amino acids. Fortunately, the oligo T8 PNA generated from this route has sufficient solubility for HPLC purification and subsequent reaction. However, due to the deprotected primary amines on the PNA, another conjugation strategy which is orthogonal to amide coupling was needed for polymer functionalization. Herein, we chose thiol-maleimide click chemistry for the following functionalization reaction (**Scheme 4.3**). First, the obtained bio reducible polymer backbone was functionalized by maleimide NHS ester, affording maleimide-grafting bio reducible polymer (MFBP). Then both Cys-terminated linear functional peptide (HS-CHKHKHKW) and Cys-terminated oligo T8 PNA were conjugated onto the polymer backbone through thiol-maleimide click chemistry. A control sample (PTBP-control) without PNA incorporation was obtained for comparison. Two samples with different amounts of T8 PNA functionalization were obtained for further study. For simplicity, the **PTBPs** were named as PTBP-T8-*X*, where *X* indicates the percentage of PNA functionalization. The details of synthesized PTBPs can be found in **Table 4.1**. All details for the peptide, PNA, and polymer synthesis and characterization can be found in **Section 4.7 – 4.8**.

Scheme 4.2 Synthetic route to oligo T8 PNA.



Scheme 4.3 Synthetic route to PTBP.

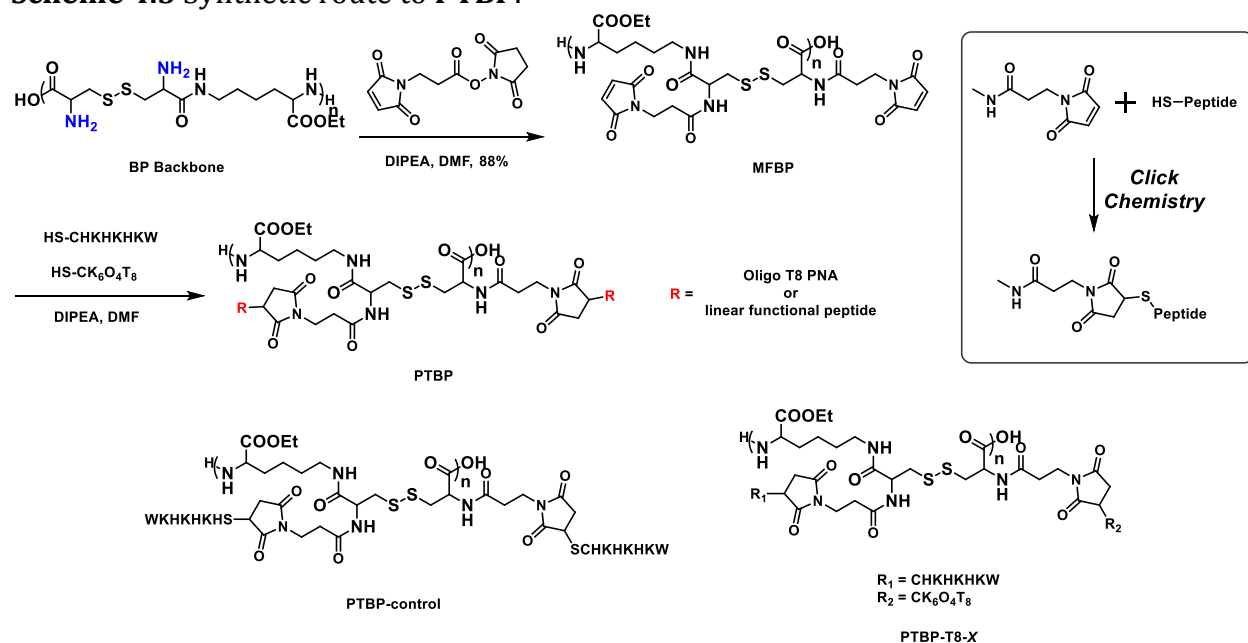


Table 4.1 Detailed summary of synthesized **PTBPs**.

Sample name	Molecular weight per repeating unit (g/mol)	Primary amine per repeating unit	Functionalization
PTBP-control	2573	7.25	87.5 mol% CHKHKHKW
PTBP-T8-11	3150	7.93	11.6 mol% T8 PNA 75.8% CHKHKHKW
PTBP-T8-19	3547	8.42	19.0 mol% T8 PNA 68.5% CHKHKHKW

4.3 Biophysical Study of PTBP-mRNA Complexes

PTBP-control and **PTBP-T8-11** were chosen as representative vectors for mRNA complexation studies. The complexation processes are illustrated in **Figure 4.4**. First, eGFP mRNA was heated at 55 °C for 5 minutes and chilled in ice. This process was used to unfold mRNA secondary structure. Second, different **PTBP** vectors were complexed with mRNAs in the media of high salt concentration, which suppressed electrostatic interaction between cationic peptides and anionic mRNAs. Third, the complex solution was subjected to a thermal annealing process, which facilitated the interaction between poly-T PNA and poly-A mRNA. Finally, the complex solution was eluted through a desalting column, in order to change complex media back to water. The decreased ionic strength allowed stronger coulombic interaction between vectors and mRNAs, which further condensed the complexes into smaller nanoparticles. The **PTBP**-mRNA complexes in both high salt media and water were analyzed by dynamic light scattering (DLS) (**Table 4.2**). In high salt media, **PTBP-control** and **PTBP-T8-11** formed large nanoparticles (~500 nm) with mRNA whereas both complexes became significantly smaller after desalting. No significant differences were observed for these two vectors, possibly due to the overwhelming presence of electrostatic interaction. With a higher N/P ratio (N/P = 10), **PTBP** vectors were able to form small nanoparticles of less than 100 nm size in diameter with eGFP mRNA. Further zeta potential tests (**Section 4.7**) showed that both **PTBP-control**-mRNA and **PTBP-T8-11**-mRNA complexes were close to neutral (**Table 4.2**), which are beneficial for lower toxicity and aggregation in biological transfections.

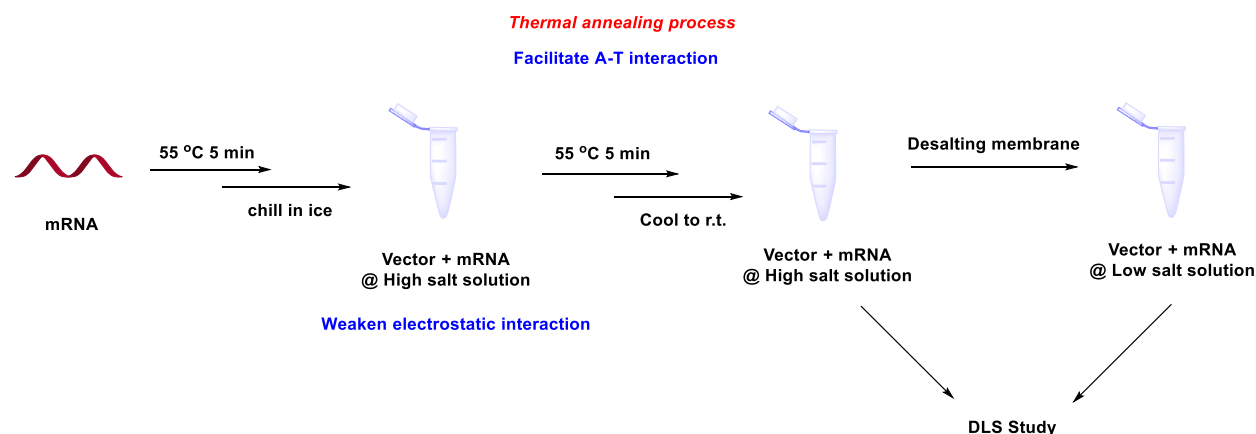


Figure 4.4 Graphic illustration of PTBP-mRNA complexation processes.

Table 4.2 Nanoparticle sizes of **PTBP**-eGFP mRNA complexes determined by DLS. The particles were tested in two different media, 2 M NaCl solution and nano-pure water.

Sample	Solvent	N/P ratio	Z-average size (nm)	PDI	Zeta Potential (mV)
PTBP-control	2 M NaCl	5	542.3	0.280	—
PTBP-T8-11	2 M NaCl	5	519.6	0.270	—
PTBP-control	water	5	272.7	0.355	—
PTBP-T8-11	water	5	283.3	0.344	—
PTBP-control	water	10	94.13	0.262	-5.70
PTBP-T8-11	water	10	74.50	0.329	0.52

Gel binding assays were performed to further study the complexation between **PTBPs** and mRNAs. First, different **PTBPs** were complexed with mRNA at various N/P ratios and the nanoparticle complexes were subjected to gel electrophoresis study (**Figure 4.5A**). The results showed that both **PTBP**-control and **PTBP**-T8-11 completely bound to mRNA starting at very low N/P ratio (N/P = 1), indicating that the **PTBP** vectors have strong binding affinity to mRNA cargos. To differentiate the vectors with and without poly-T PNA functionalization, a series of dextran sulfate competitive binding assays were

performed (**Figure 4.5B**). First, different PTBP vectors were complexed with mRNA at $N/P = 2$ by following aforementioned protocol (**Figure 4.4**). Dextran sulfate (MW = 25 kDa), an anionic polymer was added to challenge the complexation between **PTBPs** and mRNAs. For this purpose, the **PTBP**-mRNA complexes were incubated with different amount of dextran sulfate (different S/P ratio, the molar ratio of sulfate groups from DS and phosphate groups from mRNA) to compete with mRNA. As shown in the results, mRNA release was observed at S/P = 10 for **PTBP**-T8-19-mRNA complexes whereas the mRNA cargo was released at S/P = 5 for **PTBP**-control-mRNA complexes. This indicated that oligo T8 PNA functionalization induced stronger mRNA binding for the **PTBP** vectors.

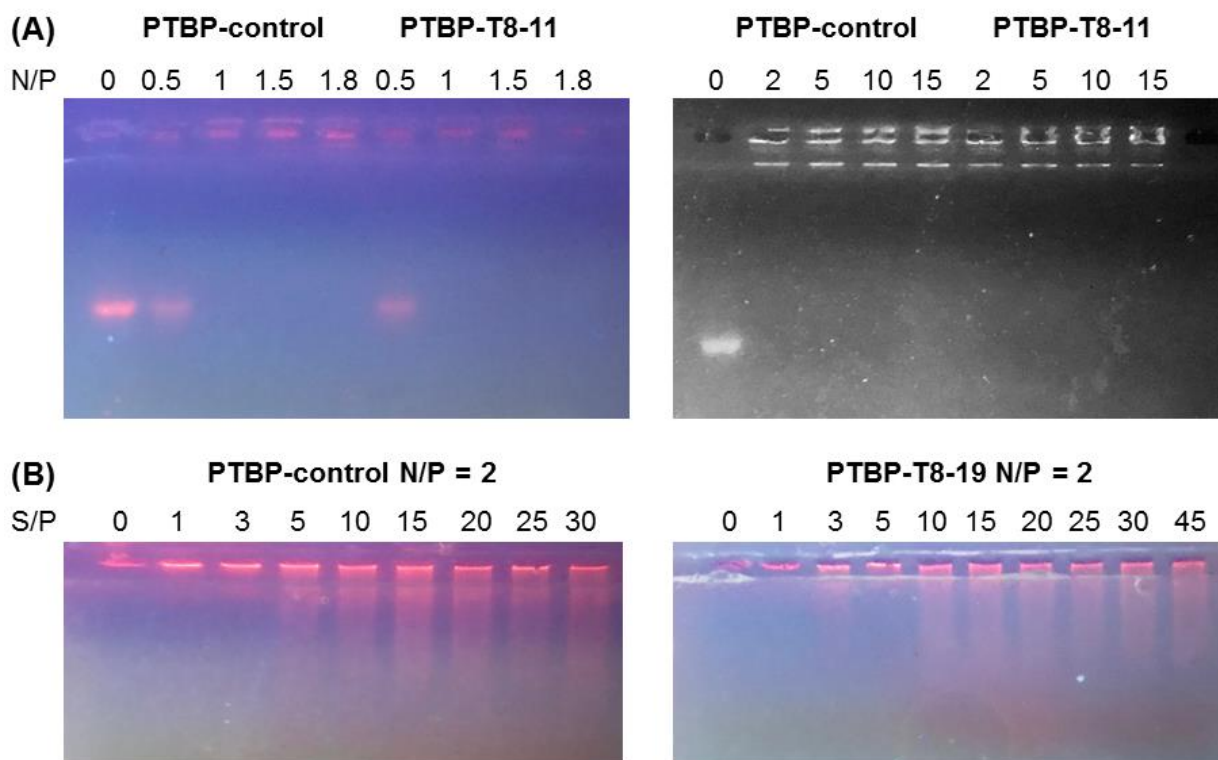


Figure 4.5 Gel binding assays of PTBP-eGFP mRNA complexes. (A) Gel electrophoresis study of PTBP-eGFP mRNA complexation. (B) Dextran sulfate competitive assays of different PTBP-eGFP mRNA complexes. $N/P = 2$.

4.4 mRNA Delivery

After establishing the vector-mRNA complexation method, the **PTBPs** were used to deliver Fluc mRNA and eGFP mRNA. First, **PTBP** vectors were complexed with mRNAs at different N/P ratios by following aforementioned protocol. Then NIH 3T3 cells were treated with different **PTBP**-mRNA nanocomplexes. Lipofectamine MessengerMAX (LF MM) was used as a positive control and naked mRNA alone and untreated cells were used as negative controls. After 24 hours following transfection, the luciferase activity was assayed by an IVIS camera for Fluc mRNA delivery and eGFP expression was measured via flow cytometry for eGFP mRNA delivery. The transfection results are presented in **Figure 4.6 – 4.7**.

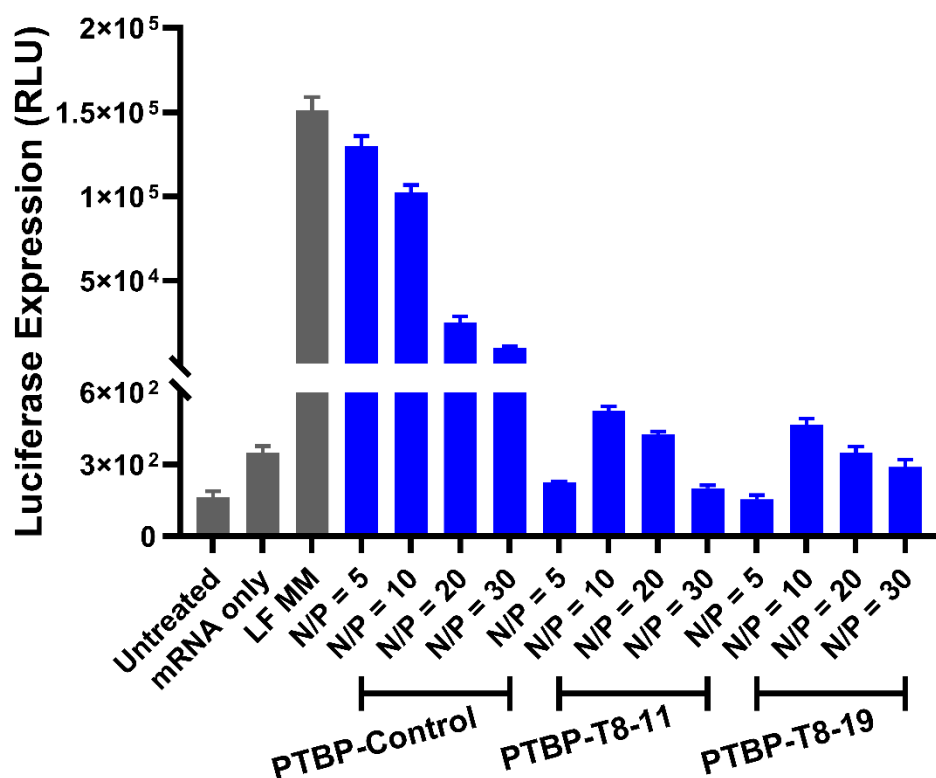


Figure 4.6 Fluc mRNA transfection using different **PTBPs** at different N/P ratios in NIH 3T3 cells (150 ng mRNA per well), serum-free media.

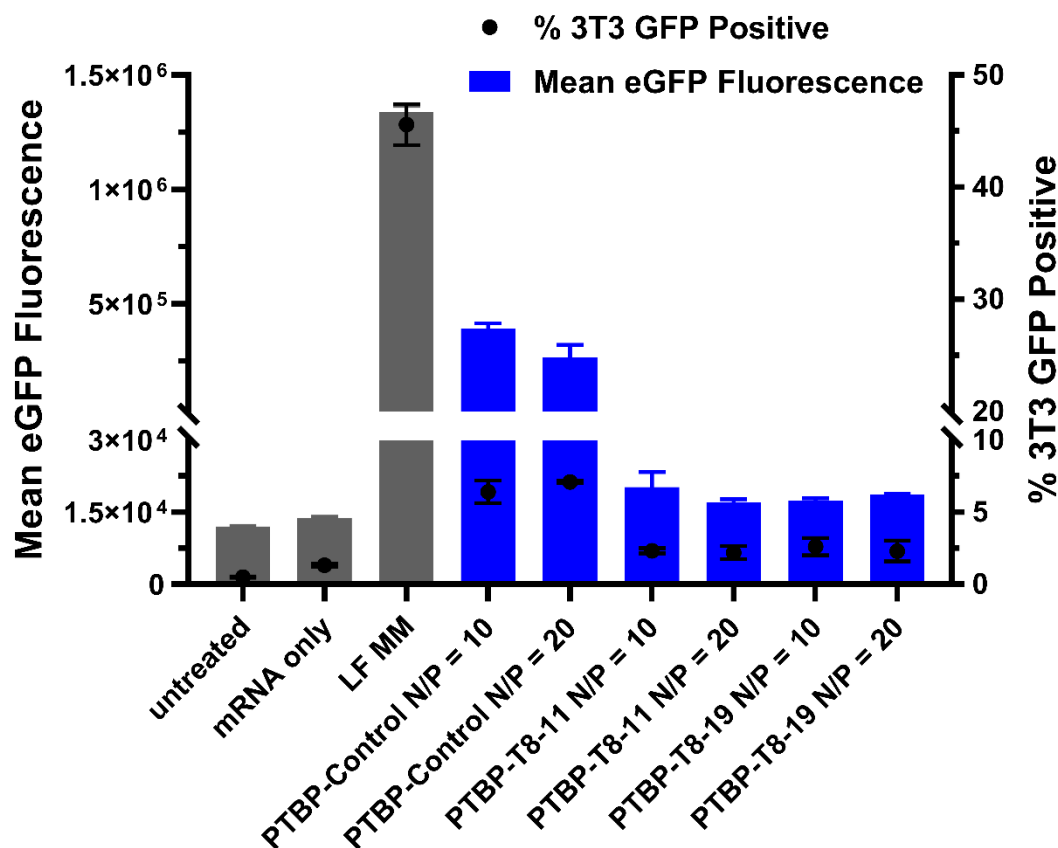


Figure 4.7 eGFP mRNA transfection using different **PTBPs** at different N/P ratios in NIH 3T3 cells (150 ng mRNA per well), serum-free media.

PTBP vectors without oligo T8 PNA functionalization, **PTBP-control** exhibited similar transfection efficacy to LF MM in Fluc mRNA delivery. However, all vectors with oligo T8 PNA functionalization were not effective for neither Fluc mRNA nor eGFP mRNA delivery. From eGFP mRNA delivery, less than 5% NIH 3T3 cells were successfully transfected for **PTBP-T8** series vectors. We believe this is due to the excessively strong base pairing between oligo T8 PNA and poly-A tail on mRNA. Several studies have shown that poly-A tail actually plays important role in mRNA translation processes. 3'-terminal poly-A tail and the 5'-terminal caps are the canonical stimulators of protein synthesis in

ribosome. It is shown that the poly-A-binding protein (PABP) in the cytoplasm associated with poly-A tail stimulates translation initiation.³⁰ Several models and mechanisms were proposed to illustrate the effect of PABP on translation (**Figure 4.8**).³¹⁻³² Further gel binding assay confirmed that the **PTBP** vectors were not able to efficiently release mRNA after disulfide degradation by glutathione (**Section 4.7**). This indicated that the strong hydrogen bonding between poly-A and poly-T inhibited the interaction between poly-A tail and PABP, which prevented the successful mRNA translation. For further studies, structural modification of the **PTBP** vectors is needed to weaken the A-T interaction in order to enhance transfection efficacy.

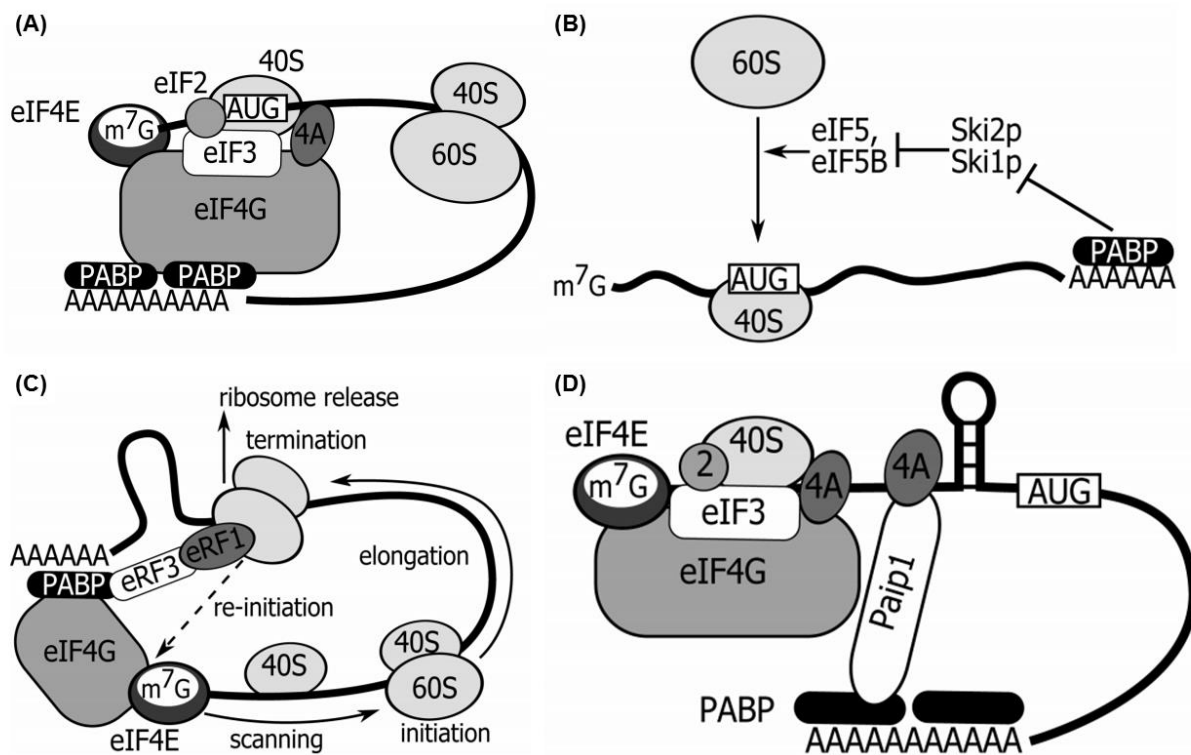


Figure 4.8 Models of initiation processes in protein synthesis. (A) "Closed loop" model. (B) Model of PABP effect on 60S subunit recruitment stimulation. (C) Ribosome recycling model. (D) Paip1-induced translation stimulation model. Adapted and reprinted from Ref.³⁰

4.5 Conclusions

In summary, we designed and constructed a series of poly(thymine) peptide nucleic acid-functionalized bio reducible polymers (**PTBPs**) for mRNA delivery. Oligo T8 PNA and linear short peptides were used to functionalize the biodegradable polymer backbone. Oligo T8 units were used to bind poly-A tail of mRNA cargo, serving as a template for further complexation. Gel electrophoresis studies confirmed the high binding affinity between **PTBP** vectors and mRNAs. DLS studies exhibited the vectors were able to form small (less than 100 nm) and stable nanoparticle complexes with mRNA cargos. Unfortunately, cell transfection study showed the mRNA delivery by **PTBP** vectors was unsuccessful, possibly because the overwhelming strong base pairing between poly-A and poly-T inhibited the binding between poly-A tails and poly(A)-binding proteins. Nonetheless, we believe the idea of introducing hydrogen-binding interaction into vector-RNA complexation and the design and synthesis of PNA-functionalized biodegradable polymers are still interesting and beneficial to the design and development of mRNA delivery materials. For further studies, the vector structure need to be further optimize to address the current issue.

4.6 References

- (1) Sahin, U.; Kariko, K.; Tureci, O., mRNA-based therapeutics--developing a new class of drugs. *Nat. Rev. Drug Discov.* **2014**, *13* (10), 759-780.
- (2) Kaczmarek, J. C.; Kowalski, P. S.; Anderson, D. G., Advances in the delivery of RNA therapeutics: from concept to clinical reality. *Genome Med* **2017**, *9* (1), 60.
- (3) Zhong, Z.; Mc Cafferty, S.; Combes, F.; Huysmans, H.; De Temmerman, J.; Gitsels, A.; Vanrompay, D.; Portela Catani, J.; Sanders, N. N., mRNA therapeutics deliver a hopeful message. *Nano Today* **2018**, *23*, 16-39.
- (4) Mitragotri, S.; Burke, P. A.; Langer, R., Overcoming the challenges in administering biopharmaceuticals: formulation and delivery strategies. *Nat. Rev. Drug Discovery* **2014**, *13* (9), 655-672.
- (5) Nguyen, J.; Szoka, F. C., Nucleic Acid Delivery: The Missing Pieces of the Puzzle? *Acc. Chem. Res.* **2012**, *45*, 1153-1162.
- (6) Dowdy, S. F., Overcoming cellular barriers for RNA therapeutics. *Nat. Biotechnol.* **2017**, *35* (3), 222-229.
- (7) Behr, J. P., Synthetic Gene Transfer Vectors II: Back to the Future. *Acc. Chem. Res.* **2012**, *45*, 980-984.
- (8) Mattison, K. W.; Dubin, P. L.; Brittain, I. J., Complex formation between bovine serum albumin and strong polyelectrolytes: Effect of polymer charge density. *J Phys Chem B* **1998**, *102* (19), 3830-3836.
- (9) Kranz, L. M.; Diken, M.; Haas, H.; Kreiter, S.; Loquai, C.; Reuter, K. C.; Meng, M.; Fritz, D.; Vascotto, F.; Hefesha, H.; Grunwitz, C.; Vormehr, M.; Husemann, Y.; Selmi, A.; Kuhn, A. N.; Buck, J.; Derhovanessian, E.; Rae, R.; Attig, S.; Diekmann, J.; Jabulowsky, R. A.; Heesch, S.; Hassel, J.; Langguth, P.; Grabbe, S.; Huber, C.; Tureci, O.; Sahin, U., Systemic RNA delivery to dendritic cells exploits antiviral defense for cancer immunotherapy. *Nature* **2016**, *534* (7607), 396-401.
- (10) Youn, H.; Chung, J.-K., Modified mRNA as an alternative to plasmid DNA (pDNA) for transcript replacement and vaccination therapy. *Expert Opin. Biol. Ther.* **2015**, *15* (9), 1317-1348.
- (11) Guhaniyogi, J.; Brewer, G., Regulation of mRNA stability in mammalian cells. *Gene* **2001**, *265*, 11-23.
- (12) Sarkar, N., Polyadenylation of mRNA in Prokaryotes. *Annu. Rev. Biochem.* **1997**, *66*, 173-197.
- (13) Lewis, J. D.; Gunderson, S. I.; Mattaj, I. W., The influence of 50 and 30 end structures on pre-mRNA metabolism. *J. Cell. Sci. Suppl.* **1995**, *19*, 13-19.
- (14) Wickens, M.; Anderson, P.; Jackson, R. J., Life and death in the cytoplasm: messages from the 30 end. *Curr. Opin. Genet. Dev.* **1997**, *7*, 220-232.
- (15) Tian, B.; Hu, J.; Zhang, H.; Lutz, C. S., A large-scale analysis of mRNA polyadenylation of human and mouse genes. *Nucleic Acids Research.* **2005**, *33* (1), 201-212.

- (16) Sabale, P. M.; Ambi, U. B.; Srivatsan, S. G., A Lucifer-based environment-sensitive fluorescent PNA probe for imaging poly(A) RNAs. *ChemBioChem*. **2018**, *19*, 826-835.
- (17) Thomsen, R.; Nielsen, P. S.; Jensen, T. H., Dramatically improved RNA in situ hybridization signals using LNA-modified probes. *RNA* **2005**, *11*, 1745-1748.
- (18) Resnier, P.; Montier, T.; Mathieu, V.; Benoit, J. -P.; Passirani, C., A review of the current status of siRNA nanomedicines in the treatment of cancer. *Biomaterials* **2013**, *34*, 6429-6443.
- (19) Nielsen, P. E.; Egholm, M., An introduction to peptide nucleic acid. *Current Issues Molec. Biol.* **1999**, *1* (2), 89-104.
- (20) Nielsen, P. E., Peptide nucleic acids (PNA) in chemical biology and drug discovery. *Chem. Biodiversity* **2010**, *7*, 786-804.
- (21) Gupta, A.; Mishra, A.; Puri, N., Peptide nucleic acids: advanced tools for biomedical applications. *J. Biotechnol.* **2017**, *259*, 148-159.
- (22) Wu, J.; Meng, Q.; Ren, H.; Wang, H.; W, J.; Wang, Q., Recent advances in peptide nucleic acid for cancer bionanotechnology. *Acta Pharmacol. Sin.* **2017**, *38*, 798-805.
- (23) Son, S.; Namgung, R.; Kim, J.; Singha, K.; Kim, W. J., Bio-reducible Polymers for Gene Silencing and Delivery. *Acc. Chem. Res.* **2012**, *45*, 1100-1112.
- (24) Midoux, P.; Pichon, C.; Yaouanc, J. J.; Jaffres, P. A., Chemical vectors for gene delivery: a current review on polymers, peptides and lipids containing histidine or imidazole as nucleic acids carriers. *Br. J. Pharmacol.* **2009**, *157* (2), 166-178.
- (25) Jobin, M. L.; Blanchet, M.; Henry, S.; Chaignepain, S.; Manigand, C.; Castano, S.; Lecomte, S.; Burlina, F.; Sagan, S.; Alves, I. D., The role of tryptophans on the cellular uptake and membrane interaction of arginine-rich cell penetrating peptides. *Biochim. Biophys. Acta* **2015**, *1848* (2), 593-602.
- (26) Thomson, S. A.; Josey, J. A.; Cadilla, R.; Gaul, M. D.; Hassman, C. F.; Luzzio, M. J.; Pipe, A. J.; Reed, K. L.; Ricca, D. J.; Wiethe, R. W.; Noble, S. A., Fmoc mediated synthesis of peptide nucleic acids. *Tetrahedron* **1995**, *51*, 6179-6194.
- (27) Zeng, H.; Little, H. C.; Tiambeng, T. N.; Williams, G. A.; Guan, Z., Multifunctional dendronized peptide polymer platform for safe and effective siRNA delivery. *J. Am. Chem. Soc.* **2013**, *135* (13), 4962-4965.
- (28) Amant, A. H. St.; Hudson, R. H. E., Synthesis and oligomerization of Fmoc/Boc-protected PNA monomers of 2,6-diaminopurine, 2-aminopurine and thymine. *Org. Biomol. Chem.*, **2012**, *10*, 876-881.
- (29) Siddiquee, S.; Rovina, K.; Azria, A., A review of peptide nucleic acid. *Adv. Tech. Biol. Med.* **2015**, *3* (2), 1000131.
- (30) Eliseeva, I. A.; Lyabin, D. N.; Ovchinnikov, L. P., Poly(A)-binding proteins: structure, domain organization, and activity regulation. *Biochemistry* **2013**, *78* (13), 1377-1391.

- (31) Gray, N. K.; Coller, J. M.; Dickson, K. S.; Wickens, M., Multiple portions of poly(A)-binding protein stimulate translation *in vivo*. *EMBO J.* **2000**, *19*, 4723-4733.
- (32) Wells, S. E.; Hillner, P. E.; Vale, R. D.; Sachs, A. B., Circularization of mRNA by Eukaryotic translation initiation factors. *Mol. Cell*, **1998**, *2*, 135-140.

4.7 Experimental

Materials. All commercially available chemicals were used without further purification unless otherwise noted. Protected amino acids were purchased from Advanced ChemTech (Louisville, KY) and Aroz Technologies, LLC. (Cincinnati, OH). Coupling reagents were purchased from GL Biochem Ltd. (Shanghai, China). CleanCap® eGFP mRNA (5moU) and Fluc mRNA (5moU) were obtained from TriLink Biotechnologies (Sorrento Mesa, CA). Lipofectamine MessengerMAX was purchased from Invitrogen (Carlsbad, CA) and used as positive controls following the manufacturer's protocol. All reactions were performed using HPLC grade solvents unless otherwise noted. All water used in biological experiments was Nanopure water obtained from Barnstead Nanopure Diamond (Waltham, MA). Unmodified NIH 3T3 cells were a generous gift from Professor Young Jik Kwon (Department of Chemical Engineering, UC Irvine, CA). Dulbecco's modified Eagle's medium (DMEM), fetal bovine serum (FBS), and OptiMEM were purchased from Invitrogen (Carlsbad, CA).

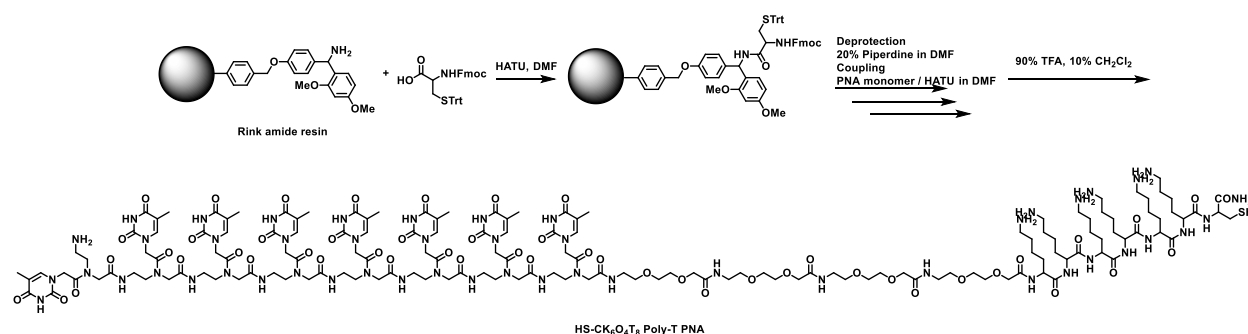
Instruments. Nuclear Magnetic Resonance (NMR) spectra were recorded on 500 MHz or 600 MHz Bruker spectrometers. Chemical shifts were reported in ppm. Coupling constants (*J* values) were reported in Hertz. ¹H NMR chemical shifts were referenced to D₂O (δ = 4.79 ppm), CD₃OD (δ = 3.31 ppm), and DMF-d₇ (δ = 8.03, 2.92, 2.75 ppm). The molecular weight and molecular weight distribution of the polymer backbone was measured by gel

permeation chromatography (GPC). GPC was performed on an Agilent 1100 SEC system using an OHpak SB-803 HQ column from Shodex. The molecular weight was determined with respect to poly(ethylene glycol) (PEG) S3 standards purchased from Aldrich. DMF with 0.1% LiBr (wt/v) was used as the eluent at a flow rate of 1.0 mL/min with column temperature at 45°C. The Z-average size and zeta potential of **PTBP**-mRNA polyplexes were measured at 633 nm using Zetasizer (NanoZS) dynamic light scattering instrument (Malvern Instruments, Malvern, UK) at 25 °C with detection angle of 173°. Flow cytometry was performed on a BD ACCURI C6 flow cytometer (BD Biosciences, San Jose). Solid-phase peptide synthesis and PNA synthesis were performed on a Protein Technologies PS3 synthesizer. Matrix assisted laser desorption ionization spectral data (MALDI) was obtained from the UC Irvine Mass Spectrometry Facility and collected with an AB SCIEX TOF/TOF 5800 System. NapTM-5 columns (SephadexTM G-25 DNA Grade) was purchased from GE Healthcare.

PTBP synthesis and characterization

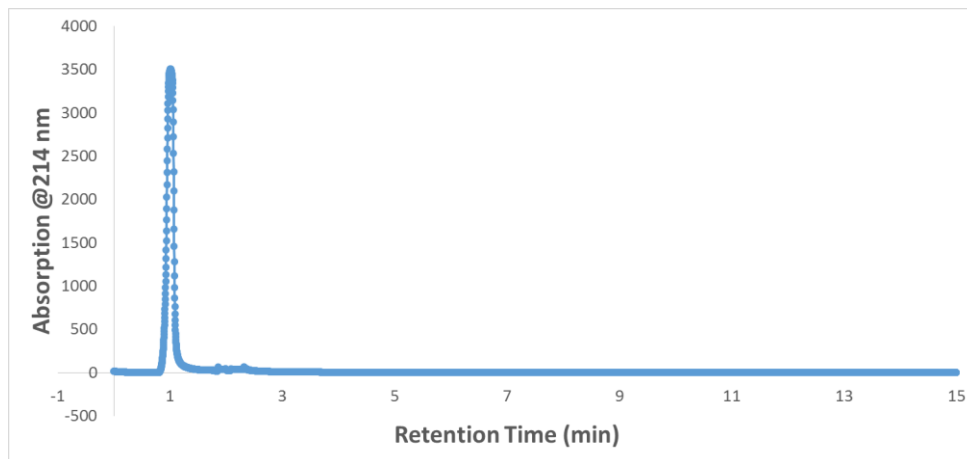
Functional linear peptide (H-WKHKHKHC-OH): Rink amide resin was first loaded with Fmoc-Cys-OH at the loading density of 0.283 mmol/g. Following the sequence of HKHKHKW, Cys-loaded resin (300 mg, 1.0 equiv., 0.085 mmol) was coupled with 3 different side-chain protected amino acids on a PS3 solid-phase peptide synthesizer. For each coupling step, one amino acid was added for reaction: Fmoc-His(Trt)-OH (263 mg, 5.0 equiv., 0.42 mmol), Fmoc-Lys(Boc)-OH (199 mg, 5.0 equiv., 0.42 mmol), or Boc-Trp(Boc)-OH (172 mg, 5.0 equiv., 0.42 mmol). HATU (145 mg, 4.5 equiv., 0.38 mmol) was utilized as coupling reagent and HOAt (52 mg, 4.5 equiv., 0.38 mmol) was included to suppress the

possible epimerization. 20% collidine in DMF was used in the coupling reaction and 20% piperidine in DMF was used to deprotect the Fmoc group. After the synthesis was finished, the functional linear peptide was cleaved from the resin and deprotected by using 90% TFA in anhydrous CH_2Cl_2 . After removal of the solvent under reduced pressure, the residue was obtained as a white solid to give 66 mg (71%) of **functional linear peptide (H-WKHKHKHC-OH)**. The synthesized linear peptide was purified by C18 reverse-phase chromatography and utilized for the following click reactions.



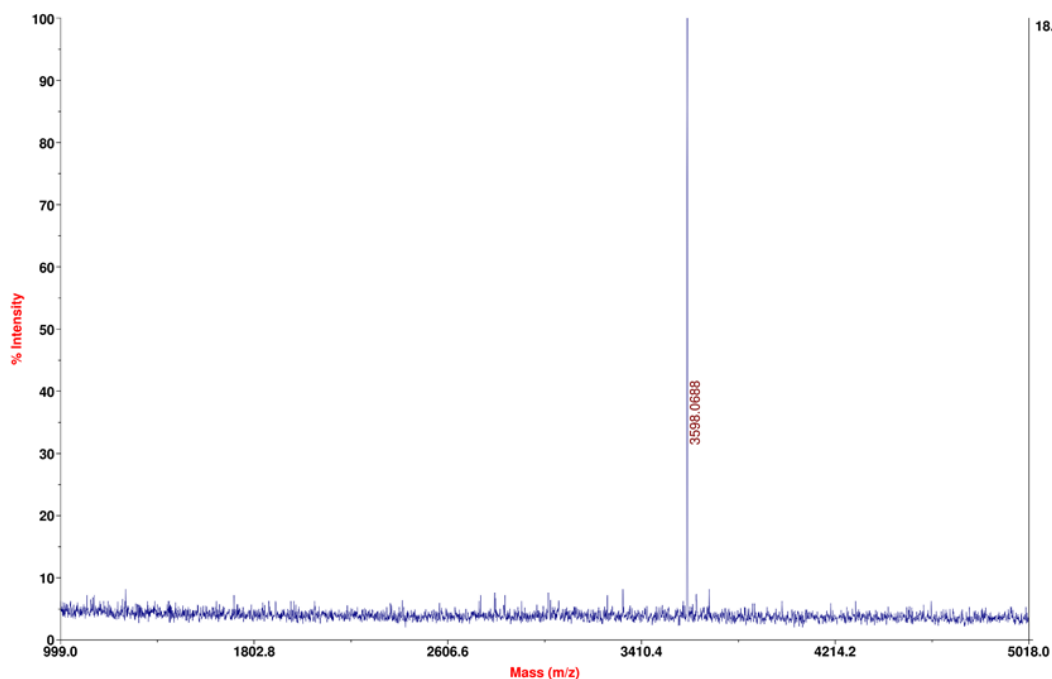
Oligo T8 PNA synthesis (H-T₈O₄K₆C-OH): Rink amide resin was first loaded with Fmoc-Cys-OH at the loading density of 0.312 mmol/g. Following the sequence of KKKKKKOOOOTT TTTT TTTT, Cys-loaded resin (250 mg, 1.0 equiv., 0.078 mmol) was coupled with 3 different side-chain protected amino acids on a PS3 solid-phase peptide synthesizer. For each coupling step, one amino acid was added for reaction: Fmoc-Lys(Boc)-OH (183 mg, 5.0 equiv., 0.39 mmol), Fmoc-O linker-OH (150 mg, 5.0 equiv., 0.39 mmol), or Fmoc-T monomer-OH (198 mg, 5.0 equiv., 0.39 mmol). HATU (133 mg, 4.5 equiv., 0.35 mmol) was utilized as coupling reagent and HOAt (48 mg, 4.5 equiv., 0.35 mmol) was included to suppress the possible epimerization. 20% collidine in DMF was used in the coupling reaction and 20% piperidine in DMF was used to deprotect the Fmoc group. After the synthesis was finished, the functional linear peptide was cleaved from the resin and

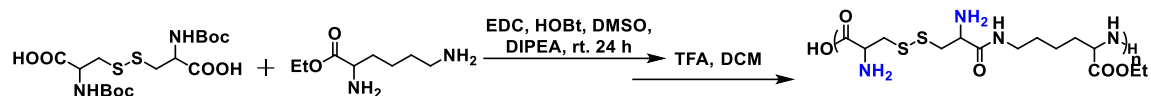
deprotected by using 90% TFA in anhydrous CH₂Cl₂. After removal of the solvent under reduced pressure, the residue was obtained as a white solid to give 78 mg (28%) of **Oligo T8 PNA (H-T₈O₄K₆C-OH)**. The synthesized peptide nucleic acid was purified by C18 reverse-phase chromatography, characterized by analytical HPLC and MALDI-TOF MS, and utilized for the following click reactions. MALDI-TOF MS m/z : 3598.0688 [M+H]⁺.



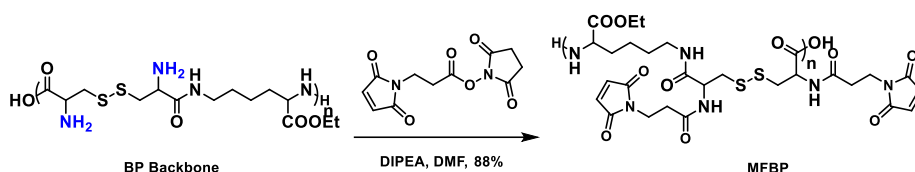
Applied Biosystems MDS Analytical Technologies TOF/TOF™ Series Explorer™ 72039

TOF/TOF™ Reflector Spec #1=>NF0.7[BP = 3600.1, 18]

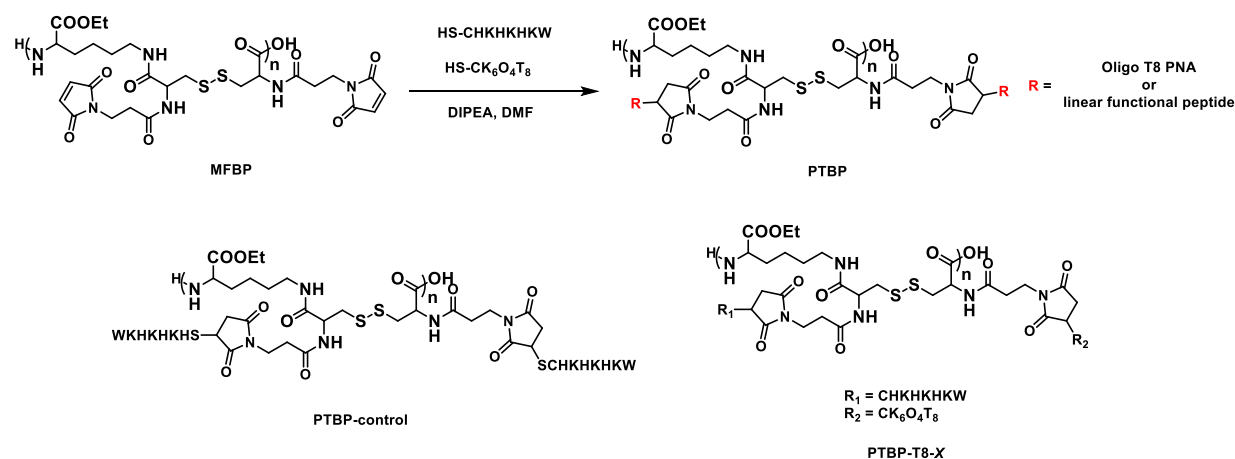




The **PTBP** polymer backbone was synthesized and characterized by following the published protocol (Chapter 2).²⁷ ¹H NMR (600 MHz, CD₃OD, 298 K, ppm): δ 4.46 – 4.39 (m, 2H), 4.24 – 4.21 (m, 3H), 3.59 – 3.21 (m, 8H), 3.74 – 3.56 (m, 12.5H), 1.91 – 1.79 (m, 2H), 1.59 – 1.57 (m, 2H), 1.42 – 1.41 (m, 2H), 1.28 (t, J = 7.0 Hz, 3H).



Maleimide-functionalized bio-reducible polymer (MFBP): A solution of BP backbone (30.0 mg, 4.94×10^{-2} mmol repeating units), maleimide-NHS ester (31.7 mg, 1.19×10^{-1} mmol), and DIPEA (25.8 μ L, 1.48×10^{-1} mmol) in DMF (200 μ L) was stirred at room temperature for 24 h under nitrogen. After removal of the solvents under reduced pressure, the residue was dissolved in MeOH and purified via dialysis (MWCO = 6 – 8 kDa) against MeOH for 24 h. Then MeOH was removed *in vacuo* to give **MFBP** (23 mg, 75%) as a clear oil. ¹H NMR (600 MHz, DMF-d₇, 298 K, ppm): δ 7.00 (s, 3.5H), 4.86 – 4.72 (m, 2H), 4.32 – 4.14 (m, 3H), 3.74 – 3.56 (m, 12.5H), 3.18 (s, 3.5H), 2.60 (s, 4H), 1.82 – 1.43 (m, 7H), 1.22 (m, 3H).



General procedure for synthesis of PTBP: A solution of **MFBP** (1.0 equiv), Cys-terminated linear peptide (HS-CHKHKHKW), oligo T8 PNA (HS-CK₈O₄T₆), and DIPEA (2 equiv) was stirred at room temperature for 24 h under nitrogen. The amounts of HS-CHKHKHKW and HS-CK₈O₄T₆ were determined according to the functionalization ratio. For instance, 0.2 equiv HS-CK₈O₄T₆ and 1.8 equiv HS-CHKHKHKW for sample PTBP-T8-10. After removal of the solvents under reduced pressure, the residue was dissolved in MeOH and purified via dialysis (MWCO = 6 – 8 kDa) against MeOH for 24 h. Then MeOH was removed *in vacuo* to give **PTBP** vector as a clear oil. The accurate functionalization ratios were determined by ¹H NMR.

PTBP-control (50% isolated yield): ¹H NMR (600 MHz, CD₃OD, 298 K, ppm): δ 8.18 (s, 3H), 7.66 – 7.02 (m, 8H), 4.67 (s, 2H), 4.35 – 3.80 (m, 8H), 3.20 – 3.11 (m, 4H), 2.92 (s, 2H), 1.83 – 1.12 (m, 14H).

PTBP-T8-11 (28% isolated yield): ¹H NMR (600 MHz, CD₃OD, 298 K, ppm): δ 8.19 (s, 3H), 7.66 – 7.02 (m, 6H), 4.66 (s, 2H), 4.35 – 4.01 (m, 4H), 3.68 – 3.46 (m, 4H), 3.20 – 3.11 (m, 4H), 2.92 (s, 2H), 1.83 – 1.23 (m, 15H).

PTBP-T8-19 (22% isolated yield): ^1H NMR (600 MHz, CD_3OD , 298 K, ppm): δ 8.27 (s, 3H), 7.66 – 7.01 (m, 5.4H), 4.68 (s, 2H), 4.35 – 4.02 (m, 5H), 3.68 – 3.46 (m, 6H), 3.23 – 3.12 (m, 4H), 2.92 (s, 3H), 1.86 – 1.23 (m, 18H).

PTBP/RNA Binding Study

PTBP-mRNA complexation

First, eGFP mRNA was heated at 55 °C for 5 minutes and chilled in ice. Second, different amount of **PTBP** solutions (10 mg/mL) were added to mRNA solution to achieve different N/P ratio (the molar ratio of primary amine groups from **PTBPs** and phosphate groups from mRNA, imidazole groups of histidine residues not counted because they are not protonated at pH 7.4) in the media of high salt concentration (2 M NaCl), which suppressed electrostatic interaction between cationic peptides and anionic mRNAs. Third, the complex solution was subjected to a thermal annealing process (55 °C for 5 minutes, gradually cool to room temperature for 30 minutes), which facilitated the interaction between poly-T PNA and poly-A mRNA. Finally, the complex solution was eluted through a Nap-5 desalting column, in order to change complex media back to water. The decreased ionic strength allowed stronger coulombic interaction between vectors and mRNAs, which further condensed the complexes into smaller nanoparticles.

Gel electrophoresis

The binding of mRNA to **PTBPs** was studied by agarose gel electrophoresis. **PTBP** vectors and mRNAs were complexed by following aforementioned protocol. 2 μL 6X RNA loading dye was added to each sample and 10 μL of the mixture was loaded to each well in 1%

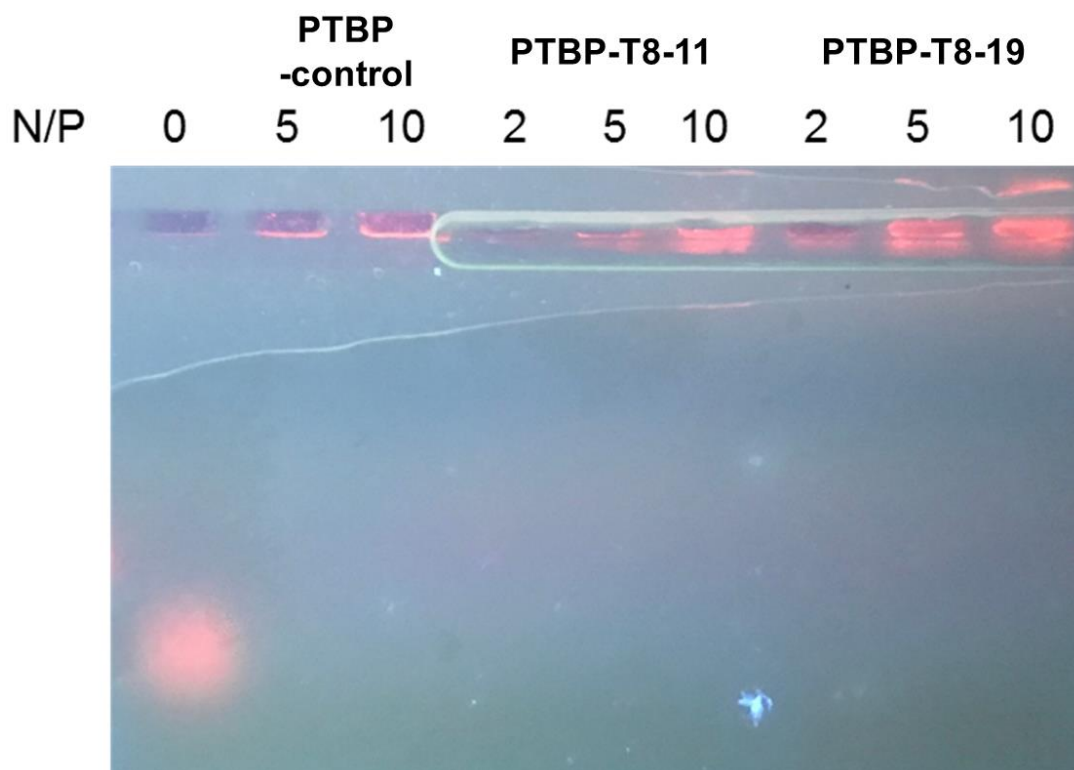
agarose gel with 1X GelRed dye. The electrophoresis was run in TBE buffer (pH 7.9) at 60 V for 90 min and the gel was visualized under a UV transilluminator. Related results are shown in **Figure 4.5A**.

Dextran sulfate competitive binding assay

The binding strength of mRNA to **PTBPs** was studied by competitive binding assay with dextran sulfate (DS). **PTBP**-mRNA complexes at N/P = 2 were prepared by following aforementioned protocol. 1 μ L DS solution of different concentration was added to the complex to achieve different S/P ratio (the molar ratio of sulfate groups from DS and phosphate groups from mRNA) and incubated for another 30 minutes. The samples were then subjected to agarose gel electrophoresis under the aforementioned condition. Related results are shown in **Figure 4.5B**.

Glutathione release binding assay

The PTBP-mRNA complexes were prepared at different N/P ratios via aforementioned protocol. Then glutathione (GSH) solution was added to achieve the concentration of 5 mM. The mixture was incubated at room temperature for 30 minutes and subjected to gel electrophoresis to detect mRNA release. The results (shown in the figure below) exhibited all PTBP vectors still strongly binds to mRNA cargos after polymer degradation, which also explains the mRNA transfection deficiency in biological experiments.



DLS measurements

The size and zeta potential of **PTBP**-mRNA complexes were measured at 633 nm using Zetasizer (NanoZS) dynamic light scattering instrument (Malvern Instruments, Malvern, UK) at 25 °C with detection angle of 173°. Both **PTBP** and mRNA were diluted in nanopure water and complexed under aforementioned condition. After 10 min incubation at room temperature, DLS measurement was taken. The solution was then diluted with 600 µL PBS and subjected to zeta-potential measurement. At least three measurements were taken for each sample and the mean Z-average values were reported.

Biological Studies

mRNA transfections

(1) **PTBP**-mRNA complex preparation

Before performing the mRNA transfections, the area was sterilized with bleach and RNase ZAP (Ambion), and special care was taken to use RNase free products when handling the mRNA. Lipofectamine MessengerMAX was used as a positive control and prepared as instructed in the product manual. The mRNA was thawed and diluted to a concentration of 0.05 µg/µL with OptiMEM. Different **PTBP**-mRNA complexes at various N/P ratios were prepared by following aforementioned protocol. Finally, the mixture is diluted to 60 µL with OptiMEM so that 20 µL of the complex solution will contain 150 ng of mRNA.

(2) Transfection in NIH 3T3 cells.

Transfections were performed in triplicate in a cell culture treated clear-bottom 96-well plate (Corning). After passaging, the cells were plated in 96-well plates so that they were 60~70% confluent at the time of transfection. The **PTBP**-mRNA complex solutions were prepared using the aforementioned protocol. The culture media was switched to 80 µL OptiMEM (with or without 10% FBS) per well and 20 µL of the complex solution was added to each well. The cells were cultured for 24 hours prior to analysis.

(3) Transfection analysis in Fluc mRNA transfected cells

24 hours post-transfection, the culture media was removed and replaced with 100 µL of a 150 µg/mL solution of firefly D-luciferin in FluoroBrite™ DMEM. Without any further

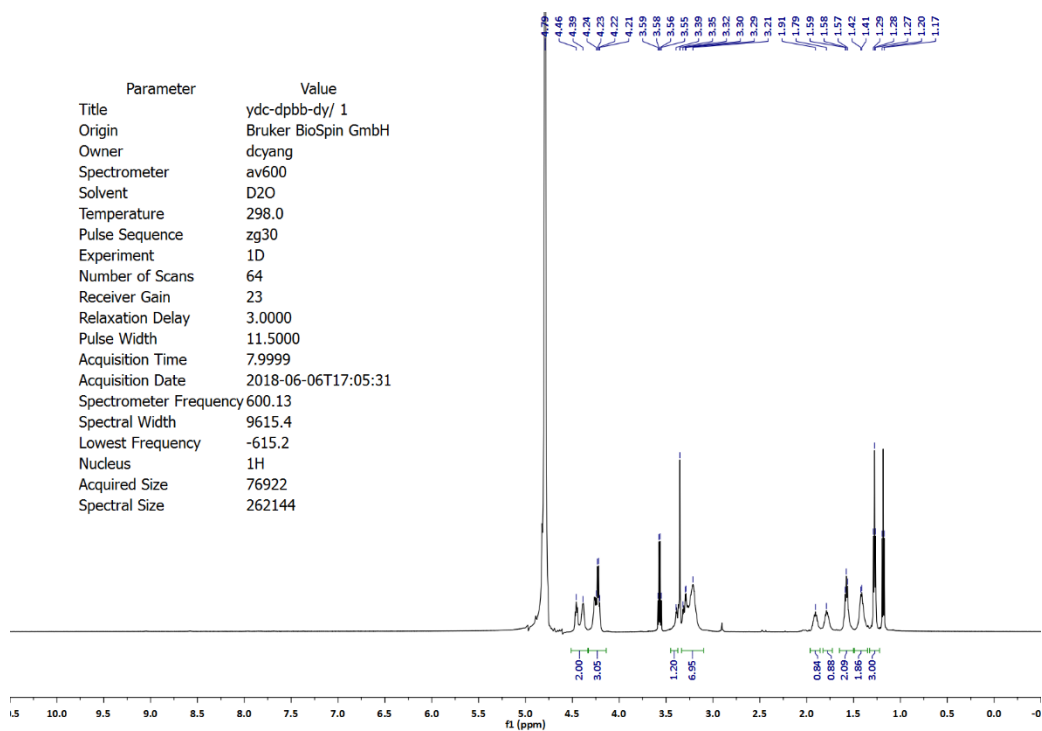
treatment, the cells were incubated at 37 °C for 5 minutes after which they were imaged using an IVIS lumina II camera and the luminescence was determined.

(4) Transfection analysis in eGFP mRNA transfected cells via flow cytometry.

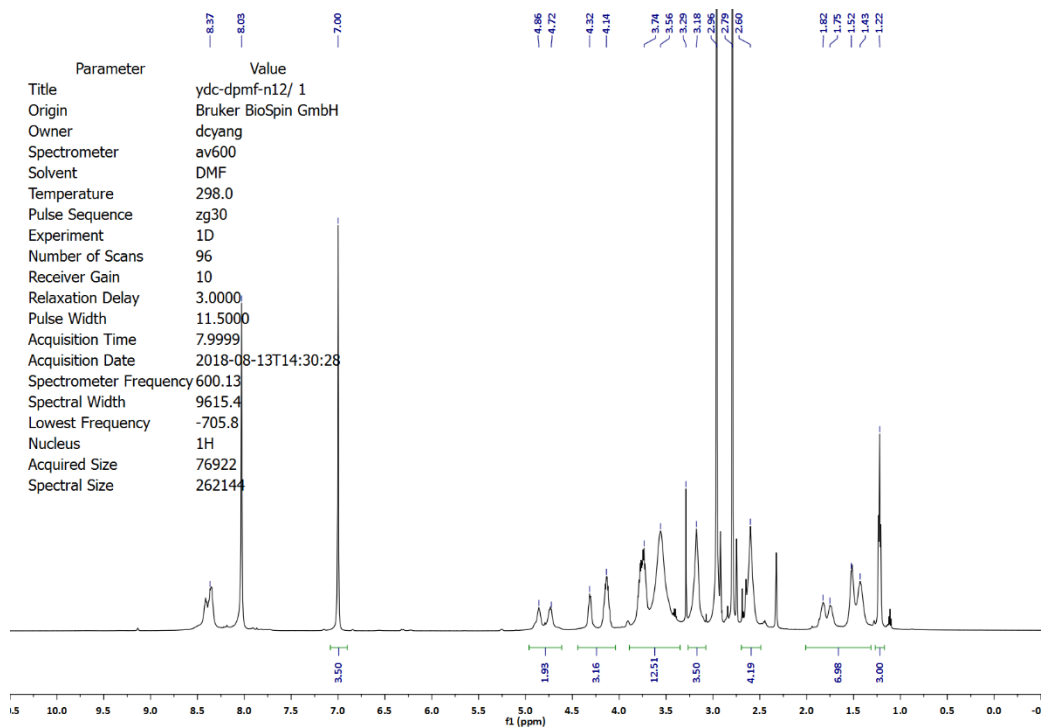
24 hours post-transfection, the culture media was removed and replaced with 30 μ L trypsin and incubated at 37 °C for 5 minutes. 70 μ L of complete media were added to the plate and the cells were transferred to a 96-well non-cell treated plate for flow cytometry. Fluorescence of the transfected cells was measured on a Becton-Dickinson LSR II flow cytometer with argon ion excitation laser. 5000 events were recorded per sample and each value reported is the average of 3 samples.

4.8 ^1H NMR Spectra

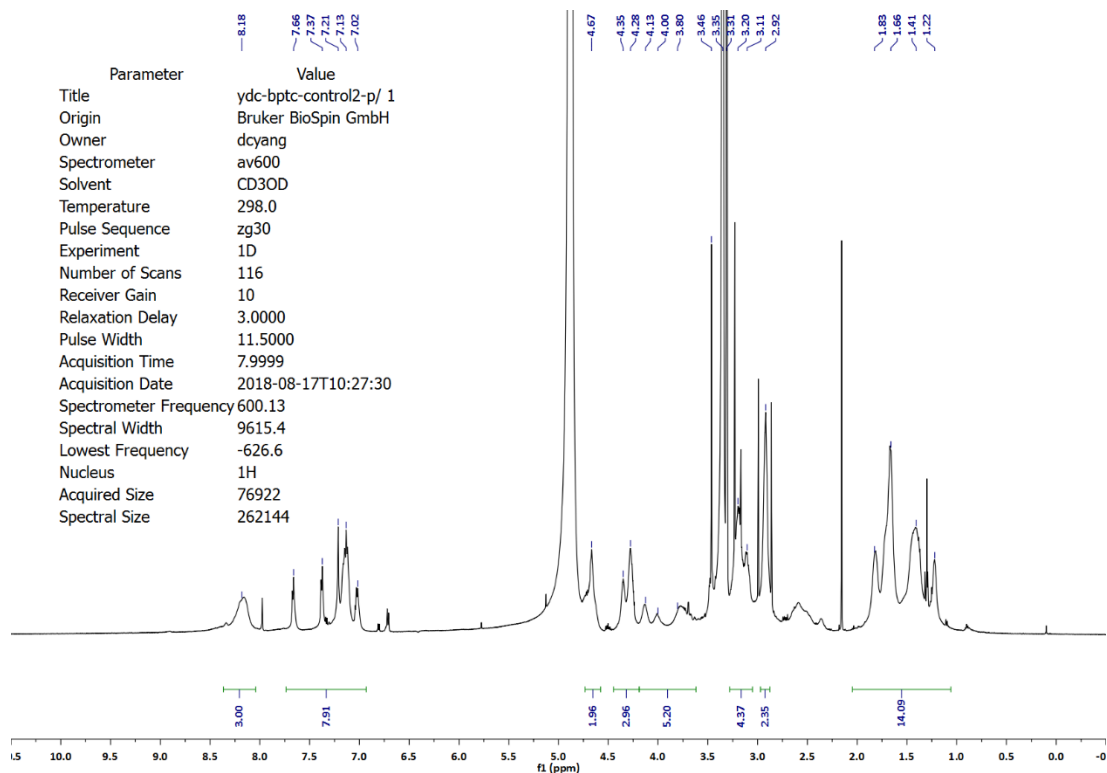
BP backbone



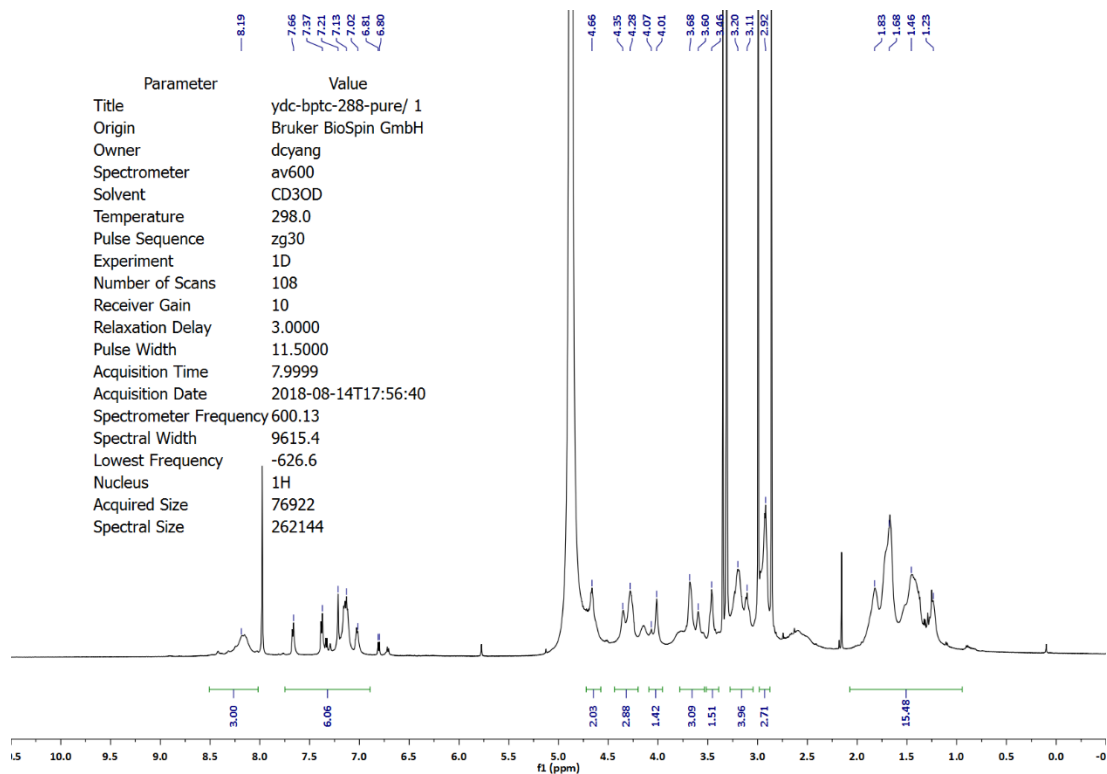
MFBP



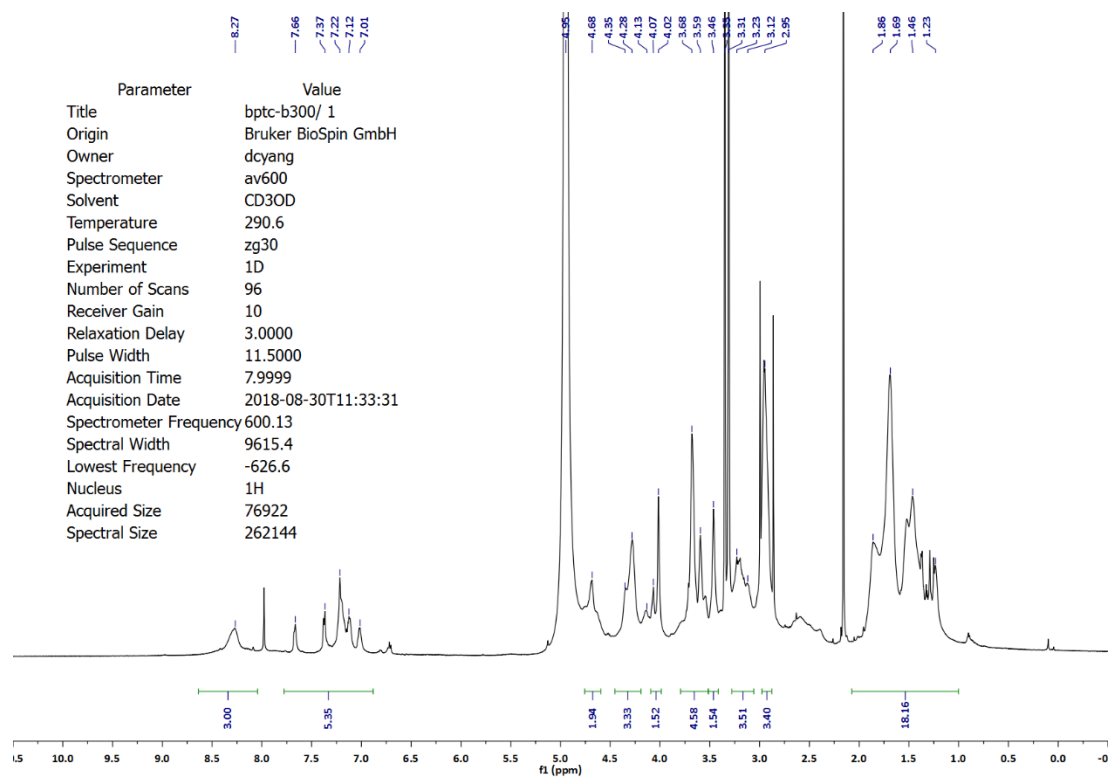
PTBP-control



PTBP-T8-11



PTBP-T8-19



Chapter 5: Hybrid Organic-Inorganic Quantum Dot Superlattices for Enhanced Charge Transport

5.1 Introduction and Project Design

Thin films of semiconductor quantum dots (QDs) represent a promising platform for low-cost optoelectronic devices. In particular, solar cells based on thin films of colloidal PbX QDs (X = S, Se, Te) have been demonstrated and developed rapidly.¹⁻⁴ Compared to bulk or thin film semiconductors, which require high temperature, high-vacuum processing⁵⁻⁶, QD Photovoltaics (PV) technology offers significant advantages in improving device efficiency and stability.⁷⁻¹⁰ However, the discrete nature of QDs results in drastically reduced charge transport properties compared to those in bulk and polycrystalline films.¹¹⁻

12

All QD solar cells to date employ amorphous films of QDs capped with short organic or inorganic ligands that achieve substantial electronic coupling only by forfeiting medium and long range order.¹³⁻¹⁵ To improve the electronic performance of QD materials, well-ordered QD arrays which have the superlattices structure have been emphasized recently.¹⁶⁻¹⁷ The band-like transport can be realized in the QD films with a long-range positional order, while charge carriers can only be transported via a sequence of phonon assisted tunneling events in disordered structures.¹⁸ We believe that fabricating superlattice QD films with excellent long-range positional and orientational order can combine the high-mobility band transport of crystalline semiconductors with the unique photophysics and processing advantages of QDs.

Therefore, we report the fabrication of well-ordered QD arrays that are electronically coupled with bis-functional and mono-functional organic molecular wires

(MWs). It is well established that colloidal solutions of PbSe QDs decorated with long alkyl ligands readily form poly-supracrystalline QD thin films with large grain sizes (> 100 nm) and face-centered cubic (fcc) dominated packing structure via spin coating.¹⁹ We postulated that in situ exchange of the non-conducting alkyl ligands with conjugated, conducting MWs of similar dimension to the native ligands would retain the poly-supracrystalline order²⁰ and enable dynamic self-assembly from solution.

Figure 5.1 summarizes three ways in which the hybrid superlattice nanocomposites (HSNs) can be fabricated using the bis- and mono-functional wires. As shown in Pathway A, the bis-functional wires are used for solid-state ligand exchange of oleate-capped QD superlattices deposited by spin coating to produce HSNs. Besides being used in this way, the mono-functional wires can be employed in solution-phase ligand exchange to form stable QD-MW solution that yield HSNs upon assembly by spin coating/drop casting (Pathway B). Since the mono-functional wires do not covalently crosslink the QD array in the fashion of the bi-functional wires, solvent annealing of mono-HSNs made by either Pathway A or B can be used to further improve the superlattice order and grain size (Pathway C).

The mono- and bis-functional molecular wires can result in high carrier mobility by reducing the effective height of the tunnel barrier between QDs and favoring the emergence of extended states across the superlattice grains.²¹ In addition, the structures of molecular wires can be adjusted to investigate the impact of the HOMO/LUMO energy level, band gap, interfacial transmission barrier and wire length on carrier mobility, and electronic device performance.

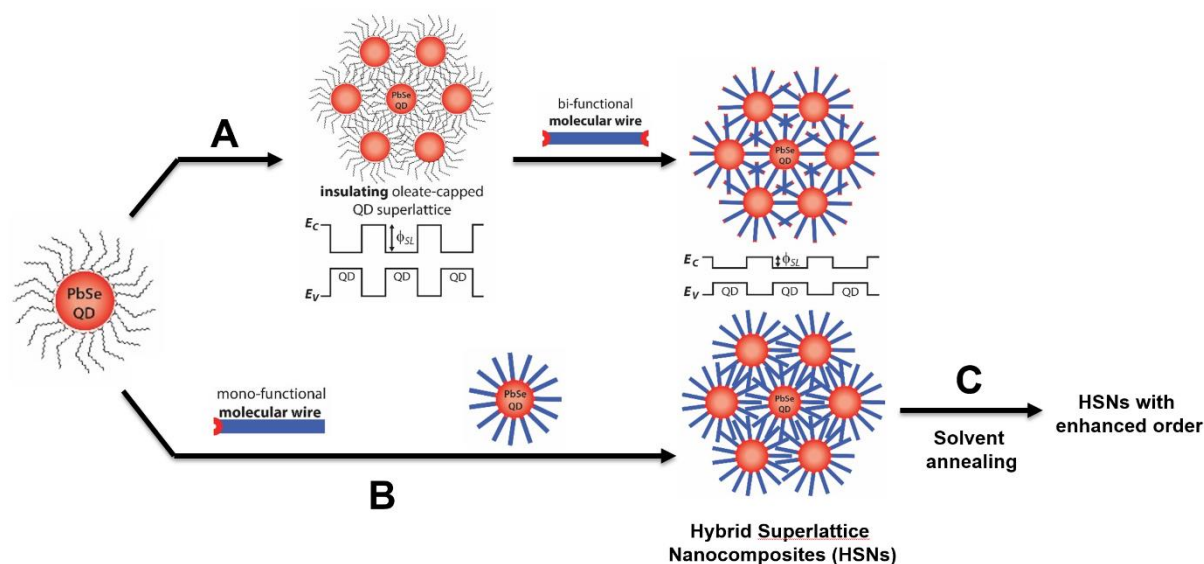


Figure 5.1 Hybrid superlattice nanocomposites (HSNs) of PbSe QDs and molecular wires.

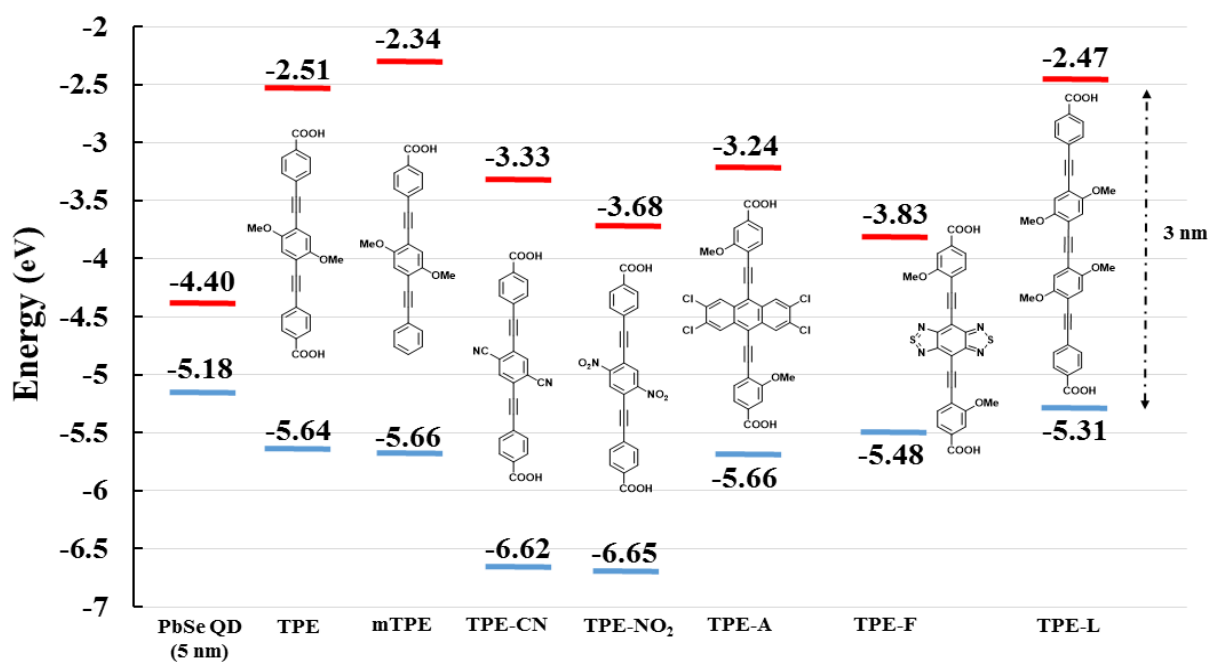
5.2 Design, Synthesis and Characterization of Functional Molecular Wires

A bis-carboxylic acid triphenylene ethynylene (**TPE**) ligand was chosen for our initial concept demonstration.²² Due to the ethynyl π spacer between the phenyl rings, there is no steric restriction to conformation, and co-planarity guarantees relatively high conductance and good state delocalization. **Figure 5.2** shows the structures of our designed functional molecules and their estimated HOMO/LUMO energy levels from DFT calculation.²³

Through varying electronic substituents on the phenyl rings, we can adjust the HOMO/LUMO energy levels of these **TPE** analogs while keeping the energy gap relatively constant. From the results of DFT calculation, the barrier height for electron tunneling is smallest for **TPE-NO₂** and largest for **mTPE**, while the inverse holds for hole tunneling. Across this series, we can use the substituent inductive effects to selectively tune the

barrier height for electron and hole transport and make *n*-type and *p*-type HSNs via barrier engineering.²⁴

Additionally, the HOMO-LUMO energy gap can be decreased by changing the central conjugated core. The band gaps of **TPE-A** and **TPE-F** are closer to the PbSe QD band gap, which offers lower barriers to the transport pathways of both electrons and holes. Furthermore, using molecular wires with lengths as similar as possible to the inter-QD spacing of oleate-capped films can avoid disorder caused by volume changes and improve HSN order. Through iterative Sonogashira cross-coupling reaction²⁵, the length of molecular wires can be enlarged to approach the inter-QD spacing observed in oleate-capped superlattices (**TPE-L**).

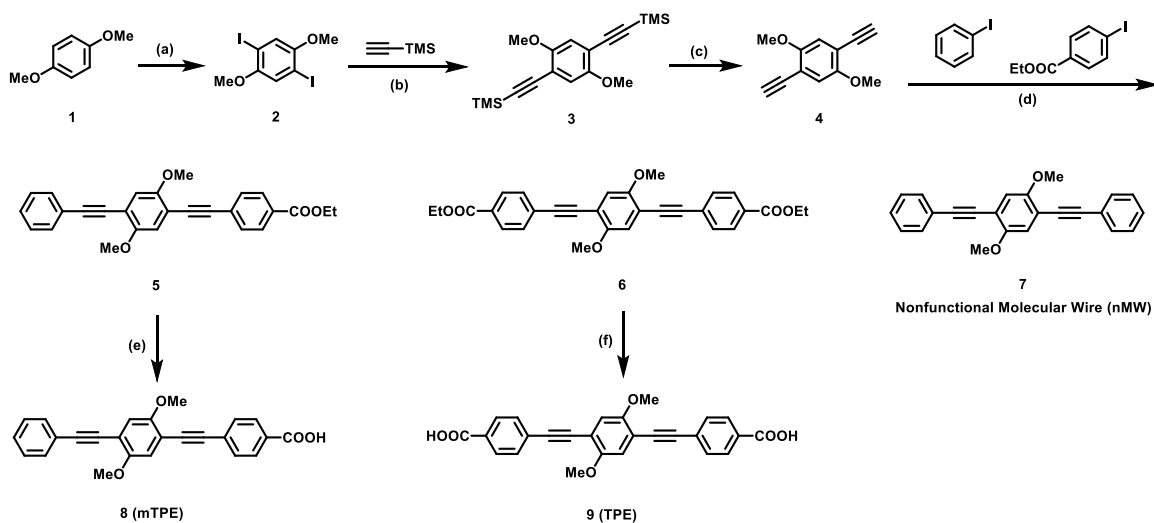


Calculated at B3LYP/6-311g(d,p) level

Figure 5.2 Structure and HOMO/LUMO positions of functional molecular wires. A 5 nm PbSe QD was used for the calculation and its energy levels were obtained from cyclic voltammetry and photoemission spectroscopy.²⁶

The bis-functional molecular wire (**TPE**) and the mono-functional molecular wire (**mTPE**) were synthesized for our preliminary study. The synthetic route is illustrated in **Scheme 5.1**. A diiodination was first performed on 1,4-Dimethoxybenzene to produce compound **2**,²⁷ which was further coupled with Trimethylsilylacetylene through a Sonogashira cross-coupling reaction.²⁸ After deprotection of the trimethylsilyl groups, compound **4** was subjected to another Sonogashira cross-coupling reaction with one equivalent of Iodobenzene and Ethyl-4-iodobenzoate to afford a statistical mixture of mono-functional molecular wire precursor (**5**), bis-functional molecular wire precursor (**6**), and nonfunctional molecular wire (**7**). Finally, these two molecular wire precursors were hydrolyzed with KOH in THF/EtOH to produce **mTPE** (**8**) and **TPE** (**9**) in 90% yield.²⁹

Scheme 5.1 Synthetic route to mTPE and TPE.



Reagents and conditions: (a) I₂, H₅IO₆, H₂SO₄, HOAc, H₂O, CH₂Cl₂, 75 °C, 15 h, 76%. (b) Pd(PPh₃)₄, CuI, *i*Pr₂NH, DMF, rt, 12 h, 71%. (c) K₂CO₃, MeOH, CH₂Cl₂, rt, 1 h, 81%. (d) Pd(PPh₃)₄, CuI, *i*Pr₂NH, DMF, rt, 12 h, **5** (30%), **6** (27%), **7** (35%). (e) KOH, THF, EtOH, 45 °C, 5 h, 90%. (f) KOH, THF, EtOH, 45 °C, 15 h, 92%.

In absorption spectra (**Figure 5.3**), compounds **7-9** all exhibited two identical major absorption peaks from $\pi \rightarrow \pi^*$ excitation. Both **mTPE** and **TPE** exhibited red-shifted absorption maxima and onsets relative to those of nonfunctional molecular wire; this is attributed to the electron-withdrawing effect of carboxyl groups.³⁰ As the amount of carboxyl groups in the molecular structure increased, the absorption maxima and onsets redshifted gradually. Calculated from onset values, the optical band gaps of all functional molecular wires are all around 3 eV and match the results from DFT calculation well. (**Table 5.1**)

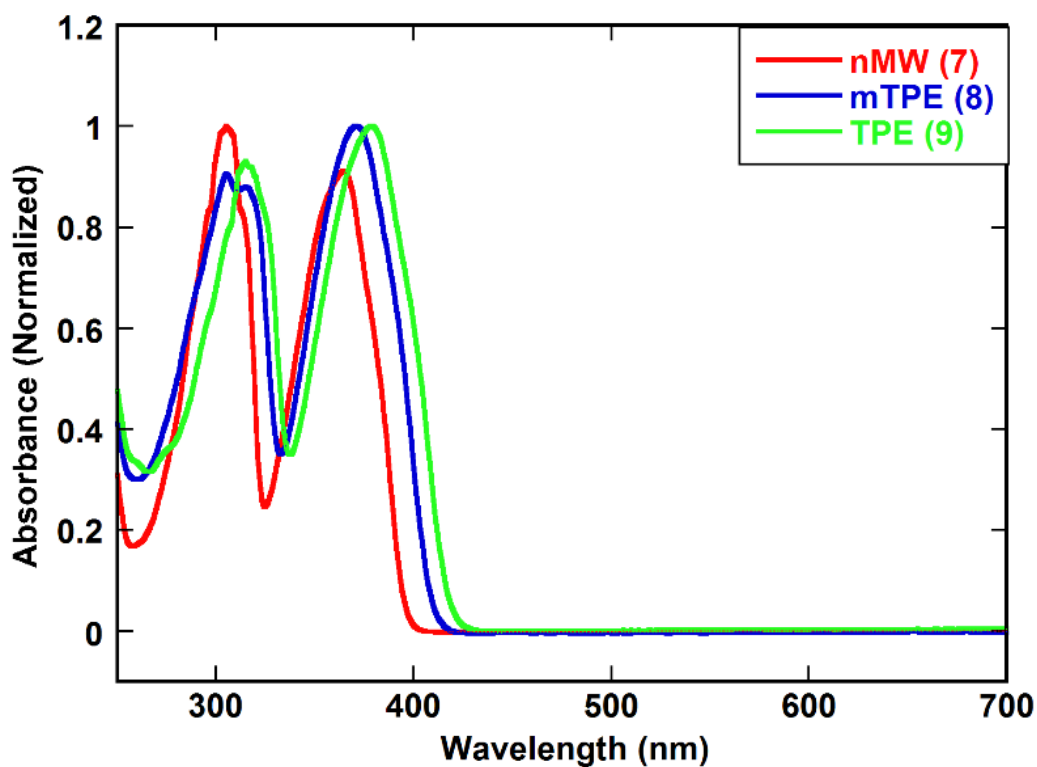


Figure 5.3 Normalized absorption spectra of nonfunctional molecular wire (nMW), mTPE and TPE in THF (1×10^{-5} M).

Table 5.1 Summary of the photophysical properties of compounds **7-9**.

Compound	λ_{abs}^{max} (nm)	λ_{abs}^{onset} (nm)	E_g^{opt} (eV) ^[a]	E_{HOMO} (eV) ^[b]	E_{LUMO} (eV) ^[b]	E_g^{cal} (eV) ^[b]
nMW (7)	305, 365	396	3.14	—	—	—
mTPE (8)	306, 371	410	3.03	-2.34	-5.66	3.32
TPE (9)	315, 379	417	2.98	-2.51	-5.64	3.13

[a] Calculated from absorption spectra. Optical band gap is calculated from equation: $\frac{hc}{\lambda_{onset}} = E_g$. [b] Determined from DFT calculation.

5.3 Solid-state Ligand Exchange with TPE and Characterization

The conductive TPE-functionalized PbSe (**PbSe-TPE**) QD thin film fabrication is illustrated in **Figure 5.4a**. Poly-supracrystalline PbSe-TPE QD films were fabricated through spin-coating and in situ solid-state ligand exchange. For control, we also constructed glassy **PbSe-TPE** QD thin film nanocomposites by dip-coating for comparative studies. Complete exchange of native oleate ligands for **TPE** was confirmed by FTIR following established protocols (**Figure 5.4b, c**).³¹ The lack of a free carboxylic acid resonance indicates that both ends of **TPE** are quantitatively complexed to QDs, which suggests that substantial chemical QD bridging is occurring. Extinction spectra of the hybrid nanocomposite films show a larger red-shift as well as substantial peak-broadening when compared to their oleate-capped counterpart. We attribute this larger redshift/broadening to an enhanced dielectric screening and better electronic coupling between QDs facilitated by the MWs (**Figure 5.4d**).¹⁶

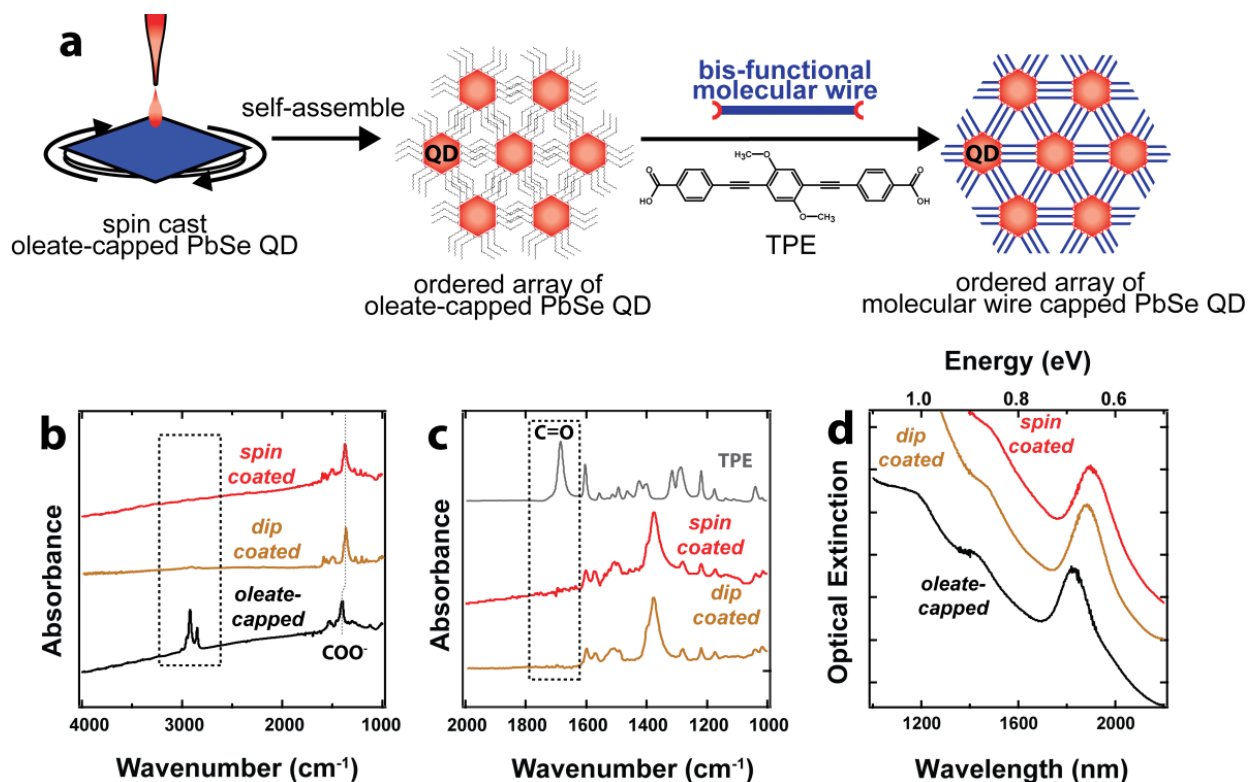


Figure 5.4 Solid-state ligand exchange and characterization. (a) Concept illustration of our fabrication process. Spin coating oleate-capped PbSe QD yield superlattice films, which can be soaked in a solution of TPE to replace oleate for TPE and retain the structural order. (b) FTIR spectra of PbSe QD films. Black: oleate-capped films. Gold: TPE-capped films made by dip coating. Red: TPE-capped films made by spin coating. (c) Magnified views of the spectra in (a); both gold and red traces retains <1% of the C-H stretch observed in the black trace. (d) Comparative optical extinction spectra of oleate-capped (black), dip coated (gold) and spin coated (red) TPE exchanged PbSe QD films on glass substrates. Film thicknesses: 100 nm.

5.4 Solution-phase Ligand Exchange with mTPE and Characterization

First, oleate-capped PbSe QDs were synthesized and purified using standard air-free Murray synthesis.³² The absorption spectrum displays an 1800 nm first excitation peak (Figure 5.5) and corresponding TEM image illustrates that the size of synthesized QDs is around 6 nm (Figure 5.6).³³⁻³⁴ Next, solution-phase ligand exchange and further purification was performed by following standard procedures (see Section 5.10).

Complete exchange of native oleate ligands for **mTPE** was confirmed by FTIR and ^1H NMR spectra. The entire disappearance of internal alkene signals (5.36 ppm) and alkyl signals (0.92 ppm, 1.34 ppm, 2.07 ppm) from oleic acids in ^1H NMR spectrum suggests the ligand exchange was fully conducted (**Figure 5.7a, b**). The line broadening is generally attributed to the transversal interproton dipolar relaxation mechanism that is rendered more efficient by the restricted rotational mobility of the ligands when bound to the PbSe QD surface.³⁵⁻³⁷ The absence of a (C=O) stretch at 1680 cm^{-1} and a shift in the asymmetric (COO^-) stretch suggest **mTPE** is bound to the surface of PbSe QDs (**Figure 5.7c**). In contrast to the results of solid-state ligand exchange with **TPE**, the band gap of PbSe QDs did not change in a distinguishable scale after the solution-phase ligand exchange with **mTPE** as evidenced by the absorption spectra (**Figure 5.7d**).

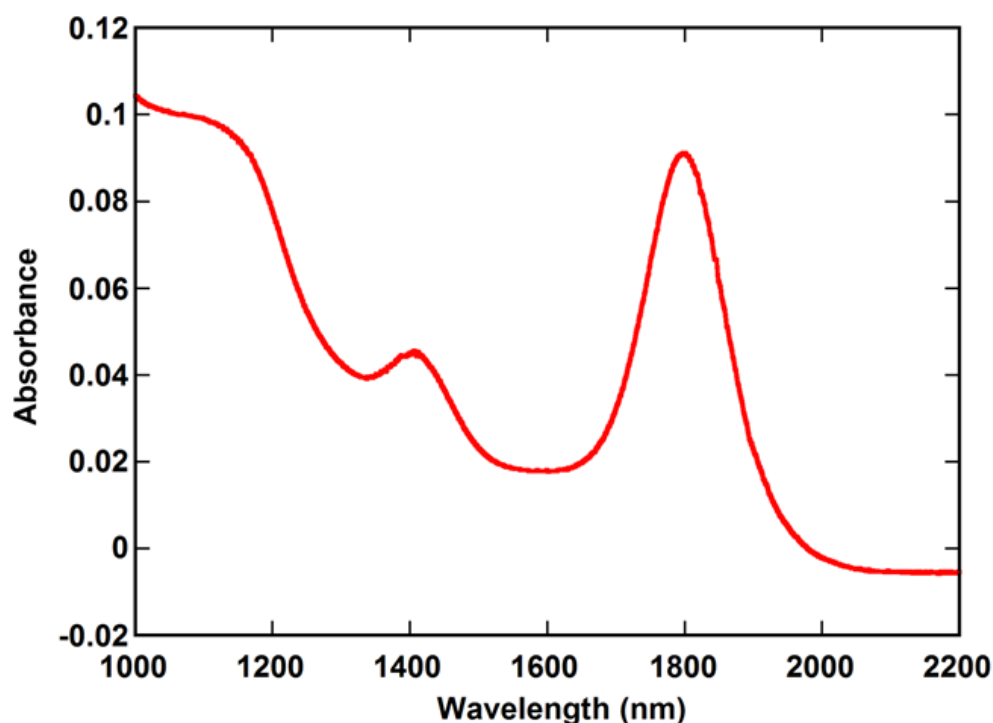


Figure 5.5 Absorption spectrum of synthesized oleate-capped PbSe QDs in 1-octadecene (ODE) ($1 \times 10^{-5}\text{ M}$).

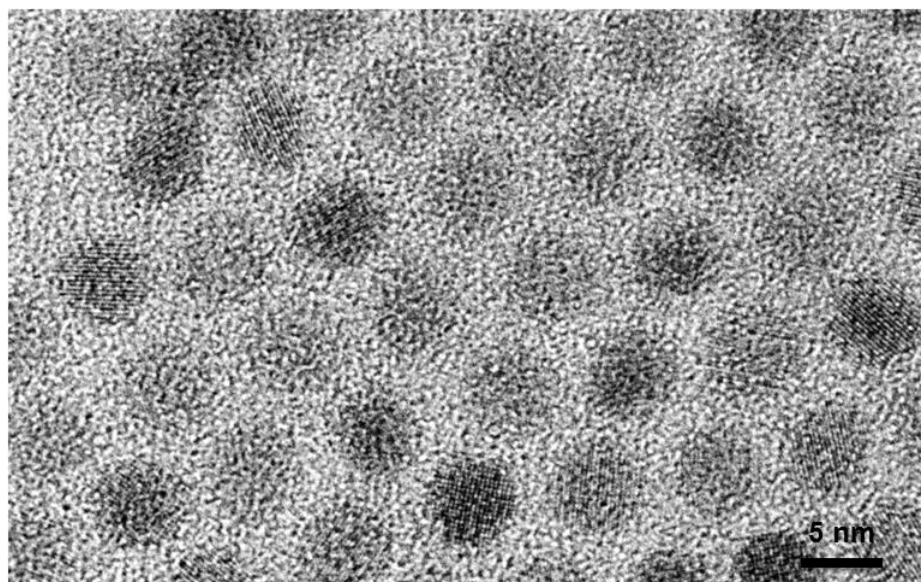


Figure 5.6 TEM image of synthesized oleate-capped PbSe QDs.

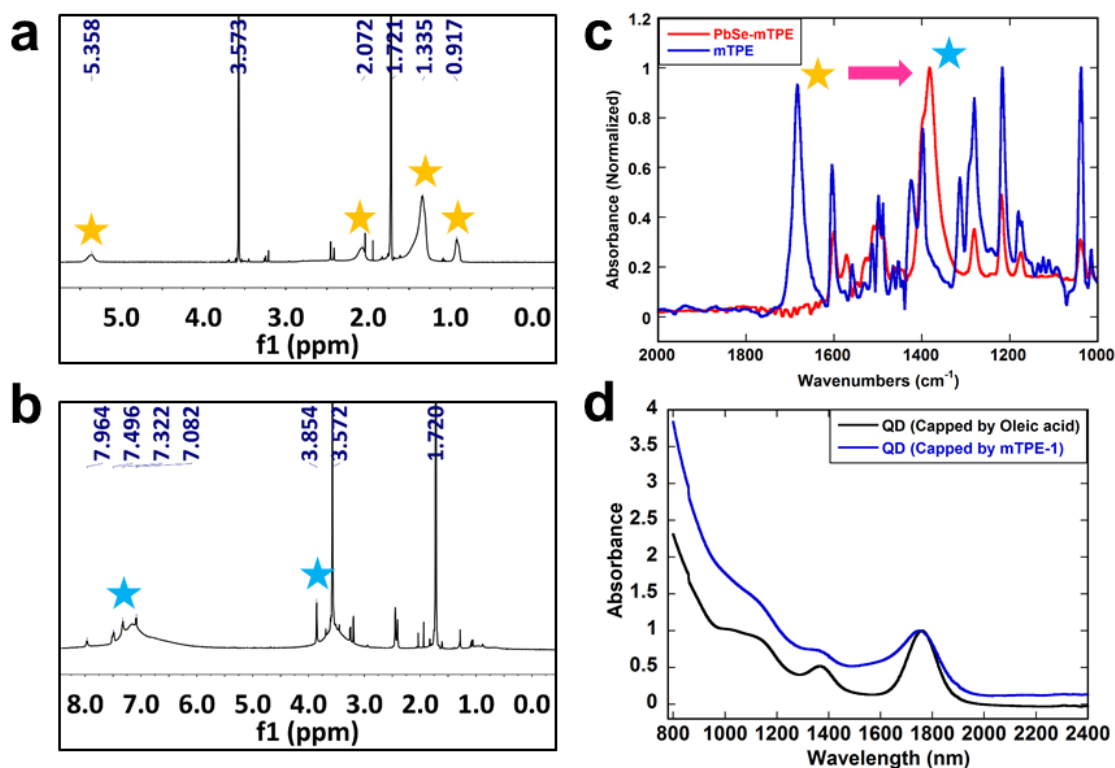


Figure 5.7 Characterization of solution-phase ligand exchange. (a, b) ^1H NMR spectra of PbSe-OA, PbSe-mTPE QDs in d_8 -THF. Several broad resonances were observed, with a chemical shift comparable to the chemical shift of capping reagents (Yellow: oleic acid, Blue: mTPE). (c) Normalized FTIR spectra of mTPE (blue) and PbSe-mTPE (red) QD films. (d) Absorption spectra of PbSe QD solutions in CBrCl_3 (1×10^{-4} M).

5.5 Film Construction and Morphology Study

We confirmed the desired poly-supracrystalline order of spin-coated oleate-capped PbSe QDs by scanning electron microscope (SEM) images. The SEM image in **Figure 5.8** shows that the poly-supracrystalline order was mostly retained after the solid-state ligand exchange with **TPE**. The TPE-functionalized PbSe (**PbSe-TPE**) QD superlattice structure was further characterized by grazing incidence small angle X-ray scattering (GISAXS) patterns (**Figure 5.8**)³⁸ and related analyses about lattice constant and crystal system were shown in **Section 5.10**.

After solution-phase ligand exchange with **mTPE**, thin films of mTPE-functionalized PbSe (**PbSe-mTPE**) QD were constructed through spin-coating and the morphology was investigated by SEM images (**Figure 5.9**). Compared to the superlattice structures of oleate-functionalized PbSe (**PbSe-OA**) QD and **PbSe-TPE** QD films, the **PbSe-mTPE** QD film lacked long-range order (For Fast Fourier Transformation, see **Figure 5.9**). We believe this amorphous structure is due to the rigidity of **mTPE** molecular skeleton and strong $\pi - \pi$ interaction between the aromatic rings. After a comprehensive screening of appropriate solvents (**Table 5.2**) and spin-coating conditions (**Table 5.3**), a series of subsequent solvent annealing experiments were conducted to enhance the degree of order of the **PbSe-mTPE** QD films. As evidenced by the SEM images (**Figure 5.10**), the solvent with lower vapor pressure (DMF) can help the QDs rearrange their packing structures without disturbing the integrity of QD films. More solvent-annealing conditions are being attempted based on the small enhancement of film order (~ 20 nm lattice domains) (**Figure 5.10d**) now. In addition, other superlattice film construction methods, including liquid-air interface self-assembly and vapor diffusion, are also being tested (**Figure 5.11**).

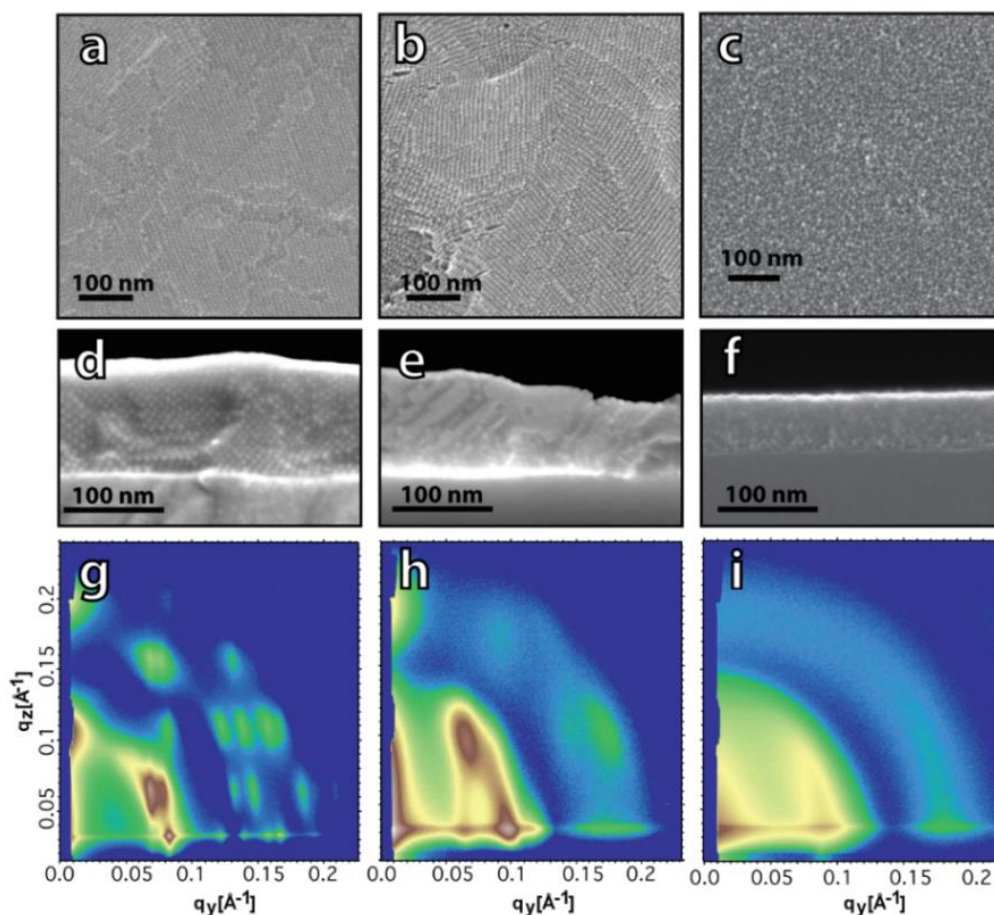


Figure 5.8 SEM plan view images of PbSe QD films. (a) An oleate-capped film prepared by spin-coating. (b) A TPE-capped film made by in situ ligand exchange of the spin-coated film. (c) A disordered TPE-capped film made by layer-by-layer dip coating. (d-f) Corresponding SEM cross sections and (g-i) 2D GISAXS patterns.

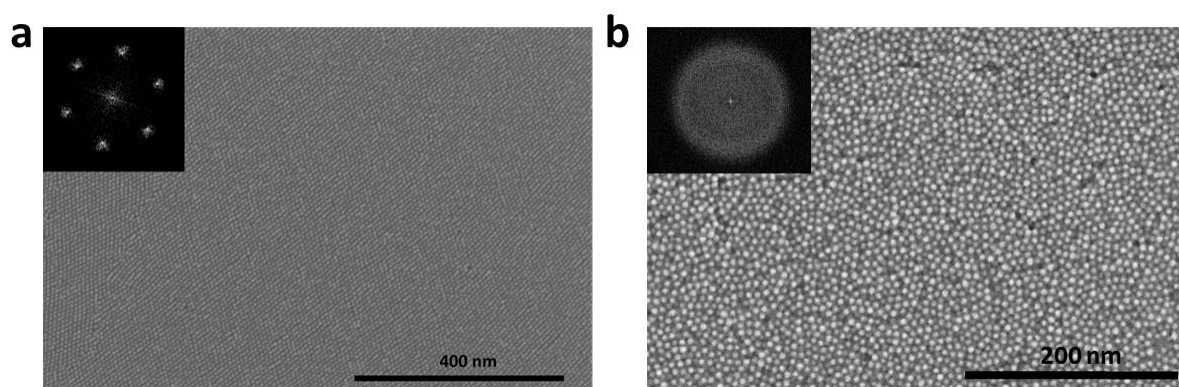


Figure 5.9 SEM plan view images and related fast fourier transformation analyses of PbSe QD films. (a) An oleate-capped QD film prepared by spin-coating. (b) An mTPE-capped QD film made by spin-coating with 20 mg/mL PbSe-mTPE QDs solution in THF.

Table 5.2 Results of solubility tests of PbSe-mTPE QDs^[a]

Solvent	Result	Solvent	Result	Solvent	Result	Solvent	Result
THF	Good	DMF	Good	Toluene	Medium	IPA	Poor
Hexane	Poor	Octane	Poor	ODE	Poor	TCE	Poor
EtOH	Poor	Acetonitrile	Poor	Acetone	Poor	CHCl ₃	Poor

[a]. All solubility tests were performed on PbSe-mTPE QDs films drop-casted on silica substrates.

Table 5.3 Screening results of spin-coating conditions^[a]

Entry	Spin 1	Spin 2	Spin 3	Results
1	300 rpm, 30 s	—	4000 rpm, 10 s	No film formed
2	600 rpm, 30 s	—	4000 rpm, 10 s	Uniform film
3	300 rpm, 30 s	600 rpm, 20 min	4000 rpm, 10 s	Uneven film
4	600 rpm, 30 s	900 rpm, 20 min	4000 rpm, 10 s	Uniform film
5	300 rpm, 30 s	900 rpm, 20 min	4000 rpm, 10 s	Uniform film
6	1300 rpm, 30 s	4000 rpm, 20 s	—	Uniform film

[a]. All spin-coating experiments were conducted with 20 mg/mL PbSe-mTPE QDs solution in THF on single-side-polished silicon wafer substrates.

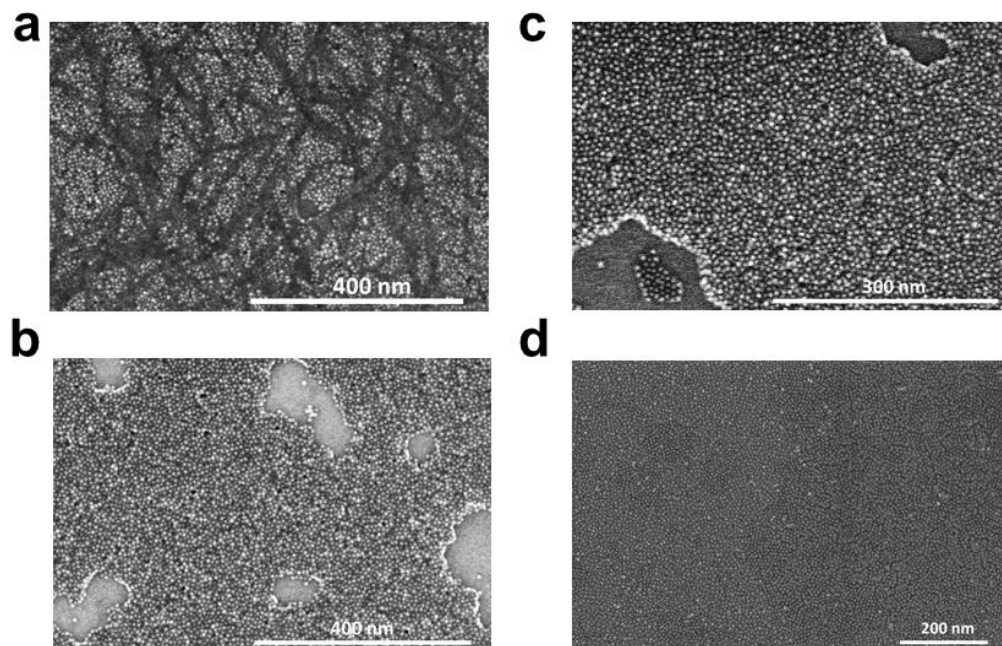
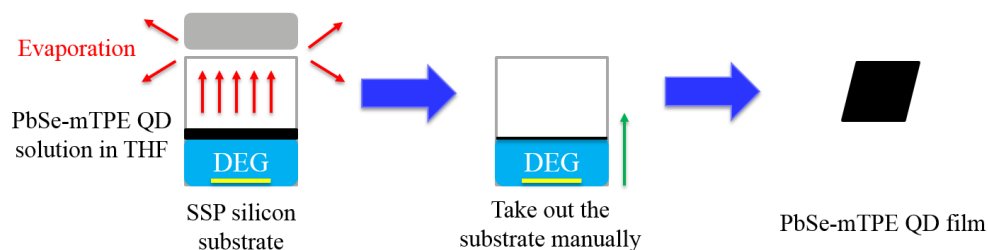


Figure 5.10 SEM plan view images of PbSe-mTPE QD films after solvent annealing. (a) Solvent-annealed with THF at room temperature for 12 h. (b) Solvent-annealed with toluene at room temperature for 12 h. (c) Solvent-annealed with toluene at 60 °C for 12 h. (d) Solvent-annealed with DMF at room temperature for 24 h.

(a) Liquid-air interface self-assembly



(b) Vapor diffusion

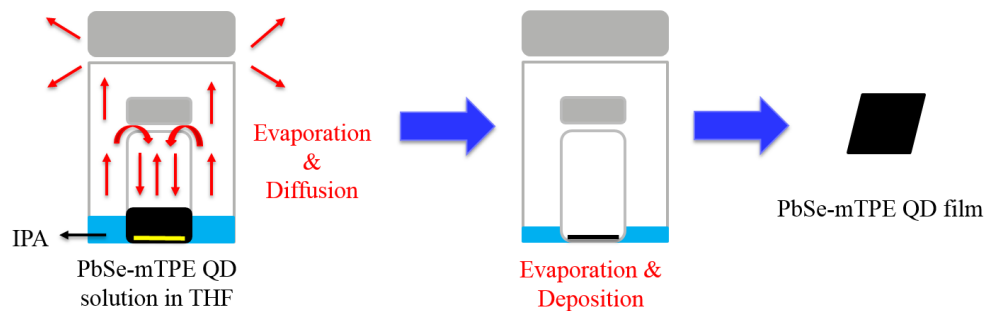


Figure 5.11 Graphic illustration of methods for constructing QD superlattice films. (a) Liquid-air interface self-assembly. (b) Vapor diffusion.

5.6 FET Measurements

The carrier mobilities of **PbSe-TPE** QD films (ordered and amorphous) were measured in field-effect transistors (FET) geometry with the help of Law group (**Figure 5.12**). At room temperature, both ordered and disordered films act as *p*-type depletion-mode devices with mobilities of $3.10 \times 10^{-2} \text{ cm}^2 \text{ V}^{-1} \text{ s}^{-1}$ and $1.62 \times 10^{-4} \text{ cm}^2 \text{ V}^{-1} \text{ s}^{-1}$, respectively. The electrical performance of these *I-V* measurements were also obtained at 80 K with both ordered and glassy films acting as unipolar *p*-type devices with mobilities of $2.04 \times 10^{-1} \text{ cm}^2 \text{ V}^{-1} \text{ s}^{-1}$ and $1.74 \times 10^{-3} \text{ cm}^2 \text{ V}^{-1} \text{ s}^{-1}$, respectively. There is an over 100-fold increase in mobility value from glassy to ordered films at both room and low temperature.

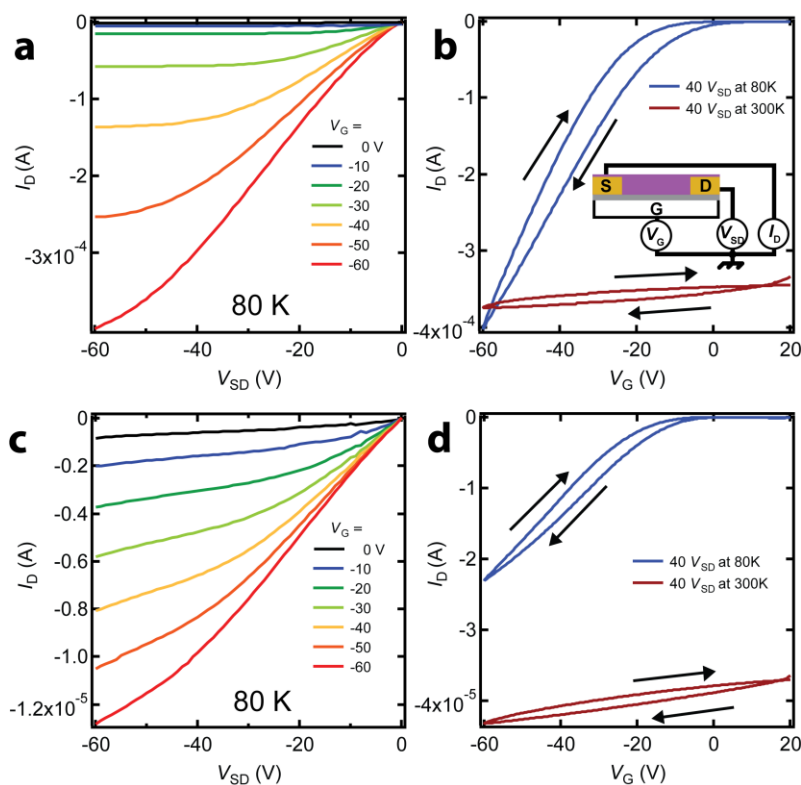


Figure 5.12 *I-V* plot of TPE-capped PbSe QD FETs. (a) Output curves obtained at 80 K and (b) comparative transfer curves obtained at 80 and 300 K for ordered TPE-capped PbSe QD films. Similar output and transfer curves for the control disordered TPE-capped PbSe QD films are shown in (c) and (d), respectively. QD diameter: 6.1 nm. Film thickness: 20-35 nm. Channel length: 10 μm in (a,b); 5 μm in (c,d). Channel width = 1000 μm . Sweep rate = 50 V s^{-1} . Inset in (b) is a schematic of the device.

5.7 Conclusions

In summary, we demonstrated a modular self-assembly approach to synthesize the first conductive hybrid organic-inorganic QD superlattice films. Long conjugated molecular wire ligands were used to fabricate conductive, long diffusion length QD superlattices. The results from FET tests (**Figure 5.12**) supported the hypothesis that improved QD ordering will result in improved transport. However, more FET measurements are being reproduced to optimize the device performance and verify the reproducibility of FET results. Overall, our hybrid nanocrystal-molecular wire design represents a general approach to improve order in nanocrystal films, across the whole range of nano-electronic applications.

On the other hand, we are still optimizing the conditions of film construction and solvent-annealing to enhance the packing order of **PbSe-mTPE** QD film. In addition, the library of designed organic molecular wires will be synthesized to investigate the impact of MW length, band gap, and energy level on the tunnel barrier heights, superlattice order and electronic properties.

5.8 Acknowledgement

I acknowledge Alex Abelson for the help in thin film construction, FET measurements, and GISAXS study. I acknowledge Jason Tolentino for the help in thin film construction and FET measurements.

5.9 Notes and References

- (1) Malik, M. A.; Revaprasadu, N.; O'Brien, P., Air-Stable Single-Source Precursors for the Synthesis of Chalcogenide Semiconductor Nanoparticles. *Chem Mat.* **2001**, *13*, 913-920.
- (2) Smith, A. M.; Nie, S., Semiconductor Nanocrystals: Structure, Properties, and Band Gap Engineering. *Acc Chem Res.* **2010**, *43*, 190-200.
- (3) Luther, J. M.; Law, M.; Beard, M. C.; Song, Q.; Reese, M. O.; Ellingson, R. J.; Nozik, A. J., Schottky Solar Cells Based on Colloidal Nanocrystal Films. *Nano Letters.* **2008**, *8*, 3488-3492.
- (4) Semonin, O. E.; Luther, J. M.; Choi, S.; Chen, H.-Y.; Gao, J.; Nozik, A. J.; Beard, M. C., Peak External Photocurrent Quantum Efficiency Exceeding 100% via MEG in a Quantum Dot Solar Cell. *Science* **2011**, *334*, 1530-1533.
- (5) Bishop, K. J. M.; Wilmer, C. E.; Soh, S.; Grzybowski, B. A., Nanoscale Forces and Their Uses in Self-Assembly. *Small* **2009**, *5*, 1600-1630.
- (6) Shah, A.; Torres, P.; Tscharnner, R.; Wyrsh, N.; Keppner, H., Photovoltaic Technology: The Case of Thin-Film Solar Cells. *Science* **1999**, *285*, 692-698.
- (7) Pattantyus-Abraham, A. G.; Kramer, I. J.; Barkhouse, A. R.; Wang, X.; Konstantatos, G.; Debnath, R.; Levina, L.; Raabe, I.; Nazeeruddin, M. K.; Grätzel, M.; Sargent, E. H., Depleted-Heterojunction Colloidal Quantum Dot Solar Cells. *ACS Nano.* **2010**, *4*, 3374-3380.
- (8) Kramer, I. J.; Sargent, E. H., The Architecture of Colloidal Quantum Dot Solar Cells: Materials to Devices. *Chem Rev.* **2014**, *114*, 863-882.
- (9) Luther, J. M.; Gao, J.; Lloyd, M. T.; Semonin, O. E.; Beard, M. C.; Nozik, A. J., Stability Assessment on a 3% Bilayer PbS/ZnO Quantum Dot Heterojunction Solar Cell. *Adv. Mater.* **2010**, *22*, 3704-3707.
- (10) Liu, Y.; Gibbs, M.; Perkins, C. L.; Tolentino, J.; Zarghami, M. H.; Bustamante, J.; Law, M., Robust, functional nanocrystal solids by infilling with atomic layer deposition. *Nano Lett.* **2012**, *11*, 5349-5355.
- (11) Nozik, A. J.; Beard, M. C.; Luther, J. M.; Law M.; Ellingson, R. J.; Johnson, J. C., Semiconductor Quantum Dots and Quantum Dot Arrays and Applications of Multiple Exciton Generation to Third-Generation Photovoltaic Solar Cells. *Chem Rev.* **2010**, *110*, 6873-6890.
- (12) Mane, R. S.; Lokhande, C. D., Chemical deposition method for metal chalcogenide thin films. *Mater. Chem. Phys.* **2000**, *65*, 1-31.
- (13) Jiang, C. W.; Green, M. A., Silicon quantum dot superlattices: Modeling of energy bands, densities of states, and mobilities for silicon tandem solar cell applications. *J Appl Phys.* **2006**, *99*, 114902.
- (14) Lazarenkova, O. L.; Balandin, A. A., Miniband formation in a quantum dot crystal. *J Appl Phys.* **2001**, *89*, 5509-5515.

- (15) Bolivar-Rodriguez, S.; Campos-Gomez, F. M.; Luque-Rodriguez, A.; Lopez-Villanueva, J. A.; Jimenez-Tejada, J. A.; Carceller, J. E., Miniband structure and photon absorption in regimented quantum dot systems. *J Appl Phys.* **2011**, *109*, 074303.
- (16) Liu, Y.; Gibbs, M.; Puthussery, J.; Gaik, S.; Ihly, R.; Hillhouse, H. W.; Law, M., Dependence of Carrier Mobility on Nanocrystal Size and Ligand Length in PbSe Nanocrystal Solids. *Nano Lett.* **2010**, *10*, 1960-1969.
- (17) Law, M.; Beard, M. C.; Choi, S.; Luther, J. M.; Hanna, M. C.; Nozik, A. J., Determining the Internal Quantum Efficiency of PbSe Nanocrystal Solar Cells with the Aid of Optical Model. *Nano Lett.* **2008**, *8*, 3904-3910.
- (18) Ip, A. H.; Thon, S. M.; Hoogland, S.; Voznyy, O.; Zhitomirsky, D.; Dehnath, R.; Levina, L.; Rollny, L. R.; Carey, G. H.; Fischer, A.; Kemp, K. W.; Kramer, I. J.; Ning, Z.; Labelle, A. J.; Chou, K. W.; Amassian, A.; Sargent, E. H., Hybrid passivated colloidal quantum dot solids. *Nature Nano.* **2012**, *7*, 577-582.
- (19) Hanrath, T., Colloidal nanocrystal quantum dot assemblies as artificial solids. *J. Vac. Sci. Technol, A* **2012**, *30*, 030802.
- (20) Luther, J. M.; Law, M.; Song, Q.; Perkins, C. L.; Beard, M. C.; Nozik, A. J., Structural, Optical, and Electrical Properties of Self-Assembled Films of PbSe Nanocrystals Treated with 1,2-Ethanedithiol. *ACS Nano.* **2008**, *2*, 271-280.
- (21) Sze, S. M.; Ng, K. K. *Physics of Semiconductor Devices, Third Edition*, Wiley, New York, **2007**.
- (22) Li Q.; Zhang, W.; Miljanic, O. S.; Sue, C.-H.; Zhao, Y.-L.; Liu, L.; Knobler, C. B.; Stoddart, J. F.; Yaghi, O. M., Docking in Metal-Organic Frameworks. *Science* **2009**, *325*, 855-859.
- (23) Calculations were performed using the Gaussian 09 software package. The geometries were optimized at the B3LYP/6-311G(d,p) level, and energies were calculated at the same level.
- (24) Yuan, M.; Zhitomirsky, D.; Adinolfi, V.; Voznyy, O.; Kemp, K. W.; Ning, Z.; Lan, X.; Xu, J.; Kim, J. Y.; Dong, H.; Sargent, E. H., Doping control via molecularly engineered surface ligand coordination. *Adv. Mater.* **2013**, *25*, 5586-5592.
- (25) Hwang, J.-J.; Tour, J. M., Combinatorial synthesis of oligo(phenylene ethynylene)s. *Tetrahedron* **2002**, *58*, 10387-10405.
- (26) Ellingson, R. J.; Beard, M. C. Johnson, J. C.; Yu P.; Micic, O.; Nozik, A. J.; Shabaev, A.; Efros, A. L., Highly Efficient Multiple Exciton Generation in Colloidal PbSe and PbS Quantum Dots. *Nano Lett.* **2005**, *5*, 865-871.
- (27) Schaate, A.; Roy, P.; Preube, T.; Lohmeier, S. J.; Godt, A.; Behrens, P., Porous interpenetrated zirconium-organic frameworks (PIZOFs): a chemically versatile family of metal-organic frameworks. *Chem. Eur. J.* **2011**, *17*, 9320-9325.
- (28) Zhao, Y.-L.; Liu, L.; Zhang, W.; Sue, C.-H.; Li, Q.; Miljanic, O. S.; Yaghi, O. M.; Stoddart, J. F., Rigid-strut-containing crown ethers and [2]catenanes for incorporation into metal-organic frameworks. *Chem. Eur. J.* **2009**, *15*, 13356-13380.

- (29) Polyansky, D. E.; Danilov, E. O.; Voskresensky, S. V.; Rodgers, M. A. J.; Neckers, D. C., Delocalization of Free Electron Density through Phenylene-Ethynylene: Structural Changes Studied by Time-Resolved Infrared Spectroscopy. *J. Am. Chem. Soc.* **2005**, *127*, 13452-13453.
- (30) Wang, X.-Y.; Yang, D.-C.; Zhuang, F.-D.; Liu, J.-J.; Wang, J.-Y.; Pei, J., Postfunctionalization of BN-Embedded Polycyclic Aromatic Compounds for Fine-Tuning of Their Molecular Properties. *Chem. Eur. J.* **2015**, *21*, 8867-8873.
- (31) Law, M.; Luther, J. M.; Song, Q.; Hughes, B. K.; Perkins, C. L.; Nozik, A. J., Structural, optical, and electrical properties of PbSe nanocrystal solids treated thermally or with simple amines. *J. Am. Chem. Soc.* **2008**, *130*, 5974-5985.
- (32) Murray, C. B.; Sun, S. H.; Gaschler, W.; Doyle, H.; Betley, T. A.; Kagan, C. R., Colloidal synthesis of nanocrystals and nanocrystal superlattices. *IBM J. Res. Dev.* **2001**, *45*, 47-56.
- (33) Moreels, I.; Lambert, K.; De, Muynck, D.; Vanhaecke, F.; Poelman, D.; Martins, J. C.; Allan, G.; Hens, Z., Composition and Size-Dependent Extinction Coefficient of Colloidal PbSe Quantum Dots *Chem. Mater.* **2007**, *19*, 6101-6106.
- (34) Moreels, I.; Fritzinger, B.; Martins, J. C.; Hens, Z., Surface chemistry of colloidal PbSe nanocrystals. *J. Am. Chem. Soc.* **2008**, *130*, 15081-15086.
- (35) Hens, Z.; Martins, J. C., A Solution NMR Toolbox for Characterizing the Surface Chemistry of Colloidal Nanocrystals. *Chem. Mater.* **2013**, *25*, 1211-1221.
- (36) Sachleben, J.; Wooten, E.; Emsley, L.; Pines, A.; Colvin, V.; Alivisatos, A., NMR studies of the surface structure and dynamics of semiconductor nanocrystals. *Chem. Phys. Lett.* **1992**, *198*, 431-436.
- (37) Hostetler, M. J.; Wingate, J. E.; Zhong, C.-J.; Harris, J. E.; Vachet, R. W.; Clark, M. R.; Londono, J. D.; Green, S. J.; Stokes, J. J.; Wignall, G. D.; Glish, G. L.; Porter, M. D.; Evans, N. D.; Murray, R. W., Alkanethiolate Gold Cluster Molecules with Core Diameters from 1.5 to 5.2 nm: Core and Monolayer Properties as a Function of Core Size. *Langmuir* **1998**, *14*, 17-30.
- (38) This project is a collaboration project of Guan Lab and Law Group. The GISAXS measurements and FET tests were conducted by Dr. Brandon Mercado from Law group.

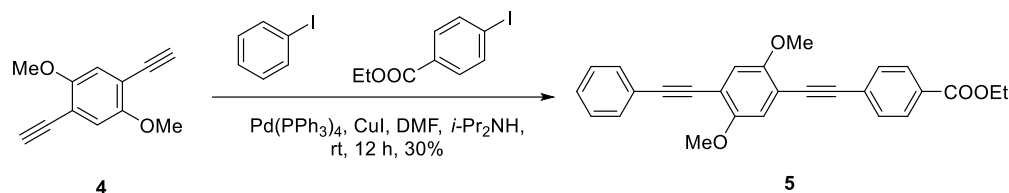
5.10 Experimental

General. All commercially available chemicals were used without further purification unless otherwise noted. Column chromatography was performed with silica gel. Analytical thin-layer chromatography (TLC) was performed on 0.2 mm silica gel-coated glass sheets with F254 indicator. All yields given refer to isolated yields. Nuclear Magnetic Resonance (NMR) spectra were recorded on 500 MHz or 600 MHz Bruker spectrometers. Chemical shifts were reported in ppm. Coupling constants (J values) were reported in Hertz. ^1H NMR chemical shifts were referenced to CDCl_3 ($\delta = 7.26$ ppm) or d_6 -DMSO ($\delta = 2.50$ ppm). ^{13}C NMR chemical shifts were referenced to CDCl_3 ($\delta = 77.00$ ppm) or d_6 -DMSO ($\delta = 39.52$ ppm). ESI-HRMS spectra were recorded on a Waters (Micromass) LC-TOF Mass Spectrometer. Transmission electron microscopy (TEM) characterization was performed on a Philips CM20 operating at 200 kV. Scanning electron microscopy (SEM) images were obtained by an FEI Magellan 400 XHR scanning electron microscope operated at an accelerating voltage of 1.0 kV. Absorption spectra were recorded on PerkinElmer Lambda 950 UV-Vis Spectrometer. FTIR measurements were carried out on nanocrystal films deposited on double-side polished intrinsic silicon substrates using either a JASCO 4100 or Nicolet 6700 spectrometers.

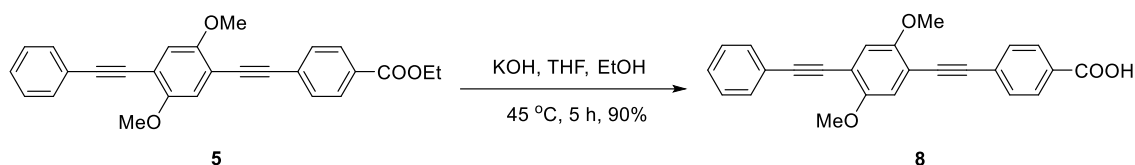
Synthetic Procedures

Organic Synthesis

Compounds **1-4** were synthesized by following previous literature¹⁻³.



Compound 5. A mixture of compound **4** (250 mg, 1.34 mmol), iodobenzene (274 mg, 1.34 mmol), ethyl 4-iodobenzoate (370 mg, 1.34 mmol), $\text{Pd(PPh}_3)_4$ (31 mg, 0.027 mmol), CuI (10 mg, 0.05 mmol), diisopropylamine (5 mL), and DMF (20 mL) was degassed for 30 min. The degassed solution was stirred at room temperature overnight under a nitrogen atmosphere. The reaction mixture was cooled to room temperature and extracted with CH_2Cl_2 . The organic layer was washed with brine and dried over anhydrous Na_2SO_4 . After removal of the solvent under reduced pressure, the residue was purified by column chromatography over silica gel (eluent: Hexane/ EtOAc = 7:3) to give compound **5** as a white solid (165 mg, 30%). ^1H NMR (600 MHz, CDCl_3 , 298 K, ppm): δ 8.03 (d, J = 8.6 Hz, 2H), 7.62 (d, J = 8.6 Hz, 2H), 7.59–7.56 (m, 2H), 7.38–7.33 (m, 3H), 7.05 (s, 1H), 7.04 (s, 1H), 4.39 (q, J = 7.1 Hz, 2H), 3.92 (s, 3H), 3.91 (s, 3H), 1.41 (t, J = 7.1 Hz, 3H); ^{13}C NMR (125 MHz, CDCl_3 , 298 K, ppm): δ 165.9, 153.9, 153.7, 131.6, 131.4, 129.7, 129.3, 128.4, 128.2, 127.7, 123.0, 115.5, 115.4, 113.9, 112.5, 95.2, 94.0, 88.6, 85.5, 61.0, 56.30, 56.26, 14.19; HRMS (ESI) m/z : Calcd for $\text{C}_{27}\text{H}_{22}\text{O}_4$: 411.1596; Found: 411.1595 $[\text{M} + \text{H}]^+$.



Compound 6. A solution of KOH (684 mg, 1.22 mmol) in EtOH (10 mL) was added dropwise into a solution of compound **5** (500 mg, 1.22 mmol) in THF (60 mL). The reaction mixture was heated to 45 °C and stirred for 5 h. After cooling to room temperature, the reaction mixture was acidified by 1 M HCl and extracted with CH₂Cl₂. The organic layer was washed with brine and dried over anhydrous Na₂SO₄. After removal of the solvent under reduced pressure, the residue was purified by recrystallization with isopropyl alcohol to give compound **6** as a pale yellow solid (419 mg, 90%). ¹H NMR (600 MHz, *d*₆-DMSO, 298 K, ppm): δ 13.17 (s, 1H), 7.98 (d, *J* = 8.3 Hz, 2H), 7.66 (d, *J* = 8.3 Hz, 2H), 7.56–7.54 (m, 2H), 7.47–7.41 (m, 3H), 7.23 (d, *J* = 8.5 Hz, 2H), 3.86 (s, 6H); ¹³C NMR (125 MHz, *d*₆-DMSO, 298 K, ppm): δ 166.7, 153.6, 153.5, 131.4, 131.3, 130.6, 129.6, 129.0, 128.8, 126.7, 122.4, 115.7, 115.6, 113.1, 112.0, 94.9, 93.9, 88.8, 86.0, 56.33, 56.31; HRMS (ESI) *m/z*: Calcd for C₂₇H₁₇O₄: 381.1127; Found: 381.1128 [M - H]⁻.

QD Synthesis

PbSe QDs were synthesized and purified using standard air-free Murray synthesis.⁴ In a typical synthesis, a solution of 1.57 g PbO (7.03 mmol), 5.11 g oleic acid (18.1 mmol), and 10.0 g 1-octadecene (ODE) (39.6 mmol) was degassed in a three-neck flask and heated at 100 °C for one hour to dissolve the PbO and dry the solution. 9.5 mL of a 1 M solution of TOP-Se containing 0.214 g diphenylphosphine (DPP) (1.15 mmol) was then rapidly injected into this hot solution. The QDs were grown for short times (~1.5 minutes), and the

reaction was then quenched with a water bath and 10 mL of anhydrous hexane. The QDs were purified by three rounds of dispersion/precipitation in hexane/ethanol and stored in a glove box as a powder.

Ligand Exchange and Film Construction

*Solid-state Ligand Exchange with **TPE** and QD Film Deposition*

Films of oleate-capped QDs (“as-made films”) were made by spin coating a 30 mg mL⁻¹ solution of QDs in octane at 600 rpm for 30 seconds, followed by 4020 rpm for 10 seconds. In a similar fashion to the as-made QD films, TPE treated PbSe QD films were fabricated by first spin coating a 30 mg mL⁻¹ solution of QDs in octane. Thin films for FETs were made at 1200 rpm for 30 seconds, followed by 4020 rpm for 10 seconds. Thick films for XRD and FTIR studies were made at 600 rpm for 30 seconds, followed by 4020 rpm for 10 seconds. All films were subsequently immersed in 23.5 mM solution of TPE for 20 minutes and subsequently washed with DMSO and hexane to remove any unbound ligand remaining on the surface.

A mechanical dip coater mounted inside of a glovebox (DC Multi-4, Nima Technology) was used to prepare PbSe QD films via a layer-by-layer procedure described in detail elsewhere.⁵ Briefly, the substrates (silicon or pre-patterned FET cleaned by sonication in isopropyl alcohol followed by drying under an N₂ flow) were alternately dipped into a 2 mg mL⁻¹ solution of QDs in dry hexane and then a 2.0 mM solution of molecular wire in dimethyl sulfoxide (DMSO). A third beaker containing neat, dry DMSO was used to rinse the films after each dip in the molecular wire solution in order to remove any residual ligand. A fourth beaker containing neat, dry acetonitrile was used for a final

wash of the QD film and to aid in the removal DMSO. We fabricated films with thicknesses in the range of 25-100 nm (thin for FETs, thicker for FTIR and XRD studies).

*Solution-phase Ligand Exchange with **mTPE** and QD Film Deposition*

Replacement of oleate ligands for **mTPE** was accomplished by first dissolving 200 mg (0.523 mmol) of mTPE in 4 mL THF, which was slowly added to a 5 mg mL⁻¹ solution of oleate-capped PbSe QDs (4 mL). The flocculated solution was centrifuged and washed with a 1:1 mixture of THF and isopropanol to remove any excess ligand. This washing procedure was repeated twice more. The resulting QD pellet was re-dispersed in THF (5 mg/mL) for immediate film fabrication.

Films of oleate-capped QDs were made by spin coating a 30 mg mL⁻¹ solution of QDs in hexane at 600 rpm for 30 seconds, followed by 4020 rpm for 10 seconds. Thin films of mTPE-1 capped QDs were made by spin coating a 20 mg mL⁻¹ solution of QDs in THF under different conditions (**Table 5.3**).

Morphology Study of TPE-functionalized PbSe QD Film

While SEM images provide a limited window into QD arrangement, grazing incidence small angle X-ray scattering (GISAXS) patterns provide quantitative measurements of millimeter-wide areas of our thin films. **Figure 5.8g-i** shows a portion of the GISAXS patterns for the as-made oleate-capped, ordered and glassy TPE-capped PbSe QD films. The as-made oleate-capped PbSe QD films fabricated by spin coating produced a spot pattern indicative of a high degree of crystalline order between QDs. We azimuthally integrated the intensity profile for the GISAXS patterns over all q vectors in order to extract

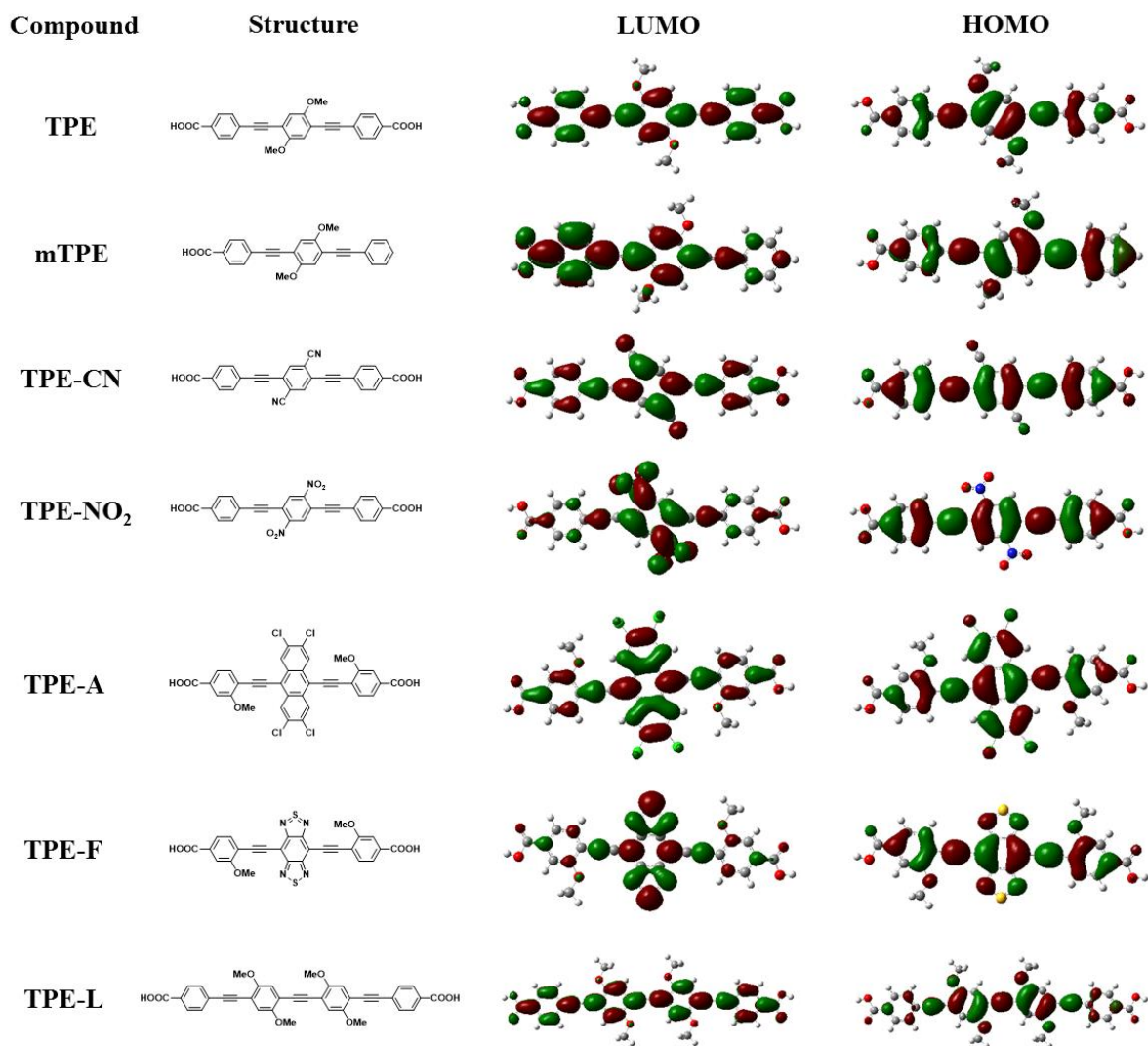
the lattice constant and crystal system. The peak positions were indexed and found to closely align with an fcc structure. The lattice constant of this fcc-like pattern was determined to be $a_{fcc} = 13.2 \pm 0.5$ nm, which matches well with previous reports of PbSe QD superlattices made from particles of similar size.⁶ We determined the PbSe QD separation by analyzing the spacing between QD surfaces along the closest-packed [hkl] direction. In an fcc lattice, the nearest neighbor distance between QD surfaces, δ_{NN} , is along the [110] diagonal of the PbSe QD lattice and determined to be 3.25 nm.⁷

FET Device Fabrication and Characterization

The linear mobilities (μ_{lin}) were extracted from the transfer curves at constant V_{SD} according to established methods.⁸ At room temperature, both ordered and disordered films act as *p*-type depletion-mode devices with mobilities of $3.10 \times 10^{-2} \text{ cm}^2 \text{ V}^{-1} \text{ s}^{-1}$ and $1.62 \times 10^{-4} \text{ cm}^2 \text{ V}^{-1} \text{ s}^{-1}$, respectively. The value obtained from ordered TPE-capped PbSe QD films is comparable to values reported for glassy films with short diacid ligands, which is notable considering the substantially larger inter-dot distances (~ 2 nm) in our ordered TPE-capped PbSe films when compared to the traditional QD films with small ligands (< 0.5 nm).⁹⁻¹¹ The electrical performance of these *I-V* data were also obtained at 80 K with both ordered and glassy films acting as unipolar *p*-type devices with mobilities of $2.04 \times 10^{-1} \text{ cm}^2 \text{ V}^{-1} \text{ s}^{-1}$ and $1.74 \times 10^{-3} \text{ cm}^2 \text{ V}^{-1} \text{ s}^{-1}$, respectively. There is an over 100-fold increase in mobility value from glassy to ordered films at both room and low temperature.

Computational Studies

Calculations were performed using the Gaussian 09 software package.¹² The geometries were optimized at the B3LYP/6-311G(d, p) level, and energies were calculated at the same level. The calculated molecular orbitals and corresponding energy levels of designed functional molecular wires are shown below.



5.11 References for Experimental

- (1) Schaate, A.; Roy, P.; Preube, T.; Lohmeier, S. J.; Godt, A.; Behrens, P., Porous interpenetrated zirconium-organic frameworks (PIZOFs): a chemically versatile family of metal-organic frameworks. *Chem. Eur. J.* **2011**, *17*, 9320-9325.
- (2) Zhao, Y.-L.; Liu, L.; Zhang, W.; Sue, C.-H.; Li, Q.; Miljanic, O. S.; Yaghi, O. M.; Stoddart, J. F., Rigid-strut-containing crown ethers and [2]catenanes for incorporation into metal-organic frameworks. *Chem. Eur. J.* **2009**, *15*, 13356-13380.
- (3) Polyansky, D. E.; Danilov, E. O.; Voskresensky, S. V.; Rodgers, M. A. J.; Neckers, D. C., Delocalization of Free Electron Density through Phenylene-Ethynylene: Structural Changes Studied by Time-Resolved Infrared Spectroscopy. *J. Am. Chem. Soc.* **2005**, *127*, 13452-13453.
- (4) Murray, C. B.; Sun, S. H.; Gaschler, W.; Doyle, H.; Betley, T. A.; Kagan, C. R., Colloidal synthesis of nanocrystals and nanocrystal superlattices. *IBM J. Res. Dev.* **2001**, *45*, 47-56.
- (5) Law, M.; Luther, J. M.; Song, Q.; Hughes, B. K.; Perkins, C. L.; Nozik, A. J., Structural, optical, and electrical properties of PbSe nanocrystal solids treated thermally or with simple amines. *J. Am. Chem. Soc.* **2008**, *130*, 5974-5985.
- (6) Hanrath, T.; Choi, J. J.; Smilgies, D.-M., Structure/Processing Relationships of Highly Ordered Lead Salt Nanocrystal Superlattices. *ACS Nano*. **2009**, *3*, 2975-2988.
- (7) Choi, J. J.; Bealing, C. R.; Bian, K.; Hughes, K. J.; Zhang, W.; Smilgies, D. M., Controlling Nanocrystal Superlattice Symmetry and Shape-Anisotropic Interactions through Variable Ligand Surface Coverage. *J Am Chem Soc.* **2011**, *133*, 3131-3138.
- (8) Kagan, C. R.; Andry, P. *Thin-Film Transistors*. Marcel Dekker, Inc.: New York, **2003**.
- (9) Zarghami M, H.; Liu, Y.; Gibbs, M.; Gebremichael, E.; Webster, C.; Law, M., p-Type PbSe and PbS Quantum Dot Solids Prepared with Short-Chain Acids and Diacids. *ACS Nano*. **2010**, *4*, 2475.
- (10) Smith, A. R.; Yoon, W.; Heuer, W. B.; Baril, S. I. M.; Boercker, J. E.; Tischler, J. G.; Foos, E. E., Effect of Ligand Structure on the Optical and Electronic Properties of Nanocrystalline PbSe Films. *J Phys Chem C*. **2012**, *116*, 6031-6037.
- (11) Choi, J.-H.; Fafarman, A. T.; Oh, S. J.; Ko, D.-K.; Kim, D. K.; Diroll, B. T.; Muramoto, S.; Gillen, J. G.; Murray, C. B.; Kagan, C. R., Bandlike Transport in Strongly Coupled and Doped Quantum Dot Solids: A Route to High-Performance Thin-Film Electronics. *Nano Lett.* **2012**, *12*, 2631-2638.
- (12) Gaussian 09, Revision C.01, Frisch, M. J.; Trucks, G. W.; Schlegel, H. B.; Scuseria, G. E.; Robb, M. A.; Cheeseman, J. R.; Scalmani, G.; Barone, V.; Mennucci, B.; Petersson, G. A.; Nakatsuji, H.; Caricato, M.; Li, X.; Hratchian, H. P.; Izmaylov, A. F.; Bloino, J.; Zheng, G.; Sonnenberg, J. L.; Hada, M.; Ehara, M.; Toyota, K.; Fukuda, R.; Hasegawa, J.; Ishida, M.; Nakajima, T.; Honda, Y.; Kitao, O.; Nakai, H.; Vreven, T.; Montgomery, J. A.; Jr.; Peralta, J. E.; Ogliaro, F. M.; Bearpark; Heyd, J. J.; Brothers, E.; Kudin, K. N.; Staroverov, V. N.; Keith, T.; Kobayashi, R.; Normand, J.; Raghavachari, K.; Rendell, A.; Burant, J. C.;

Iyengar, S. S.; Tomasi, J.; Cossi, M.; Rega, N.; Millam, J. M.; Klene, M.; Knox, J. E.; Cross, J. B.; Bakken, V.; Adamo, C.; Jaramillo, J.; Gomperts, R.; Stratmann, R. E.; Yazyev, O.; Austin, A. J.; Cammi, R.; Pomelli, C.; Ochterski, J. W.; Martin, R. L.; Morokuma, K.; Zakrzewski, V. G.; Voth, G. A.; Salvador, P.; Dannenberg, J. J.; Dapprich, S.; Daniels, A. D.; Farkas, O.; Foresman, J. B.; Ortiz, J. V.; Cioslowski, J.; Fox, D. J. Gaussian, Inc., Wallingford CT, 2010.

5.12 NMR Spectra

